Role of Oxygen on Phase Stability, Precipitation, Deformation, and Oxidation in Pure Titanium and Beta Titanium Alloys

by

Kathleen Chou

A dissertation submitted in partial fulfillment
of the requirements for the degree of
Doctor of Philosophy
(Materials Science and Engineering)
in the University of Michigan
2021

Doctoral Committee:

Professor Emmanuelle Marquis, Chair
Professor Amit Misra
Assistant Professor Liang Qi
Professor John Shaw

Kathleen Chou

kachou@umich.edu

ORCID iD: 0000-0003-1974-4766

Acknowledgements

Over the past five years of my Ph.D., I have been very fortunate to receive incredible support from many individuals who have helped and guided me throughout this journey. With the many unexpected setbacks, new challenges, and difficult or exciting moments that come with conducting research, this support has been an invaluable part of the highs and lows of my graduate school experience. I sincerely appreciate all the encouragement I have received over the years that has helped me think about problems in new ways, try different approaches, and move through obstacles during my dissertation work.

First, I would like to give my deepest thanks and acknowledgments to my advisor, Prof. Emmanuelle Marquis. It has been a joy working together to discover new knowledge, and through her mentorship and encouragement, I have certainly become a better scientist, researcher, and scholar. Our discussions have pushed me to think more critically about my results and answer meaningful questions in the process. Next, I would like to express my thanks to my dissertation committee members, Profs. Amit Misra, Liang Qi, and John Shaw, who have given me valuable guidance, suggestions, and support in completing my thesis. I would also like to thank my former and current lab mates in the Marquis Research Group at the University of Michigan for both technical support and wonderful friendship over many years. I especially want to thank Peng-Wei Chu for his mentorship during the early years of my Ph.D.

I am sincerely grateful for the support from all the staff at the Michigan Center for Materials Characterization and Electron Microbeam Analysis Laboratory for technical advice and help throughout my graduate work. In particular, Owen Neill, Haiping Sun, Allen Hunter, and Bobby Kerns have provided me with important assistance and thoughtful conversations during my experimental work and data collection. Furthermore, I would like to thank John Foltz and Noah Philips at ATI for useful discussions and providing the initial titanium materials, without which this work would not be possible. I also sincerely appreciate the technical discussions and assistance from collaborators at the University of California, Santa Barbara (Prof. Anton Van der Ven, Prof. Carlos Levi, Harsha Gunda, and Mayela Aldaz) and Los Alamos National Laboratory (Nan Li).

I would like to acknowledge funding and support for this thesis work from the National Science Foundation through grants NSF DMR-1436154 and CMMI-1729166, and the Graduate Research Fellowship Program under grant No. DGE 1256260. Additionally, I gratefully acknowledge financial and technical support from the University of Michigan Center for Materials Characterization and the Robert B. Mitchell Electron Microbeam Analysis Laboratory, as well as instrument access at the Center for Integrated Nanotechnologies at Los Alamos National Laboratory. Travel support for conferences and research data collection was generously provided through the Rackham Graduate School at the University of Michigan.

Finally, I would like to thank my friends and family for their unwavering support throughout my Ph.D. The communities that I have been part of in graduate school through the Graduate Society of Women Engineers (GradSWE) and the Materials Science and Engineering department were a wonderful source of friendship, support, and fun throughout the last five years. The friends I have made throughout my life were also an integral part of my graduate school experience, helping me celebrate the joys and push through the hard moments of my Ph.D. Lastly, I will always be grateful for the love, pep talks, and encouragement from my fiancé, Brian, and my mom, dad, sister, and brother. Thank you for being the best support team for me during this process.

Table of Contents

List of Tables

List of Figures

List of Appendices

List of Abbreviations and Acronyms

APT	Atom probe tomography
BCC	Body centered cubic
BF-TEM	Bright-field transmission electron microscopy
BOR	Burgers orientation relationship
BSE	Backscattered electron
CRSS	Critical resolved shear stress
DA	Directly aged
DFT	Density functional theory
DF-TEM	Dark-field transmission electron microscopy
EBSD	Electron backscattered diffraction
EDS	Energy dispersive spectroscopy
FIB	Focused ion beam
HAADF	High-angle annular dark-field
HCP	Hexagonal close packed
IPF	Inverse pole figure
IVAS	Integrated Visualization and Analysis Software
LEAP	Local electrode atom probe
MoE	Molybdenum equivalency
NSF	National Science Foundation
ORL	Oxygen-rich layer
OXA	Oxidized and aged
RT	Room temperature
SAED	Selected area electron diffraction
SCCM	Standard cubic centimeter per minute
SEM	Scanning electron microscopy
SEM-BSE	Backscattered scanning electron microscopy

SOP	Standard operating procedure
STEM	Scanning transmission electron microscopy
TEM	Transmission electron microscopy
TRIP	Transformation induced plasticity
TWIP	Twinning induced plasticity
WDS	Wavelength dispersive spectroscopy
XRD	X-ray diffraction

Abstract

Titanium and its alloys exhibit many desirable properties, such as a high strength-to-weight ratio and excellent corrosion resistance, which result in their continued importance as structural materials particularly for aerospace and biomedical industries. However, titanium's reactivity with oxygen presents significant challenges to mechanical performance, including embrittlement caused by oxygen in solid solution and fast oxidation during high temperature exposures. Oxygen is therefore typically considered a detrimental element for titanium alloys. Commercial alloys commonly require strict limits on oxygen impurities to prevent embrittlement and are used at relatively low service temperatures to prevent material loss by oxidation. These challenges present opportunities for titanium alloy development. Oxygen has been shown to modify phase formation and precipitation sequences in metastable β titanium alloys containing high amounts of β-stabilizing elements, which resulted in novel mechanical behavior suggestive of potential new application spaces. Regarding oxidation, while the development of protective coatings has shown significant reductions in oxidation kinetics for Ti alloys, limited understanding still exists on how alloying elements might provide protection. Consequently, this thesis is organized in two parts. First, it argues that oxygen is not always detrimental by providing advancements in our understanding of the role of oxygen as an alloying element in β alloys. Second, when oxygen concentrations and oxidation need to be controlled, it details a possible approach to creating effective coatings using silicon.

The role of oxygen was demonstrated in a model β Ti-Nb alloy and commercial Ti-15-333 and Ti-15Mo alloys. Compositionally-graded microstructures were created using high temperature oxidation followed by ageing to understand oxygen's influence on metastable ω and stable α phase precipitation kinetics and morphologies. Multi-scale microstructural characterization methods including scanning electron microscopy, transmission electron microscopy, wavelength dispersive spectroscopy, atom probe tomography, and micropillar compression were utilized to evaluate microstructural evolution and mechanical behavior as a function of oxygen content. Elevated oxygen levels induced morphology, number density, and size changes for the metastable ω phase

and accelerated α nucleation rate. Notably, oxygen partitioning to ω during ageing resulted in increased resistance of ω to precipitate shearing and suppression of catastrophic failure during micropillar compression. While both oxygen and ω are known embrittlement risk factors, the stabilization of ω with oxygen leads to promising microstructures and mechanical properties. Furthermore, oxygen-induced refinement of α precipitates provides an additional pathway to obtain fine α laths that enable precipitation strengthening of β Ti alloys and very high strengths required for structural components. Finally, mechanistic understanding of Si's improvement of titanium oxidation resistance using Si-coated Ti specimens showed that Ti_5Si_3 silicide formation during oxidation exposures inhibited inward oxygen diffusion and formation of fast growing internal TiO_2 scales. This understanding may inform not only the design of better protective coatings for alloys used at elevated temperatures but also the tailoring of alloy chemistries leading to similar oxidation mechanisms.

In conclusion, the results detailed in this thesis address existing severe limitations associated with oxygen in titanium alloys. These findings directly impact commercial applications by providing design strategies to mitigate detrimental effects from interstitial oxygen, ω precipitation, and environmental degradation. This knowledge will contribute to future titanium alloy chemistry and processing development that utilizes beneficial impacts of elevated oxygen to enable new microstructures, properties, industrial material reuse, and commercial material specifications.

Chapter 1: Introduction

1.1 Motivation and background

Titanium and its alloys offer a desirable combination of high specific strength and stiffness, corrosion resistance, and biocompatibility that result in its importance as a structural material for many industries [1]. Demands for reducing weight to improve fuel efficiency and corrosion compatibility to polymer composite structures have motivated titanium alloy development for the transportation industry, predominantly for aerospace applications [2]. Additionally, biomedical implant materials, which require structural integrity and fatigue resistance in addition to biocompatibility, frequently utilize titanium alloys for components such as hip and knee implant replacements [3]. However, within both application spaces, several challenges still exist with current industrially produced Ti alloy compositions. One such drawback is the sensitivity of Ti alloys to small composition changes and interstitial elements such as oxygen that heavily influences their final microstructures and properties after processing [2]. Another issue is the reactivity of Ti with oxygen at room and elevated temperatures that results in strict processing controls and lack of oxidation resistance in hot environments [4]. In general, high levels of oxygen in solid solution in Ti alloys are considered detrimental to mechanical properties because of embrittlement concerns [5]. These limitations increase the general development time for new titanium alloy candidates and restrict titanium alloys use at elevated temperatures. Addressing these issues would therefore allow for increased implementation of Ti alloys resulting in better light weighting capabilities particularly in the aerospace industry.

β titanium alloys contain a large amount of β stabilizing elements like Nb, Mo, and V such that the β phase matrix is stabilized to room temperatures. These alloys may also form other precipitate phases during thermomechanical processing and are particularly sensitive to small changes in alloy chemistries and processing methods. This sensitivity leads to the wide variety of microstructures, deformation pathways, and mechanical properties that are observed for β Ti alloys

[6]. Many previous studies have focused on metastable phase stability and formation in these alloys, particularly for Ti-Nb based compositions that are highly biocompatible and have shown unique mechanical behavior in "gum-metal" like alloys [7]. More generally, the formation of metastable phases in β Ti alloys has been an active area of interest due to their role in controlling deformation behavior and influence on stable α precipitation. In particular, interstitial oxygen in solid solution significantly changes metastable phase stability and precipitation sequences in these alloys that directly influence deformation behavior. For example, the metastable ω phase, which forms rapidly during low temperature ageing leading to embrittlement [8], has shown phase stability changes with oxygen [9] that necessitate further fundamental study to understand ω's evolution and mechanical contribution with oxygen. Detailed understanding of oxygen's role as an alloying element in β Ti alloys may address known embrittlement challenges from ω phase formation, as well as allow for more tolerance for oxygen in chemistry standards and controls during titanium alloy processing. Evaluation of commercially produced β Ti alloys with elevated oxygen content is also needed to connect fundamental knowledge to industrially relevant products and applications.

Additionally, oxidation mechanism studies for pure titanium and titanium alloys have focused on the rapid dissolution of oxygen during high temperature exposures and fast oxidation kinetics [4]. These oxidation mechanisms result in rapid environmental degradation of Ti alloys at elevated temperatures due to loss of load bearing structural material and surface-level embrittlement that is more susceptible to crack formation [10]. Silicon-containing coatings have been demonstrated to slow oxidation progression for Ti alloys [11,12]. However, detailed understanding of silicon's contributions to improving oxidation resistance has not been investigated. This knowledge would allow for targeted development of advanced coatings and protection systems for Ti alloys exposed to high temperatures.

Given the existing challenges for titanium alloy use related to oxygen, the main topic discussed in this thesis is how oxygen influences the microstructural evolution, degradation, and mechanical properties of titanium alloys. Specifically, the important questions that this thesis addresses are the following:

1. How does interstitial oxygen in solid solution affect ω and α thermodynamic phase stability and precipitation in β Ti-Nb alloys?

2. What are the deformation mechanisms and mechanical properties of microstructures with oxygen-free and oxygen-stabilized ω in β Ti-Nb alloys?
3. How does elevated oxygen content affect precipitation kinetics and mechanical behavior in aged commercial β Ti alloys?
4. What is the mechanistic role of silicon in Si-containing coatings on improving oxidation resistance of pure Ti?

To answer these questions, experimental work was performed using multi-scale microstructural characterization methods including scanning electron microscopy (SEM), transmission electron microscopy (TEM), wavelength dispersive spectroscopy (WDS), atom probe tomography (APT), and micropillar compression testing. In particular, the use of high temperature oxidation exposures prior to isothermal ageing studies allowed the creation of compositionally gradient specimens with respect to interstitial oxygen content that uniquely enabled a systematic investigation of oxygen effects. The results from this work contribute to fundamental understanding of oxygen's effects on phase stability, precipitation, deformation, and oxidation in titanium alloys. These findings will contribute to future designs of titanium alloy compositions and heat treatment processes tailored to mitigate oxygen-induced microstructural changes, ω phase embrittlement, oxidation environmental degradation, and improved recyclability.

1.2 Thesis structure

This dissertation thesis is divided into eight main chapters. Following the introduction, **Chapter 2** provides a review of the literature and discussions of gaps in current knowledge for β Ti alloy phase stability, precipitation, and deformation and for pure Ti oxidation mechanisms. **Chapter 3** focuses on the role of interstitial oxygen on the precipitation kinetics and sequence of ω and α phases during ageing of a Ti-Nb alloy. **Chapter 4** extends this work to understand the effect of oxygen-stabilized ω precipitates on improving work hardening behavior of ω-strengthened Ti-Nb alloys. **Chapter 5** and **Chapter 6** investigate oxygen's contributions on precipitation and deformation in two aged commercial β Ti alloys. **Chapter 7** discusses the influence of Si-containing coatings on reducing internal oxidation rate of pure Ti through formation of titanium silicide phases. Finally, **Chapter 8** summarizes the conclusions for this work and gives suggestions for future investigations. **Appendices** contain additional details on sample preparation, experimental data collection, and supplemental data for the main chapters.

Chapter 2: Literature Review of Precipitation, Deformation, Oxygen Effects, and Oxidation of Ti Alloys

This chapter reviews the literature for precipitation and deformation of β Ti alloys. Specific information related to Ti-Nb and Ti-Mo alloy systems with a focus on oxygen effects are then discussed. Other related alloy systems such as Ti-V, which show similar precipitation behavior to the Ti-Nb and Ti-Mo systems, are not presented, but detailed information is available in Refs. [13–17]. Finally, the oxidation mechanisms of pure Ti and the effect of Si-containing coatings on oxidation resistance are reviewed and discussed.

2.1 β titanium alloys

Metastable β titanium alloys that have been developed for aerospace and biomedical structural applications offer a desirable combination of properties including high specific strength and stiffness, biocompatibility, and corrosion resistance [2,6]. These alloys, which typically include significant amounts of β stabilizing elements such as Nb, Mo, and V, characteristically contain a metastable bcc β phase matrix at room temperature [6]. The stable and metastable phase diagrams for the representative Ti-Nb system show the phase stability regions for varying compositions and temperatures (**Figure 2.1**) [18]. The thermodynamically stable phases are the low temperature α (hexagonally close packed - hcp) and high temperature β (body centered cubic - bcc) phases (**Figure 2.2**). Additionally, the stability of the β phase in these alloys with respect to metastable decomposition has been widely investigated [6]. Via thermomechanical processing treatments, the β phase can transform into additional metastable phases that include martensites α' (hcp) and α" (orthorhombic) [6], ω phase (hexagonal) [19], or recently reported nanoscale phases [20–23]. Highly β-stabilized alloys also show equilibrium immiscibility in the β phase, where spinodal decomposition can occur and result in β phase separation that may affect precipitate formation of α or other metastable phases [6]. The alloys in this thesis work will focus primarily on binary Ti-Nb (**Chapter 3** and **Chapter 4**) and Ti-Mo (**Chapter 6**) based compositions. Additional work on a Ti-V containing Ti-15-333 alloy (**Chapter 5**) also shows similar phase

formation sequences, but phase stability and precipitation kinetics in this alloy are affected by the addition of minor alloying elements such as Al, which heavily stabilizes the α phase.

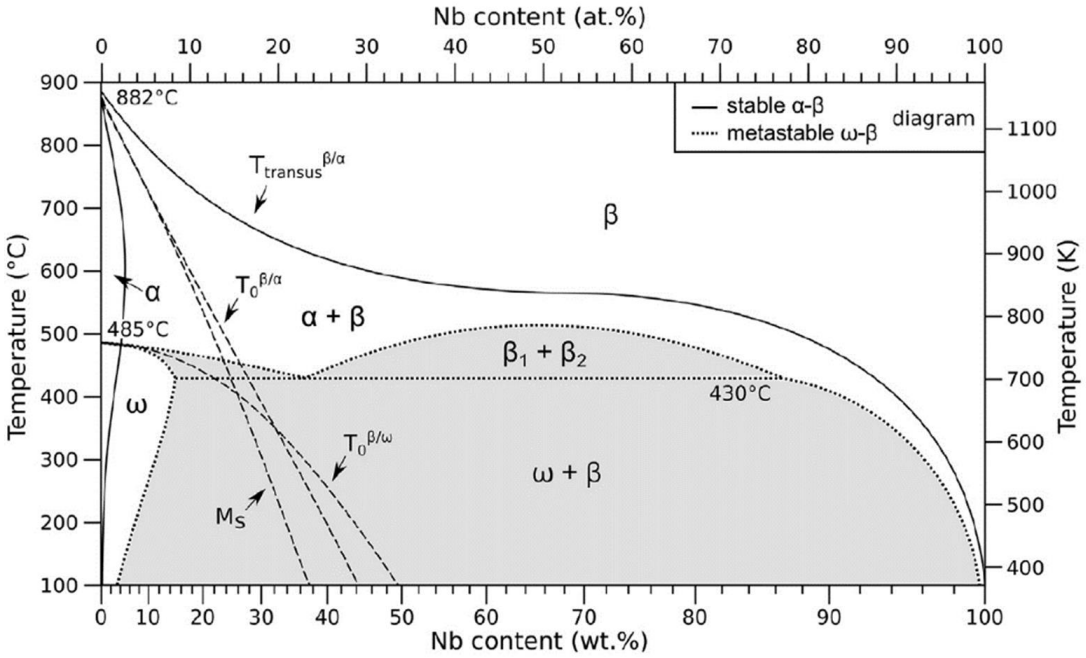

Figure 2.1: The calculated stable (α-β) and metastable (ω-β) phase diagrams of Ti-Nb. Gray areas represent two-phase regions and the miscibility gap in the metastable ω-β phase diagram. Adapted from Ref. [18].

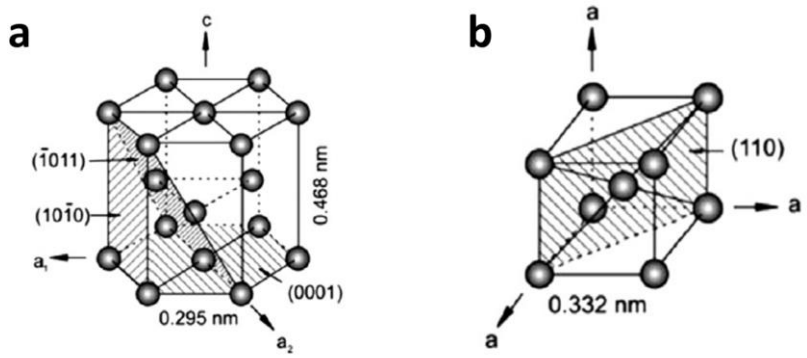

Figure 2.2: (a) The hcp (α) and bcc (β) structures of titanium. Adapted from Ref. [2].

2.1.1 Stable phases: α and β

Many properties for titanium alloys depend on microstructural evolution and phase transformation pathways for the α and β phases [1]. The ability to manipulate the structure and distribution of these phases depends on alloy composition and thermomechanical processing. The

β transus temperature is denoted as the temperature at which α transforms to β phase in the equilibrium phase diagram for a given alloy composition. Alloying elements are typically classified as α or β stabilizing elements. α stabilizers include Al, O, and N, whereas β stabilizers include Nb, Mo, V, Cr, Fe, and H [2]. These elements will partition to their respective stabilizing phases during ageing and increase thermodynamic stability of α or β. A third set of neutral alloying elements, such as Sn and Zr, do not significantly change the stability of either phase. For β stabilizing elements, isomorphous alloying elements such as Mo, V, Ta, and Nb may show a miscibility gap in their binary phase diagram with Ti but do not have invariant reactions, congruent transformations, or critical points [6]. Other β stabilizing elements such as Cr, Fe, Cu, Ni, and Si form intermetallic compounds through eutectoid reactions with Ti and are termed as eutectoid alloying elements [6].

The solid state phase transformation from β to α is governed by the Burgers orientation relationship (BOR) between these two phases: $\{110\}_\beta//(0001)_\alpha$; $<1\text{-}11>_\beta//<11\text{-}20>_\alpha$, which results in 12 possible crystallographic variants of α that can form from a single β parent grain [2]. α typically forms as a lath with broad, semi-coherent faces that contain structural ledges and dislocations [2]. In β-stabilizer rich alloys, α forms during isothermal heat treatment with a mostly uniform distribution of the 12 possible variants. α can also nucleate and grow at β grain boundaries with the BOR satisfied for one of the grains on either side of the boundary [2].

2.1.2 Metastable phases: martensite, nanoscale phases, ω

Several martensitic phases can form in β Ti alloys through a diffusionless transformation during rapid cooling from above a critical temperature called the martensite start temperature or during deformation above a critical stress level. Martensitic phases in β Ti alloys have an hcp (α') or orthorhombic (α") structure [18,24]. This crystallographic structure change for martensites occurs with greater β stabilizer solute content [25]. With high levels of β-stabilizing elements, the martensitic transformations are completely suppressed, forming only metastable β phase upon quenching [25]. The lattice correspondence between β and α" and the lath-like microstructure of α" formation are shown in **Figure 2.3**. The formation pathway for martensite from β (**Figure 2.4a**) involves several processes: 1) Bain distortion that transforms the cubic lattice to orthorhombic or hexagonal, 2) Lattice invariant shear by twinning or slip to obtain the invariant plane, 3) Shuffle

movement of atoms on alternating $(110)_\beta$ planes in a $[1\text{-}10]_\beta$ direction [2,26]. Martensitic phases may form during solution treatment and quenching from the β phase field or after the application of stress (stress-induced martensite) [24].

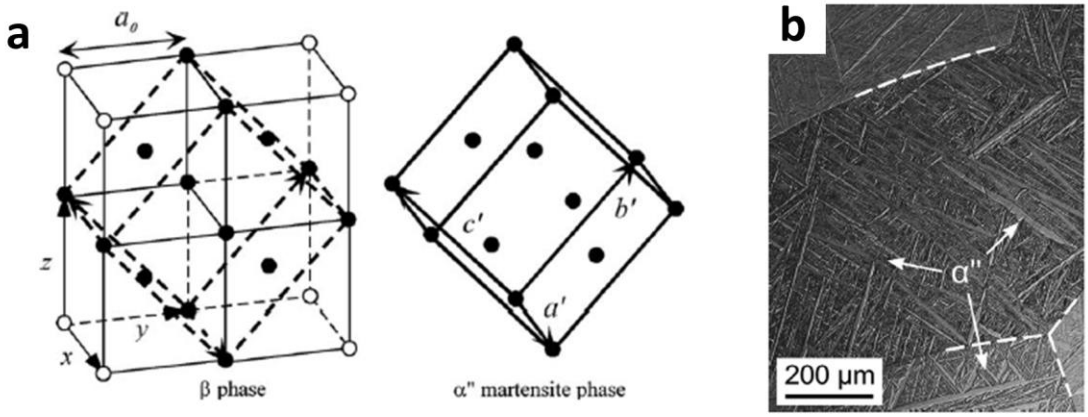

Figure 2.3: (a) A schematic illustration exhibiting lattice correspondence between β and α" phases. (b) Light microscopy images of α"-martensite in Ti-33Nb (wt. %). Adapted from Refs. [18,24].

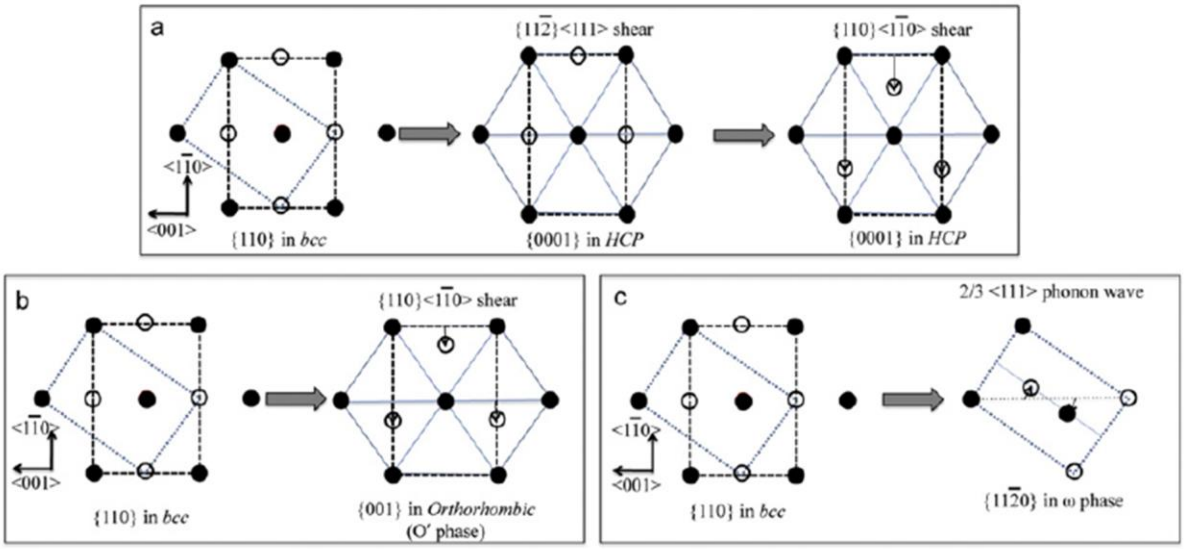

Figure 2.4: Schematic representations of the three different instabilities in the β phase in titanium alloys: (a) β to martensite; (b) β to nano-domains (O′ phase); (c) β to ω phase. Adapted from Ref. [26].

Recent studies have proposed several nanoscale phases that may form from the metastable β phase during solution treatment and quenching of β Ti alloys, particularly in alloy compositions where martensite formation is suppressed. For example, diffuse streaking and intensity maxima in the selected area diffraction patterns for β Ti alloys have been associated with nanodomains that

are formed through shuffle of $\{110\}_\beta$ planes without the Bain distortion [27]. Additionally, another nanoscale phase referred to as O' due to its reported orthorhombic structure may form through a similar pathway of atomic shuffling along the $\{110\}_\beta$ planes shown in **Figure 2.4b** [20,26]. Examples of diffuse streaking in selected area diffraction patterns attributed to the O' phase and the associated electron micrographs are shown in **Figure 2.5**. These nanoscale phases have been reported to coexist with the athermal ω phase that forms upon solution treatment and quenching. Other nanoscale features that have been reported in β Ti alloys include concentration modulations formed through spinodal decomposition during quenching [28]. These modulations result in chemically heterogeneous nanoscale regions that have different β phase stabilities and may lead to novel properties such as low modulus and tunable thermal expansion [21]. These nanoscale phases and instabilities are typically linked to the instability of the β phase obtained through chemical alloying coupled with solution treatment and quenching. The presence of these phases during thermomechanical processing may have a significant impact on deformation behavior and mechanical properties; therefore, investigation into stability and evolution of reported nanoscale phases has been of continuing scientific interest.

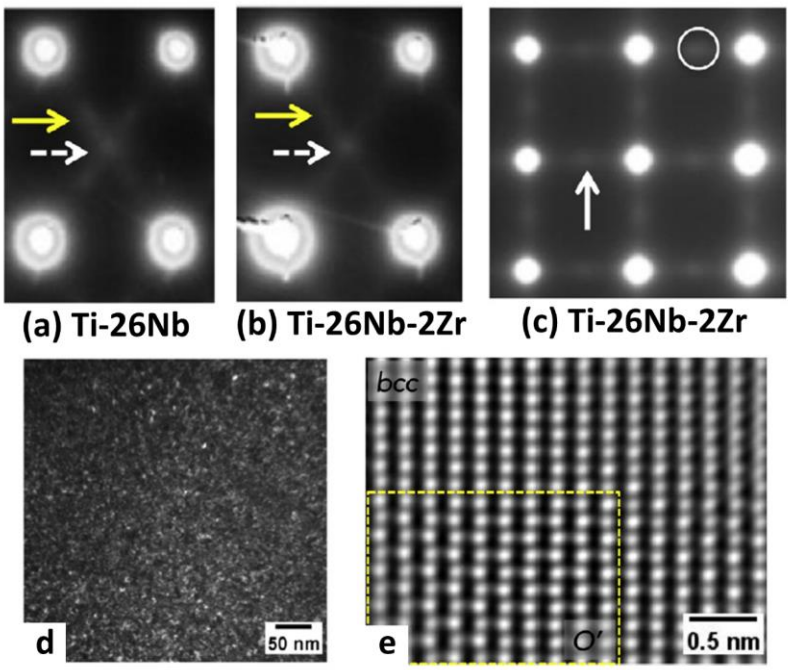

Figure 2.5: (a-c) Diffraction patterns from $[110]_\beta$ and $[100]_\beta$ zone axis of β quenched Ti–26Nb and Ti–26Nb–2Zr showing decreased intensity for ω reflections, streaking, and intensity maxima. (d) Dark-field TEM image and (e) high magnification HAADF-STEM image showing nano-domains (O' phase). Adapted from Ref. [26].

The metastable ω phase transformation in β Ti alloys occurs through diffusionless or diffusional processes. The ω phase forms rapidly during solution treatment and quenching (athermal ω) or during low temperature isothermal ageing below about 500 °C (isothermal ω) as a coherent particle in the β matrix [19]. ω's transformation pathway (**Figure 2.4c**) involves a displacive partial collapse of $\{111\}_\beta$ planes in the β structure [29,30]. The transformation continues with a complete collapse of these planes, followed by growth and coarsening of ω precipitates and diffusional rejection of β stabilizing elements from ω. The partial collapse of $\{111\}_\beta$ planes yields a trigonal structure, while a complete plane collapse will show a hexagonal structure [19]. The orientation relationship between β to ω is reported as: $\{111\}_\beta//(0001)_\omega$; $<1\text{-}10>_\beta//<11\text{-}20>_\omega$ [19]. The athermal ω transformation is the diffusionless transformation that takes place upon quenching, and the morphology of the athermal ω phase is generally an ellipsoid with the major axis aligned with the $<111>_\beta$ directions. However, during isothermal ageing, two morphologies have been observed for isothermal ω precipitates. The changes in these morphologies have been attributed to the lattice misfit between the ω and β phases in different alloy systems [19,31]. Low misfit systems such as Ti-Nb and Ti-Mo exhibit ellipsoidal ω particles, while high misfit systems such as Ti-V tend to form cuboidal ω precipitates with the edges of cuboids aligned along $<100>_\beta$ (**Figure 2.6**). Deformation may also induce the β to ω transformation, and this transformation can be triggered by elastic strain or stress without plastic deformation [32]. Finally, ω is known to form directly from the low temperature α phase at high pressures through pressure induced transformations [19].

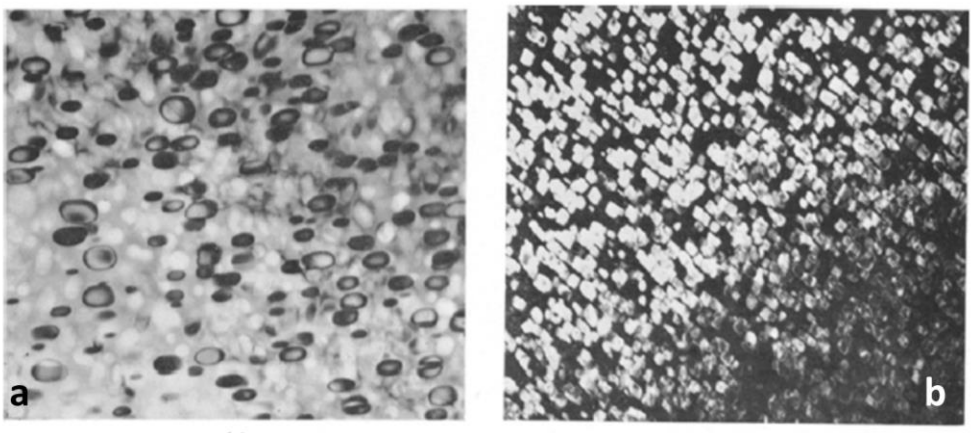

Figure 2.6: Transmission electron microscopy images showing (a) ellipsoidal ω precipitates in Ti-35 wt. % Nb and (b) cuboidal ω precipitates in Ti-20 wt. % V. Adapted from Ref. [31].

2.1.3 Phase transformation sequence and ageing behavior

Heat treatment and thermomechanical processing are commonly utilized for β Ti alloys to control microstructure and mechanical properties. Solution treatment and ageing allows for controlled second-phase formation of both stable and metastable phases, and this precipitation behavior is linked to the instability of the β phase at temperatures below the β transus. For metastable β Ti alloys, a pseudo-binary phase diagram (**Figure 2.7**) illustrates the stability regions for both stable and metastable phases and can be used to tailor heat treatment strategies [6]. During solution treatment and quenching, the alloy is heated to a sufficiently high temperature (typically above the β transus) to dissolve any second-phase particles that are not thermodynamically stable at this temperature. This dissolution forms a homogeneous β phase microstructure in the alloy, which is then rapidly cooled (called "quenching") to room temperature to retain the metastable β phase matrix with minimal second-phase formation. However, martensite phases, athermal ω, and other previously discussed nanoscale phases formed through diffusionless processes may form during quenching. Excessive lengths of time for solution treatment may also result in rapid β phase grain growth and coarsening.

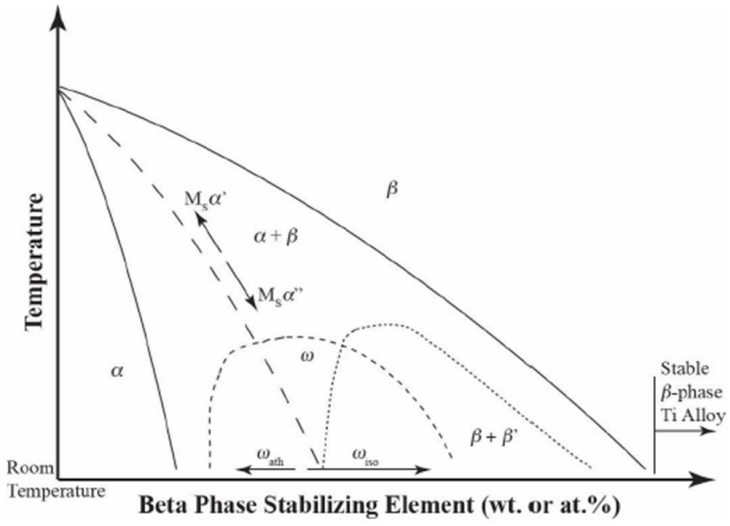

Figure 2.7: Schematic of a pseudo-binary isomorphous phase diagram showing martensite start temperature, metastable ω phase field, metastable β phase field, and equilibrium α phase field. Adapted from Ref. [6].

Ageing heat treatments are employed after solution treatment and quenching to induce precipitate formation that typically increases strength and hardness but reduces ductility of β Ti alloys [6]. Ageing is conducted at temperatures below the β transus and may consist of one or

several steps to target specific phase formation and microstructures. High and low temperature ageing treatments show different phase transformation sequences due to the stability of intermediate metastable phases [6]. High temperature ageing is conducted at approximately 450-650 °C in the α + β phase field region and results in the direct precipitation of equilibrium α at β grain boundaries and in intragranular regions. The size, volume fraction, and number density of α precipitates depend on the alloy composition and time at the ageing temperature [33]. Generally, finer α precipitates are desired to obtain higher tensile strengths for structural applications [34]. Low temperature ageing at approximately 450 °C and below may allow the formation of intermediate metastable phases such as the isothermal ω phase or phase separated β' before the equilibrium α phase. Depending on the solute levels for β-stabilizing elements, the phase decomposition sequence during low temperature ageing will be as follows [6]:

$$\text{Lower solute level: } \beta \rightarrow \beta + \omega_{iso} \rightarrow \beta + \omega_{iso} + \alpha \rightarrow \beta + \alpha$$

$$\text{Higher solute level: } \beta \rightarrow \beta + \beta' \rightarrow \beta + \beta' + \alpha \rightarrow \beta + \alpha$$

Generally, the alloy compositions in this thesis work follow the precipitation sequence for lower solute levels. During low temperature ageing, α precipitation kinetics for Ti-Nb alloy compositions in this thesis work are relatively slow, requiring long ageing times ranging from 10s-100s of hours to destabilize intermediate metastable phases. However, compositions containing Mo and V are reported to show faster transformation kinetics for metastable precipitates during ageing [13,35]. Finally, recent studies have investigated the influence of isothermal ω as a heterogeneous nucleation agent for more refined α formation during isothermal ageing [36–39] and multi-step ageing [34]. Nucleation and growth mechanisms reported for resultant α formation have suggested influences from compositional and structural instabilities of isothermal ω precipitates [38–40].

2.1.4 Deformation behavior

β phase stability and the phase decomposition sequence during heat treatment and processing directly influence the ensuing deformation mechanisms during tensile or compressive loading. Deformation may occur in the bcc β matrix through conventional dislocation slip, deformation twinning, or stress-induced phase transformations. Generally, the solution treated and quenched state for these alloys with the absence of diffusional precipitation will show higher

ductility, lower modulus, and lower yield strengths. For a given alloy, β's phase stability heavily influences and controls the resulting deformation behavior for solution treated and quenched alloys [6]. Dislocation slip generally dominates plastic deformation in stable β Ti alloys, while less stable β phase allows activation of {112}<111>$_\beta$ twinning, {332}<113>$_\beta$ twinning, and stress-induced α" martensite [6]. With the wide range of deformation mechanisms for solution treated and quenched alloys with metastable β phase, several studies have attempted to predict deformation behavior for dislocation slip, martensitic transformation, and deformation twinning using different parameters such as bond order and molecular electron d-orbital energy level (Bo-Md) [41,42]. An example of a Bo-Md plot that predicts deformation modes using alloy composition is shown in **Figure 2.8a**. Recent studies have also used parameters such as atomic radius difference and valence electron concentration, which are important for phase stability in high entropy alloys/multi-principle component alloys, to predict deformation behavior [42]. Transformation induced plasticity (TRIP) from stress-induced martensite formation and twinning induced plasticity (TWIP) from deformation twinning (**Figure 2.8b-c**) that result in high ductility and plasticity have been reported for solution treated and quenched alloys [43]. The martensitic transformation present in these alloy systems may also allow for shape memory or superelastic mechanical behavior depending on the specific martensite and austenite transformation temperatures [24,44]. Typical recoverable strains for the martensitic transformation up to ~5% for orthorhombic martensite have been reported for β Ti alloys [45].

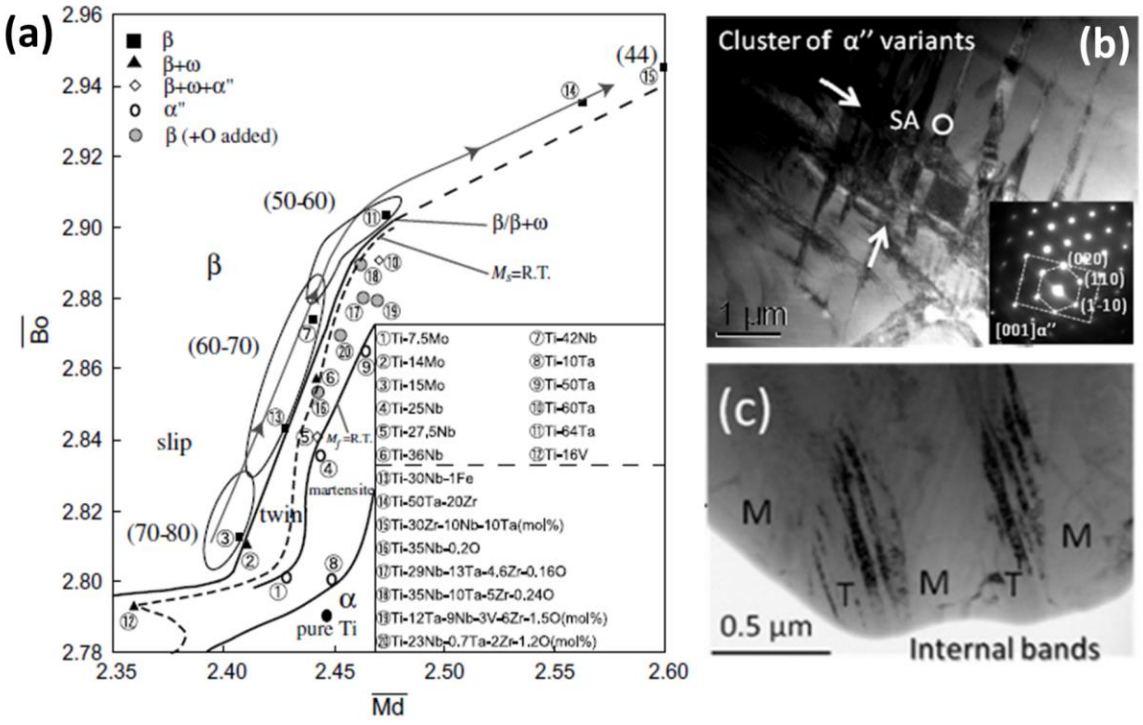

Figure 2.8: (a) Bo - Md diagram with the β/β + ω phase boundary is shown together with the boundaries for M_s = RT and for M_f = RT. The value of the Young's modulus (GPa) is given in parentheses for typical alloys. (b) Bright-field TEM image of a deformation feature in Ti-12 wt. % Mo identified as a cluster of a" variants. (c) Bright-field image of {332}<113> twin bands in Ti-12wt. % Mo. Adapted from Refs. [41,43].

After ageing heat treatments that result in precipitation of isothermal ω and/or α, deformation mechanisms typically only involve dislocation slip. In particular, the formation of isothermal ω is known to heavily embrittle β Ti alloys. Early literature shows that ω forms as small, coherent particles [46] that are sheared by moving dislocations leading to inhomogeneous slip and embrittlement (**Figure 2.9**) [8,13,47]. Microstructures with extensive ω formation and chemical partitioning of elements to ω and β typically result in reduced ductility and brittle mechanical properties [6,46]; thus, ω formation is historically problematic for structural applications [48]. However, ω phase formation in β titanium alloys has recently gathered renewed interest due to ω's roles in influencing and controlling deformation behavior. For example, short ageing treatments have reported the ability to restrict ω growth and obtain strengthening from ω formation without a significant loss of ductility [49,50]. ω has also been shown to play an integral role in changing transformation induced plasticity and twinning induced plasticity deformation mechanisms to dislocation slip that results in the aforementioned ω-induced embrittlement. ω's suppression of stress-induced martensite and twinning has been attributed to the difference in β and ω shear moduli that allows ω particles to act as local barriers to the martensitic transformation and twinning

[51], as well as the structural collapse of atomic planes and chemical partitioning with ω formation that hardens ω precipitates [52]. Finally, ω is known to act as a heterogeneous nucleation agent for stable α precipitation to obtain faster nucleation of extremely fine and dispersed α phase [37] (**Figure 2.10**), in which compositional variations and the structural interface of ω precipitates serve as preferential sites for α nucleation [36,38,39]. α precipitation is particularly important in commercially relevant β Ti alloys, since control over the balance of α and β phases enables tailoring of the resultant microstructures to promote strength, toughness, or fatigue properties [48]. Alloys that are strengthened with equilibrium α precipitates also deform generally through dislocation slip, but may show a good balance of strength and ductility with a fine dispersion of uniform α precipitates [6]. Tensile yield strength generally correlates with the inverse of α interparticle spacing, since α refinement forms a higher number of α-β interfaces that act as dislocation barriers resulting in increased strength [2,34,48]. Consequently, tailored heat treatment processes may result in various distributions, aspect ratios, and volume fractions of the α phase that optimize different property balances.

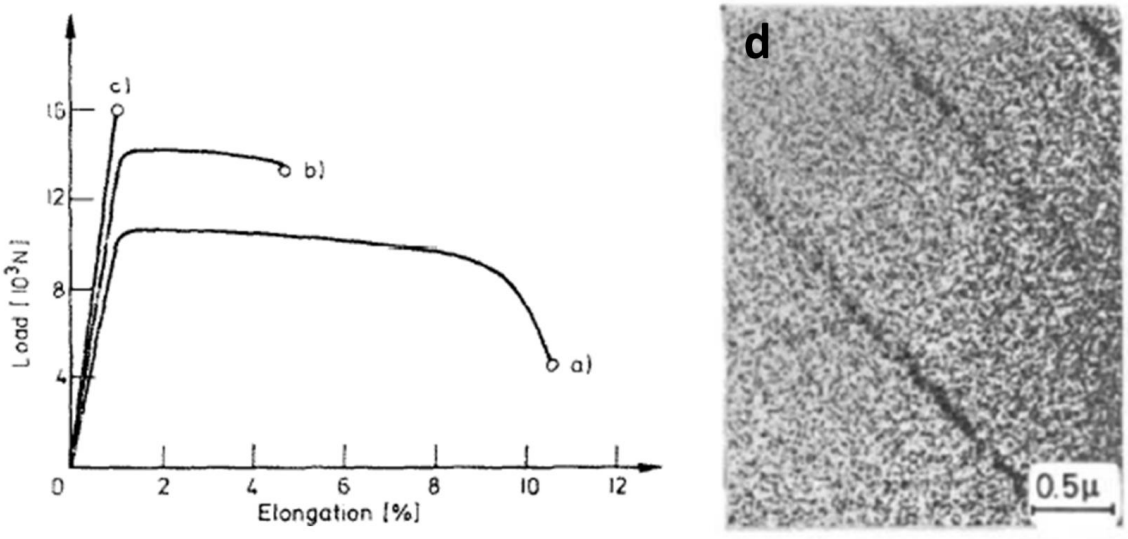

Figure 2.9: Engineering load-elongation curves for Ti-11 at. % Mo. (a) As-quenched; (b) 3 h, 350 °C; (c) 10 h, 350 °C. (d) Bright-field electron micrograph of Ti-14 at. % Mo aged for 10 h, 400 °C and 2% deformed showing slip bands. Adapted from Ref. [8].

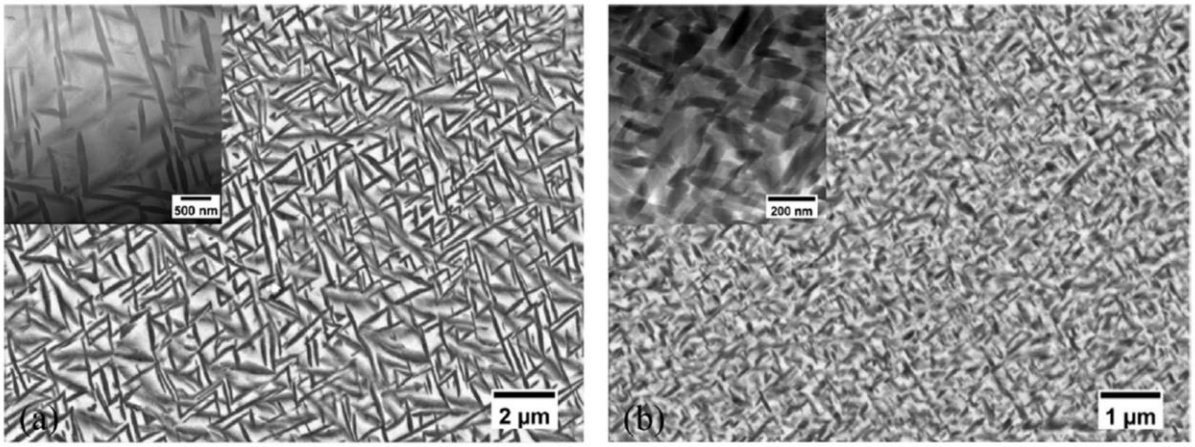

Figure 2.10: Microstructure of Ti-5553 after being heated to 600 °C at the rate of (a) 100 °C/min and (b) 20 °C/min held for 2 h at temperature and fast cooled to room temperature. Finer α precipitates are obtained in (b) which allows for ω formation prior to α. Adapted from Ref. [39].

2.2 Ti-Nb alloys

Within β Ti alloys, Ti-Nb based compositions have attracted significant interest due to novel changes in phase stability that enabled unique reported deformation behavior and properties. β titanium alloy gum metal (variations of Ti-36Nb-2Ta-3Zr-0.3O, wt. %), first developed in 2003, reported the combination of high strength, a low elastic modulus, superelasticity, and super plasticity [7]. These 'super properties' were supposedly achieved when electronic states were satisfied through: 1) a compositional average valence electron number (e/a) of 4.24; 2) a bond order (Bo) of ~2.87; and 3) a d-electron orbital energy (Md) of ~2.45 eV. Additionally, the alloy required cold working and high levels of oxygen > 0.7 at. % [7]. Although gum metals were originally reported to deform through 'giant fault' formation and bulk shearing without formation of dislocations, several other deformation mechanisms have been demonstrated, including stress-induced α" martensite phase transformation, dislocation plasticity [53], deformation twinning, ω-phase transformation, strain-glass transition [54], and complexion-mediated martensitic phase transformation [55]. These deformation modes are all critically linked to β phase instability during processing and under mechanical loads. Further development of related alloy compositions also included Nb to stabilize the β phase due to its biocompatibility and to enable useful properties such as shape memory behavior, low stiffness, and/or high strength. These alloys exploit the metastability of the β phase after solution treatment and quenching to tailor properties [45,56]. Common minor alloying elements for gum-metal alloys include Zr and Sn, which are considered neutral elements for the Ti system and do not heavily partition to α or β phases [6,56].

2.2.1 Influence of oxygen on phase stability and deformation

The high levels of oxygen reported for gum metal compositions have motivated a significant number of studies to investigate O effects on phase stability and deformation. Oxygen has been demonstrated to suppress the formation of martensitic α" upon solution treatment and induces a nanodomain arrangement with diffuse streaking in selected area diffraction patterns shown in **Figure 2.11a-c** [27]. The addition of oxygen inhibited the formation of long range martensite, and detailed investigations have suggested that these nanodomains are composed of lattice modulations due to relaxation of local strain fields around oxygen atoms [27]. Growth of preferential nanodomain variants has been reported with deformation and rolling [27]. Mechanical property investigations of gum metals have shown that increasing O concentration decreases Young's modulus due to suppression of α" and ω phases [57]. Stress-induced martensite and deformation twinning during tensile deformation are suppressed with higher O levels [58]. Increasing oxygen content also leads to a suppression in shape memory behavior and increased superelasticity [59,60]. The suppression of the stress-induced martensitic transformation resulted in non-linear elastic behavior with high oxygen levels [59]. Cyclic stress-strain loading has demonstrated that the stress-strain curve shape depends highly on oxygen content, with higher levels of oxygen showing increased apparent yield strength and narrower stress hysteresis (**Figure 2.11d**) [59]. Oxygen has also been shown to influence thermal expansion properties, with a negative linear expansion coefficient observed at 1.2 at. % O in as-rolled Ti-21Nb, and this thermal expansion behavior was reported to be determined by the amount of lattice distortion strain of the nanodomains [61]. Additionally, oxygen may enhance spinodal decomposition of the β phase in Ti-Nb alloys that affects the subsequent stress-induced martensitic transformation [62]. Finally, oxygen modified gum metal-like alloys have shown an increased fatigue limit during cyclic loading [63]. Thus, oxygen has important effects on phase stability in Ti-Nb alloys and can dramatically influence the resulting mechanical behavior.

During ageing heat treatments, interstitial oxygen affects isothermal ω and equilibrium α precipitation kinetics of β Ti alloys. Oxygen, as a potent α-stabilizing element [2], is reported to accelerate the precipitation kinetics of α from ω during low temperature ageing [35,64] due to increases in α's thermodynamic phase stability and nucleation driving force. Oxygen also partitions to the α phase during ageing, with the β matrix then containing minimal oxygen content

[65]. Oxygen in solid solution reduces ductility for both α and β [5] and can be easily accumulated during alloy thermomechanical processing and production; therefore, commercial heat treatment practices typically have stringent controls on oxygen content to prevent embrittlement and maintain toughness at relatively high strengths [48].

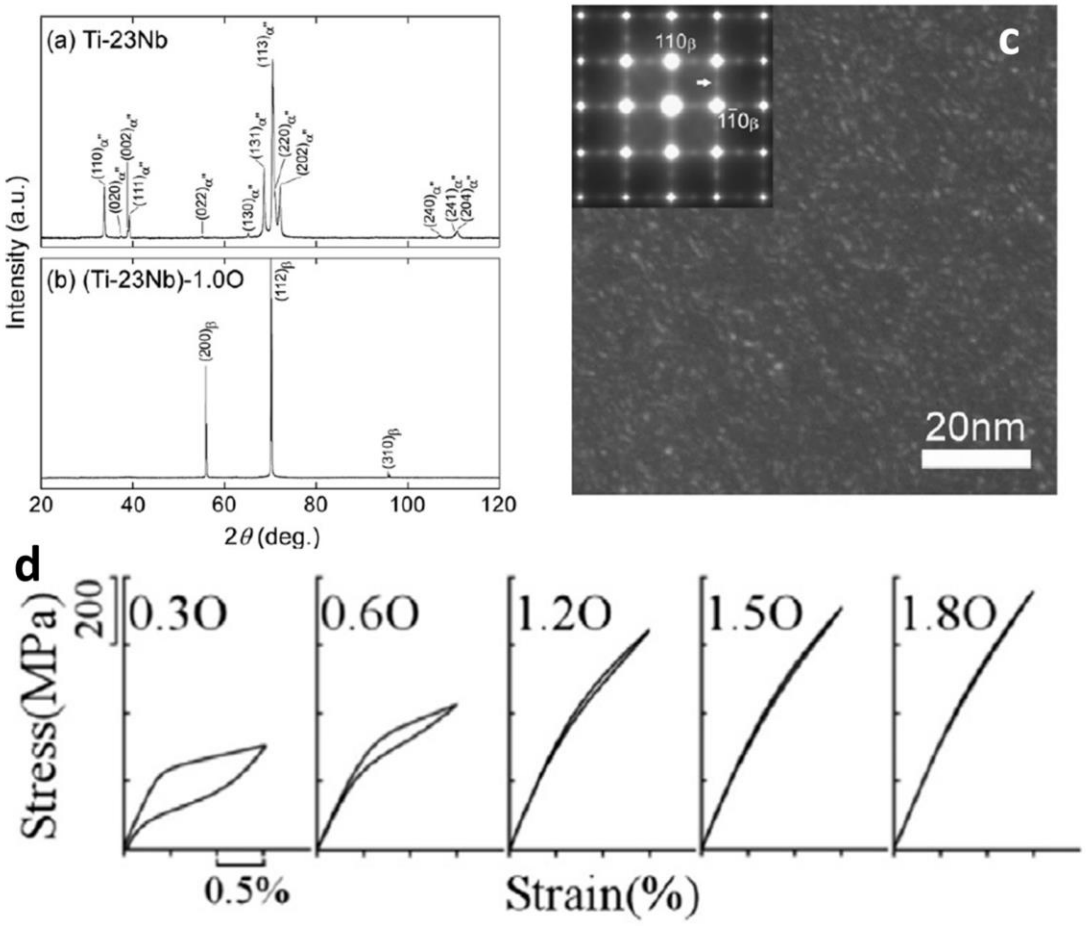

Figure 2.11: XRD profiles for (a) Ti–23Nb and (b) (Ti–23Nb)–1.0O alloys showing suppression of α" with oxygen. (c) Dark-field images of nanodomain regions in the β phase. (d) Stress-strain curves obtained at room temperature for Ti-23Nb-2Zr-0.7Ta-(0.3–1.8)O at.% alloys. Adapted from Refs. [27,59].

Conflicting results have been reported for oxygen effects on metastable ω phase stability in β Ti alloys. Oxygen has been known to suppress the formation of the ω phase during solution treatment and quenching [66,67]. First principles calculations suggested that added oxygen increases the energy barrier for phase transition from β to ω [68]. Oxygen has also been reported to reduce the amount of ω that is formed during ageing [35,64] and cold working [57]. However, more recent studies suggested that ω phase becomes more thermodynamically stable with additions of oxygen after various ageing treatments (**Figure 2.12**), with the ω phase being retained

instead of fully transforming to the α phase in alloys containing higher oxygen concentrations [9,69]. With the known issues of β Ti alloys stemming from embrittling ω formation and oxygen contamination, addressing these problems are a significant challenge for titanium alloy development and require careful process control during alloy production. However, oxygen's influence on phase stability in these alloys and effect on deformation behavior offer opportunities to mitigate these issues and design improved alloy compositions. Detailed understanding of oxygen's effect on the metastable and stable phase transformation sequence with respect to ω and α is required in order to elucidate effects on ensuing mechanical properties with elevated interstitial oxygen levels.

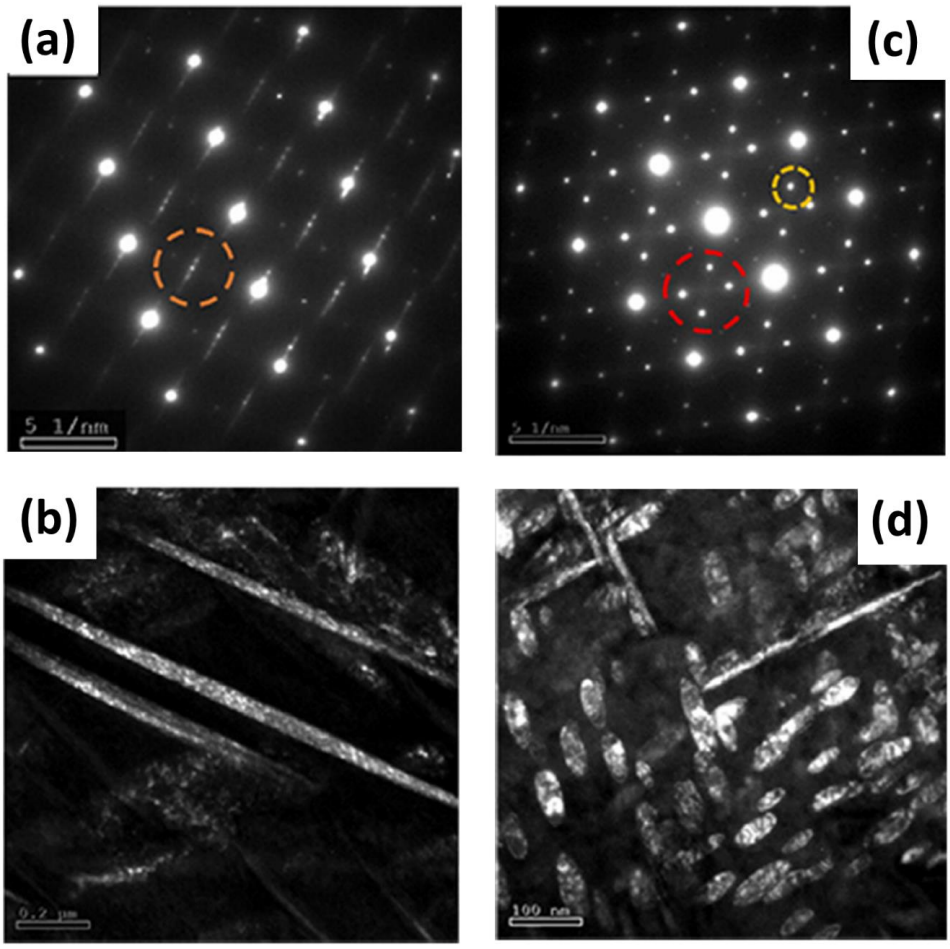

Figure 2.12: Transmission electron microscope images for Ti-29Nb-13Ta-4.6Zr-0.1O. (a) Selected area pattern from $[011]_\beta$ zone axis. (b) Dark-field image taken from circle in (a) showing large α laths. TEM images of Ti-29Nb-13Ta-4.6Zr-0.4O. (c) $[011]_\beta$ selected area diffraction pattern revealing ω reflections. (d) Dark-field image taken from circle shown in (c) revealing both ω precipitates and fine-scale α laths. Adapted from Ref. [9].

2.3 Ti-Mo alloys

Ti-Mo alloys are an important subset of β titanium alloys due to the frequent use of Mo in commercial alloy compositions. The Ti-Mo phase diagram (**Figure 2.13**) shows the α and β phase fields in addition to metastable equilibria and martensite start temperatures. Mo is a common addition to β Ti alloys due to its strong stabilization of the β phase resulting in cost-effective master alloys and low tendency for solidification segregation [48]. Of the reported β stabilizing elements, Mo has the lowest critical concentration to retain 100% of the β phase after quenching to room temperature [6]. A well-known parameter for characterizing β phase stability is the molybdenum equivalency (MoE), which is the combined measure of β stabilizing elements, α stabilizing elements, and neutral elements contained in a Ti alloy on the β phase stability [6]. The MoE value uses Mo as an arbitrarily chosen baseline to normalize other elements to an equivalent Mo value [6,48]. A MoE value of approximately 10 is required to stabilize the β phase during quenching from above the β transus temperature, and the MoE is a useful metric to rank the order of phase stability for model and commercial alloys [6]. Additionally, as β phase stability and the associated MoE values increase for β Ti alloys, their deformation mechanisms generally transition from stress-induced martensitic transformations and/or twinning for lower MoE values to dislocation slip for higher MoE values [6].

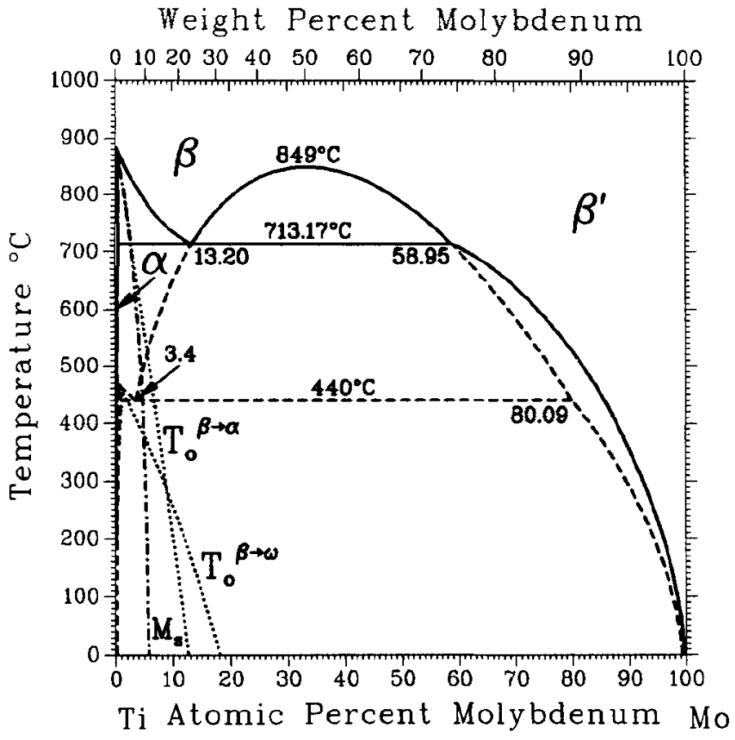

Figure 2.13: The Ti-Mo phase diagram. Metastable equilibria are indicated by dashed lines, the T_0 curves by dotted lines. The martensite start temperatures are indicated by the dot-dashed line. Adapted from Ref. [70].

Limited investigations on the influence of interstitial oxygen in Ti-Mo alloys have primarily focused on solution treated and quenched alloys. As-quenched microstructures of Ti-7.5Mo wt. % with up to 0.5 wt. % O still showed martensite formation, but formation of the α phase was also reported for high oxygen compositions due to α-stabilization with oxygen [71]. In a more solute-rich Ti-15Mo wt. % alloy, athermal ω phase formation was suppressed with higher O content upon quenching, and the deformation mechanism transitioned from twinning to dislocation slip with oxygen [72]. With nanoscale phase formation, oxygen played an important role in Ti-Nb based compositions to induce these phases. However, the absence of oxygen in Ti-Mo alloys may still allow nanoscale phase formation, as was reported for the O' phase which formed in a Ti-Mo alloy where interstitial oxygen was intentionally removed [73]. Although these studies have explored the influence of oxygen in Ti-Mo based compositions, extensive investigations have not been conducted for oxygen in relation to other metastable phases. Furthermore, allowable levels of oxygen are still restricted in commercial alloys [48]. Therefore, focused studies of oxygen's influence on phase transformations in Ti-Mo alloys would yield useful knowledge on the effects of oxygen relevant for important commercial alloy systems.

2.4 Oxidation mechanisms for titanium at elevated temperatures

Understanding and mitigating oxidation reactions have been a continuous area of focus for titanium alloy development. Titanium alloys are commonly used as structural materials due to their high specific strength and corrosion resistance, but the use of conventional Ti alloys at temperatures above 550 °C has been limited due to the formation of non-protective oxide layers [1]. In particular, the high solubility of oxygen in both the α and β phases, up to 33 and 10 at. % O, respectively, leads to embrittlement and preferential stabilization of the α phase coupled with fast diffusion and oxidation kinetics at elevated temperature exposures, resulting in severe alloy degradation in hot environments [74]. These challenges have motivated numerous studies on understanding oxidation mechanisms of titanium and its alloys as well as the development of protective coatings to improve oxidation resistance. Increasing the oxidation resistance and stable use temperature of titanium alloys would have substantial effects on industrial applications such as in aerospace and power generation industries, where increasing the maximum temperature of engines may significantly improve engine efficiency and reduce fuel consumption. Additionally, in aerospace industries where weight reduction is a major focus, improving titanium's oxidation resistance may result in replacement of heavier Ni alloy structures with Ti alloys that would increase weight savings. The following sections discuss literature studies of oxidation mechanisms for pure Ti, a model system comprised of single-phase α at room temperature, and the influence of Si-containing coatings that have shown improved oxidation resistance for Ti alloys.

2.4.1 Oxidation in pure Ti

The oxidation behavior of pure titanium has been extensively studied over the last fifty years [75–79]. A stable oxide rutile (TiO_2) phase has generally been observed to form [76], although a few reports have also found thin TiO and Ti_2O_3 metastable suboxide layers in low oxygen partial pressures (pO_2 between 10^{-12} to 10^{-6} atm) [80,81]. Most reports agree with a layered oxide scale, albeit with different microstructures. Kofstad observed a two layer TiO_2 scale with an inner porous region shown in **Figure 2.14a** [75]. Other studies have reported up to three layers, with an outer scale with many layers of equal thickness, an intermediate compact region, and an inner coarse grain oxide [78]. Finally, different microstructures have been observed with a compact outer oxide and inner set of oxide layers with short aligned cracks that were attributed to stresses

in the oxide scale [79]. Many of these studies were performed using different experimental conditions (oxidation time, temperature, environment) with no clear mechanistic connection to the observed microstructures. These results suggest that the oxide morphology may be highly sensitive to experimental conditions, and the lack of consistency has likely hindered the development of a coherent mechanistic description of titanium oxidation.

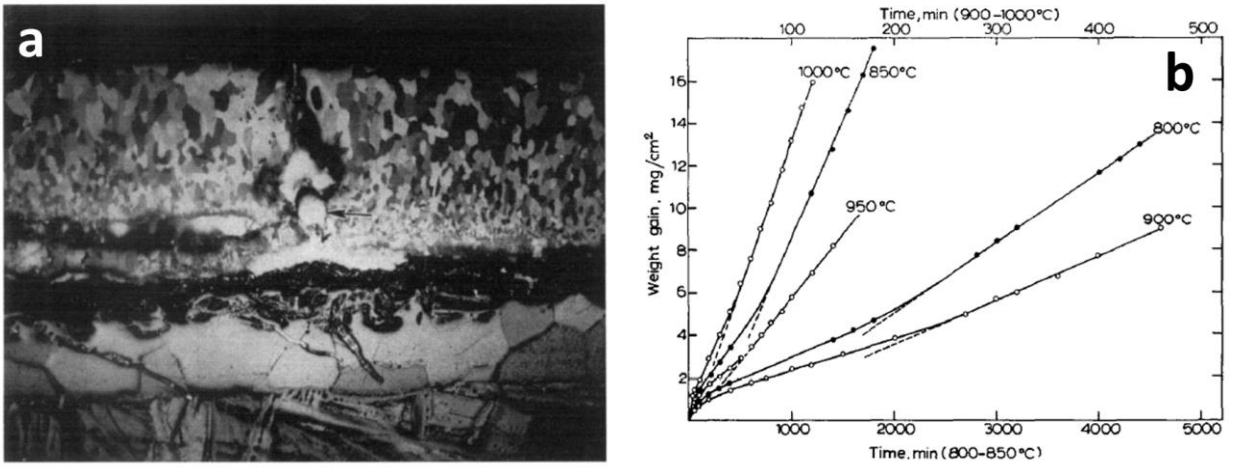

Figure 2.14: (a) Pt-marker study on Ti-specimen oxidized for 1 h at 1175 °C and 1 atm oxygen, showing the border between the transformed β-titanium and the oxygen-stabilized α-titanium next to the oxide scale. (b) Linear plot of oxidation of titanium at 800-1000 °C. Adapted from Ref. [75].

With prolonged exposure, the oxidation of uncoated titanium eventually becomes dominated by growth of the internal scale [75,79,81], and fast kinetics with an initial parabolic growth rate transitioning to a linear rate are observed for pure Ti oxidation at 700-1200 °C in atmospheric pressures (**Figure 2.14b**) [81]. The resulting internal TiO_2 scale is typically porous, does not protect the metal from the gaseous environment, and is susceptible to spallation [4]. Furthermore, the high solubility of O in the α Ti phase leads to the formation of an oxygen-rich layer (ORL) beneath the oxide scale [10]. Such levels of interstitial oxygen in Ti have an embrittling effect, and the ORL has been shown to negatively affect both tensile elongation and fatigue life of components [82]. Therefore, the degradation of titanium during oxidation occurs through the loss of load-bearing metal during continued oxidation reaction and the sustained ingress and dissolution of oxygen into the subsurface metal [74].

2.4.2 Effect of Si-containing coatings on oxidation resistance

Different strategies, including alloying or the use of coatings, have been developed to remediate the ingress of oxygen, improve scale stability, and reduce oxide growth rate of titanium

[4]. In particular, the use of Si-containing coatings, deposited using different methods that include powder siliconizing [83–86], liquid phase siliconizing [12], laser surface alloying [87,88], or physical vapor deposition [11] have been associated with improvements in titanium oxidation resistance for elevated temperature exposures exceeding 100 hours. Accordingly, thinner oxide scales with finer grain structures, less porosity, and fewer cracks in the scale (**Figure 2.15**) were observed [11,89]. Such changes in the oxidation behavior were linked to the formation of silicide phases [12,83,84,89], such as Ti_3Si, Ti_5Si_3, Ti_5Si_4, TiSi, and $TiSi_2$, identified after thermal exposure and oxidation of various Si-coated Ti systems [12,83,85,87,90]. In these systems, SiO_2 has been reported as an oxidation product in addition to TiO_2 [12,83,89,90]. It was also suggested that Si may be in solid solution in rutile TiO_2 after oxidation [11,88]. The structure and morphology of the evolved coating and oxide scales are highly dependent on coating chemistry and the method by which the coating is applied. The formation of scale porosity, cracks, or interdiffusion zones with brittle phases that show poor adhesion with the substrate significantly affect coating effectiveness [4]. However, irrespective of the coating application method, the significant improvement in titanium oxidation resistance from Si-containing coatings merits further study to comprehend the role of Si-rich coatings during oxidation.

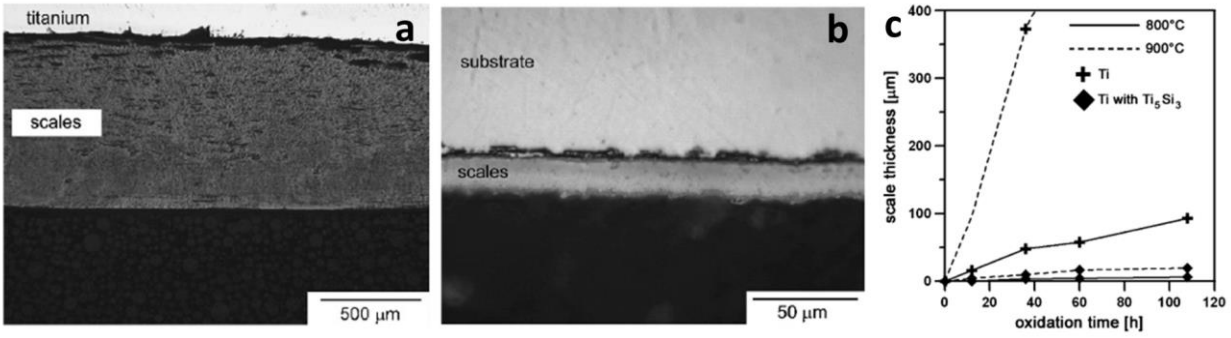

Figure 2.15: Optical images of cross-sectioned scales on pure titanium (a) and silicide-modified titanium (c). Oxidation was conducted in air at 900 °C for 108 h. (c) Oxidation kinetics expressed as the scale thickness versus oxidation time. Adapted from Ref. [11].

2.5 Summary

This chapter reviewed the phase stability, precipitation, and deformation of β Ti alloys and discussed the influence of elevated interstitial oxygen on microstructure and mechanical behavior changes. Although the influence of oxygen on martensitic phase transformations has been widely investigated in Ti-Nb alloys, detailed understanding of oxygen and metastable ω phase formation

is still needed to understand changes in phase stability and microstructural evolution. There is also a lack of understanding on how to mitigate embrittlement and ductility losses stemming from ω precipitation in β Ti alloys. Furthermore, limited investigations exist for oxygen's influence on phase transformations in commercially relevant Ti-Mo and Ti-V systems. Finally, the use of Si-containing coatings on improving oxidation resistance of Ti at elevated temperatures was also summarized in this chapter. However, a mechanistic understanding on the beneficial effect of silicon is still unknown due to the complicated chemistries and complex microstructures of developed coatings. Therefore, this thesis provides a systematic study of oxygen's effect on ω and α precipitation during isothermal ageing in β Ti alloys and the resulting changes to mechanical behavior. In addition, the phase transformation sequence and microstructural evolution of Si during Ti oxidation is identified. Overall, this work provides evidence of oxygen's beneficial microstructural effects that counter conventional knowledge of oxygen as a detrimental alloying element for Ti alloys and discusses specific reaction mechanisms for Si-based coatings to improve oxidation resistance, which will influence future alloy and processing design to utilize these benefits.

Chapter 3: Oxygen Effects on ω and α Phase Transformations in a Metastable β Ti-Nb Alloy

3.1 Introduction

Phase stability in the metastable β titanium alloy system has been an active area of investigation to develop alloys intended for applications including aerospace and biomedical industries [2]. Oxygen has been shown to have a significant influence on titanium alloy phase stability and can dramatically influence the resulting mechanical behavior. Generally, oxygen has extensive solubility in α and β before forming oxide phases, and O is known as a strong α stabilizing element. Dissolved oxygen in the α and β phases causes hardening from interstitial solid solution strengthening and reduces ductility [5]. Specifically, conflicting results have been reported for oxygen effects on metastable ω phase stability in β Ti alloys. As discussed in **Chapter 2**'s literature review, several studies note that oxygen suppresses or reduces the amount of ω phase formation during solution treatment and quenching [66,67], ageing [35,64], and cold working [57]. However, other studies have shown ω being retained with prolonged ageing in alloys with higher oxygen levels [9,69]. The presence and relative stability of the ω phase is of interest for metastable β Ti alloys due to its rising importance in influencing deformation behavior. This includes the role of ω phase as a potential heterogeneous nucleation site for α phase precipitation in aerospace β Ti alloys [34,36,38–40] and its influence in changing the deformation behavior from transformation induced plasticity (TRIP) and/or twinning induced plasticity (TWIP) mechanisms to dislocation channeling [51,91]. Deformation-induced ω phase has also been reported in β Ti alloys [32]. Finally, fine distributions of ω phase may enhance yield strength while preserving ductility [49,50]. Thus, clarifying the phase stability of ω with oxygen in metastable β Ti alloys will result in a more nuanced understanding of precipitation behavior and consequently better control of mechanical properties.

In the present work, the precipitation behavior of a model metastable β-type Ti-20Nb (at. %) alloy was studied to elucidate the effects of oxygen on ω and α phase stability. A model binary alloy was selected in order to understand precipitation without the compounding effects of

additional elements in complex engineering alloys. We utilized the extensive solubility and dissolution of oxygen in titanium alloys during high temperature oxidation exposures to obtain specimens with a wide range of dissolved oxygen contents in the β phase matrix. These compositionally graded specimens allowed the investigation of a range of oxygen levels in solid solution up to 5 at. % O. Subsequent ageing heat treatments on pre-oxidized and unoxidized (with very little oxygen) specimens were conducted at temperatures in the ω + α and α phase field regions to understand the precipitation and phase transformation sequence. The influence of oxygen on ω and α precipitation is discussed based on thermodynamic phase stability, kinetic effects, and changes in nucleation driving force.

3.2 Experimental methods

An arc-melted button with a nominal composition of Ti-32.7 wt. % Nb (Ti-20 at. % Nb) was provided by ATI. The button was remelted three times to improve homogeneity. Interstitial oxygen levels were measured in the arc-melted button as 0.019 wt. % (0.1 at. %) by inert gas fusion using a LECO analyzer. Specimens were cut from the button using a slow speed diamond saw, encapsulated with pure Ti pieces in a quartz tube backfilled with Ar gas, and solution treated at 1000 °C for 10 h, quenching by breaking in water. Interstitial oxygen levels after solution treatment were measured as 0.021 wt. % O (0.1 at. %) by inert gas fusion in a LECO analyzer. A subset of solution treated specimens were placed in an Al_2O_3 crucible and oxidized at 900 °C for 5 h in a 1 standard cubic centimeter per minute (SCCM) O_2/4 SCCM Ar environment (approximately pO_2 = 0.2 atm/20.3 kPa) using a Thermo Scientific Lindberg Blue M tube furnace. The oxidation exposure was such that specimens were inserted in the hot zone of the furnace after it was heated to 900 °C in a flowing Ar (40 SCCM) gas environment. After insertion and temperature equilibration back to 900 °C (approximately 15 minutes), the aforementioned oxidizing environment was introduced. Following the oxidation exposure, oxygen gas flow was stopped. Specimens were removed from the hot zone and cooled to room temperature in flowing Ar (40 SCCM). These specimens were termed as “pre-oxidized”.

As-solution treated specimens and pre-oxidized specimens were subsequently aged at 450 °C for 2 hours and 1, 3, 6, 14, 22, and 31 days. This particular ageing temperature was chosen due to it being near the reported upper limit of ω phase stability and therefore would show the ω to α transformation after prolonged ageing [18]. Finally, a set of as-solution treated specimens and pre-

oxidized specimens underwent a two step heat treatment: first aged at 450 °C for 3 d, then aged a second time at 600 °C for 1 h in order to promote ω phase dissolution and α precipitation. All ageing heat treatments were conducted with samples encapsulated in quartz tubes with pure Ti pieces that were backfilled with Ar gas and quenched by breaking the tubes in water.

Specimens for characterization using scanning electron microscopy (SEM) imaging were mounted and ground using 320-1200 grit SiC papers followed by polishing with 0.03 μm colloidal silica suspension. Wavelength dispersive spectroscopy (WDS) analyses were conducted on polished cross sections of pre-oxidized Ti-20Nb in order to measure dissolved oxygen content in the matrix. WDS allows for more accurate quantification of light elements such as O compared to energy dispersive spectroscopy. These measurements were performed using a Cameca SX100 electron microprobe and collected using an accelerating voltage of 15 kV, beam current of 20 nA, and a focused beam. Intensity correction was performed using the ZAF (Armstrong/Love Scott) method [92]. Standards for microprobe analysis background subtraction for the Kα or Lα x-ray lines for O, Nb, and Ti were collected using MgO (synthetic), $LiNbO_3$ (synthetic), and Ti metal, respectively, with a 30 s peak and 30 s background counting time. Interference correction to deconvolute overlapping peaks of collected spectra was performed using pure Ti metal as the interference correction standard according to the method described in Ref. [93]. SEM imaging and focused ion beam (FIB) preparation of site-specific transmission electron microscopy (TEM) foils and needle-shaped atom probe tomography (APT) specimens were performed using a Thermo Fisher Scientific FEI Helios 650 Nanolab with a Ga^+ ion FIB. TEM foils were further thinned using broad Ar ion milling in a Gatan PIPS II instrument. TEM images and selected area electron diffraction (SAED) patterns were obtained using a JEOL 3011 microscope operated at 300 kV. A region for 3D FIB tomography was prepared and imaged using a Thermo Fisher Scientific FEI Helios Nanolab 650. Bulk FIB milling of the tomography site was performed at 30 kV, 21 nA, and cleaning steps were performed at 30 kV, 2.5 nA. Individual slices for FIB tomography were milled using a 3 nm slice thickness at 30 kV, 80 pA. FIB tomography images were reconstructed using Avizo software 9.2.0. APT data collection was performed with a Cameca local electrode atom probe (LEAP) 5000 XR operated in laser mode. APT data was collected using a specimen temperature of 30 K, a detection rate of 0.005 atoms per pulse, laser pulse energy of 25 pJ, and pulse repetition rate of 200 kHz. Data reconstruction, background subtraction, peak deconvolution,

and compositional analysis were performed using the Integrated Visualization and Analysis Software (IVAS) package 3.8.2.

3.3 Results

3.3.1 Solution treated and pre-oxidized microstructures

The initial microstructure in the solution treated condition showed large β grains (> 1 mm) with α" martensite that formed upon water quenching to room temperature. Martensite formation is consistent with prior literature showing that the martensite start temperature for 20 at. % Nb is about 200 °C [18]. No athermal ω phase was observed in the as-solution treated samples.

In the pre-oxidized samples, the elevated temperature oxidation exposure resulted in the formation of a 60 μm thick layered oxide scale and long α phase laths in the subsurface metal region of the β matrix (**Figure 3.1**). The α lath region extended approximately 120 μm into the subsurface metal region of the cross section. α phase formation is attributed to the dissolution of oxygen in the subsurface region of the Ti matrix during oxidation, which thermodynamically stabilizes α at the oxidation temperature [2]. SEM backscatter (SEM-BSE) images of the subsurface metal region reveal a microstructural transition to faint laths at the interface between the α + β region and β phase matrix (**Figure 3.2a**). SAED patterns and bright-field TEM (BF-TEM) micrographs taken from a TEM sample in the matrix near the (α lath + β) / β matrix interface reveal that the matrix is actually composed of α" martensite (**Figure 3.2b**) after the oxidation exposure. WDS measurements conducted on a cross section of a pre-oxidized specimen confirmed the ingress of dissolved oxygen in the alloy below the α lath + β region. Data points and error bars for WDS data in **Figure 3.2c** report average values and one standard deviation based on five line traces. Data points collected from line traces in the matrix (**Figure 3.2c**) show that oxygen levels exponentially decayed from approximately 5 at. % at the (α lath + β) / β matrix interface closer to the sample edges to approximately 1.5 at. % in the center of the cross section. We note that possible experimental sources of error may also originate from surface oxide contributions systematically raising the apparent oxygen concentration [94]. However, bulk atom probe tomography measurements from the center region also show an oxygen concentration of 1.2 at. %, which is within the error bars of the asymptote for WDS oxygen concentration measurements. Additionally, the WDS data suggest that greater than 5 at. % O (measured at the (α lath + β) / β matrix interface)

is needed in order to sufficiently stabilize α phase formation during oxidation at 900 °C for Ti-20Nb. The measured Nb content in the matrix region using WDS was roughly 19 at. %, which agrees with the nominal button composition.

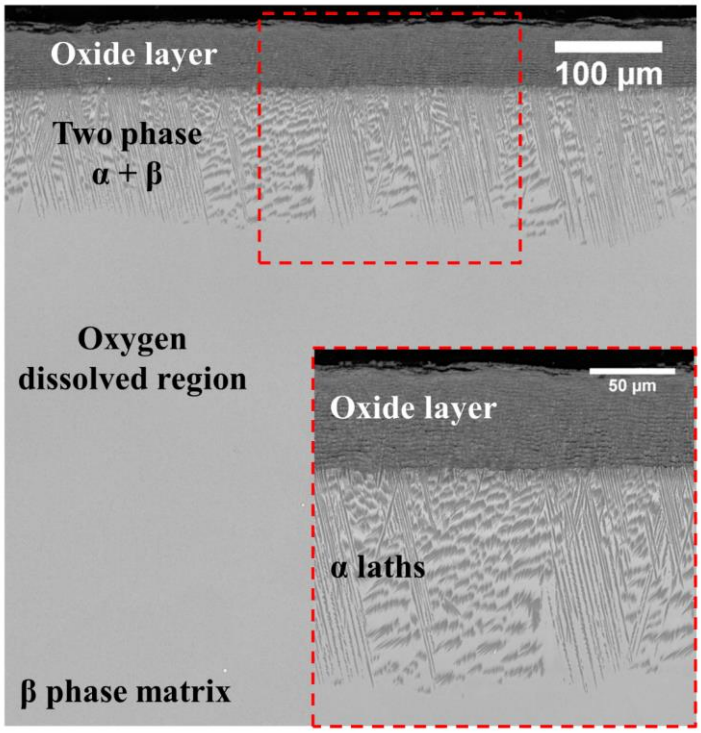

Figure 3.1: Cross-sectional SEM-BSE image of Ti-20Nb (at. %) oxidized for 5 h at 900 °C in a 20% O_2/Ar environment. Inset shows higher magnification image of location in red box showing oxide cross section and α lath formation in subsurface metal.

3.3.2 Aged microstructures at 450 °C

As-solution treated samples and pre-oxidized samples were subsequently aged at 450 °C for 2 hours and 1, 3, 6, 14, 22, and 31 days to observe ω and α phase transformations in the β matrix. The as-solution treated and aged samples (with minimal - 0.1 at. % O - and uniform oxygen concentration) are hereafter referred to as *directly aged* (DA) samples, and the pre-oxidized and aged samples (with the created oxygen gradient) are referred to as *oxidized and aged* (OXA). Investigation at different cross-sectional depths from the (α lath + β) / β matrix interface corresponded to microstructures with different oxygen contents, correlating with WDS data presented in **Figure 3.2c**, while directly aged specimens were investigated to compare microstructures with 0.1 at. % O. These oxygen levels created during oxidation are assumed to be fixed during ageing due to a slow oxygen diffusion coefficient in β Ti at the ageing temperature [95] and oxygen partitioning behavior to ω and α during annealing [9].

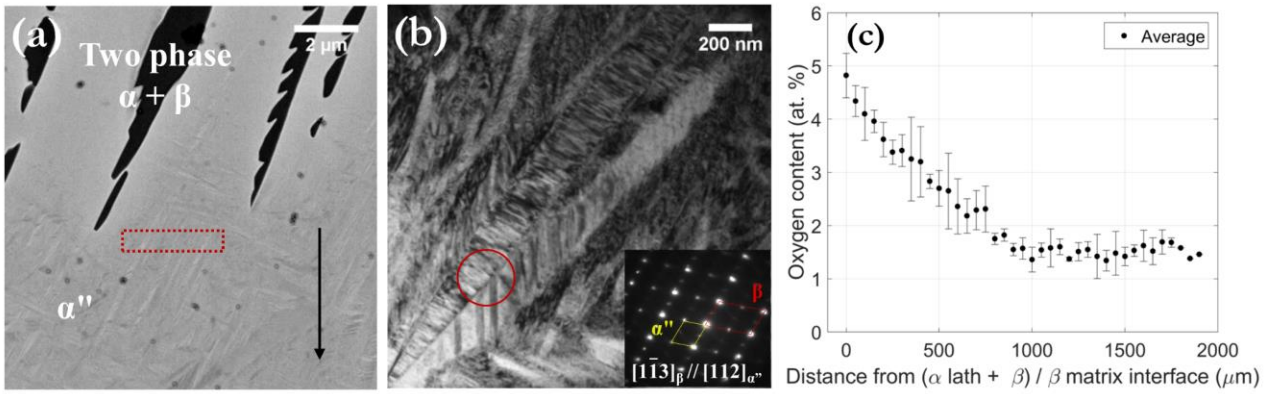

Figure 3.2: (a) SEM-BSE cross-sectional image showing microstructural transition at the (α lath + β) / β interface of oxidized Ti-20Nb (at. %). (b) BF-TEM and SAED pattern from location in red circle showing martensite formation of a TEM sample taken from region outlined by red box of oxidized Ti-20Nb. (c) WDS average line traces measuring oxygen content beginning from the (α lath + β) / β interface and traversing across the cross section of oxidized Ti-20Nb (direction of black arrow in Figure 3.2a).

SEM backscatter images (**Figure 3.3a-b**) of DA (0.1 at. % O) and OXA (4.8 at. % O) Ti-20Nb specimens after 2 h of ageing at 450 °C reveal dense second phase precipitates at both oxygen levels. These precipitates are identified as ω phase by electron diffraction (**Figure 3.3c-d**), with the $[110]_{\beta}$ SAED pattern showing diffraction intensity maxima at 1/3 and 2/3 $\{112\}_{\beta}$ positions. With minimal oxygen present, ellipsoid shaped ω phase is observed, which is characteristic of the low misfit Ti-Nb system [96]. However, dark-field TEM (DF-TEM) images for higher oxygen levels (4.8 at. % O) show ω precipitates with a more elongated shape and higher number density compared to those at minimal oxygen levels (**Figure 3.3c-d**). The evolution of the microstructure up to 31 days of ageing is illustrated in **Figure 3.4** for different oxygen contents: 0.1, 1.5, 2.7, 3.4, and 4.1 at. % O. The elongated rod shape of ω precipitates initially observed at high oxygen contents is preserved at longer ageing times (**Figure 3.4a-b, g**). Additionally, the increased number density of ω precipitates with elevated oxygen content compared to minimal oxygen is also retained. After 6 days of ageing, ω precipitates continued to grow in size (**Figure 3.4g-j**). Precipitation of α laths (about 500 nm in length) is also seen in the 4.1 at. % O condition (**Figure 3.4f**). The SAED pattern in this region confirms the presence of both ω and α phase at this oxygen level, with distinct reflections at the 1/2 $\{112\}_{\beta}$ positions corresponding to α.

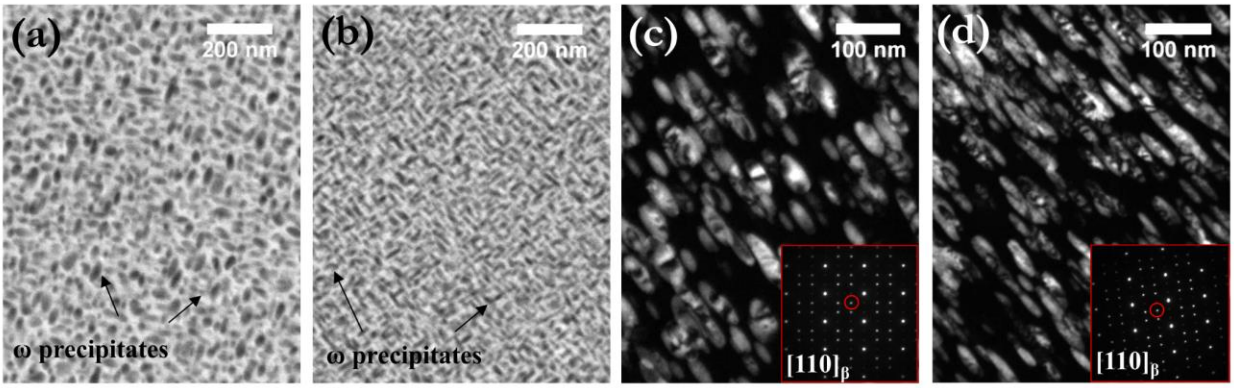

Figure 3.3: SEM-BSE images for (a) DA Ti-20Nb with 0.1 at. % O and (b) OXA Ti-20Nb with 4.8 at. % O aged for 2 h at 450 °C. SAED pattern from [110]$_\beta$ zone axis and DF-TEM images using reflection in red circle from (c) DA Ti-20Nb aged for 2 h at 450 °C with 0.1 at. % O, showing ellipsoidal ω precipitates, and (d) OXA Ti-20Nb aged for 2 h at 450 °C with 4.8 at. % O, showing elongated rod shaped ω precipitates and a higher precipitate number density.

Prolonged ageing of DA and OXA samples revealed differences in the α nucleation rate with varying oxygen content (**Figure 3.4k-o**). After 22 d of ageing, microstructures observed in backscatter SEM images show that regions with the highest oxygen contents (3.4, 4.1 at. % O) contain significant numbers of α precipitates (~500 nm length) with some ω particles. With minimal oxygen content (0.1 at. % O), a similar microstructure is also observed, but the α laths are larger (~1 μm length) and nucleated in larger packets of similar orientation. Interestingly, regions with intermediate levels of oxygen (2.7 at. % O) show primarily ellipsoidal ω phase and a small number of α precipitates. Investigation of OXA samples after 31 d of ageing (**Figure 3.4p-s**) shows that α phase does eventually nucleate in these high oxygen regions, but a significant amount of ω persists in the microstructure, in contrast with specimens containing 0.1 at. % O after 31 d of ageing (**Figure 3.4t**) showing a large number of α laths. Furthermore, the ω phase observed at 1.5 at. % O has grown to ~400-500 nm in size, with some precipitates attaching together after 31 d of ageing (**Figure 3.4s**). This attachment resulted in the formation of highly irregular precipitate chains that were distributed throughout the microstructure.

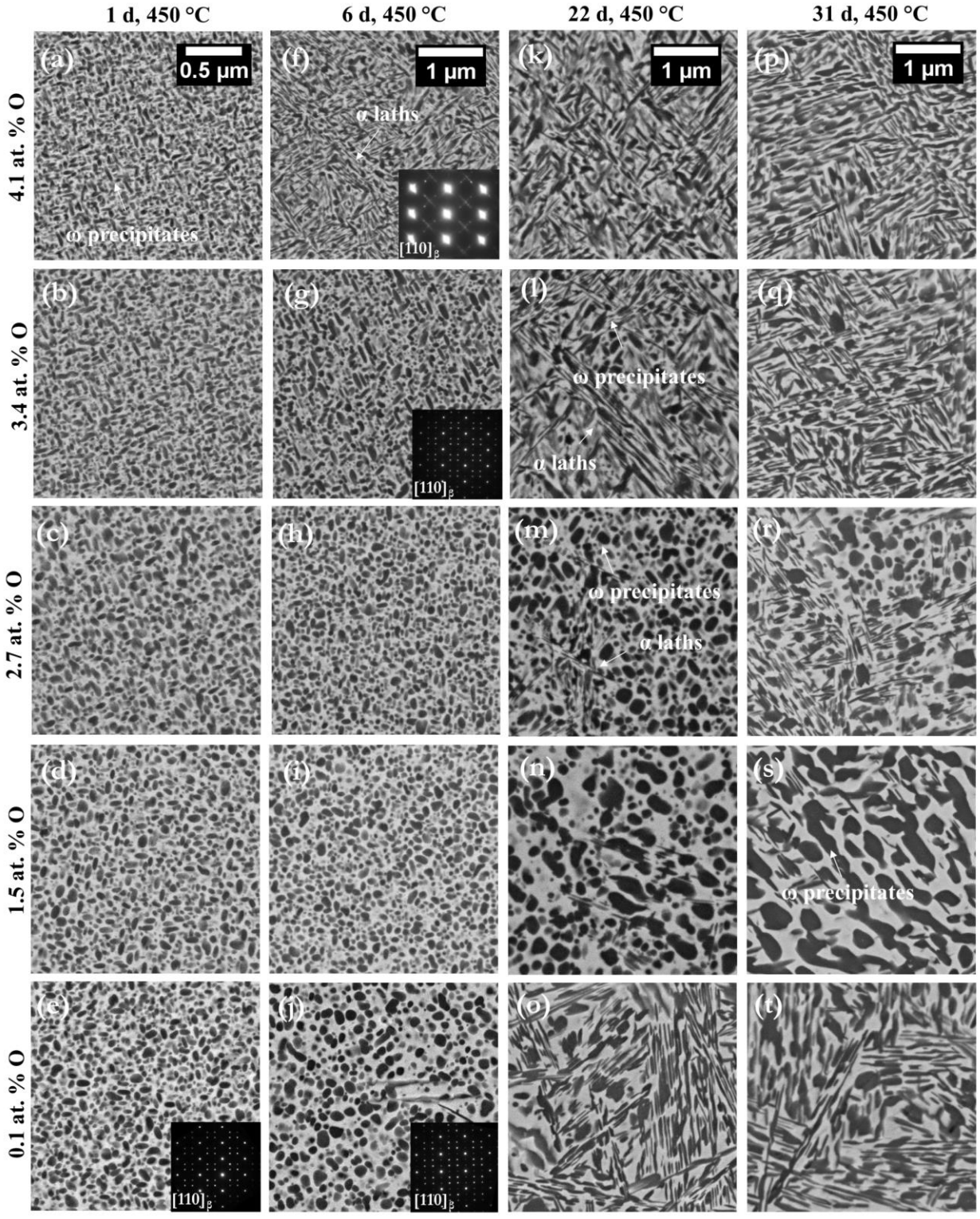

Figure 3.4: SEM-BSE images from OXA and DA Ti-20Nb aged at 450 °C corresponding to different oxygen contents: 0.1, 1.5, 2.7, 3.4, 4.1 at. % O. Microstructural images correspond to isothermal ageing after (a-e) 1 day, (f-j) 6 days, (k-o) 22 days, and (p-t) 31 days. Insets of TEM SAED patterns were taken from the [110]β zone axis.

Aged microstructures revealed that oxygen levels seemed to influence ω number density. In an attempt to quantify the ω area fraction (used as a measure of phase fraction), SEM-BSE images for Ti-20Nb aged for 1, 6, and 14 days at 450 °C with 0.1 or 3.4 at. % O were segmented using binary histogram-based image thresholding (**Figure 3.5**). The ω area fraction showed some variation depending on the specific field of view, but regardless of oxygen content ranged from approximately 44-48 %. Therefore, the phase fraction of ω with different oxygen contents was relatively constant across ageing times studied here. However, qualitative differences in the distribution of ω phase (relating to number density) with oxygen level are clearly observed, and microstructures for 3.4 at. % O are consistently more refined than those with minimal oxygen. The most significant difference for ω distributions is observed for Ti-20Nb specimens aged for 14 days at 450 °C (**Figure 3.5c, 3.5f**), with finer ω precipitates, and consequently increased number density, seen with the elevated oxygen content.

The β + ω microstructure after 6 days of ageing examined by dark-field TEM imaging shows the change in ω precipitate shape with oxygen in greater detail (**Figure 3.6**). With very little oxygen present, the ellipsoid ω phase has a major axis along the $<111>_{\beta}$ direction [19] and a maximum size of ~150 nm. At 3.4 at. % O, the ω phase shows additional lengthening along $<111>_{\beta}$ to form an elongated rod shape. The maximum observed major axis is roughly 300 nm. Aspect ratio measurements from the TEM dark-field data confirm the additional shape anisotropy for ω with higher oxygen (3.4 at. % O: up to 4.2 to 1 aspect ratio) compared to minimal oxygen (0.1 at. % O: 1.5 to 1 aspect ratio). 3D FIB tomography collected after 6 days of ageing with 3.4 at. % O clearly demonstrates that the additional lengthening is constrained to one direction to form a rod (**Figure 3.7**).

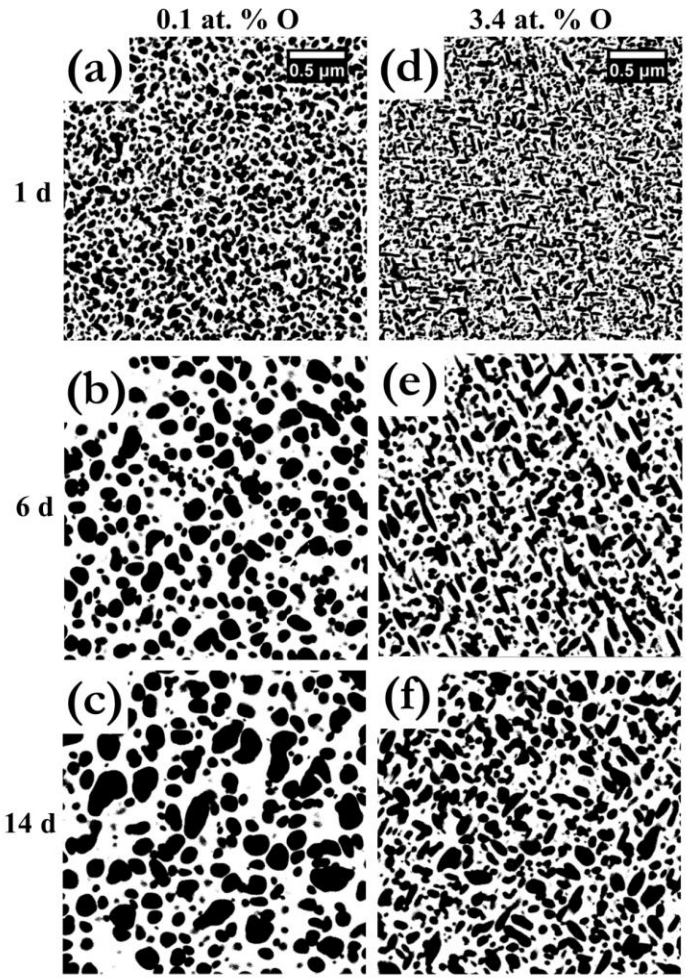

Figure 3.5: SEM-BSE images segmented using binary histogram-based image thresholding for the ω phase in aged Ti-20Nb at 450 °C in the following conditions: (a) 0.1 at. % O for 1 d, (b) 0.1 at. % O for 6 d, (c) 0.1 at. % O for 14 d, (d) 3.4 at. % O for 1 d, (e) 3.4 at. % O for 6 d, and (f) 3.4 at. % O for 14 d.

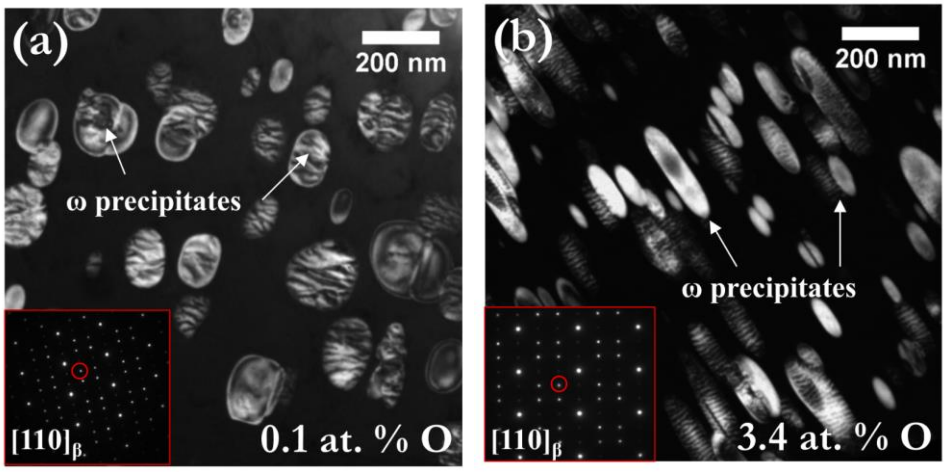

Figure 3.6: SAED pattern from $[110]_{\beta}$ zone axis and DF-TEM image using reflection in red circle from (a) DA Ti-20Nb with 0.1 at. % O aged for 6 days at 450 °C, showing ellipsoidal ω precipitates, and (b) OXA Ti-20Nb with 3.4 at. % O aged for 6 days at 450 °C, showing elongated rod shaped ω precipitates.

In order to quantify the oxygen partitioning behavior with respect to β and ω during ageing, atom probe tomography was conducted on an OXA specimen after 6 d of ageing at 450 °C with 3.4 at. % O (corresponding to microstructure in **Figure 3.4g** and **Figure 3.7**). The reconstructed APT dataset (**Figure 3.8**) shows Nb depleted and O enriched regions corresponding to ω phase and Nb enriched regions corresponding to the β matrix. A proximity histogram (or proxigram) that represents a concentration profile as a function of distance from the β/ω interface was generated using an iso-concentration surface of 63 at. % Ti (**Figure 3.8b-c**) and shows that the ω phase is rich in O and Ti, but not in Nb. Additionally, very little oxygen is measured in the β phase. Based on uniform values of the proxigram, the ω and β compositions are measured as follows: ω – Nb: 3 at. %, O: 6 at. %, Ti: Balance, β – Nb: 28 at. %, O: 0.3 at. %, Ti: Balance. Thus, oxygen partitions to ω precipitates and Nb partitions to the β matrix during ageing, as previously reported by Niinomi et al. [9].

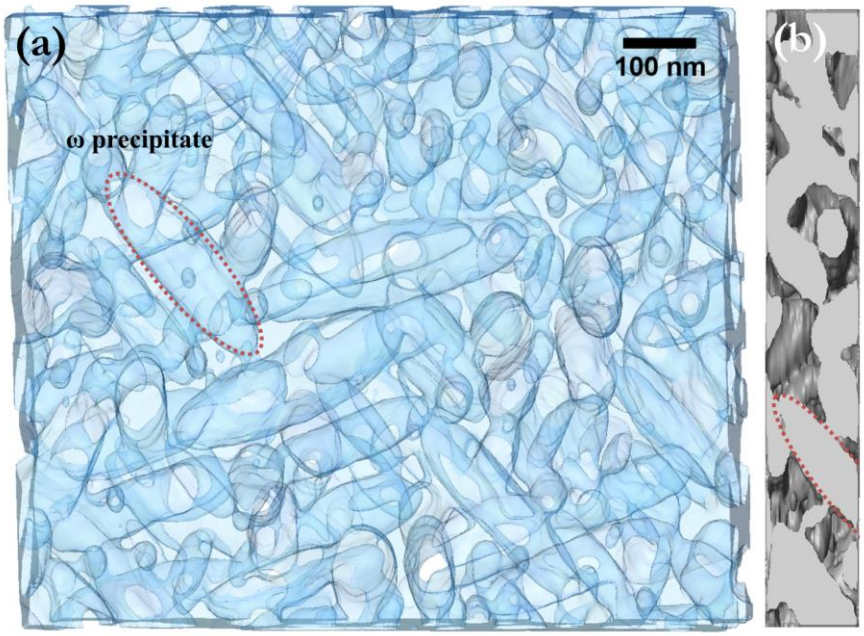

Figure 3.7: (a) Front view and (b) side view of reconstructed dataset (970 by 820 by 130 nm) collected using FIB tomography from OXA Ti-20Nb with 3.4 at. % O aged for 6 days at 450 °C corresponding to microstructure in Figure 3.4g. Red dotted line outlines an example of a rod shaped ω precipitate.

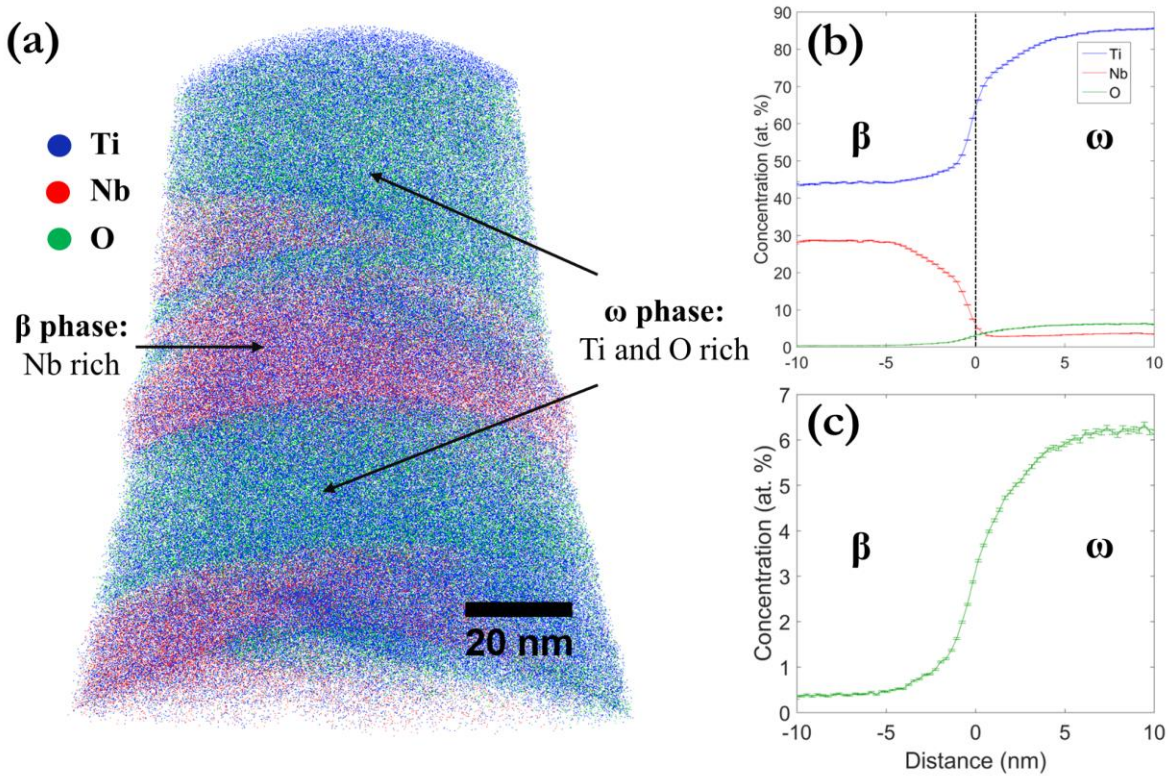

Figure 3.8: (a) APT reconstruction of sample from OXA Ti-20Nb with 3.4 at. % O aged for 6 days at 450 °C. Proxigram showing concentration profile for (b) Ti, Nb, and (c) O as a function of distance from the β/ω interface using 63 at. % Ti iso-concentration surfaces.

3.3.3 Two step ageing at 450 °C and 600 °C

A two step ageing experiment was conducted to investigate the extent of ω phase stability with oxygen. A set of DA and OXA samples with 3 d of ageing at 450 °C were subsequently aged for 1 h at 600 °C to promote ω dissolution and faster α formation. The ω solvus for pure Ti is reported to be 485 °C [18], therefore ω is not expected to be stable at 600 °C. After two step ageing, SEM backscatter images show that the resulting microstructures also strongly depend on oxygen content (**Figure 3.9**). At low oxygen contents (0.1, 1.5 at. % O), martensite formation is observed with few α precipitates (**Figure 3.9b**). As the oxygen content increases (3.6 at. % O), α precipitates appear to have nucleated in patches, with ω-like particles at the center of the patches (**Figure 3.9c**). Finally, at the highest levels of oxygen (4.1-4.8 at % O), dense distributions of α laths and ω-like particles are observed throughout the microstructure (**Figure 3.9d**). TEM SAED patterns in the 4.8 at. % O region (**Figure 3.9e**) show both ω and α reflections and confirm the co-existence of these phases [14,97].

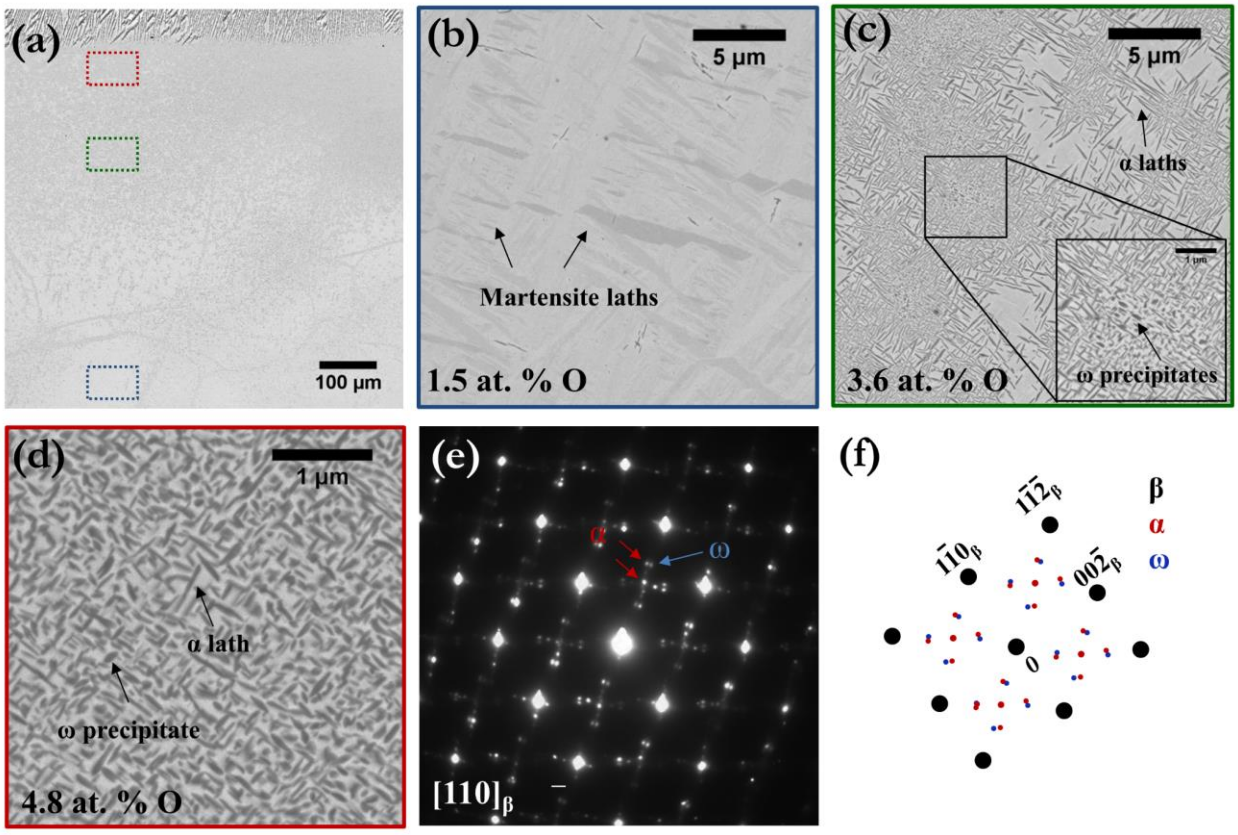

Figure 3.9: SEM-BSE images from OXA Ti-20Nb aged using a two step heat treatment for 3 d at 450 °C and 1 h at 600 °C. (a) Low magnification image of cross section. (b) Microstructure from region in blue box of low magnification image with 1.5 at. % O showing martensite and small α precipitates. (c) Microstructure from region in green box of low magnification image with 3.6 at. % O showing ω and α precipitate patches. (d) Microstructure and (e) SAED pattern with (f) key diagram from [110]$_\beta$ zone axis from region in red box of low magnification image with 4.8 at. % O showing ω and α precipitates.

3.4 Discussion

The results reveal that oxygen content significantly affects ω and α precipitation in a non-linear manner in the β matrix of Ti-20Nb. Elevated oxygen content results in a rod-like precipitate shape and higher number density of the ω phase. With additional ageing, these shape and number density differences were preserved, and ω showed a slower growth rate with high oxygen. Prolonged ageing yielded α precipitation at all observed oxygen contents, but the rate and amount of α nucleation was heavily influenced by the level of oxygen. The slowest α nucleation rate was observed with intermediate levels of oxygen in solid solution (2.7 at. % O) compared to faster precipitation with minimal (0.1 at. %) and elevated (4.1 at. %) oxygen. Below we discuss the effects of oxygen on ω and α precipitation and phase stability.

3.4.1 Role of oxygen on martensite formation and ω nucleation

Previous studies [27,58,98] have shown that oxygen in solid solution (0.5 at. % or greater) suppresses martensite formation during quenching in Ti-Nb alloys. However, the present results (**Figure 3.2**) with up to about 5 at. % O suggest that martensite suppression depends on both Nb and O content and may not be suppressed with oxygen if it is sufficiently stabilized at lower Nb contents. Oxidation of Ti-20Nb specimens resulted in a gradient of oxygen concentration in the matrix from the surface to center of specimens, and precipitation of large α laths in the subsurface metal just below the oxide layer is consistent with oxygen stabilizing the α phase. Martensite formation was confirmed in the β matrix below the α + β region upon quenching after oxidation (**Figure 3.2b**). Additionally, at higher Nb contents, martensite formation was suppressed in the matrix with high oxygen. This is shown in the β matrix between α laths in the two-phase α + β region of **Figure 3.2a** where the Nb and O contents were measured using WDS as roughly 23 at. % and 4.9 at. %, respectively. The suppression of martensite with oxygen in literature has been attributed to different factors, including an increase in the energy barrier of the transformation and formation of a semi-α" structure that acts as local barriers to long range martensite formation [99], a change in the relative stability of β and α" [100], and the presence of oxygen atoms in octahedral sites inhibiting contraction along the a-axis of α" martensite [101]. However, most previous studies were conducted with Nb content between 23-25 at. %, corresponding to a martensite start temperature (T_m) of roughly 100 °C [18]. Clearly, 1 at. % O is able to suppress martensite formation at these Nb compositions [27]. In Ti-20Nb used in this study with a T_m of about 200 °C [18], even approximately 5 at. % O, corresponding to the oxygen level measured at the (α lath + β) / β matrix interface where martensite formation was observed (**Figure 3.2**), was not enough to suppress martensite formation. Similarly, a Ti-11Nb-4O at. % alloy fabricated through powder metallurgy also showed minor α" formation after solution treatment [102]. Curiously, Ti alloys with the same 20 at. % Nb content have been reported to suppress martensite formation with only 0.7 at. % O in solid solution [103].

Upon ageing, the ω precipitate number density increased with greater oxygen content (**Figure 3.3a-b**). A simple thermodynamic basis for this observation may be attributed to oxygen increasing the phase stability of ω. According to published metastable Ti-Nb phase diagrams [18], the alloy composition and ageing temperature used in this study are to the right of the $T_0^{\beta/\omega}$ line that defines equality of the β and ω Gibbs free energies. Therefore, in the absence of oxygen, ω is

expected to form by nucleation and growth. If additions of oxygen increase the phase stability of ω (i.e. lowering its Gibbs free energy), it consequently also increases the driving force for ω nucleation, leading to a higher precipitate number density, as experimentally observed. Increases in ω phase stability with oxygen may also shift the ω Gibbs free energy curve such that the alloy concentration moves to the left of the $T_0^{\beta/\omega}$ line. There, a displacive transformation from β to ω, in which $\{111\}_\beta$ atomic planes partially collapse to form ω-like embryos [29,30], becomes possible, resulting in an increased ω precipitation rate.

3.4.2 Role of oxygen on ω precipitate morphology and growth rate

Growth and coarsening of isothermal ω during ageing require significant diffusion, with Nb being rejected from the ω phase and diffusing in the β matrix to the equilibrium composition. During ageing, oxygen partitions to ω from the β matrix, as previously shown [9,69] and further confirmed by the present APT measurements (**Figure 3.8**). The influence of oxygen content on the growth rate and morphology of the ω precipitates (**Figure 3.5, 3.6**) may stem from changes in the nature of the interface, the structure of the ω phase, and/or from kinetic limitations associated with solute diffusion and the β to ω transformation.

Increasing the alloy's oxygen concentration led to the formation of rod shaped ω precipitates with increased aspect ratio compared to ellipsoidal shapes with minimal oxygen (**Figure 3.4, 3.6**). Rod shaped ω phase at small sizes has been reported in literature [38,104] and also observed in this study (**Figure 3.3d**). Larger rod-like ω in a β Ti alloy processed with rapid heating rates and short ageing times has been shown [105], but the well-developed size of rod shaped ω that persists with long ageing times greater than 6 days (**Figure 3.6b**) has not been reported previously. If one assumes local equilibrium, precipitate shape is classically governed by the balance between interfacial energy and elastic misfit strain contributions. Density functional theory (DFT) calculations on low energy configurations of the ω/β interface suggested that the ellipsoidal shape in oxygen-free Ti-Nb may be attributed to interfacial energy anisotropy [106] and traditionally, the ellipsoidal shape has been associated with low misfit Ti alloy systems [96]. The retention of an ellipsoid shape for Ti-Nb-O ω precipitates suggests that interfacial energy may still play some role in controlling precipitate shape. However, the increase in aspect ratio to form a rod shape suggests that misfit strains through lattice distortion with added oxygen may also be relevant. Moreover, beyond equilibrium growth, precipitate shape may be affected by kinetic

effects, in which the β to ω transformation favors a particular direction or orientation during growth.

Conflicting or lack of literature results on equilibrium contributions complicates the current understanding of the role of O on ω growth rate. Without oxygen present, the nature of the ω/β interface reportedly evolves during ageing, and these structural changes may alter the influence of this interface on controlling ω growth. The nanoscale ω phase that forms upon quenching has been reported as coherent with a diffuse interface [29]. However, as ω grows during ageing, a sharp interface [29] has been observed with the existence of ledges [14,38], suggesting that growth could be interface-limited. During growth, the ω/β interfacial character may also change to semi-coherent [38], and misfit dislocations have been reported when ω has reached ~200 nm in size [107]. In contrast, it is well known that diffusion and rejection of β-stabilizers occurs during isothermal ω growth [2], and early literature suggested diffusion-controlled ω nucleation and growth for Ti-Mo alloys [108]. With oxygen, additional contributions to ω growth rate may arise from kinetic effects. As discussed above, the transformation from β to ω may happen very quickly by plane collapse, as a consequence of the oxygen stabilization of ω with respect to the β phase. As highlighted in [68], oxygen may increase the energy barrier associated with this collapse, and consequently reduce the rate of the transformation. A similar increase in energy barrier with oxygen that is expected to reduce nucleation rate has been shown for the martensitic α to ω transformation that takes place at high pressures [109], and ω suppression with oxygen has been experimentally verified for this transformation [110]. Kinetic limitations relating to high activation energy barrier for the β to ω transformation during nucleation have also been recently reported in the Ti-V system [111]. In the present results, the β to ω transformation is not suppressed with oxygen, likely due to the relatively high ageing temperature that allows for substantial diffusion, but the increase in energy barrier may slow the transformation rate during ω growth, as observed experimentally (**Figure 3.5**). Since O prefers the octahedral sites on $\{111\}_\beta$ planes, the β to ω transformation involving collapsing O atoms, which accounts for three out of four transformation pathways, requires short displacements for O to relocate to its final site and are associated with a 30-40 meV/atom energy barrier [68]. Such a high energy barrier would kinetically slow down the β to ω transformation and therefore the ω growth rate.

3.4.3 Role of oxygen on α nucleation in the presence of ω

With interstitial oxygen in the β matrix, prolonged isothermal ageing revealed that α eventually precipitated at all oxygen levels in this study (0.1-4.1 at. % O), which is consistent with ω being a metastable phase in β Ti alloys [107]. Furthermore, oxygen increases the energy of ω relative to that of α [109]. Surprisingly, α nucleation in Ti-Nb was quite slow, and ω persisted for significantly longer ageing periods in specimens both with and without oxygen. Literature reports on the effects of oxygen are conflicting, with oxygen having been reported as either reducing [9] or accelerating [35,64] the rate of α precipitation from ω. Interestingly, the α precipitation rate in the presence of the ω phase was observed to be slowest for intermediate levels of oxygen (2.7 at. %). Oxygen is a potent α-stabilizer [2], which explains the early α nucleation at relatively high oxygen levels (3.4, 4.1. at. % O). Nonetheless, the formation of ω prior to α suggests that α nucleation from β is associated with a high energy barrier and may be facilitated by ω nucleation. α nucleates at later times in oxygen-free samples and α nucleation is most delayed at intermediate levels of oxygen. Based on these results, we hypothesize that small levels of oxygen increase the ω phase stability with respect to the β phase without significantly increasing α stability, while higher levels of oxygen dramatically increase α stability over that of the ω phase. These stability changes would result in differences in the α nucleation driving force that account for the observed changes in precipitation rate. Two step ageing results (**Figure 3.9**) also suggest that elevated oxygen helps to expand the region of ω phase stability to higher temperatures. During the second ageing step at 600 °C, which is above the reported ω solvus [18], Nb and Ti diffusion is expected to dissolve the ~200 nm ω phase that precipitated during the first ageing step at 450 °C [112]. This dissolution was observed in both DA specimens and the center of OXA specimens with lower oxygen content, and martensite is formed in these regions upon quenching. However, at the highest interstitial oxygen contents (4.8 at. %), ω and α were identified using electron diffraction, indicating that the elevated oxygen content helped to stabilize the ω phase even at 600 °C. These insights on oxygen as both an α and ω-stabilizer may open new avenues of microstructural control for future design and development of β-Ti alloys.

3.5 Conclusions

The nucleation and growth of ω and α precipitates in Ti-20 at. % Nb with 0.1-4.8 at. % O was systematically investigated during isothermal ageing to elucidate oxygen effects on phase transformations in metastable β Ti alloys. The main conclusions are as follows:

- Oxidation experiments were used to investigate a range of oxygen contents in solid solution between 0.1 to 4.8 at. % on the subsequent ageing behavior of β titanium alloys.
- Ti-20Nb specimens with oxygen levels up to about 5 at. % showed martensite formation upon quenching following oxidation exposure. Therefore, the ability of oxygen to suppress martensite formation in metastable β Ti depends on both Nb and O content.
- Oxygen increases the stability of ω phase. During ageing, ω number density increases with elevated oxygen. Additionally, oxygen induces ω precipitates to form with a rod-like shape compared to an ellipsoid shape without oxygen present. Elevated oxygen content also expands the region of ω phase stability up to 600 °C, indicating that oxygen is an ω-stabilizer in β Ti alloys.
- Oxygen partitions to the ω phase during ageing and the growth rate of ω with high oxygen was slowed compared to ω formed with minimal oxygen. This growth rate change is attributed to an increased energy barrier for the β to ω transformation with oxygen. Thus, oxygen shows a dual effect on the ω phase by increasing phase stability but kinetically limiting the rate of transformation from β.
- α nucleation in the presence of ω depends on oxygen content. With high oxygen (greater than 3.4 at. % O), α precipitates at the fastest rate due to the significant increase in α thermodynamic phase stability and nucleation driving force with elevated oxygen. With intermediate levels of oxygen (2.7 at. %), α forms at the slowest rate due to a reduced nucleation driving force from increased ω phase stability, but relatively unchanged α stability. Therefore, oxygen content allows for microstructural control of ω and α transformation rates in β titanium alloys.

Chapter 4: Enhanced Work Hardening from Oxygen-Stabilized ω Precipitates in an Aged Metastable β Ti-Nb Alloy

4.1 Introduction

High levels of oxygen in solid solution in Ti alloys are considered detrimental to mechanical properties because of embrittlement concerns. In metastable β titanium alloys, the formation of isothermal ω precipitates is also known to cause severe embrittlement and ductility reduction [6,46]. ω is known to form as small, coherent particles [46] which are sheared by moving dislocations leading to inhomogeneous slip and embrittlement [8,13,47]. Therefore, ω precipitation has been historically undesirable for structural applications, and commercial heat treatment practices for β Ti alloys are usually designed to avoid ω formation [48]. However, ω phase formation in β Ti alloys remains an important area of interest due to ω's roles in controlling deformation behavior and structural properties. These roles include ω's influence as a heterogeneous nucleation agent for precipitation of the stable α phase [36,38,113], ability to change transformation induced plasticity and twinning induced plasticity deformation mechanisms to dislocation channeling [51], and contribution to enhancing ductility while preserving high strength during short ageing treatments [49,50]. While it is clear that the significant impact of ω precipitates on the deformation behavior of metastable β Ti alloys can be controlled via appropriate ageing, whether the properties of ω precipitates and consequently the mechanical response of β Ti alloys can also be tailored via chemistry is less clear.

Oxygen in solid solution has been shown to change ω's phase stability [9] and significantly influence phase transformations during heat treatment and processing of β Ti alloys [6]. In general, titanium has a high affinity for oxygen at room and elevated temperatures [2], and interstitial oxygen has been reported to reduce ductility for both the α and β phases [5]. Specifically, interstitial oxygen changes the formation of metastable phases in β Ti alloys [2,114]. Oxygen has been shown to suppress the martensitic transformation in β titanium alloys during solution treatment and quenching [114]. This suppression of martensite reportedly results in novel

deformation behavior and thermal expansion properties in gum metal-like compositions [7,59–61]. Oxygen also influences ω and α precipitation during low temperature isothermal ageing [9,69]. In particular, elevated oxygen in Ti-Nb alloys leads to changes in ω's precipitate morphology, number density, and growth rate during ageing, and in α precipitation rate (**Chapter 3**). Oxygen partitions to the ω phase after extended ageing, leaving minimal O present in the β phase matrix [9,69]. Although ω precipitates tend to promote shear band formation and slip localization, oxygen's partitioning behavior to ω and its role in refining ω precipitate distributions create an opportunity to investigate the synergy between two detrimental factors, the presence of oxygen and ω formation, on the resulting mechanical properties. Specifically, we show that oxygen-stabilized ω leads to increased resistance to shear localization and consequently to increased strength and strain hardening. The results may suggest design strategies to address the significant embrittlement and loss of ductility observed for ω-strengthened β Ti alloys without oxygen.

4.2 Experimental methods

An arc-melted button with a nominal composition of Ti-32.7 wt. % Nb (Ti-20 at. % Nb) was provided by ATI. The button was remelted three times to improve homogeneity. Specimens were cut from the button using a slow speed diamond saw, encapsulated with pure Ti pieces in a quartz tube backfilled with Ar gas, solution treated at 1000 °C for 10 h, and quenched in water. Interstitial oxygen levels were measured in the arc-melted button and after solution-treatment as 0.1 at. % by inert gas fusion using a LECO analyzer. A set of solution treated specimens was oxidized at 900 °C for 5 h in a 1 standard cubic centimeter per minute (SCCM) O_2/4 SCCM Ar environment (approximately pO_2 = 0.2 atm/20.3 kPa), which were termed as "pre-oxidized". The as-solution treated specimens and pre-oxidized specimens were subsequently isothermally aged using the following conditions: 300 °C for 3 days or 450 °C for 2 h or 3 days. Oxidation and ageing heat treatments were conducted according to methods reported in **Chapter 3**. The aged samples without the oxidation treatment are hereafter referred to as *directly aged* (DA) samples, and the pre-oxidized and aged samples (with the created oxygen gradient) are referred to as *oxidized and aged* (OXA). Investigation at different cross-sectional depths of the OXA specimens corresponded to microstructures with different oxygen contents, which were measured using wavelength dispersive spectroscopy (WDS) as reported in **Chapter 3**. Specimens for characterization were

mounted in epoxy and ground using 320-1200 grit SiC papers followed by polishing with 0.03 μm colloidal silica suspension. Scanning electron microscopy (SEM) imaging and focused ion beam (FIB) preparation of site-specific transmission electron microscopy (TEM) foils and needle-shaped atom probe tomography (APT) specimens were performed using a Thermo Fisher Scientific FEI Helios 650 Nanolab with a Ga^+ ion FIB. TEM specimens were cleaned using low energy Ar ion milling to remove damage induced during Ga^+ ion FIB milling [115]. TEM images, scanning transmission electron microscopy (STEM) images, and selected area electron diffraction (SAED) patterns were obtained using a JEOL 3011 microscope operated at 300 kV and Thermo Fisher Scientific Talos F200X G2 microscope operated at 200 kV. APT data collection was performed with a Cameca local electrode atom probe (LEAP) 5000 XR operated in laser mode. APT data was collected using a specimen temperature of 30 K, a detection rate of 0.005 atoms per pulse, laser pulse energy of 25 pJ, and pulse repetition rate of 200 kHz. Data reconstruction, background subtraction, peak deconvolution, and compositional analysis were performed using the Integrated Visualization and Analysis Software (IVAS) package 3.8.2 and AP Suite software package 6.1.

Given the compositional gradient and resulting microstructural variation of OXA Ti-20Nb specimens, micropillar compression testing was utilized to probe deformation mechanisms of localized regions within samples. Precise crystallographic grain orientations were measured using electron backscatter diffraction (EBSD) for polished DA and OXA samples. Large β phase grains (approximately 500 μm to 1 mm in size) observed in polished specimens were selected for circular micropillar fabrication (**Appendix II**). One grain in each sample was selected with an out-of-plane $(100)_\beta$ orientation to ensure a high Schmid factor for the reported operative $<111>\{112\}_\beta$ slip system for uniaxial compression of ω-enriched β Ti alloys [116,117]. Representative Schmid factor maps calculated from EBSD inverse pole figure (IPF) maps for uniaxial compression with $<111>\{112\}_\beta$ slip and $<111>\{110\}_\beta$ slip are shown in **Appendix II**. Although micropillar compression may show size-related effects based on pillar dimensions and tested microstructures [118], precipitate-strengthened alloys with fine precipitate sizes have shown a much weaker size dependence, where deformation behavior is controlled by internal microstructural length scales that dominate over specimen size effects [119,120]. In general, extrinsic size effects tend to dominate when specimen dimensions are sufficiently larger than dispersed microstructural features and the tested volume contains ample dislocation sources [121]. Under such conditions, small-scale mechanical testing methods yield meaningful yield strength values [121]. Therefore, single

crystal micropillars with 2 or 5 μm diameters (*d*) were fabricated using FIB and SEM in a Thermo Fisher Scientific FEI Helios 650 Nanolab in order to better approximate bulk-like properties. FIB micropillar fabrication was performed using an automated script with coarse annular milling at 30 kV, 9 nA and fine milling at 30 kV, 0.79 nA. Milled micropillars had a diameter-to-height aspect ratio of approximately 1 to 2.5 to avoid a triaxial stress state for low aspect ratios and pillar buckling at high aspect ratios [122], and had a maximum vertical taper angle of ~3° due to the Ga^+ ion beam profile [123]. Representative 2 and 5 μm diameter circular pillars are shown in **Appendix II**. For OXA specimens, micropillars were fabricated at distances of approximately 100, 500, and 1000 μm from the α lath/β matrix interface, corresponding to oxygen levels of 4.1, 2.7, and 1.5 at. % O, respectively, as measured by WDS (**Chapter 3**).

Compression of the micropillars was performed using in-situ and ex-situ systems. In-situ testing was performed using a Bruker Hysitron PI 85 SEM Picoindenter with a diamond flat punch indenter (11 μm diameter flat end) in a Thermo Fisher Scientific FEI Magellan SEM. Ex-situ testing was performed using a Bruker Hysitron TI 950 Triboindenter equipped with a flat punch indenter (60° cone angle, 10 μm diameter flat end) or a spherical probe indenter (60° cone angle, 50 μm diameter spherical indenter). Loading was displacement-controlled with a constant loading rate of 2.5 nm/s, resulting in a strain rate of ~0.0005 s^{-1}. Since there may not be an obvious failure point for micropillar compression testing, tests were manually stopped at a predetermined displacement amount in order to characterize compressed pillars at specific nominal strain levels. Videos collected during in-situ compression testing in the SEM show the progression of micropillar deformation for specific conditions and are reported in **Appendix II**. Buckling was not observed for any tested micropillars in this study. Additionally, compression of 2 and 5 μm diameter pillars and using different probe indenter geometries indicated no difference in observed experimental trends (**Appendix II**). Engineering stress and strain values were calculated from in-situ and ex-situ load versus displacement data. The engineering stress was calculated as $\sigma = F/A_0$ where F is the measured force and A_0 is the cross-sectional area at the top of the pillar, and the engineering strain was calculated as $\varepsilon = \Delta L/L_0$ where ΔL is the pillar displacement and L_0 is the initial pillar height [117]. During in-situ testing and after ex-situ testing, the morphology of compressed pillars was observed using SEM, TEM, and high-angle annular dark-field (HAADF) STEM imaging of deformed pillars using cross-sectional FIB liftouts similar to Refs. [124,125].

4.3 Results

4.3.1 Initial microstructures of aged Ti-20Nb with varying oxygen content

The aged microstructures for DA and OXA Ti-20Nb specimens were characterized using SEM, TEM, and APT prior to micropillar compression testing to determine differences in precipitate size, number density, and chemistry. The oxidized Ti-20Nb microstructures prior to ageing and detailed discussion of the role of oxygen on ω and α precipitation kinetics were reported in **Chapter 3**. After isothermal ageing for 3 d at 300 °C, second phase precipitates identified as the ω phase by electron diffraction formed in the β phase matrix of DA and OXA Ti-20Nb specimens (**Figures 4.1a-b**). SAED patterns of the $[110]_\beta$ zone axis for both DA and OXA specimens showed ω reflections at 1/3 and 2/3 $\{112\}_\beta$ positions. These ω reflections correspond to the diffraction spots for the ω1 and ω2 variants out of four total ω-variants that form from β. Diffraction spots for the ω3 and ω4 variants are not observed since they are overlapping with the diffraction spots for the β phase [117]. Dark-field TEM images formed by selecting an ω diffraction spot revealed that DA and OXA Ti-20Nb specimens both showed a high number density of ω precipitates distributed homogeneously throughout the β matrix (**Figure 4.1a-b**). ω's size, aspect ratio, area density, and volume fraction are listed in **Table 4.1**. The average lengths of the major and minor axes for ω were used to calculate an equivalent spherical diameter, *2r*, which were ~4-6 nm regardless of oxygen content. The measured aspect ratio of ω particles based on the major and minor axes increased slightly without oxygen present. Neglecting particles below 1 nm, ω particles were counted in **Figure 4.1a-b** for DA and OXA specimens, and then multiplied by 4 to account for the four crystallographic ω variants that form with equal population to obtain the total ω particle count. The average area densities n_s of ω were then estimated by dividing the total particle count by the area of the TEM images in **Figure 4.1a-b**. The area fraction of ω was estimated using image thresholding and measurement of TEM images using ImageJ processing software to be approximately 11% for both DA and OXA specimens. These area fractions were assumed to equal the volume fraction, *f*, of ω based on stereology [126]. Finally, the inter-particle spacing *D* for ω particles was calculated by taking into account the effect of finite obstacle size for impenetrable particles and represents the measure of the free spacing between finite obstacles [127]. The average planar radius $\langle r_s \rangle$ was calculated using $\langle r_s \rangle = \pi \langle r \rangle / 4$, which was then used to calculate *D* using the following equation [127]:

$$D = [(32/3\pi f)^{1/2} - 2] < r_s > (1).$$

Although elemental partitioning during ageing is known to occur following ω formation [9], APT measurements for OXA Ti-20Nb with 4.1 at. % O aged for 3 d at 300 °C did not display strong partitioning behavior, as shown by the lack of solute-rich and solute-depleted regions in the reconstructed APT dataset shown in **Figure 4.1c**. A proximity histogram (or proxigram) that represents a concentration profile as a function of distance from the β/ ω interface was generated using an iso-concentration surface of 77 at. % Ti, which showed only slight concentration differences between the ω and β phases with respect to Ti, Nb, and O (**Figure 4.1d**). In particular, interstitial oxygen was still present in both the β and ω phases at approximately 2.5 at. %. These results suggest that elemental partitioning of Ti, Nb, and O has begun, but full partitioning has not yet occurred after ageing at 300 °C.

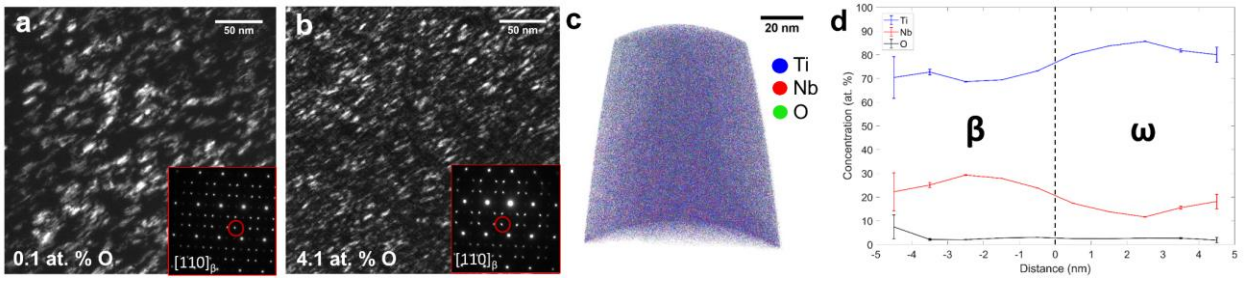

Figure 4.1: Dark-field TEM images of Ti-20Nb aged for 3 d at 300 °C with (a) 0.1 at. % O and (b) 4.1 at. % O. Insets show SAED patterns for the [110]$_\beta$ zone axis showing β and ω diffraction spots. Dark-field images were formed using selected ω diffraction spot in red circle shown in inset. (c) APT reconstruction of OXA Ti-20Nb aged for 3 d at 300 °C with 4.1 at. % O and (d) proxigram showing Ti, Nb, and O concentration as a function of distance from 77 at. % Ti iso-concentration surfaces.

Table 4.1: Quantification of initial microstructural features for ω precipitates in aged Ti-20Nb with varying oxygen content.

Specimen	Ageing Treatment	Oxygen Concentration (at. %)	Equivalent Diameter, *2r*, (nm)	Aspect Ratio	Area Density, n_s (um^{-2})	Volume Fraction, *f*	Inter-particle spacing, *D* (nm)
DA	3 d, 300 °C	0.1	6.1	3.0	12837	0.11	8.6
OXA	3 d, 300 °C	4.1	4.5	2.5	28877	0.11	6.3
DA	2 h, 450 °C	0.1	33	2.8	1457	0.34	15
OXA	2 h, 450 °C	4.1	27	3.8	1796	0.34	12
DA	3 d, 450 °C	0.1	115	1.6	88	0.45	34
OXA	3 d, 450 °C	1.5	110	1.6	84	0.45	32
OXA	3 d, 450 °C	2.7	104	1.9	102	0.45	31
OXA	3 d, 450 °C	4.1	86	3.9	127	0.45	25

Ageing times at 450 °C and oxygen levels were selected to clarify the influence of elevated oxygen on ω precipitation kinetics and morphologies. After ageing for 2 h at 450 °C, ω precipitates grew in size, and the DA and OXA microstructures showed fine ~30 nm ω precipitates with partitioned elements as evidenced from high compositional contrast in backscattered SEM (SEM-BSE) images (**Figure 4.2a-b**). SEM-BSE images also showed a higher number density and elongated precipitate morphologies for ω with elevated oxygen levels. Previous TEM imaging had revealed that a more elongated and rod-like shape was observed for ω precipitates aged for 2 h at 450 °C with elevated O compared to ellipsoidal shapes with minimal oxygen (**Chapter 3**). Similar quantifications for ω's size, aspect ratio, area density, volume fraction, and inter-particle spacing were obtained for DA and OXA specimens after ageing for 2 h at 450 °C (**Table 4.1**). For these specimens, ω's size, area density, and volume fraction were estimated using SEM-BSE images that showed all ω variants. In particular, the aspect ratio for ω in OXA Ti-20Nb with 4.1 at. % O is higher than for DA specimens without oxygen, which reflects the elongated shape of ω that develops with oxygen. The volume fraction for ω precipitates increased to ~34% for DA and OXA specimens. APT measurements were also conducted to investigate the extent of elemental partitioning after ageing at 450 °C. A reconstructed APT dataset for OXA Ti-20Nb with 4.1 at. % O (**Figure 4.2c**) showed strong elemental partitioning as well as Ti-rich regions and Nb-rich

regions corresponding to the ω and β phase, respectively. Furthermore, proxigram measurements using a 77 at. % Ti iso-concentration surface showed up to 5 at. % O in the ω phase and ~1 at. % O in the β phase (**Figure 4.2d**). Therefore, oxygen partitioned to the ω phase after ageing at 450 °C, leaving low levels of oxygen present in the β matrix. Such elemental partitioning behavior is consistent with ageing results reported for similar Ti-Nb-O containing alloys [9,69], and is also consistent with oxygen acting as an ω-stabilizer for Ti-Nb alloys (**Chapter 3**).

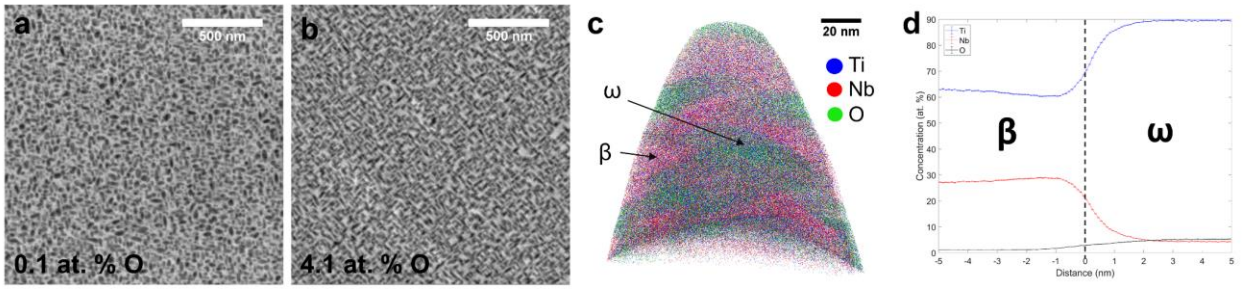

Figure 4.2: SEM-BSE images of Ti-20Nb aged for 2 h at 450 °C with (a) 0.1 at. % O and (b) 4.1 at. % O. (c) APT reconstruction of OXA Ti-20Nb aged for 2 h at 450 °C with 4.1 at. % O and (d) proxigram showing Ti, Nb, and O concentration as a function of distance from 77 at. % Ti iso-concentration surfaces.

Prolonged ageing for 3 d at 450 °C resulted in continued growth and coarsening of ω precipitates at all oxygen levels. SEM-BSE images and bright-field TEM observations showed changes in ω's size, number density, and morphology related to oxygen content (**Figure 4.3** and **Table 4.1**). The OXA specimens with elevated oxygen content exhibited a higher number density of ω precipitates than the DA specimens, and the shape of ω precipitates changed from ellipsoidal to rod-like with increasing oxygen levels. Such changes are consistent with previously reported results for Ti-Nb alloys with elevated oxygen (**Chapter 3**). The volume fraction of ω precipitates after 3 d of ageing for both DA and OXA specimens at all oxygen levels was approximately 45%, which is likely the maximum volume fraction for this alloy at 450 °C. Regardless of oxygen content, no α phase was noted after ageing for 3 d at 450 °C. Additionally, as expected from prior work [9] and the high compositional contrast in SEM-BSE images (**Figure 4.3**), significant elemental partitioning was observed, with the β and ω phases being rich in Nb and Ti, respectively. For OXA specimens, oxygen partitioned to the ω phase up to 6 at. % during isothermal ageing and minimal oxygen of ~0.3 at. % O was present in the β matrix, in accordance with previously reported ω partitioning behavior [9] and ω stabilization with oxygen (**Chapter 3**).

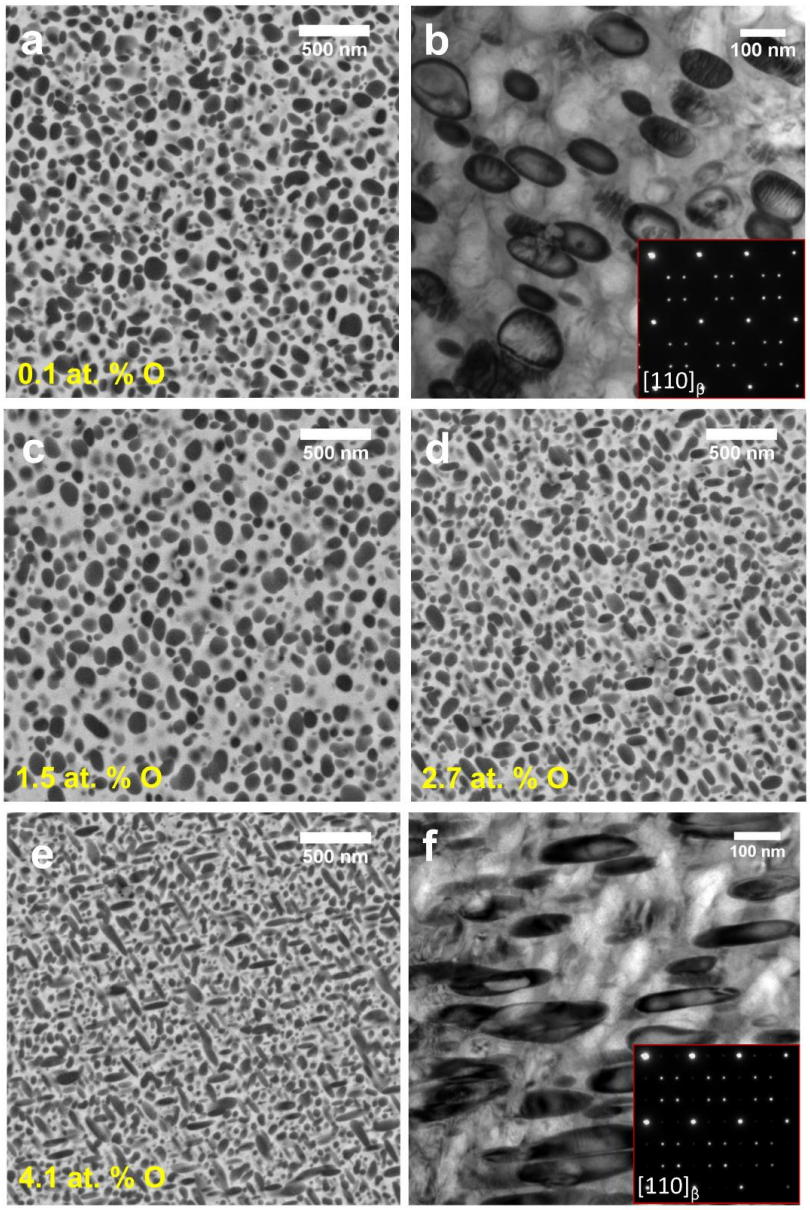

Figure 4.3: (a) SEM-BSE and (b) bright-field TEM images of Ti-20Nb aged for 3 d at 450 °C with 0.1 at. % O. SEM-BSE images of Ti-20Nb aged for 3 d at 450 °C with (c) 1.5, (d) 2.7, and (e) 4.1 at. % O. (f) Bright-field TEM image of Ti-20Nb aged for 3 d at 450 °C with 4.1 at. % O. Insets for bright-field TEM images in (b) and (f) show SAED patterns for the $[110]_\beta$ zone axis showing β and ω diffraction spots.

4.3.2 Micropillar compression and deformed microstructures of Ti-20Nb aged at 300 °C

Micropillar compression testing of DA and OXA specimens aged at 300 °C was conducted to determine the deformation behavior of microstructures with a high number density of nanometer-sized ω precipitates and interstitial oxygen that has not yet strongly partitioned to ω. Post-compression images of 2 μm diameter pillars for Ti-20Nb with 0.1 or 4.1 at. % O aged for 3 d at 300 °C deformed to 15-20% strain showed a large number of slip bands regardless of oxygen

content (**Figure 4.4a-b**). In-situ observations showed slip band formation and fast catastrophic pillar failure for both DA and OXA micropillars (**Appendix II**). The associated compressive engineering stress-strain curves showed that serrated flow and several large drops in stress values were observed after initial yielding for both DA and OXA specimens (**Figure 4.4c**). In-situ compression testing revealed that the observed load drops matched the activation of macro-scale slip events on favorable slip planes (**Appendix II**). The similarity in behavior for the DA and OXA micropillars aged at 300 °C suggests that elevated oxygen levels did not affect the deformation mode.

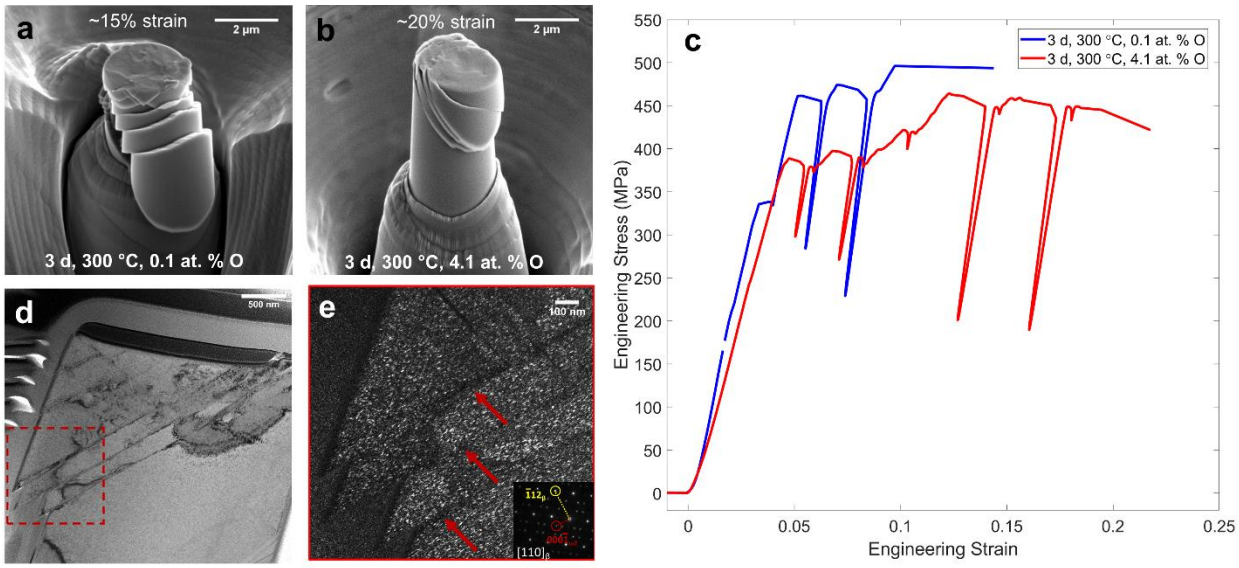

Figure 4.4: SEM-BSE images of compressed micropillars for Ti-20Nb aged for 3 d at 300 °C with (a) 0.1 at. % O and (b) 4.1 at. % O. (c) Engineering stress-strain curves for compressed micropillars in (a) and (b). (d) Bright-field and (e) dark-field TEM images of liftout sample from compressed pillar with 4.1 at. % O in (b) showing depleted ω precipitates and precipitate free channels (red arrows).

In order to evaluate the deformed microstructure, TEM imaging was performed on liftout samples from cross-sections along $[110]_\beta$ for a deformed pillar from Ti-20Nb with 4.1 at. % O aged for 3 d at 300 °C. Several parallel slip bands were observed spanning the pillar's width (**Figure 4.4d**) and the ω phase was depleted in the slip bands (**Figure 4.4e**), resulting in the formation of precipitate-free channels located in the slip bands. Slip trace analysis and direction of the slip bands revealed that the bands were parallel to the $[000\text{-}1]_{\omega 2}$ // $[\text{-}22\text{-}2]_\beta$ directions and perpendicular to the $(\text{-}112)_\beta$ plane, as expected for dislocation activity on the $<111>\{112\}_\beta$ slip system. These results suggest that the removal of ω precipitates is related to localized dislocation slip that accounts for slip band formation. Similar observations of localized dislocation activity, removal of ω precipitates along the $<111>\{112\}_\beta$ slip system, and formation of precipitate-free

channels have been reported in several other β Ti alloys containing nanometer-sized ω with and without oxygen [8,51,116,117]. In particular, micropillar compression of β Ti-10V-2Fe-3Al alloy with nanometer-sized ω precipitates reported the formation of precipitate-free channels with localized dislocation slip that resulted in serrated flow and load drops observed during micropillar compression testing [117].

4.3.3 Micropillar compression and deformed microstructures of Ti-20Nb aged at 450 °C

To determine differences in mechanical properties and deformation behavior with varying oxygen content, micropillar compression testing was also performed for DA and OXA specimens aged at 450 °C for 3 days such that elemental partitioning to the ω precipitates and β matrix occurred. Without oxygen present, macroscopic slip bands readily formed across the pillars (**Figure 4.5a**, **Appendix II**). However, with increasing oxygen levels, the formation of slip bands after compression was gradually suppressed, and micropillars with 2.7 and 4.1 at. % O did not show any step formation or slip bands after compression (**Figure 4.5c-d**, **Appendix II**). A similar series of micropillar compression tests was conducted for DA and OXA specimens aged for only 2 hours so that they contained finer ω precipitates. Comparable trends with increasing oxygen content were observed for compressed micropillars (**Figure 4.5e-f**). Micropillars for the DA specimen without oxygen showed several slip bands after deformation (**Figure 4.5e**). In contrast, deformed pillars for the OXA sample with 4.1 at. % O showed fewer slip bands with smaller step features (**Figure 4.5f**), and comparing the pillar's shape before and after compression showed slight bulging that suggests more distributed deformation. The significant reduction in the size and number of slip bands formed with increasing oxygen for these pillars also supports the observation of suppressed slip bands for deformed micropillars with high oxygen after 450 °C ageing.

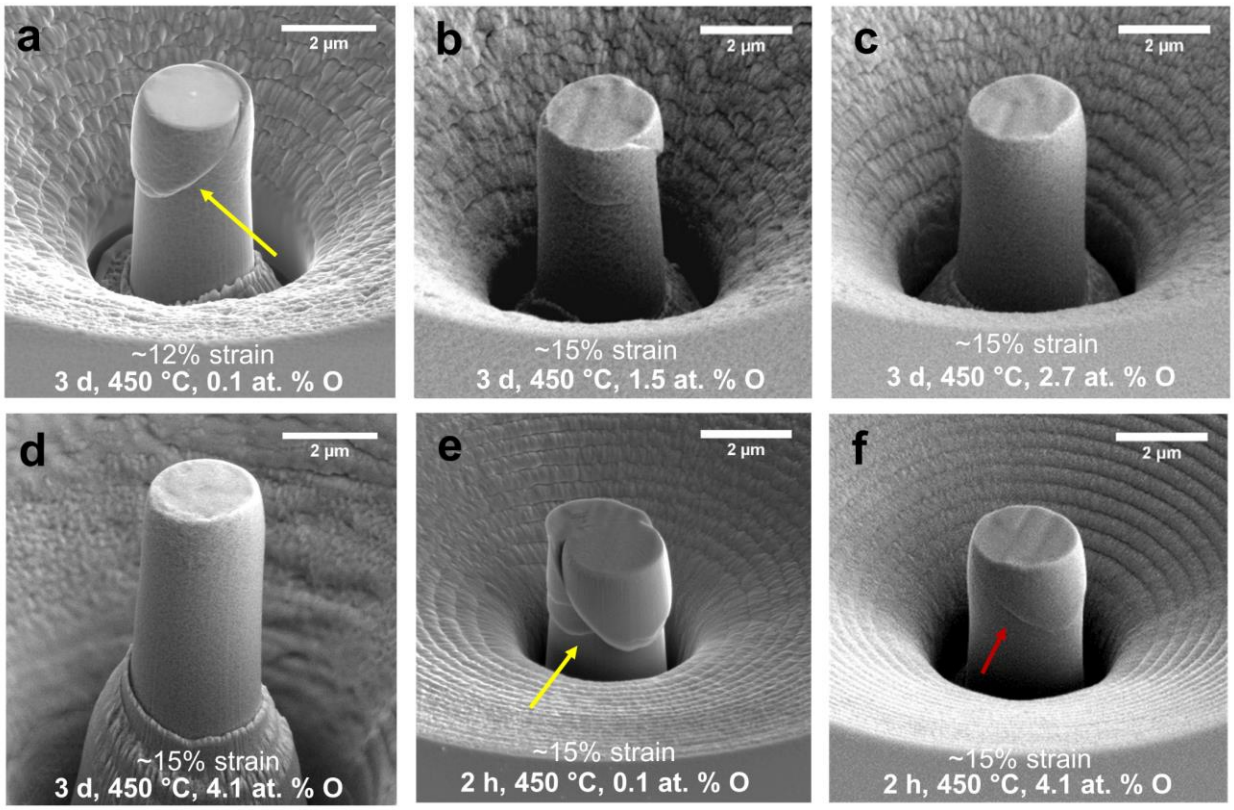

Figure 4.5: SEM-BSE images of compressed micropillars for Ti-20Nb aged for 3 d at 450 °C with (a) 0.1, (b) 1.5, (c) 2.7, and (d) 4.1 at. % O, and for Ti-20Nb aged for 2 h at 450 °C with (e) 0.1 and (f) 4.1 at. % O. Yellow and red arrows show slip bands formed on micropillars during compression testing.

Compressive engineering stress-strain curves up to 15% strain calculated from the collected load versus displacement data during compression of DA and OXA specimens aged for 3 d at 450 °C were plotted to evaluate the influence of ω's size, number density, and oxygen content (**Figure 4.6a**). In the absence of oxygen, the stress-strain curve showed a flat curve after initial yielding and a drop in the stress with increasing strain, which corresponded to macro-scale slip band and step formation (**Appendix II**). In contrast, the stress-strain curves for pillars fabricated on the OXA specimen with higher oxygen contents exhibited smooth and continuous flow, as well as increased work hardening after initial yielding. The average compressive yield strengths based on 0.2% offset values of four tested micropillars for each condition were approximately 294, 358, 364, and 464 MPa for the DA specimen without oxygen and the OXA specimen with 1.5, 2.7, and 4.1 at. % O, respectively. Therefore, comparing the DA specimen without O and OXA specimen with 1.5 at. % O revealed that yield strength increased with higher oxygen levels for the same ω size. For OXA Ti-20Nb with 2.7 and 4.1 at. % O, the higher oxygen levels and more refined ω sizes likely both contributed to the observed increases in yield strengths. Changes in strain

hardening behavior were evaluated using true stress-true strain curves for micropillars tested on DA and OXA specimens. Strain hardening behavior is given by Ludwik's equation [128]:

$$\sigma = \sigma_0 + K\varepsilon^n \quad (2)$$

where σ_0 is the initial yield stress, K is the strengthening coefficient, and n is the strain hardening exponent. Strain hardening exponents for compressed micropillars were estimated by fitting the plastic region of true stress-true strain curves to **Eq. (2)** for specimens aged for 3 d at 450 °C. For the DA specimen that showed a load drop in the stress-strain curve, n was calculated based on the plastic region up to the onset of the first load drop corresponding to slip band formation (located at blue arrow in **Figure 4.6a**). Notably, the strain hardening exponent *n* was approximately ~0.12 for the DA specimen and ~0.25 for the OXA specimen with 1.5, 2.7, and 4.1 at. % O, respectively, based on four tested micropillars per condition, confirming the increase in work hardening for OXA specimens with higher oxygen. These trends were also observed in engineering stress-strain curves for DA and OXA micropillars aged for 2 h at 450 °C (**Figure 4.6b**). More instability in the stress-strain curve was observed for DA micropillars aged for 2 h (blue curve in **Figure 4.6b**) attributed to the activation of more slip bands that was observed for deformed pillars compared to after 3 d of ageing (**Figure 4.5a** and **Figure 4.5e**). With high oxygen content, stress-strain curves for micropillars fabricated on OXA specimens aged for 2 h with 4.1 at. % O exhibited similar yield strength values and work hardening capability as those with coarser ω precipitates aged for 3 d with 4.1 at. % O.

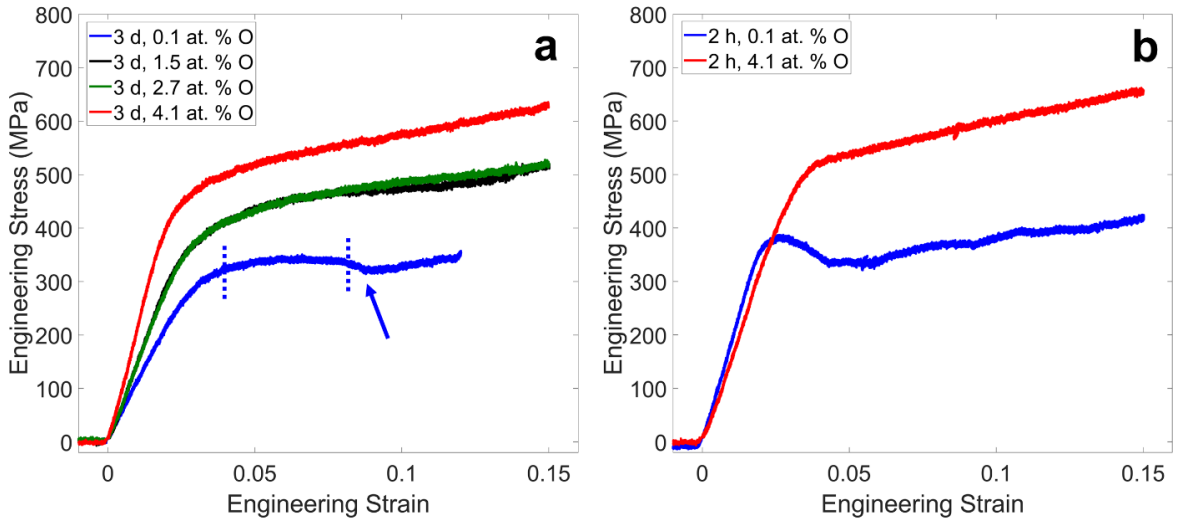

Figure 4.6: (a) Engineering stress-strain curves for compressed micropillars from Ti-20Nb aged for 3 d at 450 °C with varying oxygen content. Dashed lines in (a) show regions used for fitting to Equation 2 to estimate strain hardening exponents for micropillars with a load drop (located at blue arrow). (b) Engineering stress-strain curves for compressed micropillars from Ti-20Nb aged for 2 h at 450 °C with 0.1 and 4.1 at. % O.

After compression, micropillars were cross-sectioned along $[110]_\beta$ and examined using SEM and TEM to observe the deformed microstructures. SEM imaging of a compressed micropillar deformed to ~15% strain for DA specimens without O aged for 3 days at 450 °C was consistent with ω precipitate shearing, and a slip band that propagated across the entire pillar diameter suggested significant localized deformation (**Figure 4.7a**). Dark-field TEM images formed using ω reflections showed a continuous slip band that cut through ω precipitates (**Figure 4.7b**). Similar to deformed microstructures after 300 °C ageing, the slip bands that formed were also parallel to the $[0001]_{\omega 1}$ // $[2\text{-}2\text{-}2]_\beta$ directions and perpendicular to the $(1\text{-}12)_\beta$ plane, indicating that dislocation activity took place along the $<111>\{112\}_\beta$ slip system. The larger sizes of ω after 450 °C ageing prevented the complete disappearance of ω precipitates after shearing, but a deformation channel was still formed by shearing of precipitates that propagated in a continuous line across the entire pillar width. Similar ω-free channels have been reported with larger ω precipitates after bulk tensile testing of a Ti-Mo alloy [91]. Therefore, deformation of the oxygen-free pillar for DA Ti-20Nb aged for 3 d at 450 °C resulted in shearing of ω precipitates along the $<111>\{112\}_\beta$ slip system in a continuous channel spanning the entire pillar.

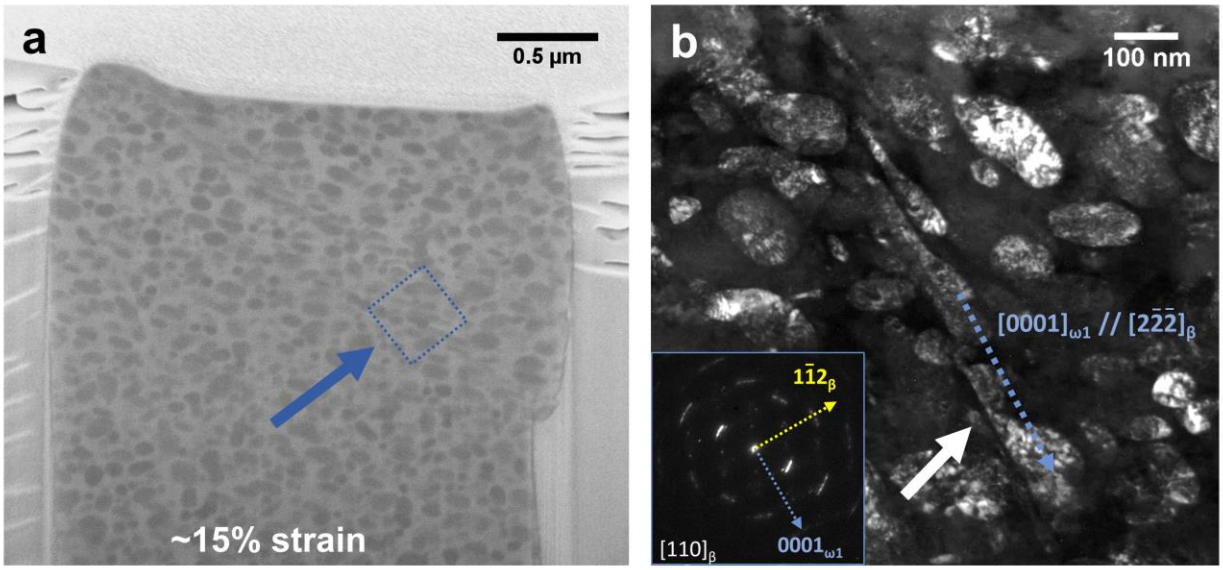

Figure 4.7: (a) SEM-BSE image of cross-section for compressed micropillar with 15% strain for Ti-20Nb aged for 3 d at 450 °C with 0.1 at. % O. (b) Dark-field TEM image of liftout from blue outlined region in compressed pillar shown in (a). Inset shows TEM SAED pattern. White arrow points to slip bands and sheared ω precipitates along $<222>_\beta$ direction.

The higher number density of rod-like ω precipitates in Ti-20Nb aged for 3 d at 450 °C with 4.1 at. % O complicated observation of potential precipitate shearing in FIB cross-sectioned pillars (**Figure 4.8a**). SEM-BSE images of the cross-sectioned pillar did not show obvious slip

band formation or ω shearing after deformation to ~15% strain (**Figure 4.8a**). HAADF STEM images for a liftout sample with a $[110]_{\beta}$ zone axis showed that the shape of ω precipitates remained largely intact without obvious channel formation (**Figure 4.8b**). However, possible indications of precipitate shearing were visible on select ω precipitates exhibiting a disruption in their surface curvature and cutting features that aligned with the $[0001]_{\omega 1}$ // $[2\text{-}2\text{-}2]_{\beta}$ directions and perpendicular to the $(1\text{-}12)_{\beta}$ plane corresponding to the $<111>\{112\}_{\beta}$ slip system (**Figure 4.8c-d**). These presumably sheared precipitates tended to be isolated features, and no extended shearing across multiple precipitates was observed. Imaging was also conducted for an OXA Ti-20Nb micropillar aged for 2 h at 450 °C with 4.1 at. % O to understand the deformed microstructure with smaller ω precipitates that still showed significant chemical partitioning. HAADF STEM images of a cross-sectioned liftout for a deformed pillar to 15% strain also revealed regions with isolated shearing of ω precipitates aligned with the $<111>\{112\}_{\beta}$ slip system (located at pairs of red arrows in **Figure 4.9**), but no extended shearing was observed. While ω precipitates can still be sheared with elevated oxygen, the formation of a continuous channel spanning the entire pillar's diameter that results in localized deformation was hindered.

4.4 Discussion

Micropillar compression testing of elevated oxygen and oxygen-free microstructures in aged metastable β Ti-20Nb alloys showed significant changes in deformation behavior and mechanical properties depending on initial microstructures and oxygen content. In specimens with nanometer-sized ω (smaller than ~6 nm), compression testing resulted in the formation of shear bands, and engineering stress-strain curves showed serrated flow and several load drops regardless of oxygen content. In specimens with larger ω sizes (50-120 nm), the oxygen content strongly influenced the deformation response and the associated compressive stress-strain data. In the absence of oxygen, compression testing resulted in the formation of shear bands and low work hardening. In contrast, the presence of 2.7 and 4.1 at. % O suppressed shear band formation, and the associated stress-strain curves showed enhanced work hardening after initial yielding, even though the microstructures consisted of known embrittling features in the form of interstitial oxygen and metastable ω phase formation.

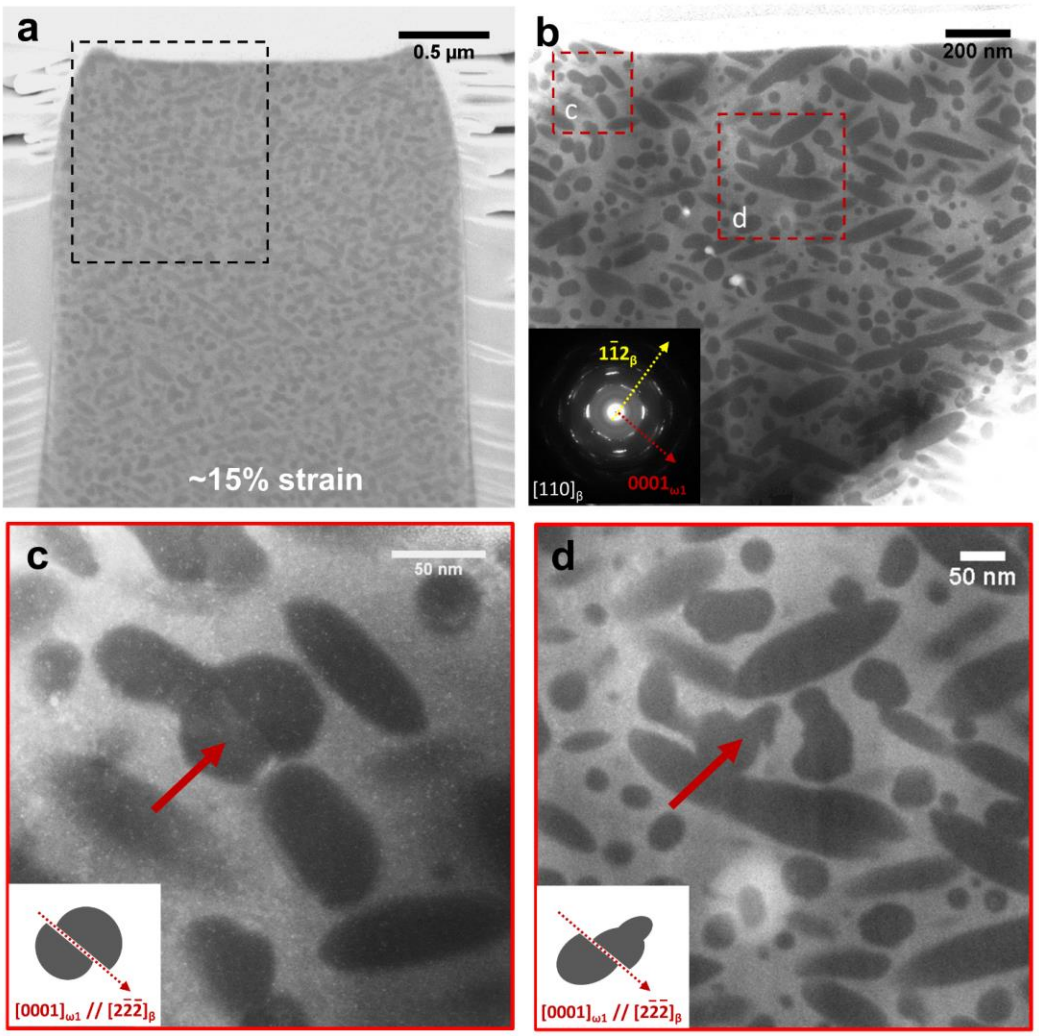

Figure 4.8: (a) SEM-BSE image of cross-section for compressed micropillar with 15% strain for Ti-20Nb aged for 3 d at 450 °C with 4.1 at. % O. (b) HAADF STEM image of black outlined region in compressed pillar shown in (a). Inset shows TEM SAED pattern. (c-d) Higher magnification images of (b) with inset showing schematic diagram of precipitate shearing. Red arrows point to sheared ω precipitates along <222>$_\beta$ direction.

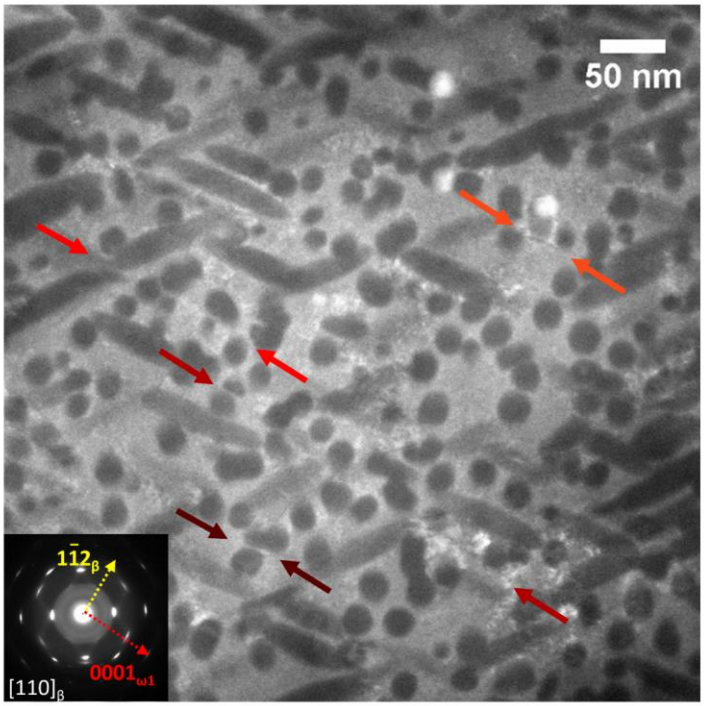

Figure 4.9: HAADF STEM image of liftout sample from compressed micropillar with 15% strain for Ti-20Nb aged for 2 h at 450 °C with 4.1 at. % O. Pairs of arrows colored in shades of red show regions with sheared ω precipitates.

Precipitate shearing, slip localization deformation mechanisms, and fast catastrophic failure in β Ti alloys containing ω precipitates is not unexpected. Similar observations have been reported for several nominally oxygen-free β Ti alloys in bulk testing [8,46,116] and micropillar investigations [52,117,129,130]. The ω phase formed during quenching or very short ageing, where significant elemental partitioning has not yet taken place, generally does not result in loss of ductility [49,50,91]. However, upon isothermal ageing, increased tensile strengths with reduced ductility are typically observed [6]. The loss of ductility has been attributed to the ω structural transition from trigonal to hexagonal and the onset of solute partitioning, both contributing to the hardening of ω precipitates and suppression of twinning [52]. Differences in shear modulus between β and ω may also account for the suppression of transformation induced plasticity and twinning induced plasticity deformation mechanisms [51]. Deformation then occurs by shearing of coherent ω particles resulting in planar slip and formation of localized slip bands [8], primarily for the <111>{112}$_\beta$ slip system [116], leading to negligible work hardening and fast fracture. Upon the onset of localized slip, dislocation channeling may occur, where dislocation activity is confined to precipitate-free channels that are devoid of ω particles due to shearing through the reverse transformation of ω to β phase during deformation [51,116]. The deformation mode may

be controlled by the deformation anisotropy of ω variants, in which the ω1 variant is easily sheared in continuous slip but the other variants show strong lattice resistance to dislocation slip leading to pile-up that triggers ω lattice disordering [52,117]. With these mechanisms, the removal of ω precipitates creates softer channels that concentrate and limit plastic flow in narrow slip bands leading to fracture [8,116,117]. With larger ω sizes, shearing of ω precipitates along a continuous channel similarly lead to slip band formation, localized plastic flow, and fast fracture with negligible ductility as demonstrated in literature bulk testing [8,91].

The investigated microstructures aged at 300 and 450 °C showed a wide range of ω sizes related to ageing conditions and oxygen content that changed the growth kinetics for ω (**Table 4.1**). To understand the relative roles of precipitate size and oxygen in suppressing shear band formation, the average and standard deviation of yield strengths based on four tested micropillars for each condition were plotted against ω's equivalent diameter (**Figure 4.10**). For ω particles with an equivalent diameter smaller than 10 nm, corresponding to Ti-20Nb aged at 300 °C, pillars with and without oxygen showed similar yield strength values, and the large error bars for yield strengths at these ω sizes are attributed to the stochastic nature of the triggering events for fast catastrophic failure. At equivalent diameters between 20-40 nm corresponding to specimens aged at 450 °C for 2 h, micropillars containing oxygen showed a significant increase in yield strength while the strengths for those without oxygen remained constant or decreased. With equivalent diameters increasing above 80 nm for specimens aged at 450 °C for 3 d, the yield strength decreased with larger ω sizes for both oxygen-containing and oxygen-free pillars, and the oxygen-containing micropillars maintained higher yield strengths than those of oxygen-free pillars.

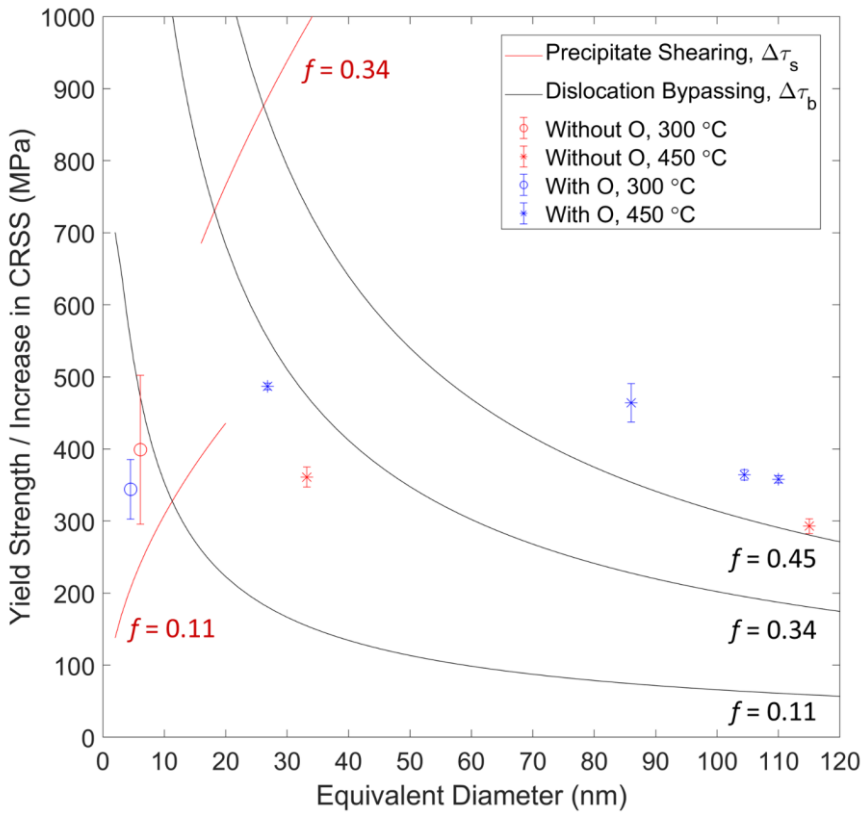

Figure 4.10: Average compressive yield strength dependence on ω equivalent diameter for tested micropillars and calculated stresses for precipitate shearing and dislocation bypassing mechanisms for aged Ti-20Nb with and without interstitial oxygen.

The transition in yield strength dependence with oxygen at ~10 nm equivalent diameters for ω suggests a change in the dislocation interactions. Dislocations are known to shear through coherent ω particles or bypass them through Orowan looping [8]. The increase in the critical resolved shear stress (CRSS) when dislocations shear through ordered misfit-free ω particles was estimated using the following equation derived by Gysler et al. [8,131]:

$$\Delta\tau_s = 1.02\gamma^{3/2}G^{-1/2}b^{-2}r^{1/2}f^{1/2} \quad (3)$$

where γ is the anti-phase boundary energy, G the shear modulus, b the Burgers vector of the β matrix, $2r$ the equivalent diameter for ω, and f the volume fraction of ω particles. The increase in CRSS due to a dislocation bypassing mechanism through Orowan looping was also estimated for the investigated microstructures using the following equation [8,132]:

$$\Delta\tau_b = \frac{1}{1-\nu}\frac{Gb}{2\pi D} ln\frac{\sqrt{2/3}r}{b} \quad (4)$$

where D is the inter-particle spacing. The values of Poisson's ratio ν and G have been estimated for a similar Ti-Nb based gum metal alloy as 0.39 and 25 GPa, respectively, using single crystal

elastic constants measured with in-situ synchrotron x-ray diffraction [53,116]. Additionally, γ for ω particles in Ti-11Mo (at. %) has been estimated to be 0.3 J/m^2 [8]. Assuming the same values for Ti-20Nb and using the microstructural parameters given in **Table 4.1**, $\Delta\tau_s$ and $\Delta\tau_b$ were calculated using the observed volume fractions in the initial ω microstructures (**Figure 4.10**). $\Delta\tau_s$ for f = 0.45 is not shown, but such a high volume fraction would lead to even higher stresses for precipitate shearing. Importantly, the smaller applied stress for these two mechanisms transitions from precipitate shearing to dislocation bypassing at equivalent diameters of ~12 nm for f = 0.11, which is a similar value to the transition size noted for the experimental data (**Figure 4.10**). Furthermore, the stresses for dislocation bypassing estimated using f = 0.34 and f = 0.45 are lower than that of precipitate shearing for equivalent diameters greater than 20 nm. This simple analysis suggests that precipitate shearing is easiest for nanometer-sized ω in Ti-20Nb aged at 300 °C, while dislocation bypassing becomes possible at larger ω sizes obtained after ageing at 450 °C. Previous investigations have reported the presence of dislocation loops indicating the activation of dislocation bypassing and Orowan looping for deformed microstructures with larger ω precipitates after bulk tensile testing [8,46]. We now discuss the effect of oxygen with the different ω precipitate sizes.

The mechanical response of specimens aged at 300 °C with nanoscale ω precipitates was similar with and without oxygen. The similar precipitate distributions and the lack of strong chemical partitioning during low temperature ageing suggest that oxygen did not significantly change the observed microstructures and the active deformation mechanisms, as was previously observed in related Ti-Nb-O gum metal alloys containing nanometer-sized ω precipitates [116]. Dislocation bypassing and Orowan looping of ω particles is unlikely considering the much higher stresses required compared to precipitate shearing. The predominance of shearing with and without oxygen contributed to the formation of precipitate-free channels observed after compression (**Figure 4.4**), resulting in negligible work hardening and fast failure.

For specimens containing ω precipitates with equivalent diameters greater than ~15-30 nm depending on the specific ω volume fraction, dislocation bypassing of ω particles becomes feasible. The activation of dislocation bypassing at larger ω sizes can account for the shape of the stress-strain curves of DA specimens without O aged for 3 d at 450 °C (blue curve in **Figure 4.6a**). Some amount of plastic deformation was observed after initial yielding and prior to load drops that correspond to slip band formation, suggesting that some amount of distributed plasticity via

Orowan bypassing is possible before localization and catastrophic failure (**Appendix II**). Note that shearing and disordering of 3 of the 4 ω variants requires very high stresses [117] and therefore Orowan bypassing becomes a viable way to account for distributed plasticity. Eventually, shearing and disordering of ω particles leading to formation of a continuous deformation channel eventually still occurred (**Figure 4.7b**). This suggests that although the stresses to shear ω are quite high at large ω sizes, dislocations pile-up will eventually reach sufficient levels to shear and disorder ω variants [116,117]. This behavior differed significantly from those of micropillars aged at 300 °C where the high stresses required for Orowan bypassing allowed precipitate shearing to be the only possible deformation mechanism, and steep load drops occurred immediately after yielding (**Figure 4.4**, **Appendix II**).

The presence of oxygen that partitioned to larger ω precipitates during the ageing treatment at 450 °C not only contributed to increasing the alloy's yield strength, but also significantly increased the work hardening capability and prevented shear band formation. Oxygen's partitioning behavior from β to ω during ageing, which was also previously noted in Refs. [9,69] and in **Chapter 3**, mitigates the ductility reduction known to occur with higher oxygen levels for β Ti [5]. Interstitial oxygen in ω may impede dislocation motion along the $<111>\{112\}_{\beta}$ slip system and improve ω's resistance to precipitate shearing and disordering during deformation. The preferred site for interstitial oxygen atoms in the ω lattice is the octahedral site according to previous density functional theory calculations [109]. Consequently, oxygen in the octahedral site is also in the path of dislocation movement and may directly interfere with the ability of dislocations to pass through or disorder ω variants along the $<111>\{112\}_{\beta}$ slip system [116,117]. We note that the presence of oxygen in Ti-Nb-Fe alloys similarly hindered atomic movement and shearing along the same crystallographic system $<111>\{112\}_{\beta}$ during martensitic transformation [133]. The presence of oxygen atoms in ω likely increases the critical resolved shear stress required to shear through and disorder ω variants, improving the resistance to shearing. Consequently, dislocations are less likely to continuously shear ω particles to form precipitate-free channels that result in planar slip during deformation. Dislocation bypassing of ω precipitates accounts for the homogeneous deformation and improved work hardening observed during compression (**Figure 4.6**). Oxygen-stabilized ω precipitates with partitioned O at these sizes may therefore behave similar to non-shearable particles, and the deformation of these microstructures would then be controlled by the inter-particle spacing during micropillar compression testing, as has been

demonstrated in an oxide dispersion strengthened Ni alloy [119]. It is thus the combination of larger ω sizes that enable dislocation bypassing during deformation and oxygen's partitioning to ω that increases its resistance to precipitate shearing and disordering that lead to the suppression of precipitate-free channels and low work hardening behavior observed for DA Ti-20Nb specimens without oxygen.

These results directly address the structural issues of ω precipitation and embrittlement during ageing of metastable β titanium alloys and may inform subsequent chemistry and heat treatment design strategies to improve and expand the use of β Ti alloys. Furthermore, these findings contradict the conventional wisdom that interstitial oxygen causes embrittlement in Ti alloys and must be kept at low levels. With oxygen-containing compositions, ageing treatments designed to promote ω growth and oxygen partitioning mitigate known challenges of embrittlement from isothermal ω precipitates and interstitial oxygen present in the β matrix. A significant outcome of forming oxygen-stabilized ω with sizes that allow for dislocation bypassing is the suppression of plastic flow localization responsible for severe embrittlement and poor ductility of ω-strengthened β Ti alloys without oxygen. This behavior combined with the high yield strengths generally observed for microstructures containing isothermal ω precipitates may enable new opportunities to develop new types of β Ti alloy chemistries and processing that intentionally utilize oxygen as a beneficial alloying element.

4.5 Conclusions

Micropillar compression studies of aged Ti-20Nb specimens with varying oxygen content were investigated to understand the effect of oxygen partitioning to ω on compressive deformation behavior. The following conclusions were drawn:

- Ti-20Nb (at. %) aged at 300 and 450 °C showed extensive ω precipitation irrespective of oxygen content. For the same ageing condition, high oxygen levels slowed the growth kinetics for ω, resulting in higher number densities of smaller ω precipitates in samples with elevated O compared to specimens without O. In oxygen-containing specimens up to 4.1 at. % O, oxygen partitioned to ω precipitates from the β matrix for aged samples at 450 °C, but little oxygen partitioning was observed for those aged at 300 °C.
- Different oxygen levels did not change the deformation behavior and pillar morphologies of Ti-20Nb aged at 300 °C. Compressed pillars showed slip bands on pillar surfaces,

serrated flow in stress-strain curves, and the formation of precipitate-free channels in post-deformation TEM imaging regardless of oxygen content. These results are attributed to precipitate shearing and disordering of the nanometer-sized ω precipitates present after ageing at 300 °C that contributed to the formation of precipitate-free channels, slip localization, and fast fracture of compressed pillars.

- Elevated oxygen content significantly changed the compressed micropillar morphologies and engineering stress-strain curve shapes for Ti-20Nb aged at 450 °C containing larger ω precipitates. Deformed pillars without oxygen showed large slip bands on pillar surfaces and negligible work hardening with load drops in stress-strain curves. In contrast, slip band formation was suppressed for tested pillars with elevated oxygen containing oxygen-stabilized ω precipitates, and stress-strain curves showed improved work hardening with smooth, continuous plastic flow after initial yielding. These differences with oxygen content are attributed to oxygen's partitioning to ω during ageing that improved ω's resistance to precipitate shearing and impeded the formation of continuous deformation channels, which allowed for dislocation bypassing and homogeneous deformation resulting in improved work hardening behavior.
- Microstructures with oxygen-stabilized ω precipitates offer significant benefits and pathways for future development of metastable β Ti alloys by mitigating two known challenges for embrittlement from interstitial oxygen impurities and isothermal ω formation.

Chapter 5: Oxygen-Induced Refinement of α Precipitates in an Aged Metastable β Ti-15-333 Alloy

5.1 Introduction

During ageing of metastable β Ti alloys, significant precipitation strengthening may occur from extensive intragranular α precipitation in the β matrix [6]. Many studies have focused on obtaining increasingly finer α precipitate sizes that yield very high strengths for applications such as aerospace components [6,48]. Specifically, the use of different heating rates, multi-step ageing treatments, ω-assisted α precipitation, and pseudospinodal mechanisms have been investigated to control α volume fraction, size, and number density [33,34,36,37,39,134–137]. With ω-assisted α nucleation mechanisms, previous investigations have focused on the influence of structural and compositional changes associated with ω phase formation to induce finer α precipitation [36,37,39]. It has also been hypothesized that oxygen-rich regions near ω embryos may assist the formation of α precipitates [38]. More generally, any structural and/or compositional heterogeneity can promote heterogeneous α nucleation, leading to higher nucleation rates and consequently increased refinement of α laths [6]. In addition, oxygen in concentrations of ~4 at. % was also shown to accelerate α precipitation yielding finer α precipitates in an aged Ti-20 at. % Nb alloy (**Chapter 3**). In this study, we demonstrate the use of oxygen solid solutions to refine α precipitation during ageing in a commercial metastable β Ti alloy Ti-15-333, which is known to have excellent properties including cold deformability and high strength after ageing [138].

5.2 Experimental methods

Commercial alloy Ti-15-333 (Ti-15V-3Cr-3Sn-3Al, wt. %) with nominally less than 0.1 wt. % O was provided by ATI. Specimens were sectioned using a slow speed diamond saw, encapsulated in quartz tubes with Ar gas, solution treated at 1000 °C for 24 h, and quenched by breaking the tube in water. A subset of solution treated samples were oxidized in a 1 SCCM O_2/ 4 SCCM Ar (20% O_2) environment at 900 °C for 5 hours. The oxygen concentration profile in the β

matrix after oxidation was measured on a polished cross-section using wavelength dispersive spectroscopy (WDS) in a Cameca SX100 electron microprobe as described in **Chapter 3**. Measurements of the O Kα, Ti Kα, V Kα, Cr Kα, Al Kα and Sn Lα X-rays were made using a beam current of 40 nA and accelerating potential of 15 keV. Calibration standards were synthetic MgO (O Kα), Ti metal (Ti Kα), V metal (V Kα), Cr metal (Cr Kα), synthetic NiAl alloy (Al Kα) and Sn metal (Sn Lα); Additional WDS method details are located in **Appendix III**.

As-solution treated samples and oxidized samples were subsequently encapsulated in quartz tubes with Ar gas and aged using the following conditions: 250 °C for 64 h, and 482 °C for 16 h. Specimens were inserted into a preheated furnace such that the sample heating rate was > 5 °C/s. Aged specimens were cross-sectioned using a slow speed diamond saw, mounted in epoxy, ground using SiC papers, and polished using 0.03 μm colloidal silica suspension. Scanning electron microscopy (SEM) imaging and focused ion beam (FIB) preparation of transmission electron microscopy (TEM) foils were performed using a Thermo Fisher Scientific Helios 650 Nanolab with a Ga^+ ion FIB. TEM was performed using a Thermo Fisher Scientific Talos F200X G2 microscope operated at 200 kV.

Due to the compositionally graded nature of specimens created after oxidation, micropillar compression testing was used to assess the mechanical properties as a function of oxygen content. A specific grain close to the $(100)_\beta$ out of plane orientation was selected in each specimen using electron backscattered diffraction (EBSD) (**Appendix III**). Single crystal micropillars with a 2 μm diameter were fabricated in the selected grains with a Thermo Fisher Scientific Helios 650 Nanolab using an automated script with coarse FIB annular milling at 30 kV, 9 nA and fine FIB milling at 30 kV, 0.79 nA. Milled micropillars had a diameter-to-height aspect ratio of approximately 1 to 2.5 to avoid a triaxial stress state for low aspect ratios and pillar buckling at high aspect ratios [122]. Micropillars were tested in compression in a Hysitron TI 950 Triboindenter with a flat punch indenter (60° cone angle, 10 μm diameter flat end) in displacement-controlled mode with a strain rate of ~ 0.0005^{-1}. Tests were manually stopped at a predetermined displacement corresponding to a specific strain level. Compressive engineering stress-strain curves were calculated from collected load versus displacement data [117]. After compression, deformed pillar morphologies were observed using SEM.

5.3 Results and Discussion

Solution-treated and quenched Ti-15-333 was exclusively made of the β phase with grain sizes greater than 500 μm. Previous work reported that as-quenched samples did not contain athermal ω phase [139]. However, electron diffraction from solution-treated and quenched Ti-15-333 (**Figure 5.1**) showed reciprocal lattice streaking and secondary intensity maxima at 1/3 and 2/3 $\{112\}_\beta$ locations corresponding to ω diffraction spots [29]. A dark-field TEM image formed from the secondary intensity maxima (marked by the orange circle in **Figure 5.1**) confirmed the presence of nanoscale athermal ω precipitates. After oxidation at 900 °C, the oxide scale that formed on the sample's surface spalled easily during specimen handling and sectioning, leaving the base metal exposed and unprotected. Precipitation of α laths about 60 μm in length was observed in the subsurface metal below the oxide/metal interface (**Figure 5.2a**). Given oxygen's role as a significant α stabilizer in titanium alloys, the formation of α laths during oxidation is consistent with oxygen dissolution in the β Ti matrix during high temperature oxidation that subsequently stabilizes α and promotes its precipitation [2]. Below the α lath + β matrix region, the single-phase β matrix contained a concentration gradient of oxygen created through oxygen diffusion during the oxidation exposure. This concentration profile was measured in the β matrix using WDS starting from the α lath + β region near the sample's edges and moving towards the center of the cross-sectioned specimens. The measurements (**Figure 5.2b**) illustrated that oxygen diffused to a depth of ~1 mm during oxidation and reached a maximum interstitial oxygen level of ~1.7 at. % in the β matrix near the α + β region. WDS measurements showed no change for V, Cr, Sn, and Al levels in the single-phase β matrix.

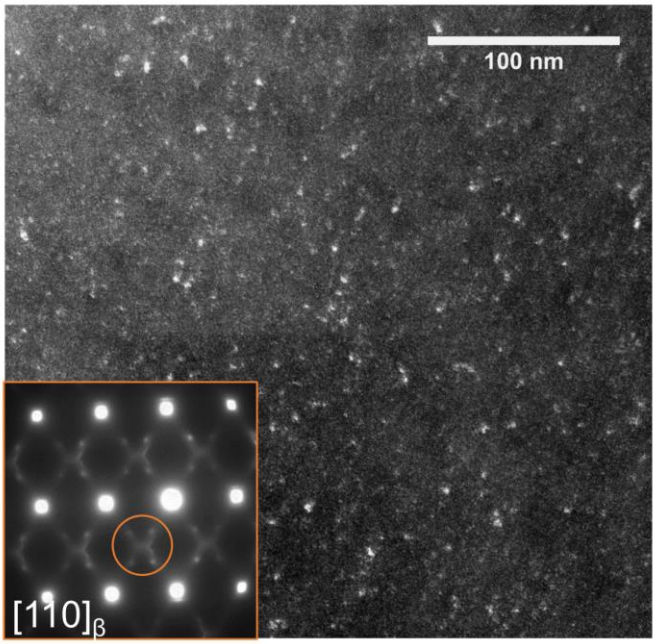

Figure 5.1: Dark-field TEM image and selected area electron diffraction (SAED) pattern of [110]β zone axis showing β and athermal ω diffraction spots for solution-treated and quenched Ti-15-333.

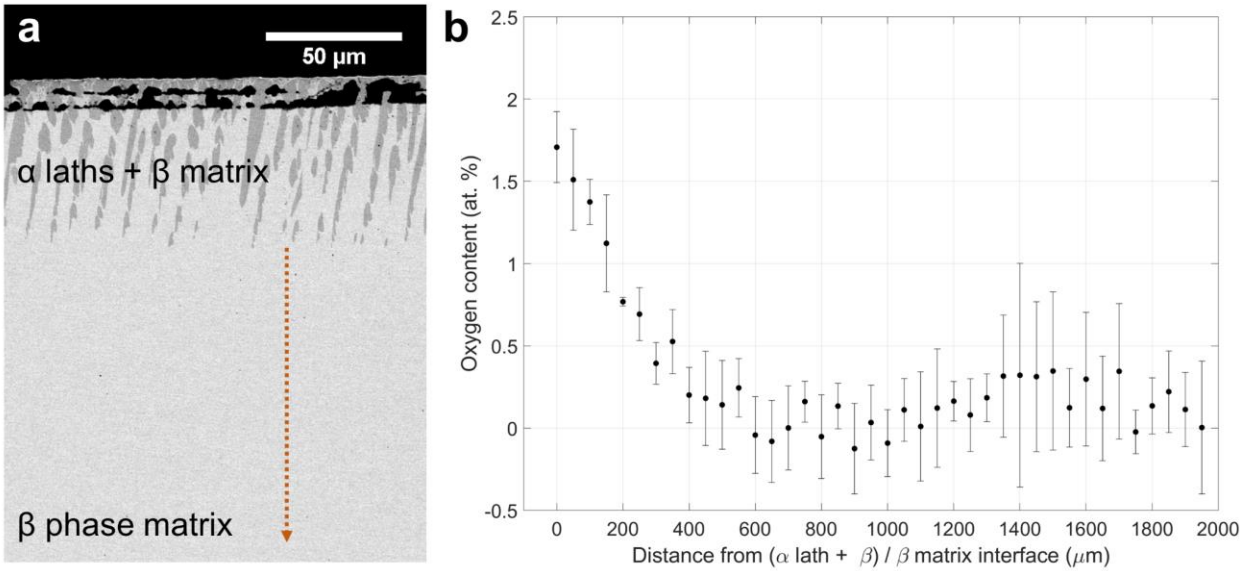

Figure 5.2: (a) Backscattered SEM (SEM-BSE) image of base metal after oxide spallation showing α lath formation after oxidation exposure at 900 °C for 5 h. Orange arrow indicates starting location and direction of WDS line traces. (b) Average and standard deviation of four WDS line traces measuring experimentally-induced oxygen concentration beginning from the (α lath + β) / β matrix interface and traversing across the cross-section of oxidized Ti-15-333.

As-solution treated specimens and oxidized specimens were subsequently aged directly at 482 °C for 16 h to promote α precipitation according to a commercial heat treatment [140]. Specimens that were solution treated and aged are hereafter referred to as *directly aged (DA)*, and

specimens that were solution treated, oxidized, and then aged are hereafter referred to as *oxidized and aged (OXA).* The heat treatment (482 °C for 16 h) resides in the region where α precipitates are known to form directly from the β matrix [138,141]. 482 °C is also above the ω solvus according to Thermo-Calc calculations of metastable phase fractions (**Appendix III**). Fast heating to 482 °C also avoided β phase separation and isothermal ω evolution that are known to promote heterogeneous α nucleation [33,141,142]. Consequently, the athermal ω phase observed in solution treated specimens and oxidized specimens was expected to dissolve quickly upon rapid heating and ageing at 482 °C. Extensive intragranular α precipitation in the β matrix was observed regardless of oxygen content (**Figure 5.3**). In DA samples without oxygen, α precipitates ranged from ~2-10 μm in size. However, α precipitates became more refined with increasing oxygen content in the OXA Ti-15-333 sample. In regions containing little oxygen (0.1 at. %) near the center of this sample, α precipitates showed similar sizes as DA specimens aged with the same treatment. In regions with the highest oxygen content such as just below the α lath / β matrix interface, corresponding to 1.7 at. % O, α laths were significantly smaller with submicron sizes. In the absence of β phase separation and ω precipitates that act as preferential nucleation sites, the observed α refinement is linked to the interstitial oxygen levels present in OXA Ti-15-333 rather than heterogeneous nucleation mechanisms. Interstitial oxygen in solid solution is known to significantly stabilize the α phase in Ti alloys [2]. This stabilization with elevated oxygen increases the nucleation driving force for α precipitation, leading to faster precipitation kinetics with a more refined lath size. Similar correlation was reported during isothermal oxidation of a β Ti Beta21S alloy with finer α laths forming in the β matrix near the surface where the oxygen content is the highest [143]. Changes in nucleation driving force have also been attributed to refined α precipitation in pseudospinodal transformation pathways [135,136], which are related to local composition fluctuations rather than intentional chemistry changes with oxygen. As a potent α-stabilizing element, oxygen is known to partition to the α phase during ageing of β Ti alloys [9], so very little oxygen is expected in the β matrix after α formation during ageing.

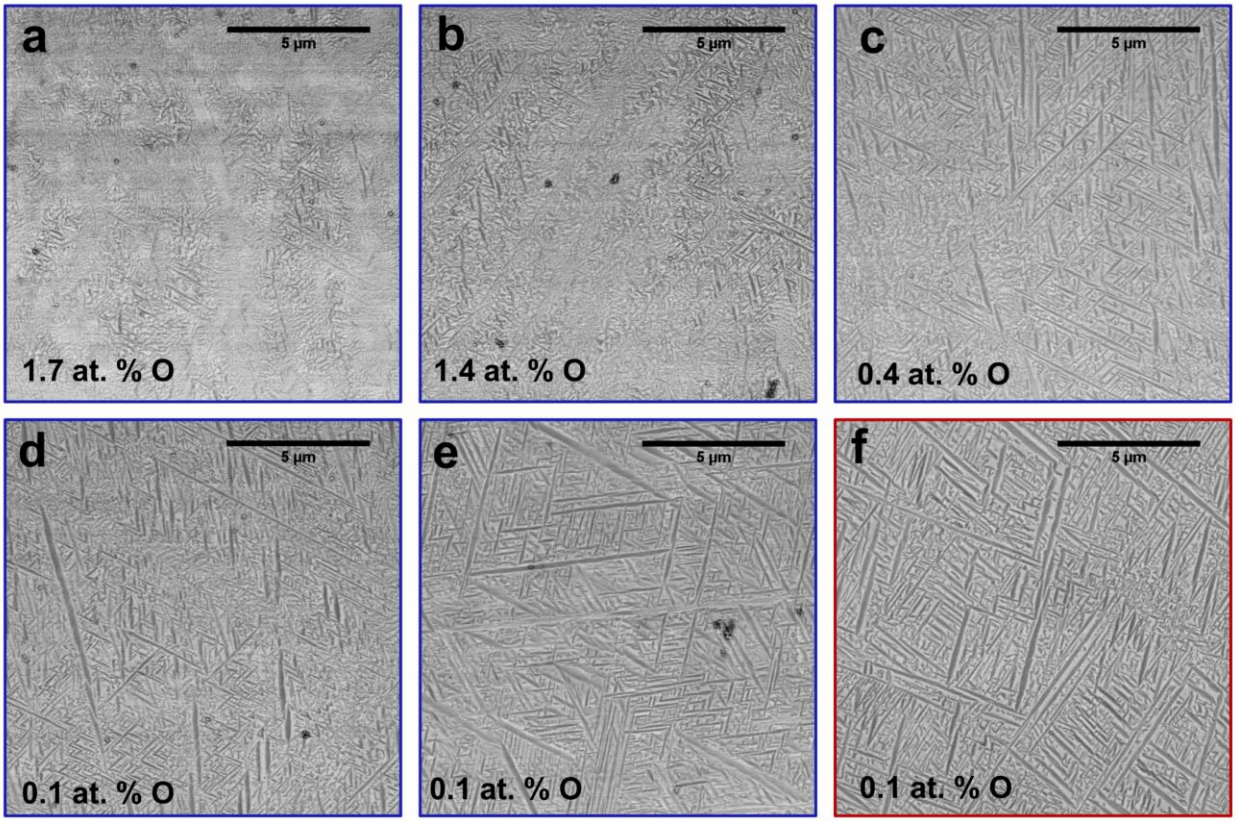

Figure 5.3: SEM-BSE images of OXA Ti-15-333 aged for 16 h at 482 °C located (a) at the α lath/β matrix interface, (b) 100 µm, (c) 300 µm, (d) 500 µm from this interface, and (e) in the center of the sample. Oxygen concentrations for (a-e) correspond to 1.7, 1.4, 0.4, 0.1, and 0.1 at. % O, respectively, from WDS measurements. (f) SEM-BSE image of DA Ti-15-333 with 0.1 at. % O aged for 16 h at 482 °C.

After ageing directly at 482 °C, DA and OXA Ti-15-333 were tested using micropillar compression to determine local mechanical behavior (**Figure 5.4a-b**). For OXA specimens, micropillars were produced at a distance of 100 µm away from the α lath / β matrix interface corresponding to 1.4 at. % O. After compression to 15% strain, deformed pillars for DA and OXA Ti-15-333 (**Figure 5.4c-d**) both showed slip traces located near α-β interfaces. Previously reported micropillar compression results for dual phase α-β Ti alloys also showed that α-β microstructures typically slip along the interface between these phases if oriented favorably relative to the deformation direction [130,144,145]. However, significant morphology differences were observed for compressed pillars depending on initial microstructure and oxygen content. DA micropillars formed macroscopic slip bands spanning the entire pillar diameter due to the larger α lath sizes present without oxygen (**Figure 5.4c**). In contrast, the refined α precipitates in compressed pillars for OXA Ti-15-333 with 1.4 at. % O resulted in numerous shorter slip traces that formed in

multiple locations along the pillar's length leading to slight bulging (**Figure 5.4d**), indicating more distributed deformation compared to DA pillars.

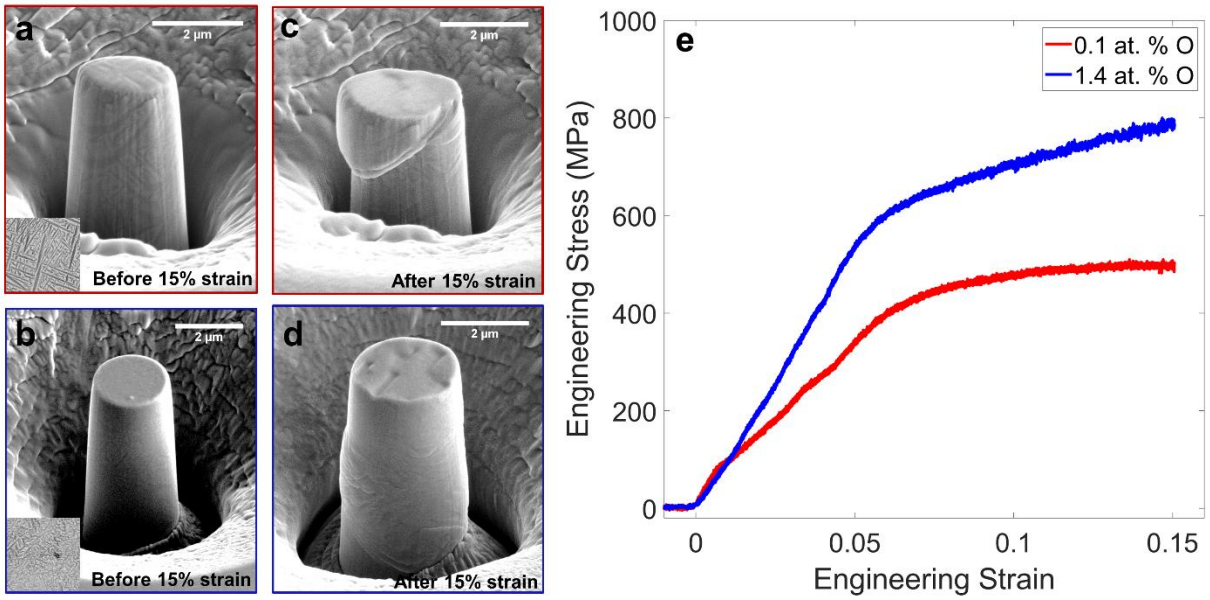

Figure 5.4: SEM-BSE images of 2 µm diameter micropillars compressed to 15% engineering strain for (a, c) DA Ti-15-333 with 0.1 at. % O and (b, d) OXA Ti-15-333 with 1.4 at. % O aged for 16 h at 482 °C before (a-b) and after (c-d) compression. Insets for (a-b) show SEM-BSE images of initial microstructure for each pillar. (e) Engineering stress-strain curves for compressed micropillars on DA Ti-15-333 with 0.1 at. % O and OXA Ti-15-333 with 1.4 at. % O aged for 16 h at 482 °C.

Compressive engineering stress-strain curves revealed that the refined α sizes obtained with higher oxygen content increased the compressive yield strength, from an average value of ~390 MPa for pillars without oxygen to 580 MPa in the presence of 1.4 at. % O. **Figure 5.4e** shows curves closest to the average yield strength out of four tested micropillars for each condition. Scatter in the stiffness and yield point values was observed in the stress-strain curves at both oxygen levels, which was attributed to intrinsic size effects stemming from the tested micropillar sizes and volumes. Indeed, intrinsic size effects can dominate when specimen dimensions are on the order of microstructural features and the specimen's volume contains a lower number density of dispersed obstacles, leading to an observed size effect on measured yield strengths [121]. Nonetheless, the increased α refinement results in more α-β interfaces that act as dislocation barriers resulting in increased strength [2,34,48]. This trend in yield strength values is consistent with prior mechanical testing of β Ti alloys where higher densities and increased refinement of α precipitates resulted in increased bulk tensile strength [6,33,34] and micropillar compression strength [130,145]. Consistently, indentation studies of oxygen-enriched sublayers formed during

oxidation of other commercial metastable β Ti alloys correlated to hardness increases with refined α precipitation [143,146].

Finally, double ageing was conducted to understand the combined effects of ω-assisted α nucleation and oxygen-induced α refinement. Ageing of DA Ti-15-333 at 250 °C for 64 hours promoted chemical partitioning and growth of isothermal ω precipitates around ~5-10 nm in size (**Figure 5.5a-b**). With oxygen's reported stabilization of the ω phase (**Chapter 3**), isothermal ω was also expected to be present in OXA Ti-15-333 aged at 250 °C for 64 h. Following the low temperature treatment, DA and OXA specimens were aged at 482 °C for 16 h. Irrespective of oxygen content, fine α precipitates were observed after the final 482 °C ageing step (**Figure 5.5c-d**). The α laths were approximately 300 nm in size for the DA specimens, while those in the OXA specimens with 1.4 at. % O were even smaller at ~50 nm. The observed refined α sizes in the DA and OXA samples are attributed to ω-assisted α nucleation, in which the structural and compositional non-uniformities stemming from isothermal ω formation act as preferred sites for heterogeneous intragranular α nucleation [33,36,37,39]. Notably, oxygen-containing Ti-15-333 showed further α refinement compared to oxygen-free specimens even though ω-assisted nucleation was active in both conditions, which suggests that oxygen-induced refinement can be used in tandem with other α refinement methods.

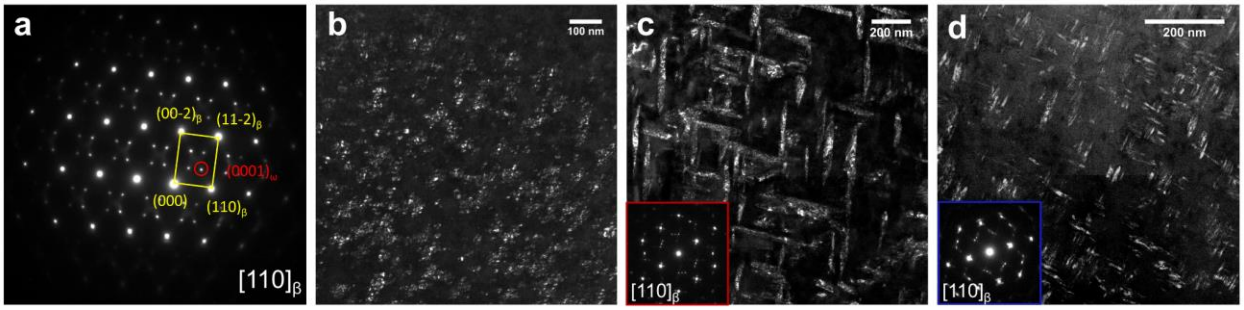

Figure 5.5: (a) TEM SAED pattern for the $[110]_\beta$ zone axis showing β and ω diffraction spots for DA Ti-15-333 with 0.1 at. % O aged for 64 h at 250 °C. (b) Dark-field TEM image formed using selected ω diffraction spot shown in red circle of (a). Dark-field TEM images of Ti-15-333 aged for 64 h at 250 °C, then for 16 h at 482 °C: (c) DA specimen with 0.1 at. % O. (d) OXA specimen with 1.4 at. % O. Insets show SAED patterns for the $[110]_\beta$ zone axis showing β and α diffraction spots.

While bulk tensile testing would be necessary to confirm scaling and applicability of the present results, this study illustrates the ability of interstitial oxygen in metastable β Ti alloys to create fine α lath microstructures with increased compressive yield strength. Since oxygen's partitioning behavior to α precipitates during ageing [9] mitigates the detrimental embrittling effects of interstitial oxygen in the β phase matrix [5], intentional additions of oxygen to metastable β Ti alloys may act as another avenue for obtaining α phase refinement during ageing and improved

precipitation strengthening. Furthermore, this oxygen-induced refinement mechanism may be used in combination with existing α refinement strategies during ageing such as ω-assisted nucleation to obtain significantly reduced α sizes, as demonstrated with multi-step ageing treatments (**Figure 5.5d**). These findings contradict the conventional wisdom that oxygen in Ti alloys is associated with embrittlement and that its level needs to be kept very low. The beneficial effects of oxygen in metastable β Ti alloys demonstrated here may have significant applications that include increased oxygen tolerance and impurities during Ti alloy manufacturing, increased recyclability of Ti alloys, and pathways for future alloy and processing design to utilize oxygen as an alloying element in β Ti alloys.

5.4 Conclusions

Elevated oxygen levels obtained through an oxidation exposure increased the nucleation driving force for α precipitation during ageing, leading to microstructures with refined α precipitates obtained with and without activation of ω-assisted α nucleation. These refined microstructures showed increased compressive strength during micropillar compression compared to those without oxygen due to a higher number of α-β interfaces that act as dislocation barriers. Therefore, ageing of β Ti alloys with high oxygen not only induces α refinement for increased strength, but also addresses the challenge of oxygen embrittlement in β Ti alloys.

Chapter 6: Role of Oxygen on the Precipitation and Deformation Behavior of an Aged β Ti-15Mo Alloy

6.1 Introduction

The results presented for Ti-Nb in **Chapter 3** showed that elevated O levels stabilized the ω phase and oxygen partitioned to ω precipitates during ageing. Furthermore, **Chapter 4** demonstrated that O partitioning to large ω precipitates suppressed slip localization resulting in improved ductility and work hardening during micropillar compression of Ti-Nb alloys. High oxygen levels also affected α precipitation leading to oxygen-induced refinement and increased compressive strengths as shown in aged Ti-15-333 (**Chapter 5**). In the Ti-Mo system, limited reports showed that oxygen also affects precipitation kinetics and metastable phase stability. Oxygen reportedly suppresses athermal ω formation in Ti-Mo [72]. With higher oxygen levels, martensite formation in Ti-Mo still occurred, but the formation of α phase was also shown due to the stabilization of α with oxygen [71]. However, detailed investigations of oxygen's influence on microstructural evolution and connection to mechanical properties have not been conducted. Understanding the effects of interstitial oxygen in Ti-Mo based alloys is an important area of investigation due to the frequent use of Mo in commercial β Ti alloy compositions and the low allowable oxygen levels in industrial alloy specifications due to embrittlement concerns. Mo is a highly effective β stabilizing element [48], which enables a metastable β phase matrix with lower solute levels leading to lower overall alloy density that is important for weight-sensitive aerospace components. Detailed study of oxygen's effect on deformation for aged Ti-Mo alloys would enable specific understanding to mitigate the conventionally accepted detrimental effects of interstitial oxygen in commercially relevant alloys. Understanding the influence of oxygen on phase transformations in Ti-Mo would also demonstrate that the previously discussed oxygen effects in **Chapter 3** and **Chapter 4** are more generally applicable to ω forming β Ti alloys rather than just the Ti-Nb system.

Similar to the approach used for Ti-Nb alloys, aged Ti-15Mo with varying oxygen content was evaluated to understand differences in ω and α precipitation kinetics and their impacts on mechanical behavior. Heat treatments were selected to promote ω nucleation and growth with oxygen partitioning to ω while preventing α phase formation. Higher temperature ageing to induce α formation was also conducted to understand oxygen's influence on α's size and precipitation rate. Micropillar compression testing of ω-containing microstructures with varying oxygen contents showed that ω with partitioned oxygen resulted in higher compressive yield strength and finer slip lines indicating less plastic flow localization than those without oxygen. Furthermore, the refinement of α precipitates with high oxygen after higher temperature ageing resulted in increased average compressive yield strengths compared to minimal oxygen specimens. These results provide evidence of oxygen's beneficial effects on phase formation and the ensuing mechanical property changes that may enable future alloy design and processing methods specifically utilizing oxygen as an alloying element in β Ti alloys.

6.2 Experimental methods

Commercial alloy Ti-15Mo wt. % (Ti-8Mo at. %) with nominally less than 0.1 wt. % O was provided by ATI. Specimens were sectioned using a slow speed diamond saw, encapsulated in quartz tubes with Ar gas, solution treated at 1000 °C for 24 h, and quenched by breaking the tube in water. A subset of solution treated samples was oxidized in a 1 standard cubic centimeter per minute (SCCM) O_2/4 SCCM Ar (20% O_2) environment at 900 °C for 5 hours. Oxygen concentration profiles in the β matrix after oxidation were measured on polished cross-sections using wavelength dispersive spectroscopy (WDS) in a Cameca SX100 electron microprobe as reported in **Chapter 3** and **Chapter 5**. Measurements of the O Kα, Ti Kα and Mo Lα X-rays were made using a focused electron beam with a beam current of 40 nA and accelerating potential of 15 keV. Calibration standards were synthetic MgO (O Kα), Ti metal (Ti Kα) and Mo metal (Mo Lα); Additional WDS method details are located in **Appendix III**.

As-solution treated samples and oxidized samples were subsequently encapsulated in quartz tubes with Ar gas and isothermally aged using the following conditions: 450 °C for 2 and 24 h, 500 °C for 24 h, and 600 °C for 4 h. Specimens were inserted into a preheated furnace such that the sample heating rate was > 5 °C/s. Complete dissolution of ω has been observed at 560 °C in Ti-15Mo [147]. Therefore, ageing treatments for ω formation were conducted at 450 and 500

°C to promote fast ω precipitation and elemental partitioning while maintaining slower α precipitation kinetics. Ageing at 600 °C was also performed to induce direct α precipitation. Finally, a two step ageing treatment was conducted with the first step at 450 °C for 2 h, followed by a second step at 600 °C for 4 h to investigate the effect of ω-assisted α precipitation with elevated oxygen content. Aged specimens were cross-sectioned using a slow speed diamond saw, mounted in epoxy, then ground using 320-1200 grit SiC papers and polished using 0.03 μm colloidal silica suspension. Scanning electron microscopy (SEM) imaging and focused ion beam (FIB) preparation of transmission electron microscopy (TEM) foils and needle-shaped atom probe tomography (APT) specimens were performed using a Thermo Fisher Scientific FEI Helios 650 Nanolab with a Ga^+ ion FIB. TEM images and selected area electron diffraction (SAED) patterns were obtained using a Thermo Fisher Scientific Talos F200X G2 microscope operated at 200 kV. APT data collection was performed with a Cameca local electrode atom probe (LEAP) 5000 XR operated in laser mode. APT data was collected using a specimen temperature of 30 K, a detection rate of 0.005 atoms per pulse, laser pulse energy of 25 pJ, and pulse repetition rate of 200 kHz. Data reconstruction, background subtraction, peak deconvolution, and compositional analysis were performed using the AP Suite software package 6.1.

Due to the compositionally graded nature of specimens created after the oxidation exposure, micropillar compression testing was used to evaluate the compressive mechanical properties of local microstructural regions with varying oxygen content (corresponding to oxygen concentration profiles measured using WDS). A specific grain for pillar fabrication was selected in each specimen to be close to the $(100)_\beta$ out of plane orientation after characterization using electron backscattered diffraction (EBSD) (**Appendix III**). Single crystal micropillars with a 2 μm diameter were fabricated in the selected grain using FIB in a Thermo Fisher Scientific FEI Helios 650 Nanolab. Pillars were fabricated with an automated script with coarse annular milling at 30 kV, 9 nA and fine milling at 30 kV, 0.79 nA. Milled micropillars had a diameter-to-height aspect ratio of approximately 1 to 2.5 to avoid a triaxial stress state for low aspect ratios and pillar buckling at high aspect ratios [122]. Micropillars were tested in compression in a Hysitron TI 950 Triboindenter with a flat punch indenter (60° cone angle, 10 μm diameter flat end) in displacement-controlled mode with a strain rate of ~ 0.0005^{-1}. Tests were manually stopped at a predetermined displacement amount to characterize compressed pillars at specific strain levels. Compressive engineering stress-strain curves were calculated from collected load versus displacement data. The

engineering stress was calculated as $\sigma = F/A_0$ where F is the measured force and A_0 is the cross-sectional area at the top of the pillar, and the engineering strain was calculated as $\varepsilon = \Delta L/L_0$ where ΔL is the pillar displacement and L_0 is the initial pillar height [117]. After compression, the morphology of deformed pillars was observed using SEM and TEM. Cross-sections and TEM foils of deformed micropillars were prepared using a cross-sectional FIB liftout technique similar to Refs. [124,125].

6.3 Results

6.3.1 Solution treated and oxidized Ti-15Mo prior to ageing

Solution treated and quenched Ti-15Mo contained a single β phase matrix with grain sizes greater than 500 μm. Following the oxidation exposure at 900 °C for 5 h, a thick, porous oxide scale without strong adherence to the base metal formed on specimen surfaces, and oxide spallation was frequently observed during specimen handling and sectioning. Specific oxide growth mechanisms and oxide morphologies are not the focus of this work. Precipitation of α laths about 50 μm in length was observed in the subsurface metal just below the oxide/metal interface of cross-sectioned specimens (**Figure 6.1a**). Given oxygen's role as a potent α stabilizing element in Ti alloys, the formation of α laths in the outermost subsurface metal region during oxidation is consistent with oxygen dissolution in the β Ti matrix that stabilizes α and promotes its precipitation [2]. Below the α lath + β matrix region, the single-phase β matrix contained interstitial oxygen that diffused in a concentration gradient during the oxidation exposure. This oxygen concentration profile was measured in the single-phase β matrix using WDS starting from the interface of the α lath + β matrix region near the sample's edges and moving towards the center of the cross-sectioned specimens (yellow arrow in **Figure 6.1a**). The average of four measured profiles (**Figure 6.1b**) illustrated that oxygen diffused to a depth of ~1 mm in the β matrix during oxidation, which is a similar diffusion depth reported for Ti-20Nb (at. %) with the same oxidation exposure (**Chapter 3**). This depth agrees with mean diffusion lengths estimated using reported oxygen diffusion parameters in β Ti [95]. The maximum oxygen concentration of approximately 2.6 at. % O was located at the interface between the α lath / β matrix regions. WDS measurements did not show changes for Mo concentration as a function of distance in the single-phase β matrix.

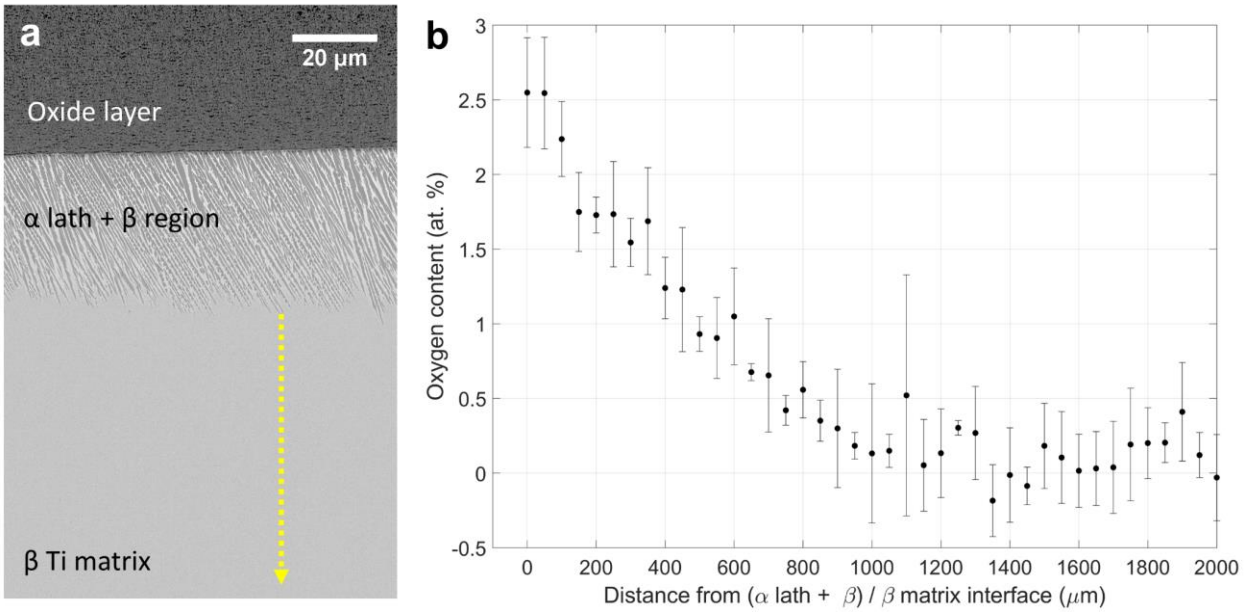

Figure 6.1: (a) SEM-BSE image of cross-section for oxidized Ti-15Mo showing porous oxide scale and α lath formation after oxidation exposure at 900 °C for 5 h. Yellow arrow indicates starting location and direction of WDS line traces. (b) Average and standard deviation of four WDS line traces measuring oxygen concentration beginning from the (α lath + β) / β matrix interface and traversing across the cross-section of oxidized Ti-15Mo.

6.3.2 ω precipitation and deformation in Ti-15Mo with varying oxygen content

As-solution treated specimens and oxidized specimens were subsequently aged to understand ω precipitation with varying oxygen levels. Specimens that were solution treated and aged with minimal oxygen content are hereafter referred to as *directly aged (DA)*, and specimens that were solution treated, oxidized, and then aged with the created oxygen diffusion gradient are hereafter referred to as *oxidized and aged (OXA).* The microstructure characterized at specific distances from the α lath / β matrix interface towards the center of the sample in OXA specimens corresponded to specific oxygen contents as measured by WDS (**Figure 6.1b**). DA and OXA specimens aged at 450 °C for 2 h resulted in dense ~10 nm metastable ω precipitates observed in backscattered SEM (SEM-BSE) images (**Figure 6.2a-b**). As expected from prior studies [148], elemental partitioning of Mo to the β matrix occurred as demonstrated by compositional contrast in SEM-BSE images. After 24 h of ageing at 450 °C, ω precipitates grew to ~20-30 nm in size. The ω particles in oxygen-free DA specimens exhibited ellipsoidal shapes, which is consistent with prior ω studies for the low misfit Ti-Mo system [148]. SEM-BSE images showed higher number densities of finer ω precipitates in the presence of oxygen compared to specimens without oxygen (**Figure 6.2c-d**). OXA Ti-15Mo with 2.2 at. % O also revealed alignment of ω precipitates

(**Figure 6.2d**). After ageing at 500 °C for 24 h, DA and OXA microstructures showed larger sizes and decreased number densities for ω precipitates (**Figure 6.3a-b**), and the morphology differences with oxygen were more pronounced than at 450 °C. Specific grains close to the $(100)_\beta$ out of plane orientation after EBSD characterization were selected to characterize ω precipitate alignment with elevated oxygen levels. SEM-BSE and bright-field TEM images confirmed that ω particles with higher oxygen were aligned along $<001>_\beta$ directions compared to more random arrangement of ω in DA specimens (**Figure 6.3a-c**). In addition, ω precipitates with oxygen formed cuboidal-like shapes faceted along the $<001>_\beta$ directions (**Figure 6.3c**) and also showed an elongated major axis aligned with $<111>_\beta$ directions that is typical for ω in Ti-Mo without O [19]. Finally, some regions with the highest oxygen levels of 2.2 at. % O in OXA Ti-15Mo after ageing at 500 °C showed the onset of lath-like α phase formation in addition to ω precipitates (**Figure 6.3d**). α precipitation was not observed for other oxygen levels in DA and OXA Ti-15Mo aged at 500 °C for 24 h.

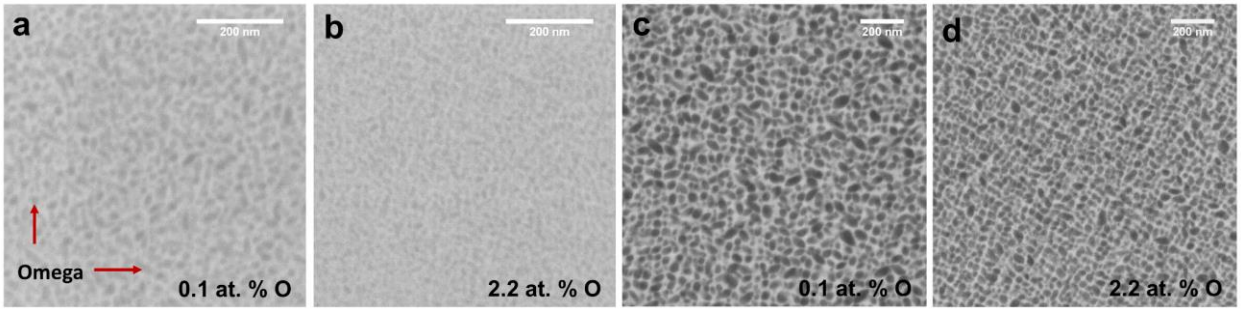

Figure 6.2: SEM-BSE images of DA and OXA Ti-15Mo after ageing at 450 ° C for (a-b) 2 h and (c-d) 24 h. DA Ti-15Mo are shown in (a) and (c). OXA Ti-15Mo are shown in (b) and (d).

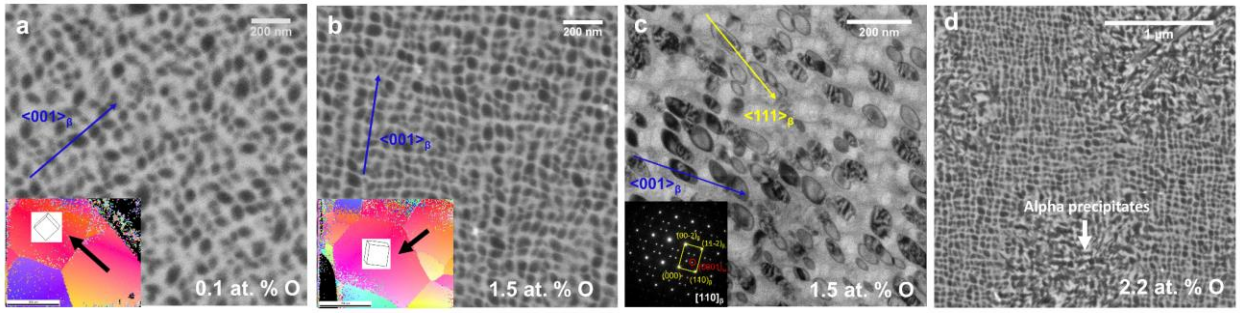

Figure 6.3: SEM-BSE images of (a) DA Ti-15Mo with 0.1 at. % O and (b) OXA Ti-15Mo with 1.5 at. % O aged for 24 h at 500 °C. Insets show EBSD IPF maps with crystal grain orientations and the selected grain denoted by the black arrow with associated cubic lattice projection for microstructures in (a) and (b). (c) Bright-field TEM image of OXA Ti-15Mo aged for 24 h at 500 °C with 1.5 at. % O. Inset shows SAED pattern for the $[110]_\beta$ zone axis showing β and ω diffraction spots. (d) SEM-BSE image of OXA Ti-15Mo with 2.2 at. % O aged for 24 h at 500 °C.

ω's size, aspect ratio, area density, and volume fraction for DA and OXA Ti-15Mo aged for 24 h at 450 and 500 °C were estimated using SEM-BSE images that showed all ω variants to

compare differences in the aged microstructures (**Table 6.1**). The average lengths of the major and minor axes for ω were used to calculate an equivalent spherical diameter, *2r*, which decreased with higher oxygen after both 450 °C and 500 °C ageing. The measured aspect ratio of ω particles based on the major and minor axes increased slightly without oxygen present. The area densities of ω particles, n_s, were estimated by counting ω particles in SEM-BSE images and dividing the total particle count by the area of the image. The area fraction of ω was estimated using image thresholding and measurement of SEM-BSE images using ImageJ processing software to be approximately 41% for both DA and OXA specimens aged at 450 °C and 500 °C. These area fractions were assumed to equal the volume fraction, *f*, of ω based on stereology [126]. The inter-particle spacing *D* for ω particles was calculated by taking into account the effect of finite obstacle size for impenetrable particles and represents the measure of the free spacing between finite obstacles [127]. The average planar radius $\langle r_s \rangle$ was calculated using $< r_s > = \pi < r > /4$, which was used to calculate *D* according to the following equation [127]:

$$D = [(32/3\pi f)^{1/2} - 2] < r_s > (1).$$

Table 6.1: Quantification of microstructural features for ω precipitates in aged Ti-15Mo with varying oxygen content.

Specimen	Ageing Treatment	Oxygen Concentration (at. %)	Equivalent Diameter, *2r* (nm)	Aspect Ratio	Area Density, n_s (um^{-2})	Volume Fraction, *f*	Inter-particle spacing, *D* (nm)
DA	24 h, 450 °C	0.1	46	2.4	271	0.41	16
OXA	24 h, 450 °C	2.2	32	2.0	501	0.41	11
OXA	24 h, 500 °C	0.1	75	2.3	181	0.41	26
OXA	24 h, 500 °C	1.5	55	1.9	216	0.41	19

In order to understand the extent of elemental partitioning to ω and β, APT measurements were performed after ageing at 450 and 500 °C. Reconstructed APT datasets of OXA Ti-15Mo aged for 24 h at 450 °C with 2.2 at. % O (**Figure 6.4**) and aged for 24 h at 500 °C with 1.5 at. % O (**Figure 6.5**) showed Ti-rich regions and Mo-rich regions corresponding to the ω and β phases, respectively. Proximity histograms (or proxigrams) that were generated using iso-concentrations surfaces of 90 at. % Ti for OXA specimens aged at 450 °C and 500 °C showed that Ti partitioned to the ω phase while Mo partitioned to the β matrix, as has been reported in literature [29,148]. However, the partitioning behavior of O changed for aged samples at 450 and 500 °C. For OXA Ti-15Mo aged at 450 °C, O did not strongly partition to either the ω or β phase, with similar

concentrations of ~3-4 at. % in both phases and across the ω/β interface (**Figure 6.4c**). In contrast, O noticeably partitioned to ω in OXA Ti-15Mo aged at 500 °C, and the ω phase with ~3 at. % O contained twice as much oxygen content as in the β matrix with 1.4 at. % O (**Figure 6.5c**). Similarly, this O partitioning behavior to ω during ageing has also been reported in the Ti-Nb-O system [9] and in **Chapter 3**. According to calculated proxigrams, the compositions for ω and β in OXA Ti-15Mo aged for 24 h at 500 °C with 1.5 at. % O are: 96 at. % Ti, 0.6 at. % Mo, 3.1 at. % O for ω and 84 at. % Ti, 13 at. % Mo, 1.4 at. % O for β. The oxygen diffusion coefficient in Ti-15Mo was estimated by fitting WDS data (**Figure 6.1b**) to the model of transient diffusion through a semi-infinite flat specimen [149], which gives a diffusion coefficient at 900 °C of approximately $8.3*10^{-12}$ m^2/s. This value agrees with the estimated diffusion coefficient at 900 °C of $7.5*10^{-12}$ m^2/s obtained from similar fitting of a previously reported oxygen concentration profile for Ti-20Nb (at. %) (**Chapter 3**) and with literature values for oxygen diffusion coefficients in β Ti at 900 °C [95]. Therefore, the difference in oxygen partitioning behavior to ω for Ti-15Mo aged at 450 and 500 °C observed in APT data is unknown and requires further investigation.

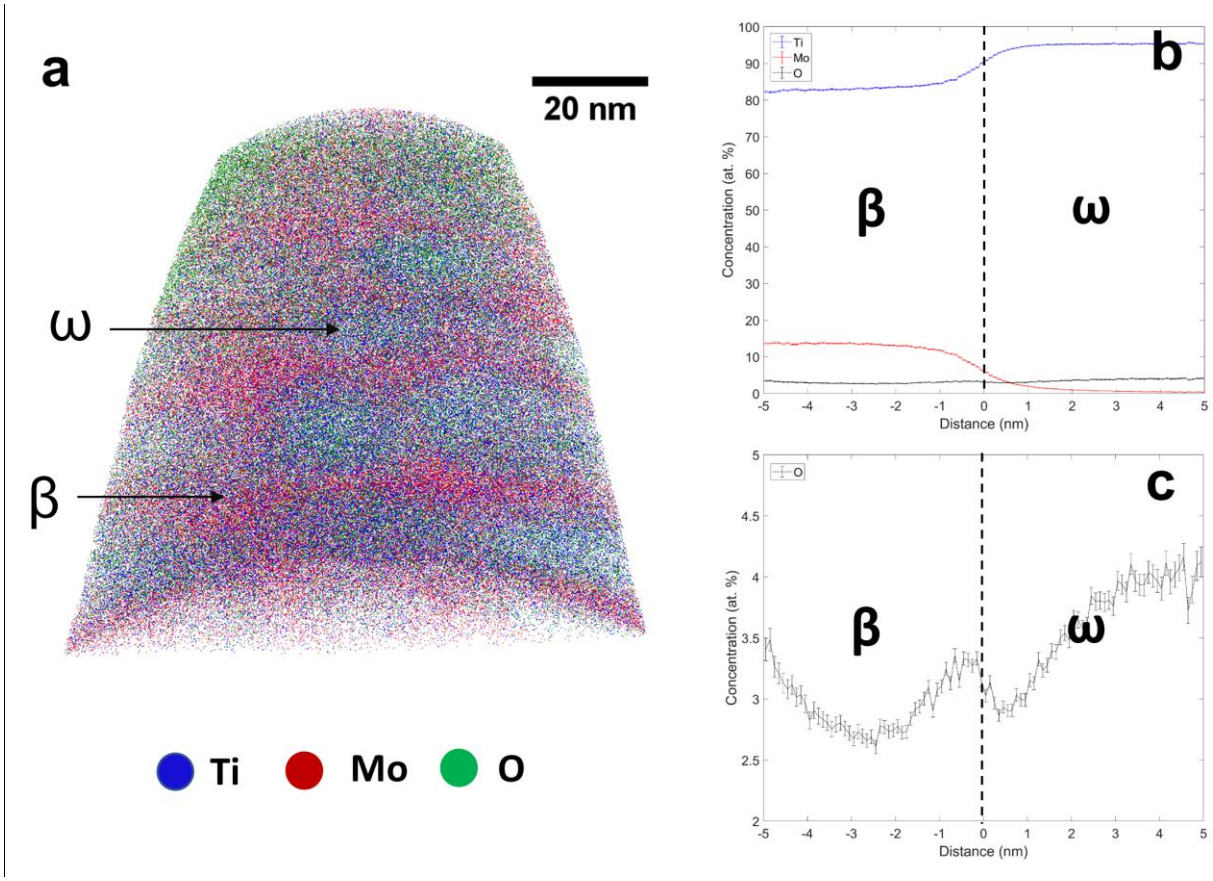

Figure 6.4: (a) APT reconstruction of OXA Ti-15Mo aged for 24 h at 450 °C with 2.2 at. % O and (b-c) proxigram showing Ti, Mo, and O concentration as a function of distance from 90 at. % Ti iso-concentration surfaces.

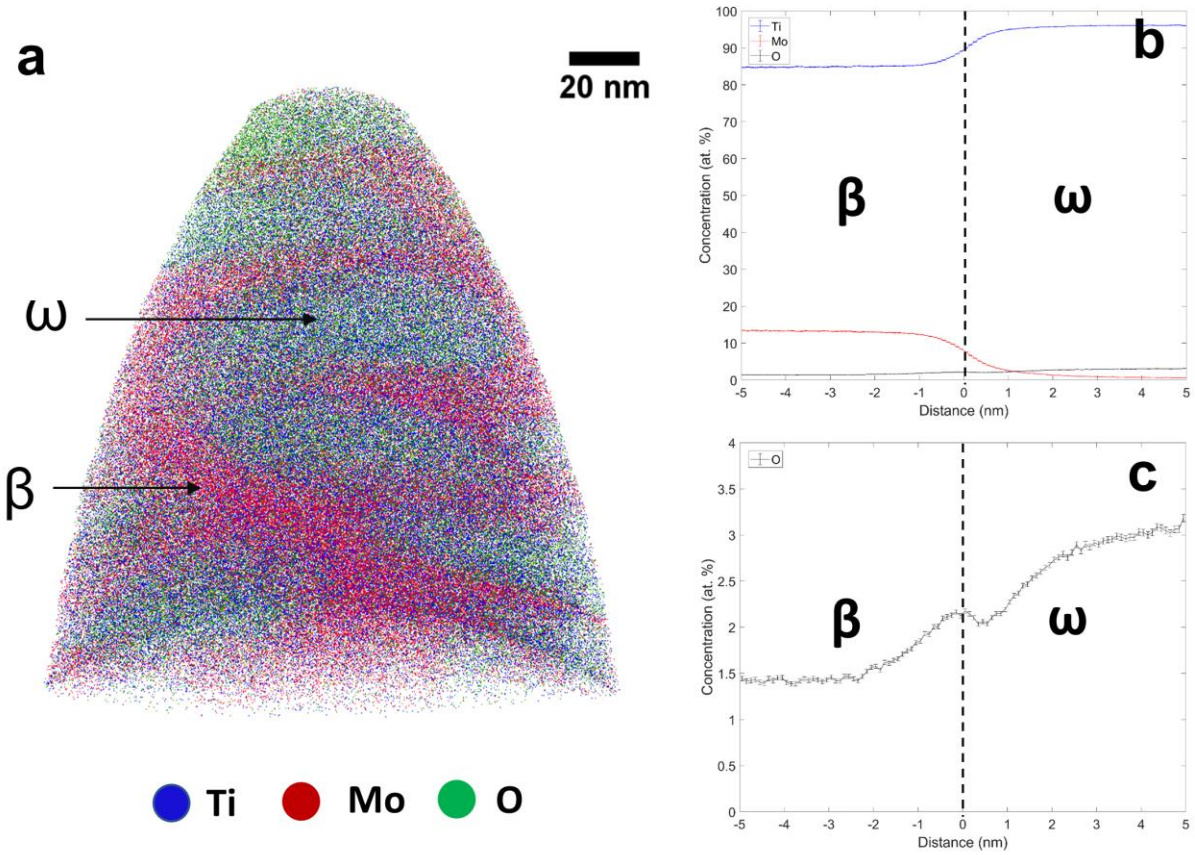

Figure 6.5: (a) APT reconstruction of OXA Ti-15Mo aged for 24 h at 500 °C with 1.5 at. % O and (b-c) proxigram showing Ti, Mo, and O concentration as a function of distance from 90 at. % Ti iso-concentration surfaces.

Micropillar compression was conducted to investigate the influence of elevated oxygen and the corresponding microstructural changes for ω on mechanical properties. For OXA Ti-15Mo aged at 450 °C for 24 h, micropillars were fabricated at distances of 100 µm from the α lath / β matrix interface corresponding to 2.2 at. % O. Since OXA Ti-15Mo with 2.2 at. % O aged at 500 °C for 24 h showed the onset of α precipitation in some regions (**Figure 6.3d**), micropillars were fabricated at a distance of 300 µm from the α lath/β matrix interface corresponding to 1.5 at. % O showing only ω precipitation. Images of post-compression micropillars for DA and OXA Ti-15Mo after 15% strain revealed differences in deformed pillar morphologies with different oxygen contents (**Figure 6.6**). Deformed micropillars for oxygen-free DA Ti-15Mo aged at 450 °C for 24 h with ω precipitates showed prominent step-like features that correspond to slip band formation during compression. Compressed pillars for OXA Ti-15Mo aged at 450 °C for 24 h with 2.2 at. % O also formed a large slip band after deformation, although other finer slip traces were observed near the base of the pillar (located at blue arrow in **Figure 6.6b**). Deformed micropillars for

oxygen-free DA Ti-15Mo and OXA Ti-15Mo with 1.5 at. % O after ageing at 500 °C showed similar post-compression morphologies as those aged at 450 °C. Notably, larger slip bands were suppressed in deformed OXA Ti-15Mo pillars with 1.5 at. % O and fine slip traces were instead observed after compression to 15% strain (located at blue arrow in **Figure 6.6d**).

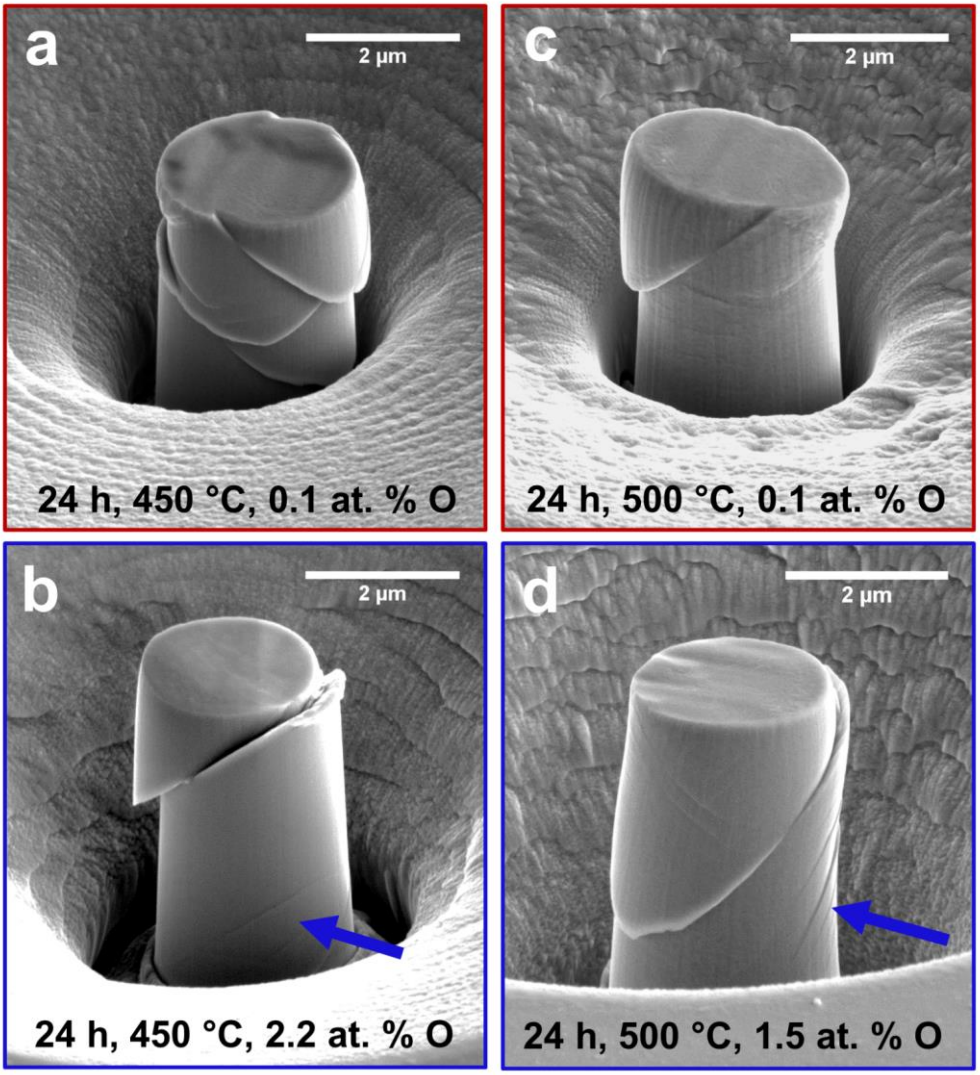

Figure 6.6: SEM-BSE images of 2 µm diameter micropillars compressed to 15% engineering strain for DA and OXA Ti-15Mo after ageing for (a-b) 24 h at 450 °C, and (e-g) 24 h at 500 °C. DA Ti-15Mo are shown in (a) and (c). OXA Ti-15Mo are shown in (b) and (d), with blue arrows showing fine slip traces.

Engineering stress-strain curves for micropillars compressed to 15% strain revealed that the influence of elevated oxygen differed for ω-enriched specimens aged at 450 °C and 500 °C (**Figure 6.7a-b**). Stress-strain curves for DA and OXA specimens aged for 24 h at 450 °C both showed discontinuous and unstable flow during compression (**Figure 6.7a**). Significant drops in measured stress values for these curves corresponded to the observed macroscale formation of slip

bands in compressed micropillars (**Figure 6.6a-b**). For DA and OXA Ti-15Mo aged for 24 h at 500 °C with larger ω precipitates, stress-strain curves showed more stable plastic flow but still displayed a slight drop or plateau in the engineering stress after initial yielding (**Figure 6.7b**). However, the compressive yield strength of micropillars increased with the elevated oxygen content and finer ω sizes for OXA Ti-15Mo aged at 500 °C for 24 h. The average yield strength of four tested micropillars for OXA Ti-15Mo aged at 500 °C with 1.5 at. % O was ~574 MPa, which significantly exceeded the average value of about 419 MPa for DA micropillars without oxygen. In order to understand the internal microstructure of deformed micropillars, TEM imaging was performed on liftout samples from cross-sections along $[110]_\beta$ for a compressed OXA Ti-15Mo pillar with 1.5 at. % O aged for 24 h at 500 °C (**Figure 6.7c**). Dark-field TEM images formed by selecting an ω reflection revealed that a continuous slip band cut through ω precipitates (blue arrow in **Figure 6.7c**). Slip trace analysis and direction of the slip bands observed in TEM images revealed that the bands were parallel to $[0001]_{\omega 1}$ // $[2\text{-}2\text{-}2]_\beta$ directions and perpendicular to the $(1\text{-}12)_\beta$ plane, indicating that dislocation activity took place along the $<111>\{112\}_\beta$ slip system. The formation of the continuous slip bands suggests that ω precipitates were sheared as a result of highly localized dislocation activity along the $<111>\{112\}_\beta$ system.

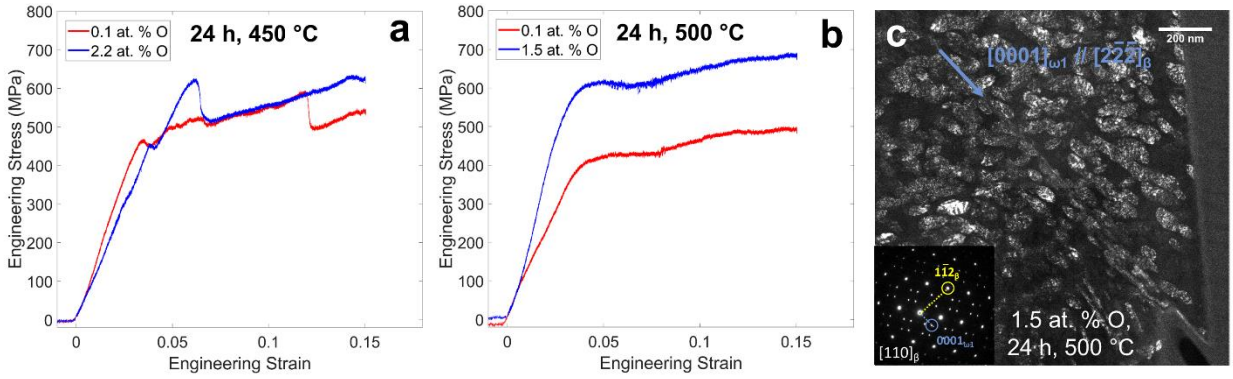

Figure 6.7: Engineering stress-strain curves for DA and OXA Ti-15Mo after ageing for (a) 24 h at 450 °C, and (b) 24 h at 500 °C. (c) Dark-field TEM image of liftout sample from compressed pillar to 15% strain for OXA Ti-15Mo aged for 24 h at 500 °C with 1.5 at. % O showing sheared ω precipitates. Blue arrow points to sheared ω precipitates along $<222>_\beta$ direction.

6.3.3 α precipitation and deformation in Ti-15Mo with varying oxygen content

Ageing treatments conducted at 600 °C yielded widespread α precipitation in DA and OXA Ti-15Mo specimens, but the size and number density of α was directly influenced by oxygen content and sequence of heat treatment steps (**Figure 6.8**). Oxygen-free DA Ti-15Mo aged for 4 h

at 600 °C formed coarse α precipitates that were ~10 μm in length (**Figure 6.8a**). In contrast, α precipitates became more refined with high oxygen levels, and OXA Ti-15Mo with 2.2 at. % O under the same heat treatment contained a higher number density of α precipitates with approximately 0.5 to 2 μm laths sizes. (**Figure 6.8b**). As a potent α-stabilizing element, oxygen is known to partition to the α phase during ageing of β Ti alloys [9], so very little oxygen is expected in the β matrix after α formation. Two step ageing results (**Figure 6.8c-d**) showed additional α refinement for both DA and OXA specimens compared to those aged directly at 600 °C. The first step at 450 °C for 2 h allowed for ω precipitation (**Figure 6.2a-b)** that then acted as heterogeneous nucleation sites for α formation in the second 600 °C ageing step through ω-assisted α nucleation mechanisms [36,37,39]. The α microstructures observed after two step ageing also showed that elevated oxygen levels significantly increased α number density compared to specimens without oxygen. The combined effects of ω-assisted nucleation and oxygen-induced precipitation yielded the finest α precipitates of all observed conditions in OXA Ti-15Mo with two step ageing.

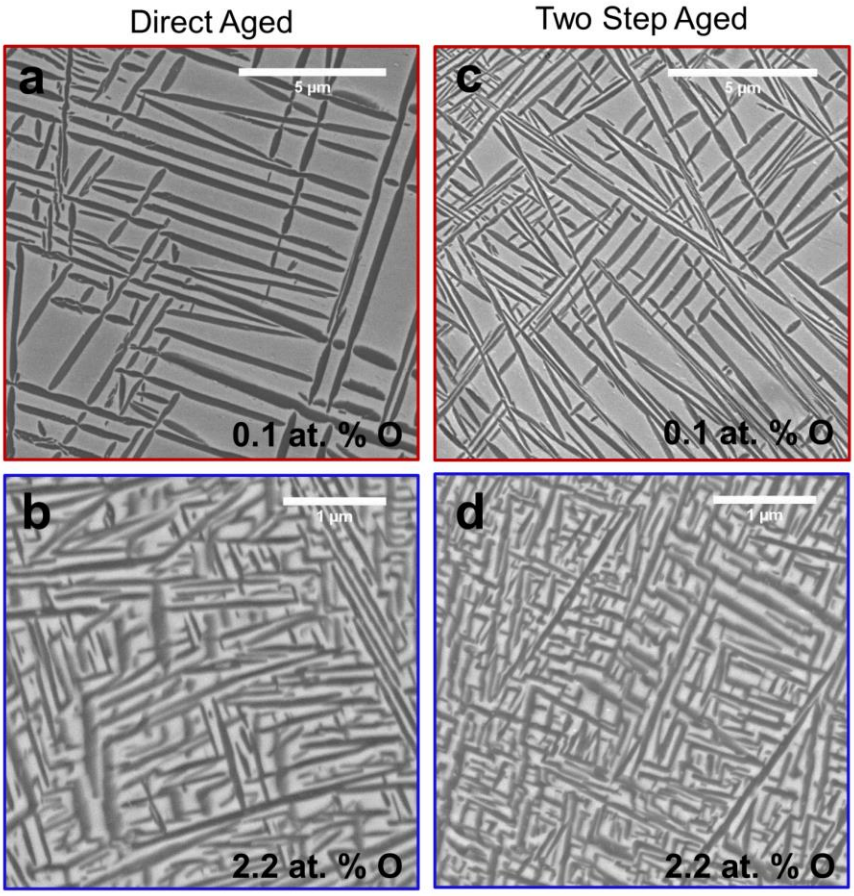

Figure 6.8: SEM-BSE images of (a) DA Ti-15Mo with 0.1 at. % O and (b) OXA Ti-15Mo with 2.2 at. % O aged for 4 h at 600 °C (Direct Aged), and (c) DA Ti-15Mo with 0.1 at. % O and (d) OXA Ti-15Mo with 2.2 at. % O aged for 2 h at 450 °C, then for 4 h at 600 °C (Two Step Aged).

After 600 °C ageing, micropillar compression testing of DA and OXA specimens was performed to understand changes in mechanical behavior with different α sizes and number densities. For oxygen-free DA Ti-15Mo aged directly for 4 h at 600 °C, compressed micropillars showed different morphologies depending on local α lath orientation in the pillar's volume. In some of these DA pillars, step formation and slip traces were observed near α/β interfaces (**Figure 6.9a**). Previously reported micropillar compression results for dual phase α-β Ti alloys also showed that slip may occur along the interface between α and β phases if oriented favorably relative to the deformation direction [130,144,145]. Alternatively, other compressed DA micropillars did not show significant step formation and instead formed fine slip traces in the β matrix (**Figure 6.9b**). These variations in deformed pillar morphology were attributed to the coarse α laths sizes observed after ageing that resulted in differences in α lath amounts and distributions in the tested micropillar volumes. In contrast, compressed pillars after 15% strain for OXA Ti-15Mo after two step ageing with 2.2 at. % O (**Figure 6.9c-d**) showed a larger number of short slip traces that formed in multiple locations on pillar surfaces, suggesting more distributed deformation occurred compared to DA samples.

Compressive engineering stress-strain curves for micropillars on DA and OXA Ti-15Mo aged at 600 °C showed that the α lath size greatly influenced yield strength and curve shape (**Figure 6.9e**). Stress-strain curves for micropillars on DA Ti-15Mo specimens directly aged at 600 °C for 4 h showed significant scatter in compressive yield strengths ranging from 200-350 MPa. Additionally, little work hardening was observed after initial yielding for all DA micropillars directly aged at 600 °C, and the associated curves showed a plateau with a flat slope after yielding. In contrast, stress-strain curves for OXA Ti-15Mo after two step ageing with 2.2 at. % O displayed less variation in curve shapes and higher compressive yield strengths with improved work hardening after pillar yielding compared to directly aged specimens without O. Accordingly, the average compressive yield strength of OXA Ti-15Mo after two step ageing was ~440 MPa, which almost doubled the average yield strength of ~230 MPa for DA micropillars without oxygen.

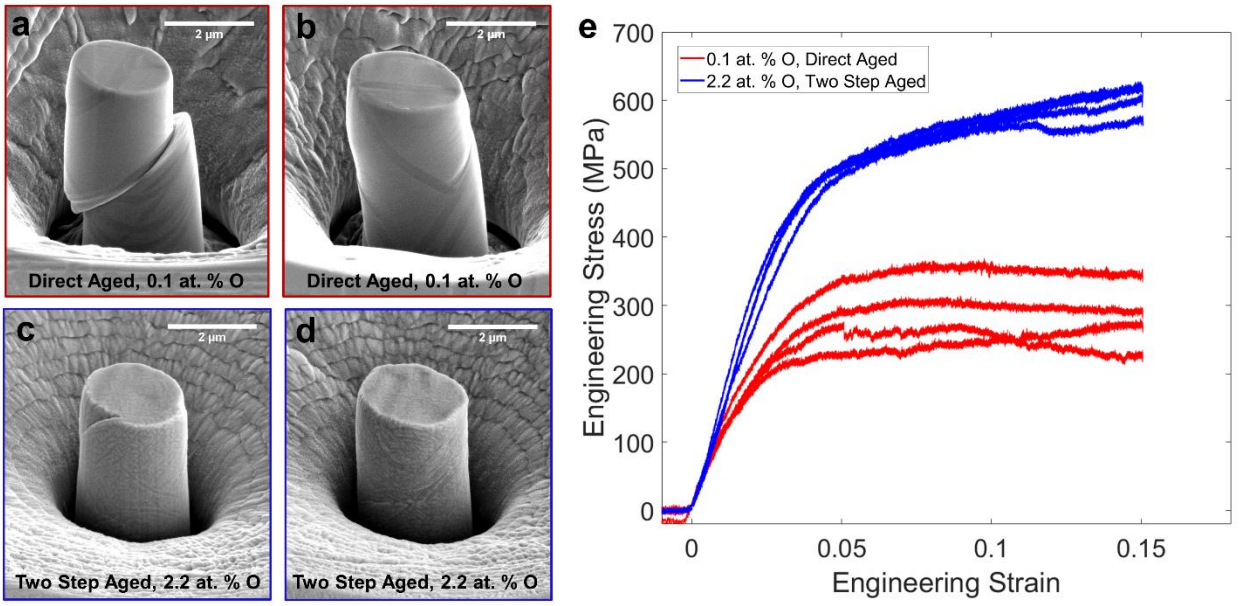

Figure 6.9: SEM-BSE images of 2 µm diameter micropillars compressed to 15% strain for (a-b) DA Ti-15Mo with 0.1 at. % O aged for 4 h at 600 °C (Direct Aged) and (c-d) OXA Ti-15Mo with 2.2 at. % O aged for 2 h at 450 °C, then 4 h at 600 °C (Two Step Aged). (e) Engineering stress-strain curves for DA Ti-15Mo with 0.1 at. % O aged for 4 h at 600 °C (Direct Aged) and OXA Ti-15Mo with 2.2 at. % O aged for 2 h at 450 °C, then 4 h at 600 °C (Two Step Aged).

6.4 Discussion

Aged microstructures and micropillar compression results for Ti-15Mo revealed that interstitial oxygen levels obtained during oxidation directly influenced subsequent precipitate evolution and the associated mechanical properties. During the oxidation exposure, α precipitation in the metal substrate near the oxide/metal interface (**Figure 6.1a**) is attributed to the thermodynamic stabilization of α with high dissolved oxygen levels [2]. α formation is also accompanied by Mo rejection and partitioning from α to the β matrix, which is consistent with Mo as a β-stabilizer in Ti alloys [150]. In the single β phase matrix, the maximum oxygen content was measured as 2.6 at. % O and is controlled by the oxygen solubility limit in the β phase before inducing thermodynamic stabilization and precipitation of α. For Ti-Mo alloys, the extent of oxygen solubility in the metal substrate during oxidation has been reported to be influenced by the level of Mo, with higher Mo concentrations reducing the level of oxygen uptake by the substrate [146]. However, other metastable β Ti systems such as Ti-Nb based compositions have shown different maximum oxygen levels up to ~5 at. % obtained similarly through oxidation (**Chapter 3**) or intentionally added to the bulk alloys [102,151,152]. The higher O solubility in the β phase for Ti-Nb compared to Ti-Mo alloys may be related to the electronic nature of the Ti atom and changes in the electron/atom (e/a) ratio based on alloy composition [146]. Decreased solid

solubility of oxygen has been reported for transition metal alloys with e/a ratios exceeding 5.75, whereas oxygen solubility increases for ratios below this value [153]. Indeed, the e/a ratios for Ti-15Mo investigated here and a previously studied Ti-20Nb (at. %) alloy (**Chapter 3**) are 4.24 and 4.2, respectively, and the lower value for Ti-20Nb may account for the higher maximum oxygen solubility of 4.8 at. % O compared to Ti-15Mo. Pure Mo shows essentially no solubility for interstitial oxygen before forming oxide phases [154,155], while pure Nb allows for limited oxygen solubility prior to oxide formation [155]. In Nb-Mo alloys, oxygen solubility also decreases with increasing Mo content from 0.35 wt. % (~2 at. %) in pure Nb to zero with 75 at. % Mo [153]. Therefore, alloying Ti with Mo would likely reduce oxygen solubility compared to alloying Ti with Nb. The tailoring of oxygen solubility and maximum saturation levels via alloy chemistry design may allow for more pronounced effects regarding oxygen-induced phase transformations. Therefore, the maximum oxygen solubility in metastable β Ti alloys may be an important design consideration during development of future alloy compositions that intentionally utilize high oxygen levels.

Upon subsequent ageing at 450-500 °C, the microstructural evolution of ω precipitates showed noticeable changes depending on oxygen content. In the absence of oxygen, ω-like embryos form in Ti-Mo from phase separation during rapid cooling after solution treatment that induces the partial displacive collapse of $\{111\}_\beta$ planes [29]. With additional ageing, the full collapse of $\{111\}_\beta$ planes completes the β to ω transformation [29], and Mo is rejected from growing ω precipitates to the β matrix [19]. With elevated oxygen, several changes were noted for ω precipitates including higher number densities and smaller sizes compared to specimens without oxygen (**Figure 6.2, 6.3**), as well as oxygen partitioning to ω precipitates (**Figure 6.5**). Such differences were also observed in the binary Ti-Nb system, and the growth rate changes in particular were attributed to possible kinetic barriers for the β to ω transformation with high oxygen (**Chapter 3**). More generally, ω precipitates grew more slowly in Ti-Mo compared to Ti-Nb for similar ageing treatments at all oxygen levels. This observation is consistent with prior studies showing slower ω nucleation and coarsening kinetics in oxygen-free specimens for Ti-Mo compared to Ti-Nb systems [156] and is attributed to the slower Mo diffusion rate compared to Nb in Ti [157] resulting in slower rejection of β-stabilizing elements during ω growth. ω precipitate morphology changes were also seen for Ti-15Mo related to oxygen content (**Figure 6.3**), with slightly faceted shapes and aligned particles seen with elevated oxygen compared to ellipsoidal

shapes and more random arrangements without oxygen. The low lattice misfit Ti-Mo and Ti-Nb systems are known to yield ellipsoidal shapes for ω precipitates, while higher misfit systems like Ti-V form cuboidal morphologies [19]. However, changes in ω's shape with elevated oxygen have been reported previously, such as for Ti-Nb that showed elongation along the major axis in the $<111>_\beta$ direction resulting in rod-like shapes (**Chapter 3**). The shape of ω in Ti-15Mo with high oxygen (**Figure 6.3c**) showed slight faceting along $<001>_\beta$ directions that matches the faceting of cuboidal ω observed in higher lattice misfit β Ti compositions such as the Ti-V system [15,31,96]. High oxygen levels may therefore result in the generation of additional misfit strains and higher lattice misfit for Ti-Mo to induce the faceted ω morphologies. The alignment of ω precipitates with elevated oxygen (**Figure 6.3b**) was not observed in prior Ti-Nb studies (**Chapter 3**). Precipitate alignment has been widely reported for other metallic systems such as nickel [158–160] and cobalt superalloy [161,162] γ/γ' microstructures driven by complex interactions between interfacial energy, misfit strains, and elastic stiffness. The aligned morphologies observed here for OXA Ti-15Mo suggest that the higher O levels may also result in possible changes for interfacial energy, misfit strains, and elastic stiffness that induce the observed aligned cuboidal-like microstructures. Finally, with the highest interstitial oxygen levels of 2.2 at. % O, α precipitation eventually occurred in addition to ω formation after ageing at 500 °C for 24 h (**Figure 6.3d**), and this faster α precipitation rate during isothermal ageing is due to the stabilization of α with higher oxygen contents [2].

The influence of oxygen on mechanical properties evaluated using micropillar compression was dependent on the degree of oxygen partitioning to ω precipitates during ageing. Without oxygen partitioning, as seen in OXA specimens aged for 24 h at 450 °C (**Figure 6.4**), little change was observed for compressive yield strength and work hardening behavior in DA and OXA specimens (**Figure 6.7a**). With partitioned oxygen to ω observed for OXA Ti-15Mo aged for 24 h at 500 °C with 1.5 at. % O, micropillars showed higher compressive yield strength and marginal improvement in work hardening compared to specimens without oxygen (**Figure 6.7b**). However, ω precipitates with oxygen were still ultimately sheared leading to plastic flow localization (**Figure 6.7c**). Shearing of isothermal ω precipitates during deformation leading to plastic flow localization, embrittlement, and loss of ductility have been extensively reported in metastable β Ti alloys without oxygen [46,91,116,163]. This embrittlement is caused by shearing and disordering of coherent ω particles along the $<111>\{112\}_\beta$ slip system to form precipitate-free channels that

promotes planar slip and localized slip band formation observed in bulk tensile testing and micropillar compression [8,116,117]. Notably, elevated oxygen levels that partitioned to larger ω precipitates during ageing of Ti-20Nb (at. %) after a similar oxidation exposure were reported to increase strength and improve work hardening behavior (**Chapter 4**). This improvement was due to oxygen partitioning that increased ω's resistance to precipitate shearing and impeded the formation of continuous deformation channels, allowing for more homogeneous deformation to occur through dislocation bypassing (**Chapter 4**). Therefore, the stresses required to shear or bypass ω particles were calculated for the Ti-15Mo microstructures observed here to understand ω-dislocation interactions. The increase in critical resolved shear stress (CRSS) from dislocations shearing through coherent ω particles was estimated as [8]:

$$\Delta\tau_s = 1.02\gamma^{3/2}G^{-1/2}b^{-2}r^{1/2}f^{1/2} \quad (1)$$

where γ is the anti-phase boundary energy, *G* the shear modulus, *b* the Burgers vector of the β matrix, *2r* the equivalent diameter for ω precipitates, and *f* the volume fraction of ω particles. The increase in CRSS due to a dislocation bypassing mechanism through Orowan looping was also estimated for the investigated microstructures using the following equation [8,132]:

$$\Delta\tau_b = \frac{1}{1-\nu}\frac{Gb}{2\pi D} ln\frac{\sqrt{2/3}r}{b} \quad (2)$$

where *D* is the inter-particle spacing. The values of Poisson's ratio *v* and *G* have been reported for a Ti-Nb based gum metal alloy as 0.39 and 25 GPa, respectively, using single crystal elastic constants measured with in-situ synchrotron x-ray diffraction [53,116]. Additionally, γ for ω particles in Ti-11Mo (at. %) has been estimated to be 0.3 J/m^2 [8]. Assuming the same values for Ti-15Mo and using the microstructural parameters given in **Table 6.1**, $\Delta\tau_s$ was calculated to exceed ~1000 MPa for all observed microstructures while $\Delta\tau_b$ ranged between ~330-640 MPa, which reveals that the smaller applied stress for these two mechanisms is dislocation bypassing. This simple analysis suggests that dislocation bypassing is possible for the ω sizes observed here, as was also reported for Ti-20Nb microstructures in **Chapter 4**. Although dislocation bypassing is possible, the load drops and formation of slip bands in compressed micropillars for DA and OXA Ti-15Mo aged for 24 h at 450 °C indicated that shearing of ω precipitates leading to continuous deformation channels still occurred. With oxygen partitioning to ω precipitates in OXA Ti-15Mo aged for 24 h at 500 °C, compressive yield strength increased compared to DA specimens. However, the work hardening behavior did not improve significantly since ω precipitates were ultimately still sheared (**Figure 6.7c**), unlike results reported for Ti-20Nb with higher O levels

where shearing of ω was suppressed (**Chapter 4**). This difference is attributed to the lower maximum O solubility in the β matrix of Ti-15Mo after oxidation compared to Ti-20Nb that resulted in a smaller amount of partitioned oxygen in ω. The lower oxygen level observed here is less effective in strengthening ω precipitates against shearing that would lead to better work hardening and ductility. Similar results were observed with lower oxygen levels during micropillar testing with 1.5 at. % O in Ti-20Nb, which also showed slip band formation indicating shearing of ω during deformation (**Chapter 4**). These results suggest that work hardening and ductility improvements stemming from partitioned elevated oxygen in ω-containing β Ti alloys are governed by the maximum solubility of O, which will need to be considered in future alloy design employing this mechanism.

After ageing at 600 °C, elevated oxygen levels resulted in significant α precipitate refinement compared to specimens with minimal oxygen (**Figure 6.8**), observed both after direct ageing and with intentional prior ω formation in two step ageing. Rapid heating and direct ageing at 600 °C, which exceeds the reported 560 °C ω solvus [147], avoided potential β phase separation and isothermal ω evolution known to promote heterogeneous α precipitation in β Ti alloys [33]. Also, athermal ω phase that has been reported for similar Ti-Mo compositions [29] and is likely present in solution treated and oxidized samples was expected to quickly dissolve upon rapid heating to 600 °C. In the absence of intermediate phases, the microstructural changes in α precipitate size and number density observed after direct ageing at 600 °C are attributed to the increase in α nucleation driving force from elevated oxygen. Such differences have been demonstrated in a prior ageing study of the metastable β Ti-15-333 alloy with varying oxygen content (**Chapter 5**). Oxygen in solid solution is a potent α stabilizer in metastable β Ti alloys, and this stabilization increased the nucleation driving force for α leading to faster precipitation kinetics with a more refined lath size (**Chapter 5**). With two step ageing that intentionally formed ω prior to the 600 °C step, ω-assisted nucleation, where ω acts as a heterogeneous nucleation agent for α [37–39], was combined with oxygen-induced α refinement to obtain the finest α lath sizes in OXA specimens with 2.2 at. % O. During micropillar compression, significant variation was observed in the yield point of stress-strain curves for DA Ti-15Mo aged directly at 600 °C (**Figure 6.9e**). This variation is attributed to intrinsic size effects related to the volume of tested micropillars relative to the α lath sizes. This type of size effect dominates when the micropillar's dimensions are on the order of microstructural features and the pillar's volume contains a small number density

of dispersed obstacles, which leads to an observed size effect on measured yield strengths [121]. With smaller lath sizes in OXA Ti-15Mo after two step ageing, this size effect was noticeably reduced, and the compressive yield strength roughly doubled compared to specimens without oxygen (**Figure 6.9e**). Many α precipitation refinement studies in metastable β Ti alloys have focused on obtaining finer α laths leading to increased tensile strengths after bulk testing [34] and compression strengths in micropillar investigations [130,145]. Since the α-β interface acts as the main barrier for dislocation motion in two phase Ti alloys, increased α number density results in a greater number of these interfaces to impede dislocation motion for higher strength in bulk testing [2,48]. Therefore, using elevated oxygen content to induce α lath refinement offers an additional pathway to obtain high strength metastable β Ti alloys and can be combined with other mechanisms such as ω-assisted nucleation to yield even further refinement.

These results revealed the influence of oxygen in Ti-15Mo on ω and α precipitation and microstructural evolution that directly impacted compressive mechanical properties. The partitioning of oxygen to ω (**Figure 6.5**) and α precipitates [9] mitigates the known embrittlement challenges with interstitial O in β Ti [5], which opens possibilities for future alloy and processing development that intentionally utilizes oxygen as an alloying element in β Ti alloys. Furthermore, these findings may be used to understand the effects of higher oxygen levels in commercially relevant Ti-Mo based compositions, which could allow for increased oxygen concentration limits in industrial materials specifications. Overall, these results demonstrate that high oxygen levels induce phase transformation and precipitation changes during ageing that result in improved mechanical properties for Ti-15Mo.

6.5 Conclusions

The impact of high interstitial oxygen contents up to 2.6 at. % O, obtained using an oxidation exposure, on ω and α precipitation and the resulting effects on compressive mechanical properties were investigated for aged Ti-15Mo. The following conclusions were drawn:

- High oxygen levels reduced the growth rate of ω precipitates and induced ω morphology changes from randomly arranged ellipsoidal shapes without O to cuboidal-like shapes aligned along $<001>_{\beta}$ directions with oxygen. Although Ti partitioning to ω and Mo partitioning to β were observed after ageing at both 450 and 500 °C, oxygen partitioning to ω precipitates was only observed after ageing at 500 °C. With the highest oxygen levels

of 2.2 at. % O, α precipitation occurred in addition to ω formation after isothermal ageing at 500 °C.

- The influence of oxygen on mechanical properties evaluated for ω-containing microstructures was dependent on oxygen partitioning to ω precipitates. After ageing at 450 °C, micropillar compression results revealed that pillars with high oxygen but without significant oxygen partitioning to ω showed similar slip band formation, unstable plastic flow, and yield strength values as oxygen-free pillars. After ageing at 500 °C, compressed pillars with partitioned oxygen to ω showed higher compressive yield strengths than oxygen-free pillars, but ω precipitates with oxygen were ultimately still sheared in a continuous deformation channel. This strength improvement was attributed to more difficult shearing of ω precipitates with partitioned oxygen.
- After ageing at 600 °C, elevated oxygen levels induced finer α precipitate sizes with a larger number density compared to oxygen-free specimens. This refinement was due to an increased nucleation driving force for α precipitation with high oxygen contents resulting in faster nucleation of finer laths. Oxygen-induced refinement was also combined with the ω-assisted nucleation mechanism to obtain even smaller sizes for α precipitates.
- Micropillar compression testing of α-containing microstructures showed that the refined α precipitates obtained with elevated oxygen and two step ageing resulted in smaller size effects and higher compressive yield strengths, which is due to a higher number of α-β interfaces that act as dislocation barriers.
- These results show the influence of high oxygen contents on ω and α precipitation with improvements to compressive mechanical properties in Ti-15Mo, which demonstrate the beneficial effects of intentional high oxygen levels in β Ti alloys and may be applicable to existing commercial alloy compositions as well as future alloy and processing design.

Chapter 7: Early Oxidation Behavior of Pure Ti and Si-Coated Ti

7.1 Introduction

Although titanium alloys are frequently used as structural materials due to their high specific strength and corrosion resistance, the use of Ti alloys has been limited above 550 °C due to poor oxidation resistance [1]. Oxidation of Ti and its alloys at elevated temperatures results in formation of a two-layered, non-adherent oxide scale and continuous dissolution of interstitial oxygen in the subsurface metal that is highly embrittling, as discussed in **Chapter 2**'s literature review. During high temperature exposures, the oxidation of uncoated titanium shows rapid kinetics with an initial parabolic growth rate transitioning to a linear rate at 700-1200 °C [81]. Titanium oxidation eventually becomes dominated by growth of the internal oxide scale [75,79,81]. A particular challenge for titanium oxidation studies is understanding the formation pathway of the complex oxide morphologies observed after long thermal exposures. Furthermore, the use of Si-containing coatings with a range of chemistries, deposition parameters, and coating microstructures on Ti alloys has shown improved oxidation resistance with thinner oxide scales, less porosity, and fewer cracks. These changes have been linked to the formation of silicide phases such as Ti_3Si, Ti_5Si_3, Ti_5Si_4, TiSi, and $TiSi_2$ [12,83,84,89]. This significant improvement with Si-containing coatings necessitates additional study to comprehend the role of Si-rich coatings during oxidation. While most prior studies focused on characterization of oxide scales after 100+ h exposures that are relevant for technological applications, this work focuses on the early oxidation of pure Ti and Ti that has been sputtered with a Si thin film to characterize the initial growth of oxide scales. The selected model system isolates the role of Si and silicide phases during oxidation, and detailed characterization clarifies the oxidation paths and mechanisms leading to slower oxidation rate of Ti when coated with Si and silicide phases.

7.2 Experimental methods

Commercially pure (99.999%) titanium plate, 3 mm thick, was purchased from Alfa Aesar. Ti specimens were sectioned using a slow speed diamond saw and cleaned using acetone and distilled water. Samples were then successively ground and polished using 30, 12, 9, 3, and 1 μm Al_2O_3 lapping films, rinsing with distilled water between steps. A set of polished pure Ti specimens were then sputtered with a 250 nm layer of amorphous pure Si using a Kurt J. Lesker Co. five source confocal, magnetron sputtering system. For another set of polished samples, one drop of 50% distilled water/50% colloidal silica (30 nm) solution (Mager Scientific AP-342) was deposited on the polished surface and air-dried. Specimens were placed in an Al_2O_3 crucible and then oxidized at 800 °C for 0.5, 2, 8, 32, or 64 hours in a 1 standard cubic centimeter per minute (SCCM) O_2/4 SCCM Ar environment (approximately pO_2 = 0.2 atm/20.3 kPa). The exposures were such that specimens were inserted in the furnace after it was heated to 800 °C in a flowing Ar (40 SCCM) gas environment. After insertion and temperature equilibration back to 800 °C (approximately 15 minutes), the aforementioned oxidizing environment was introduced. Following the oxidation exposure, oxygen gas flow was stopped. Specimens were removed from the hot zone and cooled to room temperature in flowing Ar (40 SCCM).

Coating and oxide scales were characterized using a Thermo Fisher Scientific FEI Helios 650 or Nova 200 Nanolab scanning electron microscope (SEM) equipped with a Focused Ion Beam (FIB), also used to prepare cross-sectional transmission electron microscopy (TEM) foils and site-specific atom probe tomography (APT) samples. TEM bright field images and selected area electron diffraction (SAED) patterns were obtained using a JEOL 2010F microscope operated at 200 kV. Bright field TEM figures are composites of multiple individual specimen images. Scanning transmission electron microscope (STEM) Z-contrast images and energy dispersive spectroscopy (EDS) maps were collected using a Hitachi HD-2300A microscope at 200 kV equipped with an Oxford Instruments EDS detector. EDS maps were collected using an acquisition time of 1800 s. Data visualization and analysis of EDS maps were performed using Oxford Instruments INCA software. Bulk chemistry of oxidized specimens was analyzed by atom probe tomography performed with a Cameca local electrode atom probe (LEAP) 5000 XR operated in laser mode. A specimen temperature of 50 K, a detection rate of 0.005 atoms per pulse, a laser pulse energy of 30 pJ, and a pulse repetition rate of 250 kHz were used for data collection. Data

reconstruction, background subtraction, peak deconvolution, and compositional analysis were performed using the Integrated Visualization and Analysis Software (IVAS) package 3.8.0.

7.3 Results

7.3.1 Pure titanium oxide characterization

Surface observations of pure Ti samples after oxidation for 0.5, 2, and 8 hours revealed faceted oxide crystals (**Figure 7.1**), whose sizes increased with oxidation time. The scale formed on pure Ti showed a two-layer scale morphology, with an outer dense and compact scale showing columnar grains and an inner porous scale containing fine and coarse equiaxed grains. Both layers thickened with exposure time as illustrated by cross sectional bright field TEM images (**Figure 7.2**). Thicknesses of the overall oxide and outer oxide layer for oxidized pure Ti specimens are shown in **Figure 7.3a**, which were calculated as an average of ten measurements in each region. The difference in the overall oxide and outer oxide thickness in **Figure 7.3a** corresponds to the inner oxide layer. Thickness measurements for specimens showing oxide separation from the metal (**Figure 7.2c**) did not include the separated void region. The outer layer grew at a faster rate initially and slowed down, while the inner layer showed a consistent growth rate over the exposure times considered here. Electron diffraction of the samples after the three different exposure times showed rutile TiO_2 as the oxide phase in both outer and inner layers (**Figure 7.3b**). The outer and inner scales were separated by a row of small isolated voids that grew in size over time (indicated by the yellow arrows in **Figure 7.2**). Wider gaps and voids (located at red arrows in **Figure 7.2**) were present immediately above the oxide/metal interface and interspersed voids were also observed in the inner oxide (**Figure 7.2c**). Nanocrystalline grains in the inner oxide were observed bordering both rows of voids. In both outer and inner oxide layers, no cracking in the scale was observed even after 8 h. However, after 8 h, the inner oxide layer appeared delaminated at multiple sections of the oxide/metal interface (**Figure 7.2c**).

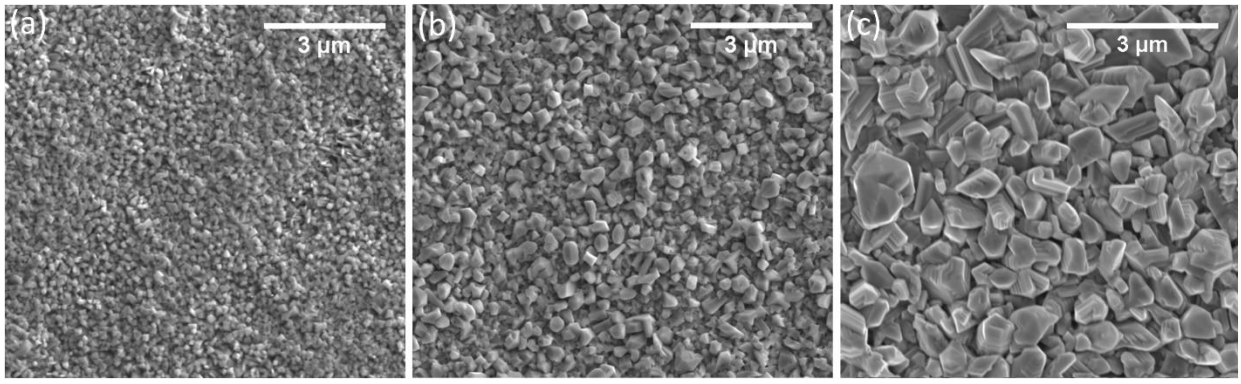

Figure 7.1: Top view SEM micrographs of the oxide scales formed on (a) Ti after 0.5 h, (b) Ti after 2 h, and (c) Ti after 8 h. All were oxidized at 800 °C in pO_2 = 0.20 atm.

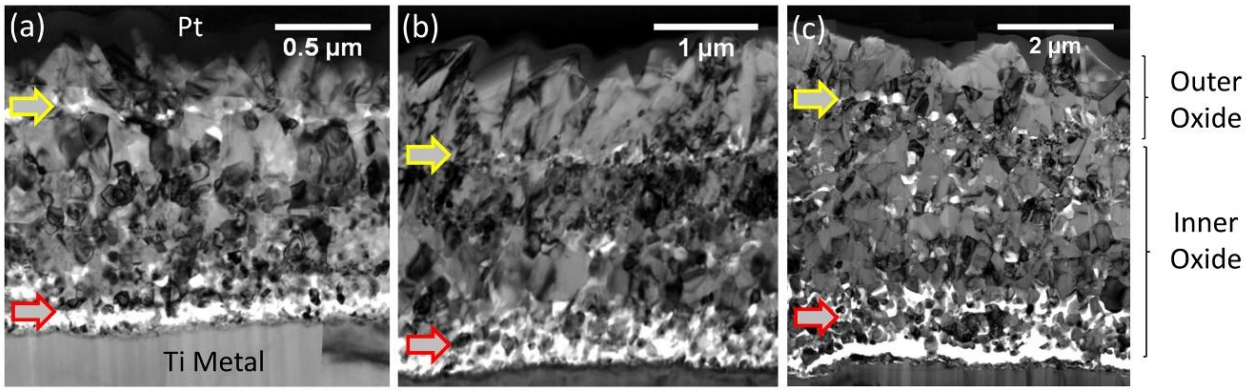

Figure 7.2: Bright field TEM images of the oxide scales formed at 800 °C on (a) Ti after 0.5 h, (b) Ti after 2 h, and (c) Ti after 8 h. Red and yellow arrows denote rows of voids observed in oxide scales.

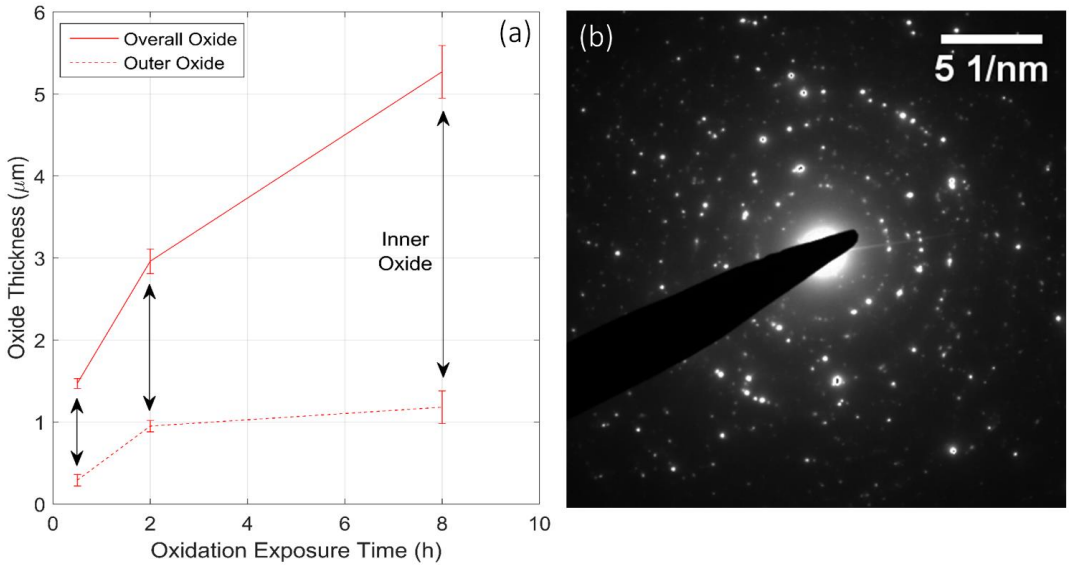

Figure 7.3: (a) Overall and outer oxide thicknesses for Ti oxidized for 0.5, 2, and 8 h. The difference between overall and outer oxide thickness corresponds to the inner oxide thickness. (b) Representative oxide electron diffraction ring pattern showing rutile TiO_2 phase in Ti oxidized for 0.5 h.

7.3.2 Colloidal silica deposited Ti oxide characterization

Colloidal silica nanoparticles were deposited on Ti samples to serve as a marker of the original metal surface prior to oxidation. After oxidation for 2 h, this sample exhibited three layers: a rod-like outer layer, an intermediate nanocrystalline layer, and an inner fine-grained, porous layer (**Figure 7.4a**). The outer and inner layers of this colloidal SiO_2 containing sample showed similar morphologies to the outer and inner oxides formed on pure Ti, but the inner layer thickness was noticeably reduced compared to that of the pure Ti specimen for the same oxidation exposure. The intermediate layer corresponded to the periodic arrangement of three to four layers of silica particles (**Figure 7.4a**), as determined through EDS mapping (**Figure 7.4b-e**).

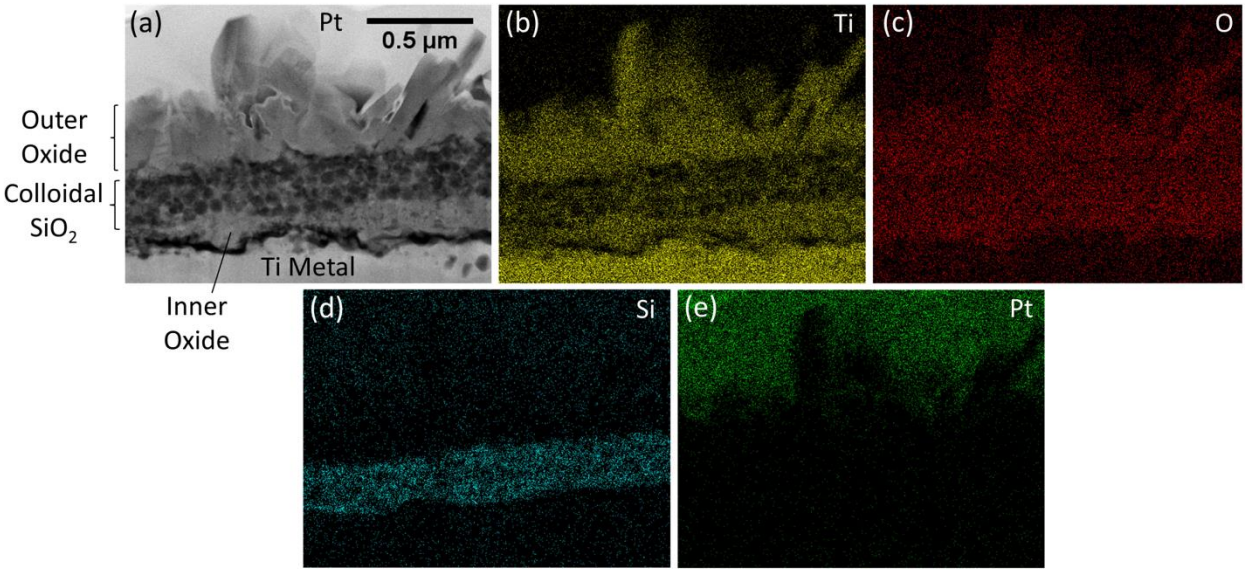

Figure 7.4: (a) STEM Z-contrast image and associated EDS maps for Ti, O, Si, and Pt (b-e) of the oxide scale for pure Ti deposited with a colloidal SiO_2 layer oxidized at 800 °C for 2 h in pO_2 = 0.20 atm.

7.3.3 Si-coated Ti oxide characterization

The evolution of the coating and surface oxides for Ti coated with a 250 nm Si thin film are shown through SEM images obtained after increasing oxidation exposure up to 64 h (**Figure 7.5**). After 2 h of exposure, irregularly shaped protrusions up to 5 µm in diameter were observed on the specimen's surface (**Figure 7.5a**), the largest of which remained visible after 8 h of exposure (**Figure 7.5f**). Nanocrystals present between the protrusions (**Figure 7.5e, f**) grew in size and density over time (**Figure 7.5g, h**). After 32 h and 64 h, the protrusions were no longer visible. Instead, the surface was fully covered by nanocrystals. The crystals' wedge-like morphology, as well as striations that were observed only on one side of the crystals, are evident in **Figure 7.5h**.

Ridge-like features were also observed on the surface of specimens after 8, 32, and 64 h of oxidation exposure (**Figure 7.5b, c, d**).

Bright field TEM images of cross sections obtained from specimens oxidized for 2 h reveal two distinct layers: a compact, polycrystalline layer above the Ti metal substrate and an amorphous layer at the surface (Layers 1 and 2 in **Figure 7.6a**). Layer 1 is identified as Ti_5Si_3 by electron diffraction (**Figure 7.6b, c**). The TEM foils used in **Figure 7.6** were prepared such that they bisected one of the protrusions observed on the specimen's surface. The surface protrusions correspond to a delaminated and buckled region of the amorphous layer. On both sides of the buckled region, the amorphous layer was depleted and fine columnar nanocrystals were instead observed, presumably corresponding to the clusters of nanocrystals observed from the surface along the edges of the protrusions (**Figure 7.5e**).

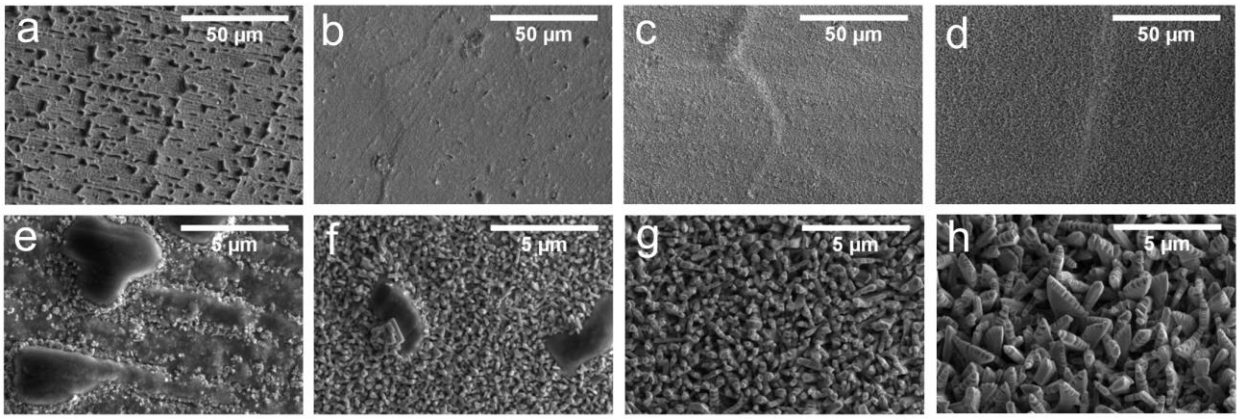

Figure 7.5: Top view SEM micrographs of coating and oxide scales formed on pure Ti coated with 250 nm Si after (a, e) 2 h, (b, f) 8 h, (c, g) 32 h, and (d, h) 64 h of oxidation exposure at 800 °C in pO_2 = 0.20 atm.

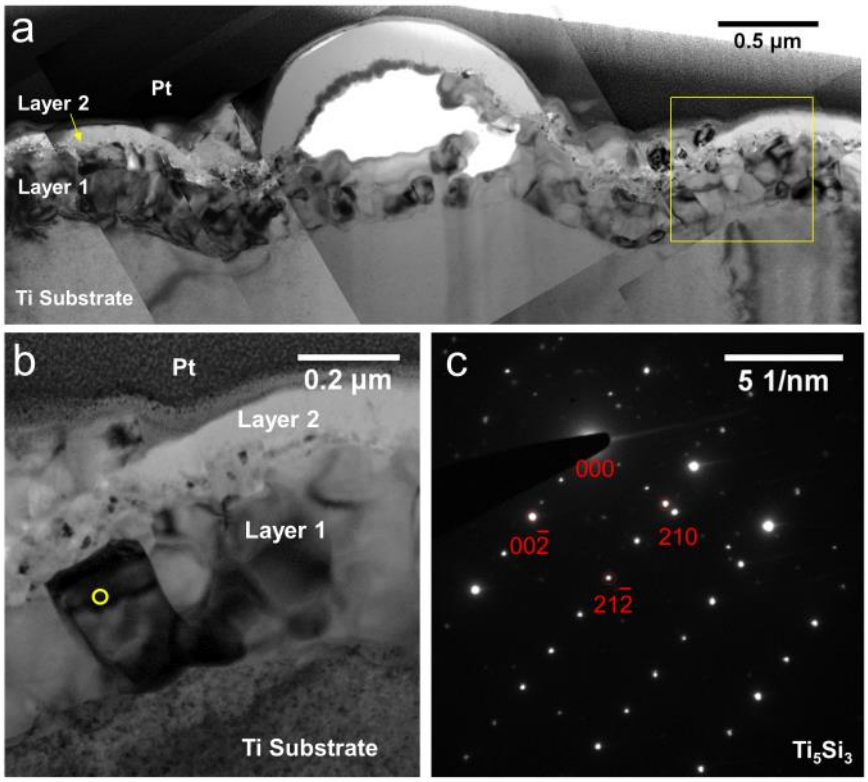

Figure 7.6: (a) Bright field TEM image of the coating and oxide cross section for Si-coated Ti oxidized at 800 °C for 2 h. (b) Subset of TEM image outlined by yellow box showing grain selected for electron diffraction (yellow circle). (c) The corresponding selected area electron diffraction pattern indexed as the [1$\bar{2}$0] zone axis of Ti_5Si_3.

Observed through STEM Z-contrast imaging, the Ti_5Si_3 layer (Layer 1 in **Figure 7.7a**) is clearly distinguished from the Ti substrate by a change in greyscale, and the amorphous layer (Layer 2 in **Figure 7.7a**) appeared as a dark region. EDS mapping of this region (**Figure 7.7b-d**) confirms that the amorphous layer is consistent with SiO_2, and the compact polycrystalline layer with Ti_5Si_3. At the location of the protrusion, the delaminated and buckled amorphous layer is again consistent with SiO_2 (**Figure 7.8**). The Ti_5Si_3 layer has not separated and is adherent to the Ti metal substrate; thus the delamination occurred at the interface between the Ti_5Si_3 layer and amorphous SiO_2 layer. The thin layer observed in the inner surface of the buckled layer is rich in Ti and Ga, and is therefore interpreted as sputtered and redeposited material during FIB milling. Underneath the protrusion above the Ti_5Si_3 layer, a thin layer rich in Ti and O but not Si was also observed (yellow arrow in **Figure 7.8a-d**).

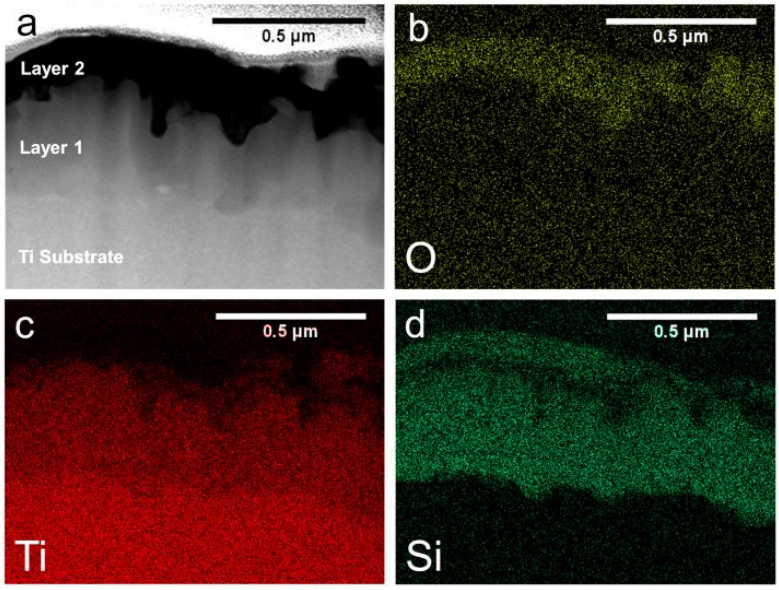

Figure 7.7: (a) STEM Z-contrast image and associated EDS maps for O, Ti, and Si (b-d) of the coating and oxide cross section for Si-coated Ti oxidized at 800 °C for 2 h.

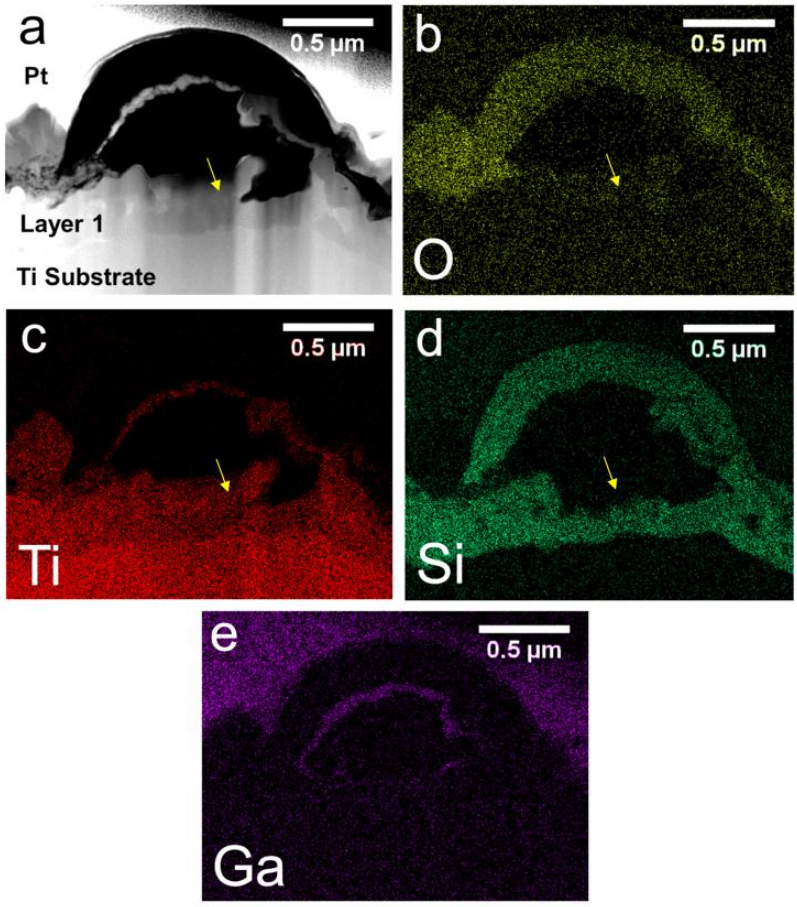

Figure 7.8: (a) STEM Z-contrast image and associated EDS maps for O, Ti, Si, and Ga (b-e) of the coating and oxide cross section at a protrusion of Si-coated Ti oxidized at 800 °C for 2 h. Yellow arrows denote region enriched in Ti and O, but not Si.

The chemistry of the Ti_5Si_3 layer and underlying Ti substrate for the 2 h oxidized specimen, obtained from APT reconstructions (**Figure 7.9**), revealed that Ti_5Si_3 contained up to 0.6 at.% O in solid solution. The Ti substrate also contained dissolved O, as well as a small amount of dissolved Si. The measured compositions for the Ti_5Si_3 layer and Ti substrate were calculated after background subtraction and decomposition of overlapping peaks. The atomic composition of Ti_5Si_3 was measured as Ti: 61.5 ± 0.2%, Si: 37.2 ± 0.1%, O: 0.6 ± 0.1%, Al: 0.3 ± 0.1%, Cr: 0.2 ± 0.01%, C: 0.1 ± 0.01%, V: 0.1 ± 0.1%. The measured level of H was on the order of 1.3 ± 0.6 at. %. The Ti substrate contained 8.9 ± 0.8 at. % O and 0.3 ± 0.04 at. % Si.

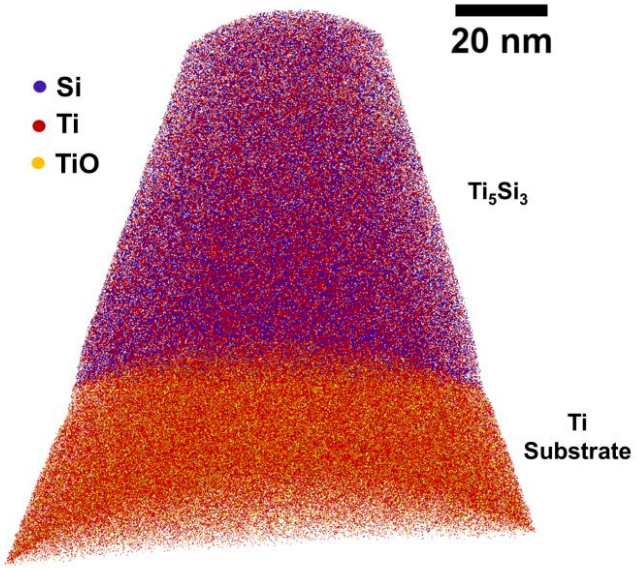

Figure 7.9: Atom probe tomography reconstruction of the Ti_5Si_3 layer and Ti substrate for Si-coated Ti oxidized at 800 °C for 2 h.

The oxide and coating morphology after 8 h of exposure observed in bright field TEM (**Figure 7.10a-d**) showed a similar polycrystalline and fine-grained Ti_5Si_3 layer above the Ti substrate. The TEM foils (**Figure 7.10**) were also prepared such that they bisected a surface protrusion. The amorphous SiO_2 layer, previously observed in the specimen oxidized for 2 h (Layer 2 in **Figure 7.6a**), was only seen at the surface protrusions and was not present elsewhere in the cross sections after 8 h of oxidation. The Ti_5Si_3 layer was now covered by a two-layer scale with an inner equiaxed, nanocrystalline layer and an outermost layer of columnar crystals (Layer 3 and 4 in **Figure 7.10a**), both identified by electron diffraction as rutile TiO_2. The observed oxide scales were compact and dense, with few voids seen within the layers. There was no evidence for SiO_2 within the diffraction patterns from the nanocrystalline oxide layer (Layer 3). The two-layer

scale was also observed underneath the protrusion above the Ti_5Si_3 layer. Thus, the Ti and O rich layer observed underneath the protrusion after 2 h of exposure (yellow arrow in **Figure 7.8a-d**) is interpreted as TiO_2.

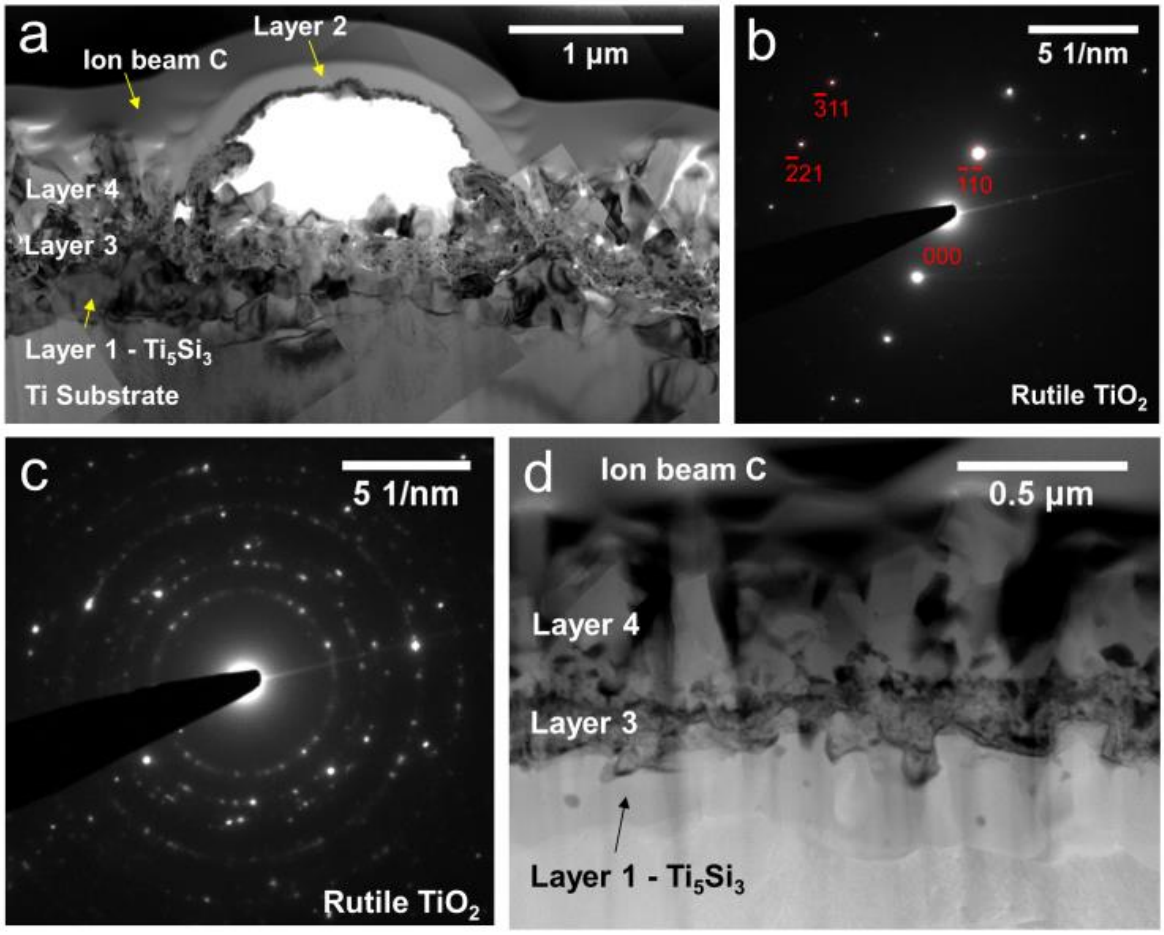

Figure 7.10: (a) Bright field TEM image of the coating and oxide cross section for Si-coated Ti oxidized at 800 °C for 8 h. (b) Selected area diffraction pattern of an external oxide grain indexed as the [11$\bar{4}$] zone of rutile TiO_2. (c) Electron diffraction ring pattern of the internal oxide showing rutile TiO_2. (d) STEM Z-contrast image of Si-coated Ti oxidized at 800 °C for 8 h.

After 32 and 64 h of oxidation exposure (**Figure 7.11**), the oxide morphologies observed in bright field TEM were similar to those of the 8 h specimen, showing fine-grained Ti_5Si_3 adjacent to the Ti substrate (Layer 1), a nanocrystalline inner oxide layer (Layer 3), and an outermost layer of oxide crystals that developed into a wedge-like shape (Layer 4). Both oxide layers (Layers 3 and 4) thickened with longer exposure time. The evolved inward growing nanocrystalline oxide scale showed compact, dense, and equiaxed grains with isolated voids concentrated at the oxide/silicide interface. EDS mapping of the 32 h oxidized specimen (**Figure 7.12**) showed that Si, in addition to being present within the layer of Ti_5Si_3, is also within the nanocrystalline oxide

(Layer 3). Within this layer, STEM Z-contrast images after 32 and 64 h of exposure (**Figure 7.11c, 7.12a**) show dark and light regions that could be attributed to mass contrast or voids. Bright field TEM shows that very few voids are observed within the nanocrystalline oxide (**Figure 7.11a, b**); therefore, the dark regions in STEM are attributed to mass contrast from SiO_2 that was present at the interface between the external and internal oxide scales and dispersed throughout the internal oxide layer. STEM imaging (red arrow in **Figure 7.12a**) and higher magnification EDS maps (**Figure 7.13**) of the 32 h oxidized specimen revealed alternating Ti-rich and Si-rich layers in some regions of the nanocrystalline oxide. Considering that O was observed in both Ti-rich and Si-rich areas of the oxygen map, the layers are hypothesized to correspond to TiO_2 and SiO_2, respectively. The layered structure was also observed in the nanocrystalline oxide of the specimens oxidized for 8 (**Figure 7.10d**) and 64 h.

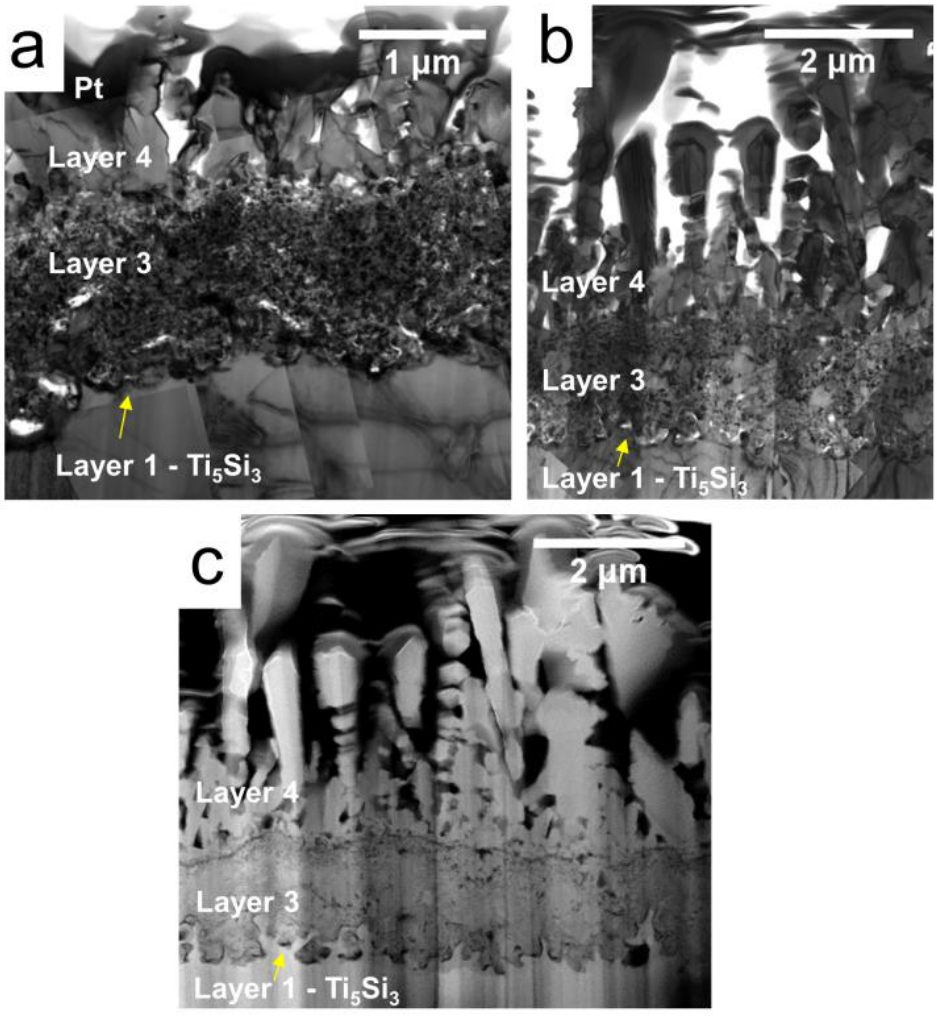

Figure 7.11: Bright field TEM image of the coating and oxide cross section for Si-coated Ti oxidized at 800 °C for (a) 32 h and (b) 64 h. (c) STEM Z-contrast image of Si-coated Ti oxidized at 800 °C for 64 h.

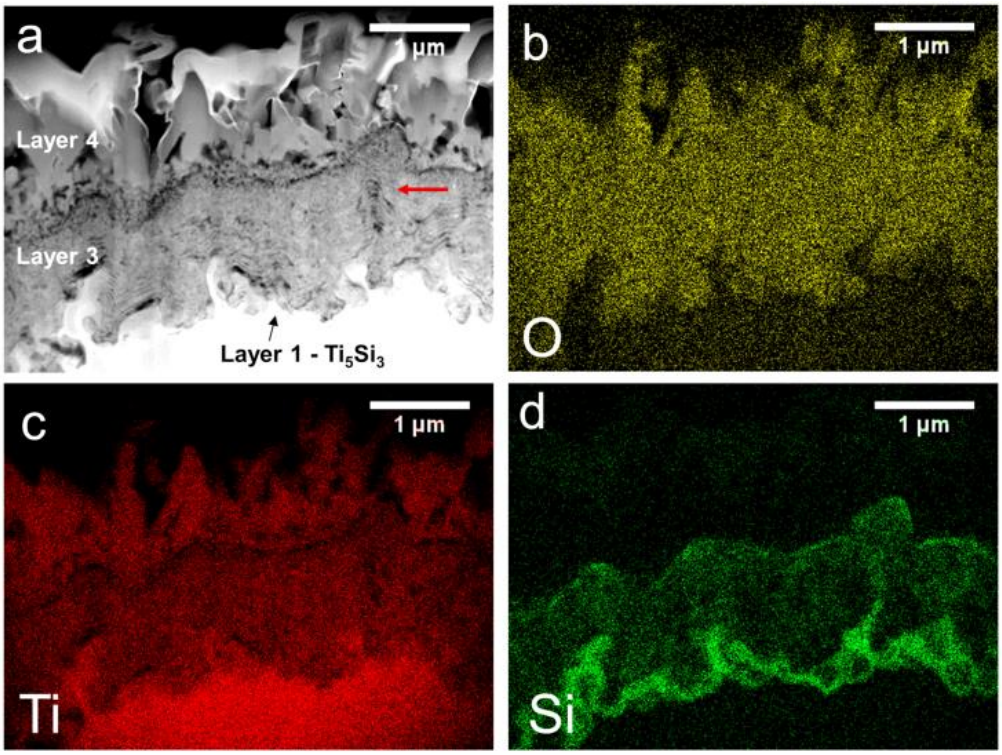

Figure 7.12: (a) STEM Z-contrast image and associated EDS maps for O, Ti, and Si (b-d) of the coating and oxide cross section for Si-coated Ti oxidized at 800 °C for 32 h. Red arrow denotes an example of alternating Ti-rich and Si-rich layers within the internal nanocrystalline oxide scale.

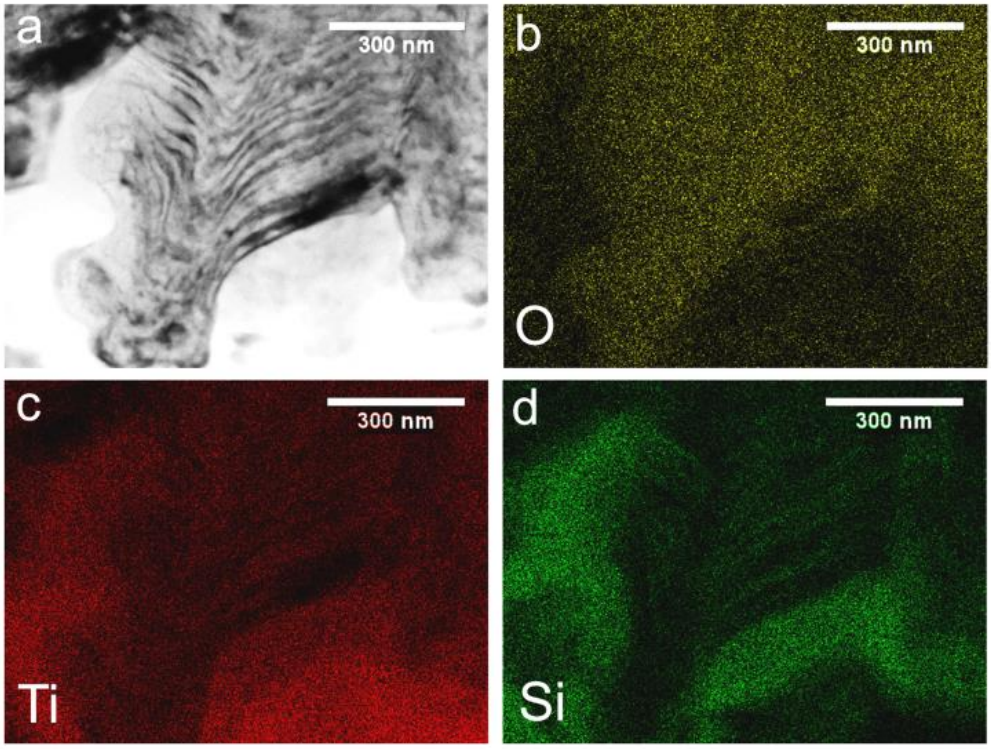

Figure 7.13: (a) STEM Z-contrast image and associated EDS maps for O, Ti, and Si (b-d) of the internal oxide scale for Si-coated Ti oxidized at 800 °C for 32 h showing regular alternating SiO_2 and TiO_2 layers.

7.4 Discussion

7.4.1 Oxide evolution of Pure Ti

The exclusive formation of rutile (TiO_2) in the oxide scale and the absence of other oxide phases that are expected from the equilibrium phase diagram [164] are in agreement with prior oxidation studies for both bulk titanium and thin films [81,165]. The estimated equilibrium parameters for the relevant redox reactions among Ti and its different oxides (**Table 7.1**) reveal that any suboxide that might form initially would readily convert to TiO_2 at $pO_2 > 10^{-26}$ atm, which clearly includes the oxidation environment in these experiments. In principle, one would anticipate that if the scale is dense, adherent and its growth is controlled by the inward diffusion of oxygen, there will be a thickness at which the pO_2 at the oxide/metal interface would be sufficiently low to enable formation of TiO_x with $x < 2$. This scenario, however, is compromised by the evolution of pores and cracks in the scale as it grows, whereupon the gaseous environment has direct access to the metal and the oxidation behavior becomes linear rather than parabolic [75]. In literature, cracking has been observed and attributed to volumetric expansion of the outer metal layer upon O ingress beyond a certain limit ($x \sim 0.35$), whereupon the spalled layer is assumed to oxidize to TiO_x and then to TiO_2 [75]. However, substrate cracking was not observed during the short oxidation time exposures in the present experiments. The more likely explanation for direct access of oxidizing gas to the metal surface is the clear evidence of extensive porosity just above the oxide/metal interface (**Figure 7.2a-c**). Porosity was observed between the outer and inner oxides, presumably at the original metal surface, and in the inner oxide at the oxide/metal interface of pure Ti specimens. Such porosity in the inner oxide has been reported in the literature for binary Ti-W specimens [166]. The present experiments did not provide sufficient insight to elucidate the specific pore formation mechanisms, which will require further investigation.

Table 7.1: Estimated equilibrium standard Gibbs free energies and oxygen partial pressures for Ti redox reactions [167,168].

Reaction	ΔG (kJ mol^{-1}) at 800 °C	log pO_2
$2Ti_3O_5 + O_2 \rightarrow 6TiO_2$	-529.2	-26.1
$6Ti_2O_3 + O_2 \rightarrow 4Ti_3O_5$	-548.6	-28.5
$4TiO + O_2 \rightarrow 2Ti_2O_3$	-719.7	-34.6
$2Ti + O_2 \rightarrow 2TiO$	-868.1	-42.4

The structure of the TiO_2 scale shows an outer and inner layer delineated by porosity. A two-layer scale has been observed in previous studies [75,79] but the underlying mechanisms are still under debate. The oxidation performed on Ti coated with colloidal silica particles (**Figure 7.4**) revealed the SiO_2 particles sandwiched between two oxide layers with characteristics of the outer and inner oxide scales found on the uncoated Ti samples. This strongly suggests that (i) the outer scale grew above the original metal surface, arguably by outward diffusion of Ti, while (ii) the inner oxide evolved underneath the surface maker layer by inward oxygen diffusion.

7.4.2 Oxide evolution of Si-coated Ti

The formation of the Ti_5Si_3 layer and its subsequent effect on the evolved oxide scales are major factors in the improved oxidation resistance of Si-coated Ti compared to uncoated material [169]. As a refractory metal silicide intermetallic, Ti_5Si_3 possesses a high melting point and excellent oxidation resistance at elevated temperatures [170]. Thus, it acts as a slow-oxidizing layer that helps to protect titanium from rapid oxide formation, and indeed the use of Ti_5Si_3 directly as a coating has been shown to improve oxidation resistance of pure Ti [11]. The present experiments demonstrate that a Si layer can also form a protective Ti_5Si_3 layer. The reaction of the Si coating to form Ti_5Si_3 and the evolution of oxide scales are discussed below, and the mechanisms of oxidation are illustrated schematically in **Figure 7.14**.

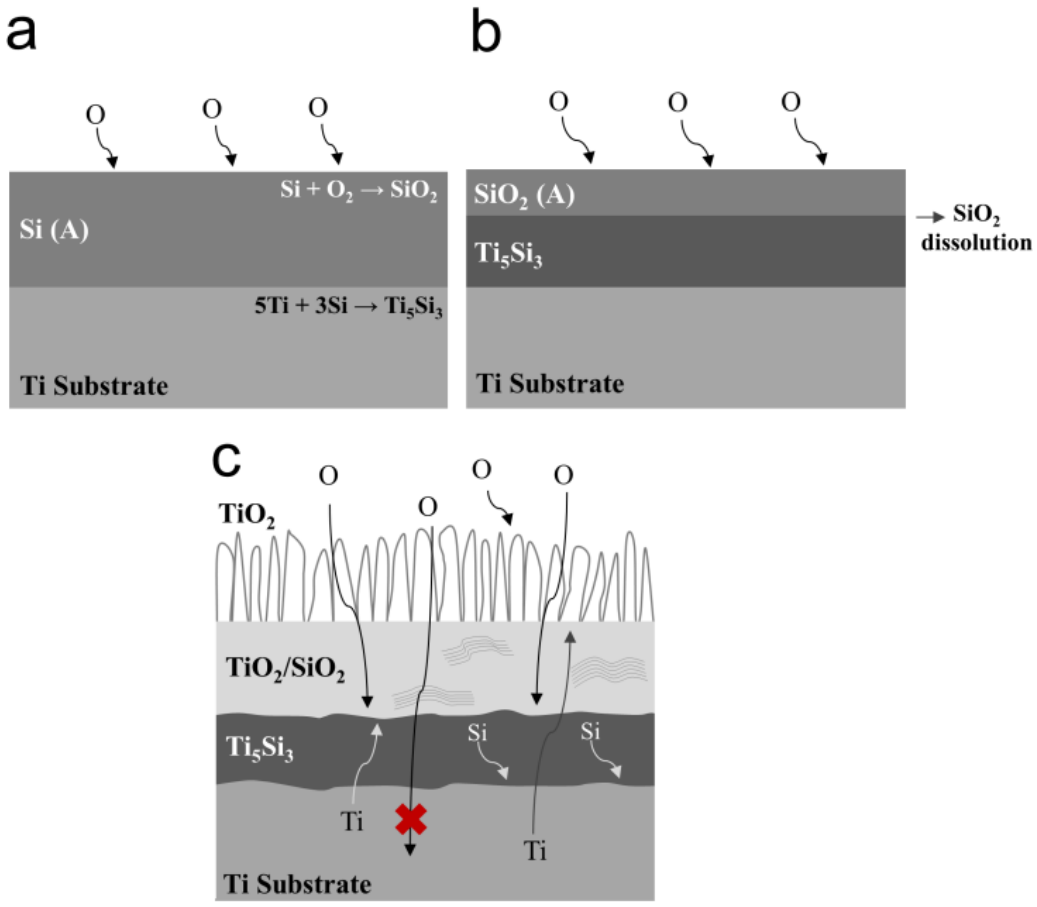

Figure 7.14: Schematic illustration of coating and oxide scale evolution for Si-coated Ti during early oxidation. Please see text for further discussion. (a) Concurrent reaction of the amorphous Si, Si(A), layer to form amorphous SiO_2 and Ti_5Si_3. (b) Amorphous SiO_2, SiO_2(A), dissolution and reaction to form additional Ti_5Si_3. (c) Formation of external rutile TiO_2 scale and internal TiO_2/SiO_2 scale with local regions of alternating TiO_2/SiO_2 layers. Arrow with a red X denotes the inhibition of oxygen inward diffusion into the Ti substrate by the Ti_5Si_3 layer.

The evolution of the coating begins with two concurrent and independent reaction fronts: $5Ti + 3Si \rightarrow Ti_5Si_3$ at the bottom interface of the Si layer and $Si + O_2 \rightarrow SiO_2$ at the top outermost interface (**Figure 7.14a**). The intermetallic silicide phase Ti_5Si_3 is formed by Ti and Si interdiffusion, and fast reaction kinetics between Ti and Si at 800 °C and higher were reported previously [171]. The ternary phase diagram of Ti-Si-O at 800 °C (**Figure 7.15**), extrapolated from previously published phase diagrams [172–177], shows that a two phase region is indeed present between α Ti and Ti_5Si_3(O) and Ti_5Si_3 is the only silicide phase that allows significant oxygen in solid solution. The formation of Ti_5Si_3 and absence of Ti_3Si are also consistent with prior literature results on Ti and Si-containing thin films [178] and with oxygen destabilization of Ti_3Si to favor Ti_5Si_3 [179]. The measured O concentrations in the Ti_5Si_3 layer near the Ti interface and in Ti are indeed non-negligible at 0.6 and ~9 at. %, respectively (**Figure 7.9**). The measured Si

concentration in Ti (0.3 at. %) is in agreement with previously reported Si solubility in Ti [177]. The compositions are reported on the phase diagram for illustration and discussion (**Figure 7.15**), even though interfacial equilibrium may not be realized. At the top of the Ti_5Si_3 layer, SiO_2 is in contact with Ti_5Si_3. The two phases may be at equilibrium (**Figure 7.15**), and the reaction paths avoided all other silicides or metastable titanium oxide phases.

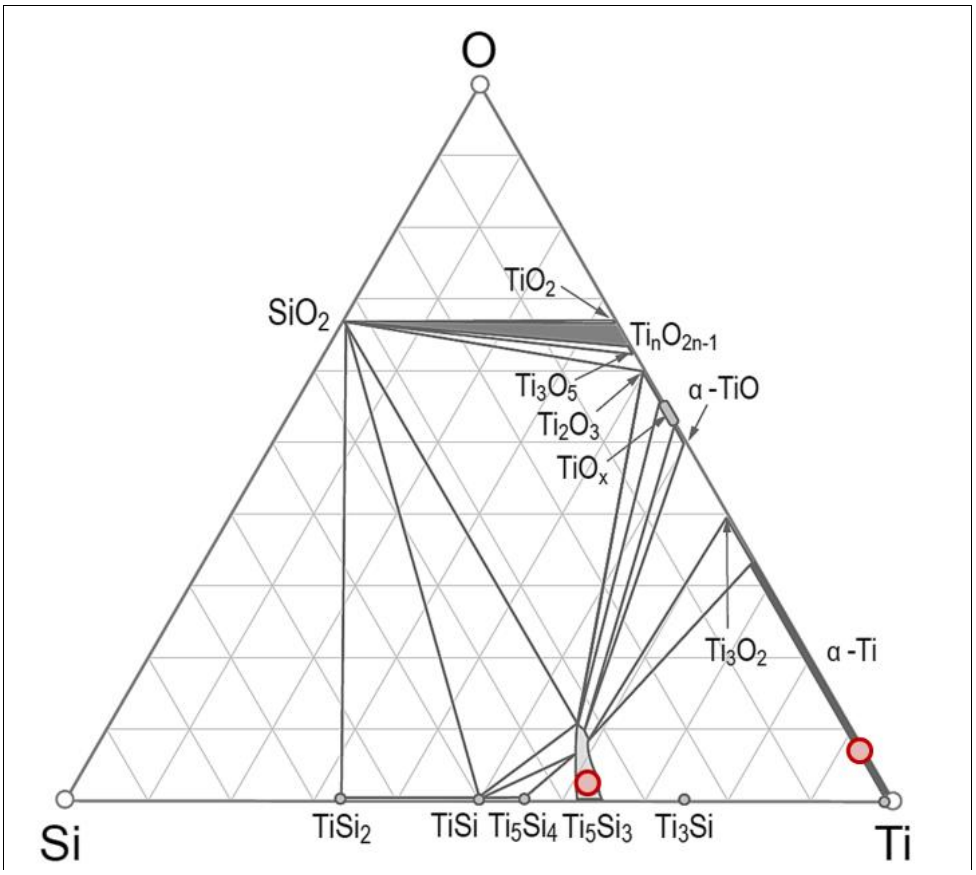

Figure 7.15: The ternary phase diagram in atomic % for Ti-Si-O at 800 °C extrapolated from previously published phase diagrams [172–177]. Red circles denote Ti_5Si_3 and α Ti compositions measured using atom probe tomography for Si-coated Ti specimens oxidized at 800 °C for 2 h.

Delamination and buckling of the amorphous SiO_2 layer, which was observed in some areas of the coating after 2 and 8 hours, may be attributed to the generation of stresses that affected the mechanical stability of the SiO_2 and Ti_5Si_3 layers. These stresses were relieved through decohesion at the interface between amorphous SiO_2 and Ti_5Si_3 and outward bowing of the more compliant SiO_2 layer (**Figure 7.6**). The observed decohesion and buckling morphologies are similar to those reported for the oxide buckling failure mechanism of protective oxide layers with a weak interface [180]. The generated stresses in the present system presumably arose from volume change during Si oxidation and/or thermal expansion mismatch between SiO_2, Ti_5Si_3, and the Ti

substrate upon cooling. A set of complementary experiments where 250 nm of amorphous SiO_2 was deposited on pure Ti and then oxidized for 2 h at 800 °C revealed that SiO_2-coated specimens showed limited delamination and no buckling (**Figure IV.2** in **Appendix IV**). Therefore, compressive stresses generated from the significant volume change during Si oxidation to SiO_2, rather than thermal stresses, are more likely to have played a role [181]. Moreover, relaxation through viscous flow of SiO_2 is reportedly not significant at the oxidation temperature of 800 °C [182].

With exception of the buckled locations, the amorphous SiO_2 layer in contact with the Ti_5Si_3 layer was unstable and reacted with Ti, diffusing outward from the substrate through the silicide, to form additional Ti_5Si_3. Such reaction had been previously observed during vacuum annealing of Ti films on SiO_2 substrates in the same temperature range yielding Ti_5Si_3 as the stable silicide product [183], and interpreted as dissociation of SiO_2, oxygen diffusion into the Ti film, and Ti and Si reaction to form Ti_5Si_3. This reaction was also confirmed here to take place in oxygen-rich environments for the amorphous SiO_2-coated Ti specimens oxidized for 2 h at 800 °C, and the silicide reaction product that formed was identified as Ti_5Si_3 (**Figure IV.1** in **Appendix IV**). For the samples originally coated with amorphous Si, once the adherent and amorphous SiO_2 layer was fully depleted, formation of an external rutile TiO_2 scale resulting from the upward diffusion of Ti through the silicide layer ensued. In locations where amorphous SiO_2 was buckled, outward growing TiO_2 nanocrystals were observed at earlier times (**Figure 7.6a**), presumably accelerated by the absence of the SiO_2 phase in contact with Ti_5Si_3 allowing for Ti to react with gaseous O_2.

Oxidation of Ti and Ti alloys generally involves outward scale growth [75,79,169]. Similarly, in the case of Si-coated Ti presented here, the growth of TiO_2 crystals on the surface with increasing exposure time required significant outward diffusion of Ti through the Ti_5Si_3 layer. Short exposures of pure Ti created dense coarse grained TiO_2 external scales (**Figure 7.2**). However, the outer scale is neither fully dense nor compact for Si-coated Ti, and is formed of individual separated TiO_2 crystals (**Figure 7.11b**). Since the externally growing scale is controlled by the outward flux of Ti, we speculate that the presence of the Ti_5Si_3 layer reduces the magnitude of the Ti outward flux, and that a change in the outward Ti flux influences the shape and morphology of the outward growing external oxide (**Figure 7.5h**). Prior work has shown that the nature of the oxidizing environment can affect the morphology of TiO_2. Under high oxygen partial

pressure in Ar, a dense scale forms on pure Ti [169], while nanowires were observed on pure Ti and Ti alloys under low oxygen partial pressure in Ar [184,185]. Additionally, the chemistry of the oxidizing gas strongly influences the morphology of the scale and characteristics of the TiO_2 nanowires [186,187]. Therefore, the use of a coating to control the outward Ti flux may offer another possible method to control TiO_2 nanostructure shape, but further work is required to understand the influence of Ti flux on the growth behavior and morphology of TiO_2 nanocrystals. The findings could apply to controlling the geometry of 1-D TiO_2 nanostructures that are of interest for applications such as chemical sensing, photo catalysis, photovoltaics [188,189], biosensors [190], and cell adhesion on biomedical implants [185,191].

Concurrently to growth of the external TiO_2 scale, the Ti_5Si_3 layer oxidizes by inward diffusion of O through the thickening internal oxide scale. The relative thermodynamic stability of Ti and Si assessed from standard Gibbs free energies of formation for the respective oxidation reactions suggests that TiO_2 is slightly more stable than SiO_2 at oxygen unit activity [192,193]. Therefore, it is conceivable that at the outermost interface of the Ti_5Si_3 layer, oxidation initially proceeds with that of Ti, leading to a local enrichment of Si. According to the ternary phase diagram, an excess of Si would then promote equilibrium between Ti_5Si_3 and SiO_2 and therefore the oxidation of Si in Ti_5Si_3 rather than Ti_5Si_3 and Ti oxide. This is in part consistent with prior observations of oxidized bulk Ti_5Si_3 that exhibited a dual scale: outer TiO_2 and inner SiO_2-rich [192,193] as well as the formation of continuous SiO_2 for non-stoichiometric, Si-rich Ti_5Si_3 [193]. However, it is also evident that the oxidation of the present silicide layer on Ti proceeds in a more complex manner than the formation of a single oxide or dual oxide scale. Oxidation of bulk Ti_5Si_3 under identical conditions leads to a 100-200 nm thin mixed nanocrystalline TiO_2/SiO_2 internal oxide scale (**Figure IV.3** in **Appendix IV**), while the internal oxide scale resulting from oxidation of the Ti_5Si_3 layer on Ti is significantly thicker (approximately 1.3-1.5 μm). Moreover, regular patterning of thin TiO_2 and SiO_2 layers formed in some areas (**Figure 7.13**), while in other areas a more mixed TiO_2 and SiO_2 nanocrystalline structure developed (**Figure 7.12**). It is conceivable that the composition of the top silicide interface alternates between being Ti-rich and Si-rich leading to the alternating formation of two equilibrium oxides: TiO_2 and SiO_2 respectively. We further hypothesize that in the case of the Ti_5Si_3 layer on Ti, Ti and Si diffusion through the silicide layer is linked to the oxide morphology and apparent accelerated oxidation of the Ti_5Si_3 layer. Such diffusion is limited in the case of bulk Ti_5Si_3. Outward diffusion of Ti, already discussed

above, may contribute to TiO_2 formation in the inner scale. Furthermore, the continued formation of Ti_5Si_3 at the Ti interface suggests that the excess Si resulting from the oxidation of Ti at the top silicide interface is not only consumed by subsequent oxidation and SiO_2 formation, but also by inward diffusion through the silicide layer and reaction with Ti to form silicide at the Ti interface (**Figure 7.14c**), which prolongs the effective thickness and effect of the silicide layer. In general, the Ti_5Si_3 layer evolved during the early stages of oxidation for Si-coated pure Ti specimens inhibited inward oxygen diffusion and the amount of oxygen ingress in the base Ti metal, which controls oxidation progression at longer exposures [81]. Indeed, the measured oxygen concentration in Ti at the silicide interface is ~9 at. %, and is significantly smaller than the maximum solubility of O in α Ti. In addition, the silicide layer persisted up to 64 h of oxidation even though only a thin 250 nm layer of Si was initially deposited, which demonstrates the extended influence of the silicide layer.

Compared to uncoated Ti oxidized in the same conditions (**Figure 7.2**), the morphology of the internally growing oxide scale for Si-coated Ti exhibited a denser scale with fewer voids and nanocrystalline grain size that continued over longer exposures (**Figure 7.11**), which is in agreement with prior literature [11,83,88]. These coated morphologies were ascribed to both the formation of SiO_2 [83,194] and Si in solid solution within TiO_2 [11,88]. In the present work, SiO_2 grains and layers were identified in the internal oxide layer, and it is hypothesized that SiO_2 contributes to pinning of TiO_2 grain boundaries thereby constraining grain growth and leading to the fine grain size of the oxide scale. Further evidence of the role of SiO_2 on the resulting TiO_2 grain morphology and size is given by the oxidation of SiO_2-coated Ti specimens for 32 h (**Figure IV.4, IV.5** in **Appendix IV**). There, the different morphologies observed in the inward growing oxide correlated with the presence of Si detected through EDS mapping. At locations where SiO_2 was present, the internal oxide was nanocrystalline and compact with few voids. However, where Si was not detected, presumably corresponding to the complete oxidation of Ti_5Si_3, the internal oxide comprised only of TiO_2 was coarse grained and porous at the oxide/metal interface.

Reduced growth kinetics and improved oxidation resistance for Ti alloys with Si-containing coatings have been linked to Ti_5Si_3 formation [83,87,88], but other titanium silicide phases including Ti_5Si_4, TiSi, and $TiSi_2$ have also been identified [12,85,90]. The formation and stability of titanium silicide phases and oxide scales may be influenced by the addition of other elements such as Al in the coating or alloy chemistry [4,195]. The reduced kinetics and improved

oxidation resistance observed with other silicides suggest the mechanisms reported here may extend to other titanium silicide phases. There is little data available for the direct oxidation of Ti_5Si_4 and TiSi compounds, but oxidation studies of $TiSi_2$ have revealed that a scale consisting of SiO_2 with TiO_2 precipitates or mixed TiO_2/SiO_2 will form depending on oxidation temperature and environment [196,197]. Furthermore, the performance of Si-containing coatings that form Ti_5Si_3 may be further improved through doping with elements such as carbon [193,198]. In general, the formation of Ti_5Si_3 during oxidation of Si-containing coatings significantly contributes to oxidation mechanisms resulting in reduced scale formation and increased protection of titanium metal.

7.5 Conclusions

The oxidation behavior of pure Ti and Si-coated Ti at 800 °C was investigated to understand the mechanisms leading to the improvement in oxidation resistance for Si-containing coatings on titanium alloys. The following conclusions have been drawn:

- A two-layer oxide scale for pure Ti was observed showing a compact, columnar outer scale and porous, equiaxed inner scale. Marker studies reveal that diffusion of oxygen and titanium both contribute to early stage titanium oxide growth, with Ti outward diffusion forming the dense outer oxide layer external to the original metal surface and O inward diffusion forming the porous inner layer.
- The pure Si coating deposited on the Ti substrate reacted to form a bi-layer structure consisting of SiO_2 and Ti_5Si_3.
- Upon further exposure, an external TiO_2 scale developed with nano-wedge shaped crystals. This outer scale required outward flux of Ti from the substrate through the Ti_5Si_3 layer. The flux for outward Ti may control the morphology and grain structure of the external TiO_2 scale.
- The internal oxide scale, which was formed by inward oxidation of Ti_5Si_3, was nanocrystalline, compact, and consisted of both TiO_2 and SiO_2. In some regions of the internal oxide scale, oxidation proceeded by regular formation of alternating SiO_2 and TiO_2 layers.

- The excess Si resulting from the oxidation of Ti in the Ti_5Si_3 layer diffused inward through the silicide layer and reacted with the Ti substrate to form additional Ti_5Si_3, allowing the silicide layer to be maintained up to 64 h of oxidation exposure.
- While allowing fast Ti and Si transport, Ti_5Si_3 significantly slowed the inward diffusion of oxygen, preventing fast growth of an internal TiO_2 layer, and therefore acted as an oxygen diffusion inhibitor.
- The silicide phase only retarded the onset of internal oxide formation. Once Ti_5Si_3 was no longer present at the oxide/Ti interface, the diffusion hindrance of O was lost, resulting in accelerated oxide growth that was coarse grained and porous.
- Oxidation of the silicide layer proceeded differently than that of bulk Ti_5Si_3, which showed a thinner mixed TiO_2/SiO_2 internal scale and did not form regularly alternating SiO_2 and TiO_2 layers. Thus, oxidation investigations of the silicide alone are not sufficient to understand the more complex interactions that occur between the coating and substrate. The present results demonstrate that the system consisting of Ti_5Si_3 and Ti must be investigated in order to understand the role of the silicide during titanium oxidation.

Chapter 8: Summary and Future Directions

Oxygen's effect on titanium alloys as an interstitial alloying element has been extensively studied in metastable β Ti alloys, but prior evaluations have lacked a systematic focus on oxygen in relation to the metastable ω phase. The ω phase remains scientifically and commercially relevant for Ti alloys due to its importance in influencing phase stability and precipitation of the stable α phase, as well as controlling deformation behavior and mechanical properties. This dissertation work presents a comprehensive investigation of oxygen as an alloying element in aged metastable β Ti alloys that focuses on ω and α precipitation with varying oxygen content. Alloy compositions that were evaluated spanned several relevant model and commercially produced β Ti systems including Ti-Nb, Ti-Mo, and Ti-V containing compositions. A high temperature oxidation exposure was used to create an oxygen concentration gradient for efficient evaluation of compositional effects during subsequent ageing studies. This work focused on evaluation of microstructural evolution and mechanical properties using multi-scale characterization methods including SEM, TEM, APT, and WDS as well as micro-scale mechanical testing methods through micropillar compression.

The study of ω and α phase transformations with oxygen in Ti-20Nb highlighted microstructural changes for ω with elevated O. Specifically, increasing oxygen concentrations yielded smaller ω sizes, increased number density, and a morphology transition from ellipsoidal shapes without oxygen to rod-like precipitate shapes. Oxygen's partitioning behavior to ω during ageing indicated that oxygen acts as an ω stabilizer in β Ti alloys. Furthermore, the precipitation rate of α with continued ageing was directly influenced by oxygen content that changed the nucleation driving force for α. Notably, the slowest α precipitation rate was observed for intermediate levels of oxygen. The effect of these microstructural changes for ω with oxygen on deformation behavior were tested using micropillar compression. Severe embrittlement and ductility losses are known to occur through planar slip localization in ω-enriched metastable β Ti alloys without oxygen. However, Ti-20Nb alloys containing elevated O that were aged such that oxygen partitioned to large ω precipitates showed improved compressive yield strength and work

hardening during micropillar compression testing. Importantly, ω precipitate shearing and the formation of continuous deformation channels were suppressed leading to the observed increases in work hardening and ductility. Two effects contributed to this mechanical response: at these ω sizes, dislocation bypassing becomes feasible during deformation and oxygen partitioning to ω precipitates increased their resistance to shearing. Finally, studies of commercial alloys Ti-15-333 and Ti-15Mo with elevated oxygen revealed similar changes in precipitation and microstructure evolution that directly influenced mechanical properties. In Ti-15-333, oxygen-induced refinement of α precipitates resulted in increased compressive yield strength. This mechanism can be combined with other refinement strategies such as ω-assisted nucleation to obtain very small α precipitates that are desired for high strength. Ti-15Mo with elevated oxygen showed slower growth kinetics for ω than Ti-Nb alloys due to slower Mo diffusion compared to Nb in Ti. In addition, the lower solubility of oxygen in this alloy compared to Ti-20Nb led to lower levels of O partitioning to ω that allowed these precipitates to still be sheared during compression. Similar to Ti-15-333, oxygen-induced α refinement and ω-assisted nucleation in Ti-15Mo led to higher compressive yield strengths. These results demonstrate the beneficial uses for interstitial oxygen in metastable β Ti alloys that contradict conventional wisdom of oxygen as a detrimental alloying element in Ti. In particular, the future development of β Ti alloys that intentionally utilize oxygen opens up new avenues for alloy chemistry, processing, and microstructural design for improved properties. Additionally, relaxing of strict commercial requirements for low oxygen levels in Ti alloys may enable improvements in commercial production such as more tolerable processing control as well as better recyclability and reuse of Ti alloys. The applications of this dissertation thesis therefore impact both our scientific understanding of metallic alloy design as well as industrially relevant alloy production and processing.

This thesis work also investigated the oxidation behavior of pure Ti with a Si coating in order to obtain a systematic understanding of reported improvements in Ti oxidation resistance with complex Si-containing coatings. This model system allowed the observation of Ti_5Si_3 silicide formation during oxidation exposures that effectively inhibited inward oxygen diffusion and prevented the growth of fast growing internal porous oxide scales. However, after the Ti_5Si_3 layer was also consumed through oxidation, the diffusion hindrance of O was lost and the resulting internal oxide was once again coarse and porous. These microstructural observations provide

insight on the mechanistic role of Si during Ti oxidation that may enable additional coating and alloy design.

The insights gained through the present results offer viable pathways for utilizing oxygen as an alloying element in metastable β Ti alloy compositions and enabling microstructural changes that directly affect mechanical behavior. However, this work primarily focused on local microstructural regions with varying oxygen content tested using micromechanical methods. Mechanical testing of bulk metastable β Ti alloys with constant elevated oxygen content is required in order to confirm results presented in this thesis work. Furthermore, several observations that were seen during this dissertation work resulted in additional unaddressed scientific questions due to limitations in material, equipment, or time. Therefore, the following sections discuss relevant open questions and future directions from this work.

8.1 Bulk mechanical testing of β Ti alloys with elevated oxygen

The elevated oxygen levels for β Ti alloys investigated in this dissertation were obtained through an oxidation exposure that produced varying local microstructures related to the created oxygen concentration gradient in the β Ti matrix. These heterogeneous microstructures necessitated the use of micromechanical testing to evaluate mechanical properties, but bulk tensile testing of homogeneous β Ti alloys with constant elevated oxygen content is also needed for further application of these materials to commercially relevant products. Directly adding small quantities of Ti oxides during alloy melting have been used to obtain bulk alloy compositions with up to ~3 at. % O [7], which would then enable bulk tensile testing to confirm the reported microstructure and deformation changes. Bulk tensile testing of polycrystalline specimens with homogeneous Ti alloy compositions containing elevated oxygen would also allow the investigation of possible oxygen segregation to grain boundaries that may affect mechanical properties and previously reported β phase embrittlement with high O levels [5]. Furthermore, bulk mechanical testing of fracture toughness and fatigue behavior are also highly relevant for structural applications [48], particularly since lifetimes of structural components are driven by fatigue crack initiation and growth. Therefore, improvements in deformation behavior and properties with oxygen-stabilized ω and oxygen-induced α refinement demonstrated in this work may need to be characterized for fracture toughness and fatigue properties depending on specific applications.

8.2 ω precipitate shape changes with elevated oxygen

Several ω precipitate morphology changes were observed for Ti-Nb and Ti-Mo alloys in this thesis work with elevated oxygen levels. Ti-Nb and Ti-Mo, which are known to be low misfit β Ti systems, typically produce ellipsoidal ω shapes [19], but high oxygen compositions showed elongated rod-like shapes for Ti-Nb (**Chapter 3**) and faceted cuboidal morphologies for Ti-Mo (**Chapter 6**). These changes are likely linked to oxygen's partitioning behavior and possible misfit strains generated from interstitial oxygen. Cuboidal ω precipitate shapes are commonly reported for high misfit Ti-V systems [15], providing evidence that misfit strains may drive ω shape changes. One avenue for further investigation of ω shape changes would be understanding the lattice changes of ω with oxygen. High resolution characterization of the ω lattice may enable direct measurements of lattice changes with partitioned oxygen as well as the investigation of possible oxygen clustering or ordering in preferred interstitial or substitutional lattice sites of ω precipitates. The generation of misfit strains from elevated oxygen contents could also be investigated using density functional theory calculations that determine the energetically favorable structures for ω with high oxygen content. These calculations would be able to inform phase field models to predict equilibrium shapes of ω precipitates in Ti systems using similar methods demonstrated for γ/γ' microstructures in cobalt-based alloys [162]. Such investigations may reveal interesting and useful knowledge on tailoring precipitate morphology evolution with the inclusion of interstitial elements such as oxygen that may influence structural properties with different ω shapes. The degree of misfit may also affect the stability of ω at higher temperatures, with low misfit systems reportedly showing ω that is stable for higher temperatures and longer times than high misfit systems [31]. Therefore, interstitial elements that influence misfit may potentially allow for tuning of ω stability relevant for strength and work-hardening improvements with oxygen-stabilized ω precipitation discussed in **Chapter 4** and **Chapter 6**.

8.3 Effect of nitrogen on phase stability in β Ti alloys and on oxide growth kinetics of Si-coated Ti

As with oxygen, interstitial nitrogen is a strong α phase stabilizer in Ti alloys, and nitrogen shows high solubility in α and β phases before forming titanium nitride phases [199]. Within β Ti alloys, higher levels of interstitial N also affect phase stability that may influence mechanical

properties. For example, N has been shown to decrease the martensite start temperature in a Ti-Nb-Zr-Ta alloy resulting in superelasticity at room temperatures [200]. Additionally, laser deposition of a Ti-Mo alloy in a nitrogen-rich environment formed α with partitioned N that provided strengthening evaluated using microhardness measurements [201]. Given nitrogen's stabilization and reported partitioning to α, it is reasonable to hypothesize that N may allow for similar mechanisms as those reported in this thesis work on oxygen-stabilization of ω precipitates (**Chapter 4**) and oxygen-induced α refinement (**Chapter 5**). Therefore, similar investigations of elevated nitrogen levels may yield complementary knowledge on nitrogen's effect on metastable β Ti alloys. These studies may include the use of high temperature nitridation exposures to produce an N concentration gradient, which can then be utilized to understand the effect of N on ω and α phase stability and precipitation during subsequent ageing of β Ti alloys. Depending on these results, similar experiments using micropillar compression could be conducted on N-rich and N-free microstructures to obtain preliminary results on the deformation mechanisms with elevated nitrogen. The understanding of both oxygen and nitrogen as alloying elements would provide synergistic understanding of interstitial element inclusions in β titanium alloys.

Understanding the effect of nitrogen on oxide scale growth of Si-coated Ti is relevant for commercial applications of silicon-containing coatings. N accounts for roughly 80% of air atmospheres, and during oxidation, nitrogen is known to reduce the oxidation rate of titanium alloys [202]. The presence of nitrogen results in a thinner and more compact oxide scale with a smaller amount of dissolved oxygen in the metal substrate [203]. The results in **Chapter 7** showed that Si-coated Ti in argon-oxygen atmospheres also reduced oxygen ingress through the formation of Ti_5Si_3 that acted as an oxygen diffusion barrier, but this effect was lost when the silicide layer was fully oxidized. Since N also reduces the amount of oxygen ingress, oxidation studies of Si-coated Ti in oxygen-nitrogen (synthetic air) atmospheres may show slower oxidation and breakdown of the silicide layer resulting in longer protection of Ti alloys. Furthermore, understanding possible effects of N on outward growing oxide scales that dominate for Si-coated Ti may allow for additional opportunities to reduce the oxide growth rate. Although Si-based coatings have shown improvements in air oxidation resistance for Ti alloys compared to uncoated material [11,88], the complex chemistries, deposition parameters, and resulting microstructures of these coatings have prevented a holistic understanding of the effect of N. Investigating specific oxidation mechanisms in nitrogen-containing atmospheres using model systems for Si-coated Ti

would provide a more comprehensive and nuanced understanding of these coatings during air oxidation relevant for industrial applications.

8.4 Future structural alloy design utilizing interstitial oxygen

Titanium alloy design has typically focused on compositions with minimal interstitial elements due to conventional knowledge of detrimental effects with elevated oxygen and/or nitrogen. Although recent development of metastable β Ti alloys employ high oxygen levels, these alloys are frequently processed with solution treatment and quenching to retain the metastable β state that enables novel deformation behaviors [7,59,61,98]. The results in this thesis work have provided evidence for beneficial effects of high oxygen content in aged microstructures particularly containing ω and α phases. With these mechanisms, new titanium alloys and processing treatments that utilize these effects of elevated oxygen may open up new microstructures and design spaces that enable desirable properties. Particular efforts may focus on developing metastable β Ti alloy compositions that allow high solubility of dissolved oxygen contents prior to the stabilization and precipitation of α. Furthermore, this knowledge may allow for better understanding of the effects of oxygen impurities in β Ti alloys that could relax the current stringent requirements for oxygen in industrial materials specifications. Finally, tangential areas that may benefit from this thesis work include the understanding of oxygen influence in other related product forms and alloy systems. These areas may include oxygen pickup in titanium alloy powders used in additive manufacturing and/or powder metallurgy. Other relevant alloy systems that may utilize these findings include ω-forming Zr alloys [19] as well as refractory-based high entropy alloys that frequently include Ti, Nb, and Mo elements and have also shown notable oxygen-induced phase stability changes [204]. Ultimately, these approaches may result in new alloys and processing methods that intentionally utilize interstitial oxygen or other interstitial elements to enable beneficial properties.

Appendices

Appendix I: Sample Preparation

I.1 Heat treatment of Ti samples

- Ti samples of interest were cut using a slow speed diamond saw to the correct dimensions and cleaned by ultrasonicating sequentially with tap water, acetone, and methanol for 2-3 minutes each. Specimens were then wrapped in pure Ti foil and encapsulated in a quartz tube backfilled with Ar gas along with 3-4 pure Ti granules. The Ti foil and granules were included to act as getters for any remaining oxygen present in the sealed tube so the oxygen would not be absorbed by samples of interest during heat treatment.
- Encapsulated samples were placed in a box furnace for ageing treatments (200-600 °C) or the vertical quench furnace for high temperature solution treatment (1000 °C). The furnace was preheated for about one hour prior to sample insertion such that the encapsulated sample was immediately exposed to the correct heat treatment temperature. After the required heat treatment time, encapsulated samples were removed from the furnace and quenched directly into a 5 gallon bucket filled partially with tap water. The encapsulated tube was then immediately broken into the water in the bucket using a heavy tool to fully quench the sample.

I.2 Oxidation exposures

- One side of Ti samples for oxidation exposure was polished by hand with alumina (Al_2O_3) grinding papers. Polishing was done successively with 30, 12, 9, 3, 1 μm papers, rinsing and ultrasonicating with tap water for 1-2 minutes between steps.
- The gas environment for the tube furnace is controlled using a flow controller and can flow mixtures of argon, oxygen, and nitrogen.
- To operate the tube furnace, open the gas cylinder and gas lines for gases that will be used for the exposure. Turn on the MKS 946 vacuum system flow controller to set gas flow. The

A1 channel is for argon gas and the B1 channel is for oxygen gas, and you can toggle between these channels using the up/down arrows. The green light indicates the active channel that you are changing. Set flow controller for each gas by pushing “Channel Setup”, which will bring you to the setup screen for the gas. Move cursor to “OP mode” for “Operation Mode”, push enter, and use up/down arrows to change from “close” to “set point”, and then push enter to save. Then change the “FlowRate SP” for Flow Rate Set Point to your intended gas flow rate, and then push enter to save it. Purge the system by setting the argon gas flow to 40 SCCM flow rate. Bubbles should be seen in the oil at the right end of the tube furnace glass column set-up when gas is flowing. Set “OP mode” to “close” to stop argon flow. Push “esc” to go back to the main screen of the flow controller.

- Place sample in the tube furnace by opening the glass tube and removing the glass specimen holder (on a long arm). Place sample(s) in an Al_2O_3 crucible, and place crucible in the specimen holder. Insert the glass specimen holder with the crucible and samples back into the glass tube, with the sample/crucible side pointing into the tube. You can move the specimen holder in the glass tube by using a magnet on the outside of the glass tube that attracts the black magnet in the specimen holder (opposite end as the sample/crucible). Close the glass tube by spreading a thin layer of vacuum grease evenly on the connection point and connect the two pieces together again such that the tube is fully sealed. Move the specimen holder with the crucible and sample to the center of the hot zone of the furnace (near end of the thermocouple in the glass tube of the furnace) using the magnet. Mark the specimen holder position on the glass tube to know where to move it to when the furnace lid is closed. Move specimen holder out of the hot zone of the furnace into the long glass tube portion outside the furnace so the crucible and samples will not be heated as furnace ramps to correct temperature. Close furnace lid and lock.
- Set argon flow rate back to 40 SCCM and set “OP mode” from “close” to “set point” to purge while heating furnace to the exposure temperature. Turn on Lindberg Blue M tube furnace and program set point to correct temperature. Press and hold “set/ent” button. Once it changes to “Node – res” (default option), then push “set/ent” once to change to Prg (program), and change this from 0 to 1 by pushing up arrow. Press “set/ent” to save. Press and hold “set/ent” button again, then push “set/ent” button repeatedly to cycle through parameters until you get to “A1”. Change A1 to 10-20° higher than your intended exposure

temperature. This is the upper maximum temperature that the furnace will allow as an emergency precaution. Press “set/ent” to save. Press and hold “set/ent” again to get back to the temperature reading of the furnace.

- Set the set point of the furnace. Press and hold “set/ent”. Push up and down arrows until “Node” reads “LCL” to set the local set point. Press “set/ent”. Push up and down arrows to change set point temperature to intended exposure temperature. Push “set/ent” to save. Furnace will make a loud clicking sound to indicate it is turning on and starting to ramp the temperature.
- Allow the furnace temperature to ramp and stabilize to correct exposure temperature. Monitor the temperature with the thermocouple and adjust the local set point so the correct temperature is reached, press “set/ent” to save new set point. The furnace set point will most likely need to be adjusted according to the thermocouple reading since it may overshoot or undershoot the temperature. The furnace should take about 20-30 minutes to stabilize temperature.
- Insert the specimen holder with the crucible and sample into the hot zone of the furnace using the magnet to move to the marker previously made on the glass tube. Allow temperature to equilibrate again to correct exposure temperature (about 10-15 minutes).
- Open oxygen cylinder and gas lines if not already opened. Change argon flow rate to 4 SCCM (4.0×10^0 on controller) by changing “FlowRate SP” on flow controller. Go back to start menu by pushing “esc”. Push down arrow to “B1” for oxygen. Set up channel by pushing “Channel Setup” and change oxygen flow rate using “FlowRate SP” to 1 SCCM. Open oxygen gas flow to set point by going to “OP mode” and changing from closed to “set point”. Press enter to start oxygen flow at set point flow rate.
- Keep furnace on with correct controlled environment/gas flow for intended exposure time. To end exposure, stop oxygen gas flow by changing “OP mode” to “close”, then close oxygen valves and gas cylinder. Change Ar gas flow back to 40 SCCM by changing the “FlowRate SP” to purge with Ar during sample cooling. Move specimen holder with crucible and sample out of the hot zone of the furnace into long glass tube region using magnet so sample is no longer being heated. Turn off furnace. Wait until furnace is cooled, then change Ar flow to closed by changing “OP mode” to close, closing Ar gas cylinder and valves, and turning off flow controller. Open glass tube and remove sample.

I.3 Mounting and polishing β Ti samples

- As-received and heat treated samples were cut using a slow speed diamond saw into small pieces and mounted in cold mounting epoxy. Red 1.25" diameter mold cups were used to mount the titanium specimens in epoxy, which were coated with a mold release agent before putting in specimens and epoxy. The region of interest for microstructural characterization was placed face down in the mold cup so that it would be exposed from the mount after subsequent grinding and polishing. After pouring the epoxy, mold cups were left to cure and harden overnight in the fume hood. After full hardening, mounted samples in epoxy were removed from the mold cups.
- Mounted samples were manually ground using the polisher in the Marquis Laboratory using 320, 600, 800, and 1200 grit SiC papers in succession. Polishing using each grit was performed for 2-4 minutes until the sample was planar and scratches from the prior grit paper were fully removed. After each grit paper, specimens were rinsed and ultrasonicated with tap water for 1-2 minutes.
- Final polishing to mirror finish was performed using the Van Vlack Laboratory autopolishers according to **Table I.1**. Polishing was conducted using 0.03 μm colloidal silica solution added directly to the polishing pad during each polishing step, with additional solution added as needed every few minutes while polishing. Additional time was added up to user discretion.

Table I.1: Colloidal silica polishing sequence for titanium samples.

Step	Description	Time (min)	Speed (rpm)	Force (N)
1	Polish with colloidal silica solution	8	200/60, Contra direction	30
2	Polish with colloidal silica solution	4	200/60, Complementary direction	30
3	Polish with colloidal silica solution	8	200/60, Contra direction	30

- Polished specimens were rinsed with tap water immediately after polishing to remove colloidal silica solution, then ultrasonicated sequentially with tap water, acetone, and

methanol for 2-3 minutes each. After cleaning with methanol, the cleaned sample was dried with compressed air. For SEM evaluation, a SEM pin stub was attached to the backside of the epoxy-mounted sample using silver paint. Silver paint was also applied around the edge and top of the mount to touch a corner of the polished sample face so that there was a conductive path between the SEM stub and polished sample to prevent charging. Additional silver paint was applied to the top face of the epoxy mount near the polished sample location to prevent charging in the SEM.

I.4 Wavelength dispersive spectroscopy

- Wavelength dispersive spectroscopy (WDS) characterization was performed at the Robert B. Mitchell Electron Microbeam Analysis Lab (EMAL) located in the North University Building on Central Campus at the University of Michigan.
- Samples for WDS evaluation were mounted, ground, and polished using the same above procedure but did not have silver paint or SEM stubs attached. Some WDS specimens were also mounted in 1" mold cups instead of 1.25".
- Dr. Owen Neill conducted chemistry measurements for WDS characterization.

I.5 Micropillar compression testing

- Samples of interest were first characterized using electron backscatter diffraction (EBSD) to identify suitable grains for micropillar fabrication. EBSD was performed on mounted and polished samples in epoxy.
- Following EBSD characterization, samples were removed from epoxy mounts because mounted samples were too tall for the nanoindentation systems used for micropillar compression. Removing samples from the epoxy mounts was performed by cutting into the epoxy close to the polished sample face using a slow speed diamond saw, then compressing the mount in a vice clamp perpendicular to the cut direction in order to promote cracking along the interface between the sample and epoxy to remove the sample. After cutting into the epoxy, the mounted sample was put in a plastic sealable sandwich bag before compressing with the vice so that the sample would not be lost after cracking of the epoxy. This specimen removal method from epoxy was suggested by Bobby Kerns at the Michigan Center for Materials Characterization (MC^2).

- After the polished sample was successfully removed from epoxy, it was cleaned by ultrasonicating sequentially with acetone and methanol for 2-3 minutes each. The cleaned sample was then attached to an SEM pin stub using silver paint, using enough silver paint so that the specimen was well attached and would not move during micropillar compression in the nanoindenter.
- Fabrication of the micropillars was performed using a focused ion beam in an SEM. Dr. Allen Hunter at MC^2 developed an automated script for pillar fabrication and provided training on micropillar fabrication. FIB ion beam currents were aligned at every session prior to micropillar fabrication to prevent misshapen pillar dimensions due to beams being out of focus or having astigmatism.
- Compression of micropillars was performed using a nanoindentation system. Dr. Haiping Sun at MC^2 provided training on micropillar compression. Compression was performed using the "High Load" mode for the nanoindenter and using a modified HL trapezoidal loading curve. Compression was conducted primarily using the flat end probe, with additional testing using a 50 μm spherical probe. Prior to testing a specific micropillar, nanoindentation with a ~700 nm displacement indent was performed in the bulk material close to the micropillar to identify precise location of the probe for better alignment of the probe to the micropillar.

I.6 Argon ion milling of TEM samples using PIPS

- After fabrication of TEM liftout samples using a focused ion beam in an SEM, focused ion beam damage was removed and cleaned using a Gatan PIPS II instrument with a broad Ar ion beam.
- PIPS milling was conducted according to the procedure available at the Michigan Center for Materials Characterization (MC^2): "SOP for PIPS II Milling of a FIB TEM Sample", The SOP is also included in the following section.

Standard Operating Procedure (SOP) for PIPS II Milling of a FIB TEM Sample

Purpose

1. This SOP provide procedure for Ar ion polishing of a standard FIB lift out sample for TEM analysis. A complete "PIPS II Manual and guide.pdf" is availble on the desk top of the PC next to the instrument.
2. Section 1 and 2 can be skipped if it's already aligned. For daily operation, you can start from section 3.

Instrument

1. Gatan PIPS II Model 695 in $(MC)^2$.

Safety Precautions

1. User must be trained by $(MC)^2$ staff before using this instrument.
2. Do not operate any regulator in the compressed gas cabinet.
3. Handeling liquid nitrogen with care and must ware necessary personal protection equipment if cold stage is used.

Procedures

1. Align center of phosphor screen with center of stage rotation

1.1. Raise the stage by moving the arrow up on the control screen, then press vent to vent the chamber.

1.2. Remove the cover, and place the phosphor screen in the sample stub holder. Replace cover and lower the stage by moving the arrow down on the control screen. This will also pump down the chamber.

1.3. Change the focus of the optical microscope so that the hole in the center of the phosphor screen is in focus. On the alignment tab, press the ***left front*** button, then draw a line starting from a recognizable feature. Press the ***left rear*** button, and then move the opposite end of the line to the same recognizable feature. Press the ***right front*** button, then draw a second line starting from the same recognizable feature, and finally, press the ***right rear*** button, then move the opposite end of the second line to the same recognizable feature. The point of intersection for the two lines should be the **center of stage rotation**.

1.4. Press the ***home*** button on the alignment tab of the control screen. Then draw a **third line** from the center of the hole to the center of rotation. The third line is relative shift between the two centers.

1.5. Raise the stage and vent the chamber. The hole in the phosphor screen will move when the stage is raised, but the relative shift won't change.

1.6. Now move the **third line** (without changing the length or endpoints) so that one endpoint is aligned with a feature, either the center of the hole or any other feature, on the image.

1.7. Using the stage movement screws, physically move the feature from one endpoint to the other endpoint. Be careful not touching the position of optical microscope.

1.8. Replace the cover and lower the stage.

1.9. Check if the center of the hole is aligned with the center of rotation. Repeat steps 3-9 until the center of the hole is aligned with the center of rotation.

2. **Align beam to center of phosphor screen (**manual section 3.10**)**

2.1. **Align beam for left gun top milling** (manual section 3.10.1)**:** Go to the milling tab on the control screen. Follow instructions for aligning the left gun (top milling) and right gun (bottom milling) in section 3.10 of the manual. Perform alignment for top milling using the left gun at +10 and +5 degrees.

2.2. **Align beam for right gun bottom milling** (manual section 3.10.2)**:** Raise stage and vent chamber. Remove the phosphor screen and insert the glass slide sample. Lower stage. Follow instructions for aligning right gun (bottom milling). Perform alignment for bottom milling using the right gun at -10 and -5 degrees.

2.3. Raise stage and vent chamber. Remove glass slide sample.

3. **Milling a TEM lamella that was thinned using FIB (mounted on side of post on Cu grid)**

3.1. Insert the TEM grid with your sample into the sample holder for PIPS II. Clamp in sample such that the flat edge containing the tops of the posts are aligned across the clamping posts. Raise stage and vent chamber. Insert sample holder with TEM grid into the sample stub holder in the chamber. Make sure the flat edge containing the tops of the posts are parallel with the front side of the PIPS II instrument. Replace cover and lower stage.

3.2. Change the focus of the optical microscope so that the TEM sample is in focus. Follow the same steps in the "**Align center of phosphor screen with center of stage rotation**" section to align the TEM FIB sample with the center of rotation.

3.3. PIPS milling on a TEM sample will be doing with the two guns in "Stationary mode" with the sample aligned in the plane of the guns. The sample will be milled using the left gun (top milling) and right gun (bottom milling) in two separate steps for each beam current and voltage combination. Draw a 35 degree line in Digital Micrograph to show the angle at which the left gun will mill from. If the TEM sample is side mounted on the **left** of the finger as shown in (a) for the following figure, on the alignment tab, change the angle to **315** degrees so that the sample is rotated and the beam from the left gun travels at an angle relative to the Cu grid to minimize redeposition on the sample. Draw a -35 degree line in Digital Micrograph to show the angle at which the right gun will mill from. Similarly, change the angle to **65** degrees so that the sample is rotated and the beam from the right gun travels at an angle relative to the Cu grid to minimize redeposition on the sample. If the TEM sample is side mounted on the **right** of the finger as shown in (b) for the following figure, on the alignment tab, change the angle to **295** degrees when milling with left gun, and then change the angle to **45** degrees when milling with right gun.

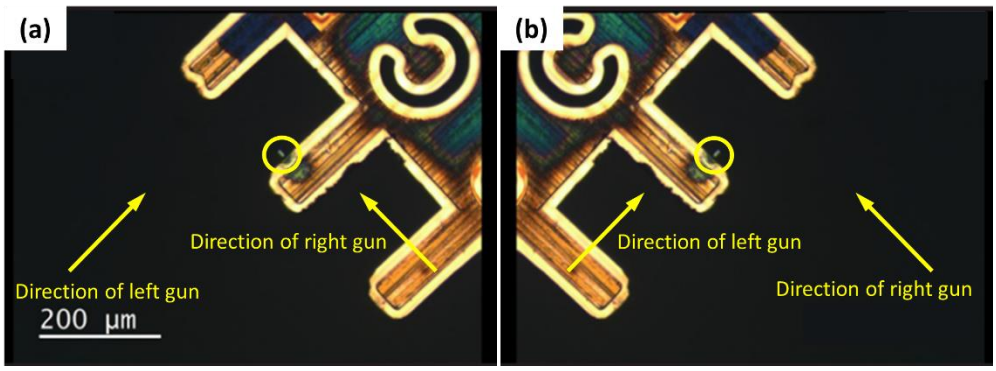

(a) TEM lamella is mounted on the left side of the finger. (b) TEM lamella is mounted on the right side of the finger.

3.4. On the milling tab, choose your beam voltage and milling time. Select "stationary left" for milling mode. This mode will only mill using the left gun, and the sample will not rotate, so it will be stationary in the position that you set.

3.4.1. The gas flow rate, which changes the beam current, can be automatically set using "Automatic gas", or can be set manually by changing to "Manual gas". At low beam voltages (1 kV or lower), more consistent beam current has been achieved using the

Manual gas mode. Some reference gas flow levels and the corresponding beam currents are listed below. These can be adjusted for your specific sample or material, but can be used as a starting suggestion.

3.4.1.1. Left gun: 0.125 SCCM = ~17 µA. Right gun: 0.170 SCCM = ~17 µA

3.4.1.2. When starting milling, the beam current usually will start out high initially (~30 µA), but then drop and stabilize out to a stable beam current.

3.4.2. The milling rate of the PIPS II is high due to the focused Ar beam, therefore since FIB prepared TEM samples are already pre-thinned, it is recommended that milling should start at 500 V and then progress to smaller beam voltages (300 V, 200 V). The 500 V step seems to mill the sample slightly if the sample is still on the thicker side but not too quickly so that the sample is completely milled away. 300 V seems to clean the sample to remove beam damage, but not mill too much of the sample, so this seems to be a good beam voltage for a longer step.

3.4.3. A sample recipe for milling a TEM sample prepared by FIB is below. These are intended to be guidelines, but may need to be adjusted for different materials or different starting thicknesses of the sample after FIB.

3.4.3.1. Ni-based alloy; starting thickness after FIB (last step in FIB – 5 kV cleaning) ~ 250 nm; 1 kV 2 min/side, 500 V 3 min/side, 300 V 3 min/side, 200 V 3 min/side.

3.4.3.2. Ti-based alloy; starting thickness after FIB (last step in FIB – 5 kV cleaning) ~ 150 nm; 500 V 3 min/side, 300 V 8 min/side, 200 V 10 min/side.

3.5. On the alignment tab, change the angle to **315** degrees so that it is aligned and slightly offset from the left gun. Press start to begin your milling cycle. This will mill the top of your sample using the left gun. (Use **295** degree when mounted on the other side of the finger, as mentioned in step 3 in **Milling a TEM lamella that was thinned using FIB**)

3.6. When the cycle is complete, go to the milling tab and select “stationary right” for milling mode. Change the manual gas flow for the right gun if you are using the Manual Gas mode so that the beam current of the right gun matches the beam current that you had for the left gun. Go back to the alignment tab, and change the angle to **65** degrees so that the sample is aligned and slightly offset from the right gun. Press start to begin your milling cycle.

This will mill the bottom of your sample using the right gun using the same parameters as the top of your sample. (Use **45** degree when mounted on the other side of the finger, as mentioned in step 3 in **Milling a TEM lamella that was thinned using FIB**)

3.7. Raise the stage and vent the chamber. Remove your sample from the sample stub holder and take your sample out of the holder.

3.8. Check the condition of the sample using the TEM. Repeat milling steps as needed for your milling recipe.

3.9. For more details, please visit Gatan's website on argon ion polishing of focused ion beam specimens in PIPS II system: http://www.gatan.com/argon-ion-polishing-focused-ion-beam-specimens-pips-ii-system. Additionally, Gatan has a video detailing the steps of using argon ion polishing for FIB samples in PIPS II at this link: https://www.youtube.com/watch?v=3P-_sAOB-bc.

Appendix II: Micropillar Dimension Effects, EBSD Maps, and Supplemental Images From In-Situ Compression Testing for Ti-20Nb

II.1 On the use of micropillar compression testing for comparing deformation behavior of ω-strengthened β Ti alloys

Small-scale mechanical testing methods such as micropillar compression, which was used to investigate deformation behavior of aged Ti-20Nb, are sensitive to local microstructural changes. Given the compositional gradient and resulting microstructural variation of OXA Ti-20Nb specimens (**Chapter 4**), micropillar compression testing was utilized to probe deformation mechanisms of localized regions within samples. Micropillar compression testing may show significant size-related effects based on pillar diameter and size that may influence operative deformation mechanisms and dislocation processes in addition to the obtained mechanical properties [118]. In particular, single crystal and single phase pillars can exhibit size-dependent mechanical behavior from intrinsic mechanisms such as single-arm source theory and dislocation starvation leading to very high measured stresses [205,206]. In contrast, precipitate-strengthened alloys with fine precipitate sizes have shown a much weaker size dependence, where deformation behavior is controlled by internal microstructural length scales that dominate over specimen size effects [119,120]. In general, extrinsic size effects tend to dominate when specimen dimensions are sufficiently larger than dispersed microstructural features and the tested volume contains ample dislocation sources [121]. Under such conditions, small-scale mechanical testing methods yield meaningful yield strength values [121]. In **Chapter 4**, TEM imaging of initial microstructures after ageing for 3 d at 450 °C (**Figure 4.3**) revealed dense distributions of ω phase precipitates with a diameter and spacing of ~50-100 nm. Consequently, micropillars were fabricated with diameters greater than 1 μm in order to better approximate bulk-like properties. The compressive stress-strain curves (**Figure 4.4** and **4.6**) displayed low strain hardening similar to ω-containing bulk materials without oxygen [51,116].

Similar values, curve shapes, and slip band features were observed for 2 and 5 μm diameter pillars, indicating that pillars in this diameter range showed minimal size-related effects for the

tested microstructures. Compressive engineering stress-strain curves up to 20% strain for 2 and 5 μm diameter pillars were plotted to compare influences of probe indenter geometry, micropillar diameter, and specimen conditions. Comparison between stress-strain curves for 2 (**Figure 4.5** and **Figure 4.6a**) and 5 μm (**Figure II.3**) diameter micropillars showed similar trends for DA and OXA specimens with ageing time and oxygen content. Compression of 2 μm diameter pillars using both flat punch and spherical probe indenters also showed good agreement of collected stress-strain data regardless of indenter shape (**Figure II.4**), which indicates probe indenter geometry does not influence relative magnitude and shape of stress-strain curves.

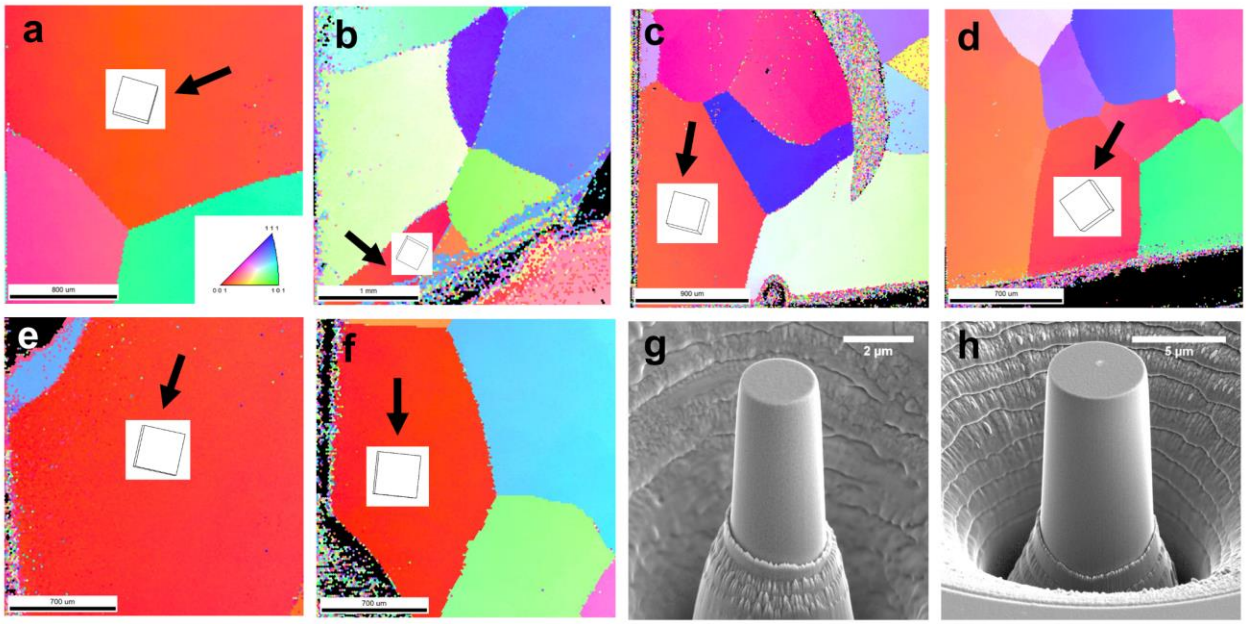

Figure II.1: EBSD inverse pole figure maps and crystal lattice outline for selected grain (black arrow) with crystallographic orientation close to out-of-plane orientation $(100)_{\beta}$ for micropillar fabrication on Ti-20Nb with the following ageing conditions: (a) DA 3 d, 300 °C with 0.1 at. % O, (b) OXA 3 d, 300 °C with an O concentration gradient, (c) DA 3 d, 450 °C with 0.1 at. % O, (d) OXA 3 d, 450 °C with an O concentration gradient, (e) DA 2 h, 450 °C with 0.1 at. % O, (f) OXA 2 h, 450 °C with an O concentration gradient. Representative micropillars fabricated using FIB with a (g) 2 μm and (h) 5 μm diameter.

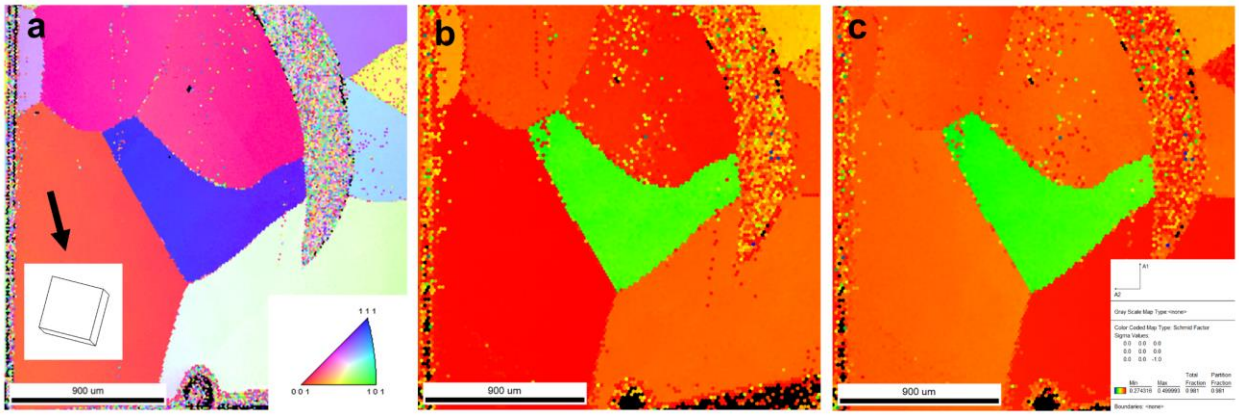

Figure II.2: Calculated Schmid factor value maps based on EBSD IPF map for Ti-20Nb aged for 3 d at 450 °C with 0.1 at. % O. (a) EBSD IPF map. (b) Schmid factor values for (11-2)[111]$_\beta$ slip system. (c) Schmid factor values for (1-10)[111]$_\beta$ slip system.

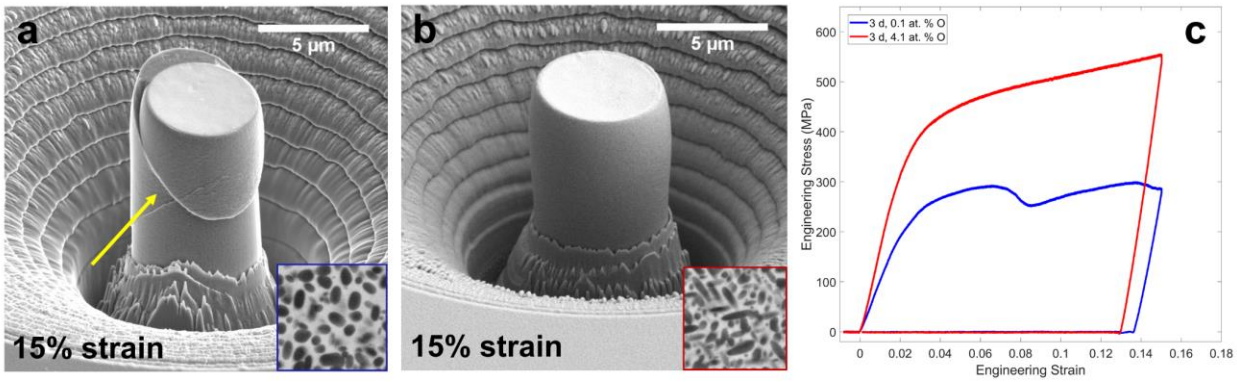

Figure II.3: SEM-BSE images of 5 µm diameter micropillars compressed to 15% engineering strain for Ti-20Nb aged for 3 d at 450 °C with (a) 0.1 at. % O and (b) 4.1 at. % O. Insets show initial microstructure prior to compression. (c) Engineering stress-strain curves for compressed micropillars shown in (a-b).

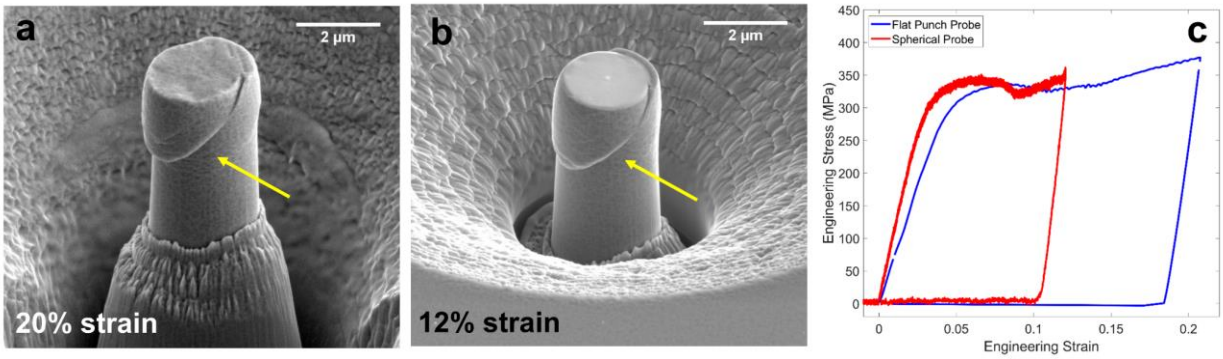

Figure II.4: SEM-BSE images of compressed micropillars for Ti-20Nb aged for 3 d at 450 °C with 0.1 at. % O tested using (a) flat punch and (b) spherical probe geometries for compression. (c) Engineering stress-strain curves for compressed micropillars in (a-b).

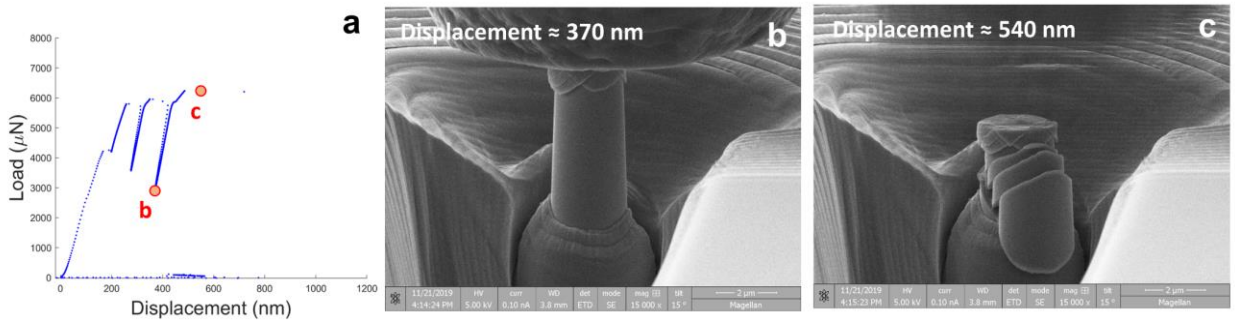

Figure II.5: (a) Load versus displacement data collected during in-situ testing of a 2 µm diameter micropillar for Ti-20Nb aged for 3 d at 300 °C with 0.1 at. % O. SEM images of pillar after (b) 370 nm and (c) 540 nm of displacement.

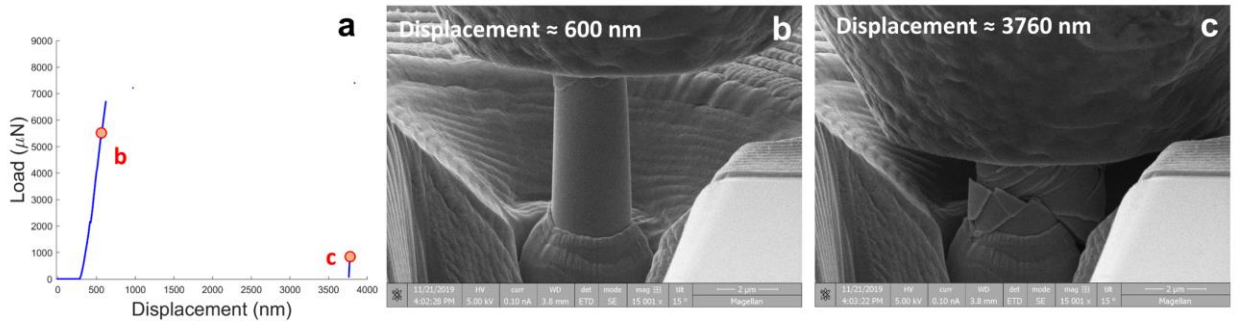

Figure II.6: (a) Load versus displacement data collected during in-situ testing of a 2 µm diameter micropillar for Ti-20Nb aged for 3 d at 300 °C with 0.1 at. % O. SEM images of pillar after (b) 600 nm and (c) 3760 nm of displacement.

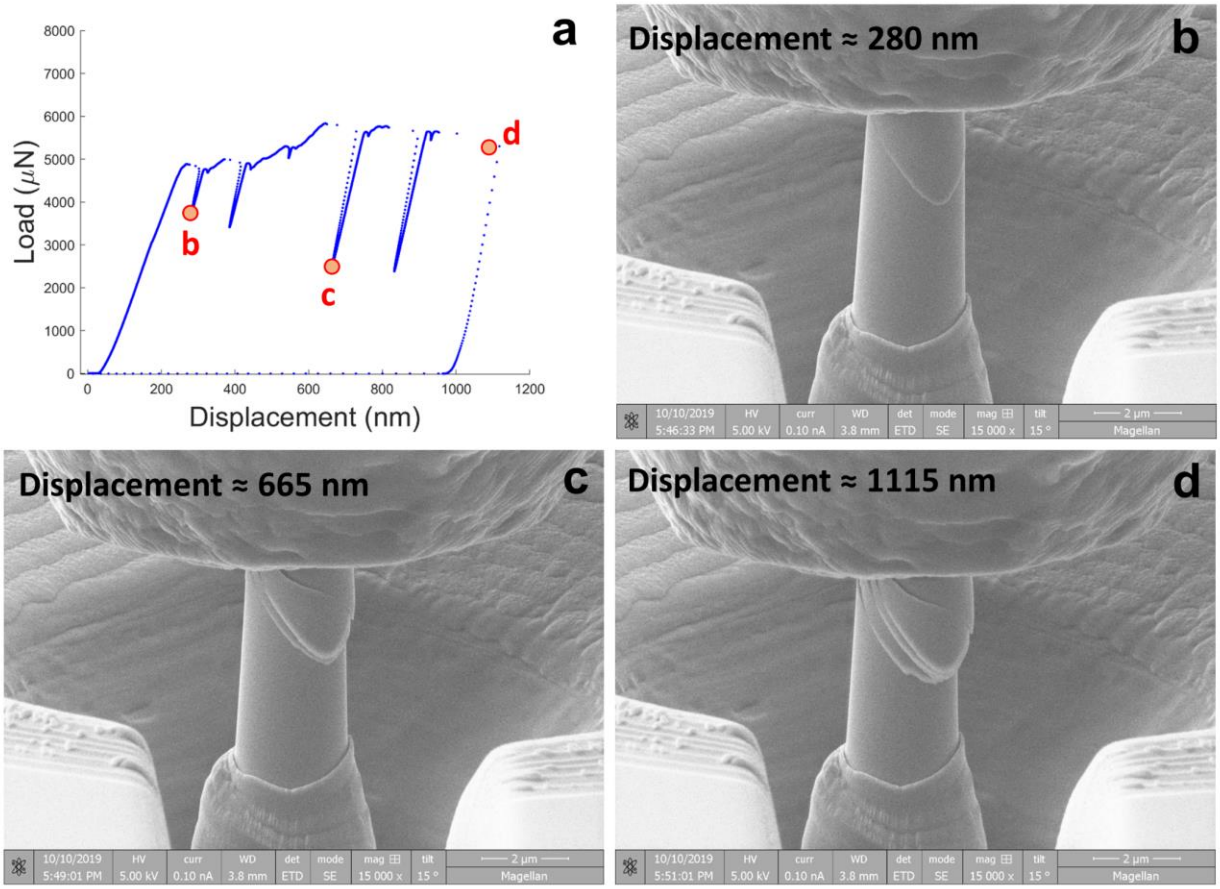

Figure II.7: (a) Load versus displacement data collected during in-situ testing of a 2 µm diameter micropillar for Ti-20Nb aged for 3 d at 300 °C with 4.1 at. % O. SEM images of pillar after (b) 280 nm, (c) 665 nm, and (d) 1115 nm of displacement.

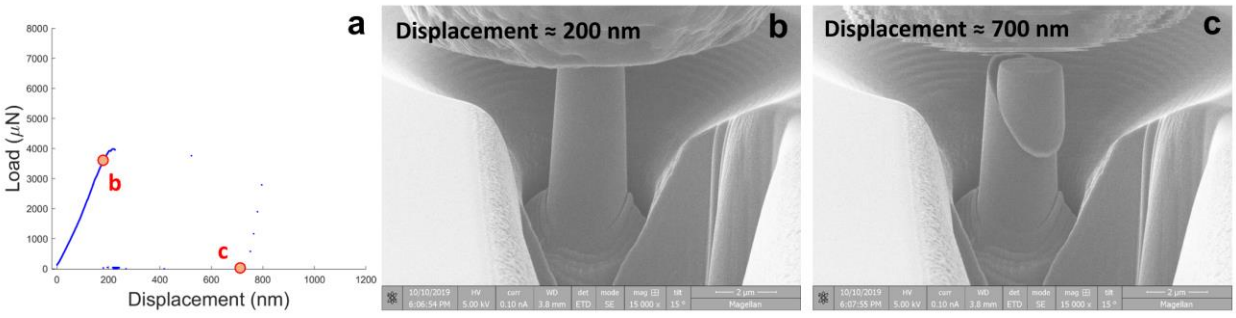

Figure II.8: (a) Load versus displacement data collected during in-situ testing of a 2 µm diameter micropillar for Ti-20Nb aged for 3 d at 300 °C with 4.1 at. % O. SEM images of pillar after (b) 200 nm and (c) 700 nm of displacement.

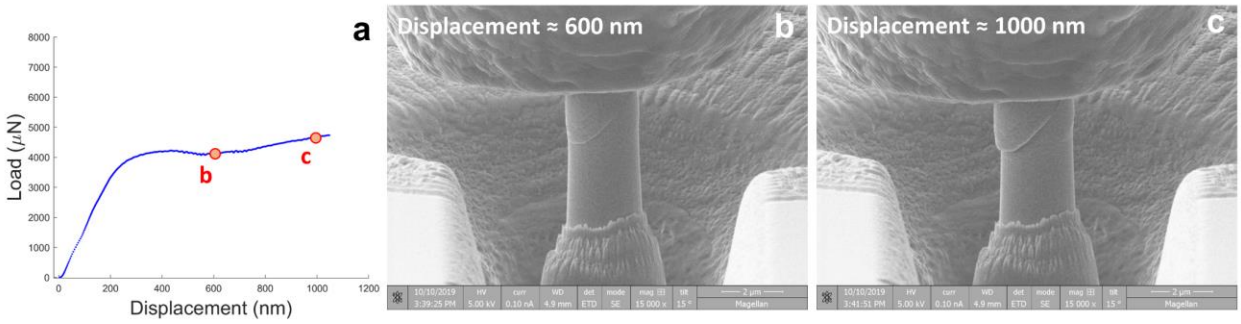

Figure II.9: (a) Load versus displacement data collected during in-situ testing of a 2 µm diameter micropillar for Ti-20Nb aged for 3 d at 450 °C with 0.1 at. % O. SEM images of pillar after (b) 600 nm and (c) 1000 nm of displacement.

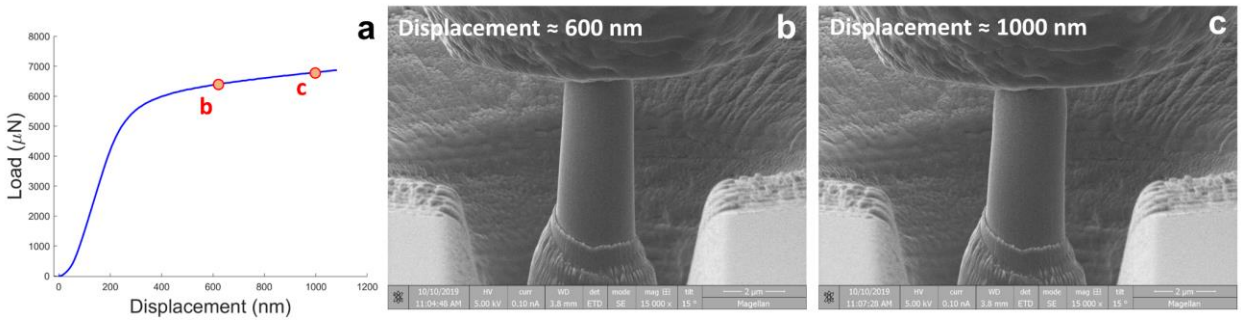

Figure II.10: (a) Load versus displacement data collected during in-situ testing of a 2 µm diameter micropillar for Ti-20Nb aged for 3 d at 450 °C with 4.1 at. % O. SEM images of pillar after (b) 600 nm and (c) 1000 nm of displacement.

Appendix III: WDS Method Details, EBSD Maps, and Thermo-Calc Simulations for Ti-15-333 and Ti-15Mo

III.1 Methods for WDS measurements

Measurements were made using a Cameca SX100 electron microprobe located in the Robert B. Mitchell Electron Microbeam Analysis Lab, part of the University of Michigan's Department of Earth and Environmental Sciences. Measurements of the O Kα, Ti Kα, V Kα, Cr Kα, Al Kα, Sn Lα, and Mo Lα X-rays were made using a focused electron beam with a beam current of 40 nA and an accelerating potential of 15 keV. Peak X-ray intensities were measured for 40 seconds, while off-peak measurements of continuum X-ray intensity were made for 20 seconds each, except for Ti Kα (10 seconds on-peak, 5 seconds each off-peak) and V Kα (20 seconds on-peak, 10 seconds each off-peak). Calibration standards and unknowns were coated with ~15nm of carbon prior to analysis, and were coated together time to minimize any differences in measured X-ray intensities due to differences in coating thicknesses. Calibration standards were synthetic MgO (O Kα), Ti metal (Ti Kα) V metal (V Kα), Cr metal (Cr Kα), synthetic NiAl alloy (Al Kα), Sn metal (Sn Lα), and Mo metal (Mo Lα); reference compositions of metal standards were adjusted to account for surface oxidation. Also, the peak position for O Kα X-ray line was adjusted between standards and unknowns to account for the peak shifts due to bonding environment [207].

Titanium alloys oxidize rapidly in air, and therefore a surface oxidation layer will develop on all samples after preparation but before analysis [94,208]. Only preparing and analyzing the samples in a completely inert atmosphere, with no exposure to oxygen during preparation, transport, or analysis, can prevent this; the layer can also be removed in situ prior to analysis, e.g. by focused ion beam. Neither of these were possible in this study, and therefore at each measured spot, the X-ray signal will include contributions from the pre-experimental oxygen present in the sample, from oxygen introduced by the post-preparation surface oxidation described above, and from oxidation induced by the experiments in presented herein.

The intrinsic oxygen in the samples prior to any oxidation experiments was provided by ATI. Also, measurements of portions of the Ti-15-333 and Ti-15Mo alloys that did not experience oxidation during the experiments conducted for this study can be used to estimate the oxygen concentration of the post-prep oxidation layer. The amount of oxygen induced by the experiments presented here can therefore be calculated by subtracting the oxygen from the oxidation layer and the intrinsic oxygen from the total measured oxygen, as follows:

$$O_{Experimental=}\, O_{Measured} - \left(O_{Intrinsic} + O_{Oxide\ Layer}\right)$$

III.2 EBSD maps and Thermo-Calc simulations

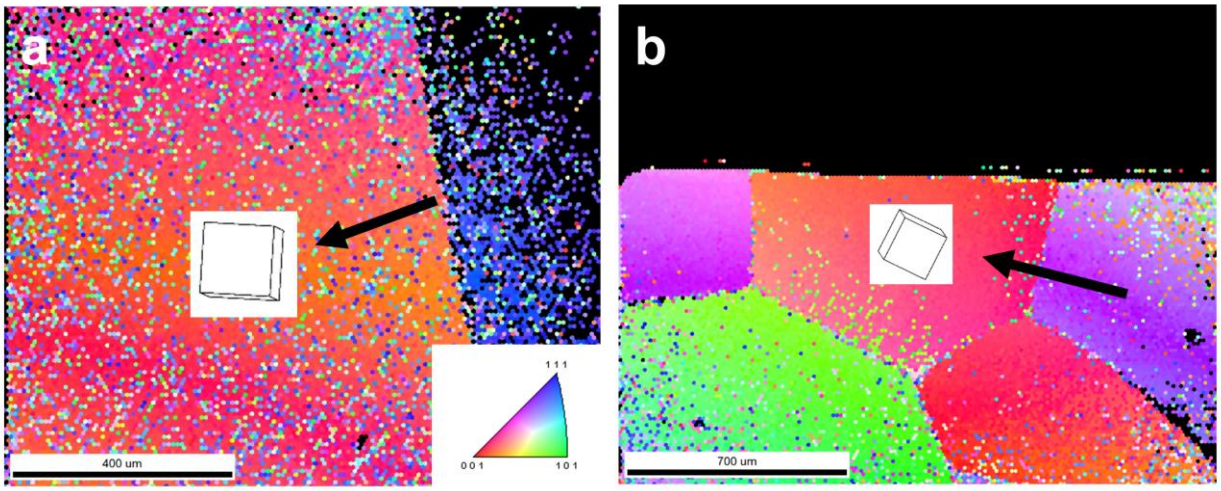

Figure III.1: EBSD inverse pole figure maps showing grain and crystal lattice outline for selected grain (black arrow) with crystallographic orientation close to out-of-plane orientation $(100)_{\beta}$ for micropillar fabrication on (a) DA Ti-15-333 with 0.1 at. % O and (b) OXA Ti-15-333 with an O concentration gradient.

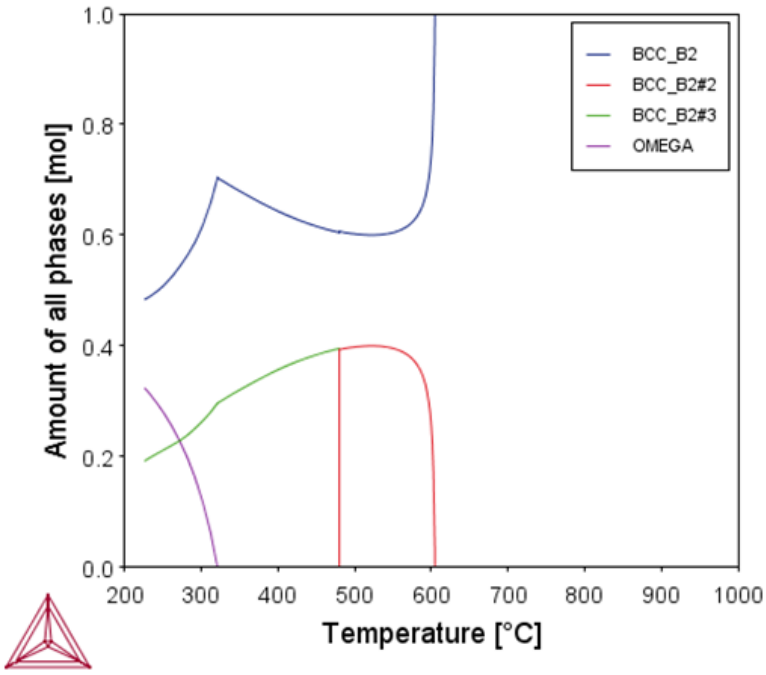

Figure III.2: Thermo-Calc simulation of metastable phase fractions with increasing temperature for Ti-15-333 alloy.

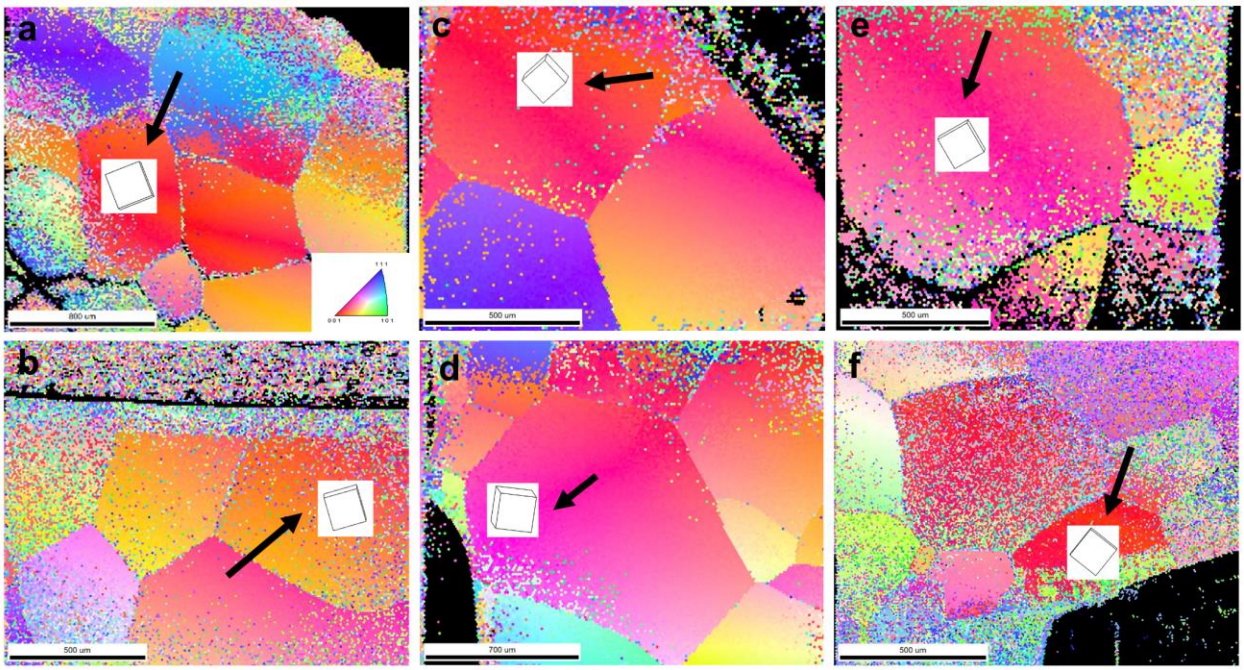

Figure III.3: EBSD inverse pole figure maps and crystal lattice outline for selected grain (black arrow) with crystallographic orientation close to out-of-plane orientation $(100)_\beta$ for micropillar fabrication on Ti-15Mo with the following ageing conditions: (a) DA 24 h, 450 °C with 0.1 at.% O, (b) OXA 24 h, 450 °C with an O concentration gradient, (c) DA 24 h, 500 °C with 0.1 at.% O, (d) OXA 24 h, 500 °C with an O concentration gradient, (e) DA 4 h, 600 °C with 0.1 at.% O, and (f) OXA 2 h, 450 °C, then 4 h, 600 °C with an O concentration gradient.

Appendix IV: Data on the Early Oxidation of SiO_2-Coated Pure Ti and Bulk Ti_5Si_3 at 800 °C

IV.1 Oxidation exposure procedure

The oxidation of pure Ti specimens sputtered with a 250 nm layer of amorphous SiO_2 was conducted for 2 or 32 h exposures at 800 ˚C in a 1 standard cubic centimeter per minute (SCCM) O_2/4 SCCM Ar environment (approximately pO_2 = 0.2 atm/20.3 kPa) using a Thermo Scientific Lindberg Blue M tube furnace. The exposures were such that specimens were inserted in the hot zone of the furnace after it was heated to 800 °C in a flowing Ar (40 SCCM) gas environment. After insertion and temperature equilibration back to 800 °C (approximately 15 minutes), the aforementioned oxidizing environment was introduced. Following the oxidation exposure, oxygen gas flow was stopped. Specimens were removed from the hot zone and cooled to room temperature in flowing Ar (40 SCCM). Sputtering of the amorphous SiO_2 layer was performed using a Kurt J. Lesker Co. five source confocal, magnetron sputtering system. Additionally, the oxidation of bulk Ti_5Si_3 was conducted for a 32 h exposure at 800 ˚C in a 1 SCCM O_2/4 SCCM Ar environment using the same procedure. The bulk Ti_5Si_3 sample was synthesized through arc melting of bulk Ti and Si pieces. The resulting bulk Ti_5Si_3 sample prior to oxidation exposure had an as-cast microstructure consisting of Ti_5Si_3 and α Ti.

IV.2 Characterization methods

Cross-sectional transmission electron microscopy (TEM) foils of the coating and oxide were prepared using a Thermo Fisher Scientific FEI Helios 650 Nanolab scanning electron microscope (SEM) equipped with a Focused Ion Beam (FIB). TEM bright field images and selected area electron diffraction (SAED) patterns were obtained using a JEOL 2010F microscope operated at 200 kV. Bright field TEM figures are composites of multiple individual specimen images. Scanning transmission electron microscope (STEM) images and energy dispersive spectroscopy (EDS) maps were collected using a Hitachi HD-2300A microscope at 200 kV equipped with an Oxford Instruments EDS detector. EDS maps were collected using an acquisition

time of 1800 s. Data visualization and analysis of EDS maps were performed using Oxford Instruments INCA software.

IV.3 Results

The coating and oxide structure for SiO_2-coated Ti oxidized for 2 h (**Figure IV.1-2**) showed similar layers to a Si-coated Ti specimen also oxidized at 800 °C for 2 h (**Chapter 7**). A compact and polycrystalline layer, identified as Ti_5Si_3 through EDS mapping and selected area electron diffraction patterns, was observed adjacent to the Ti metal. This was covered by a two-layer scale that contained an inner equiaxed, nanocrystalline layer containing TiO_2 and SiO_2 and outermost layer of TiO_2 oxide crystals, identified through EDS mapping. Delamination of the SiO_2 layer was observed in some areas at the SiO_2/Ti_5Si_3 interface (**Figure IV.2a**); however, in contrast with Si-coated Ti specimens in the accompanied study (**Chapter 7**), no outward bowing of the SiO_2 layer was observed.

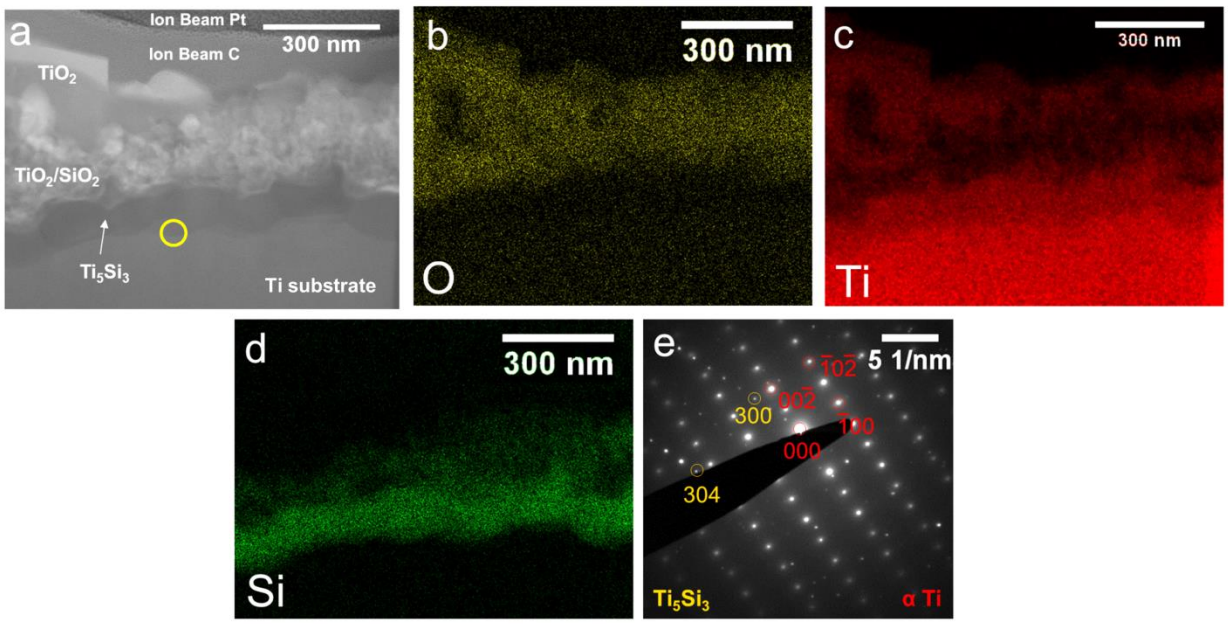

Figure IV.1: (a) STEM diffraction contrast image and associated EDS maps for O, Ti, and Si (b-d) of the coating and oxide cross section for SiO_2-coated Ti oxidized at 800 °C for 2 h. (e) Selected area diffraction pattern at location of yellow circle in (a), indexed as Ti_5Si_3 and α Ti.

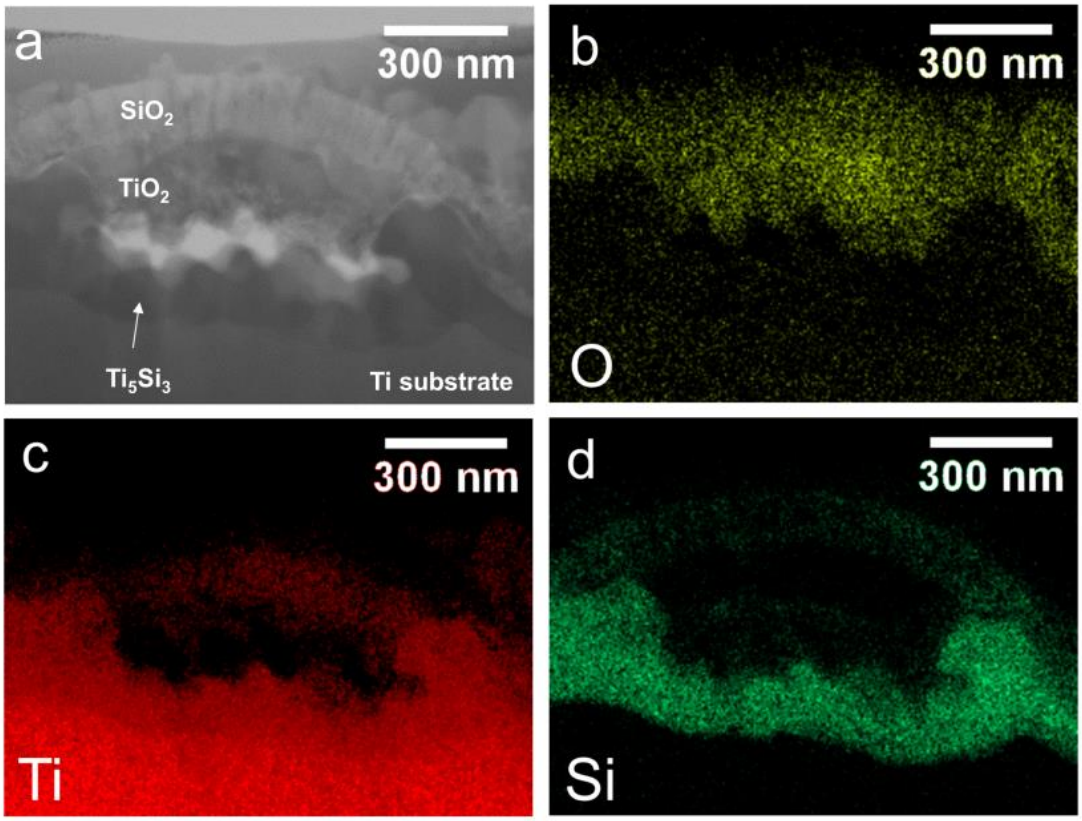

Figure IV.2: (a) STEM diffraction contrast image and associated EDS maps for O, Ti, and Si (b-d) at a delamination in the coating and oxide layers for SiO_2-coated Ti oxidized at 800 °C for 2 h.

STEM imaging and EDS mapping of oxidized bulk Ti_5Si_3 for 32 h (**Figure IV.3**) showed a two-layer scale: the outermost scale was Ti-rich and corresponded to TiO_2 and the internal scale showed mixed Ti-rich and Si-rich regions, corresponding to TiO_2 and SiO_2. In contrast with oxidation of Si-coated Ti (**Chapter 7**), no regular patterning of alternating SiO_2 and TiO_2 layers was observed for oxidized Ti_5Si_3.

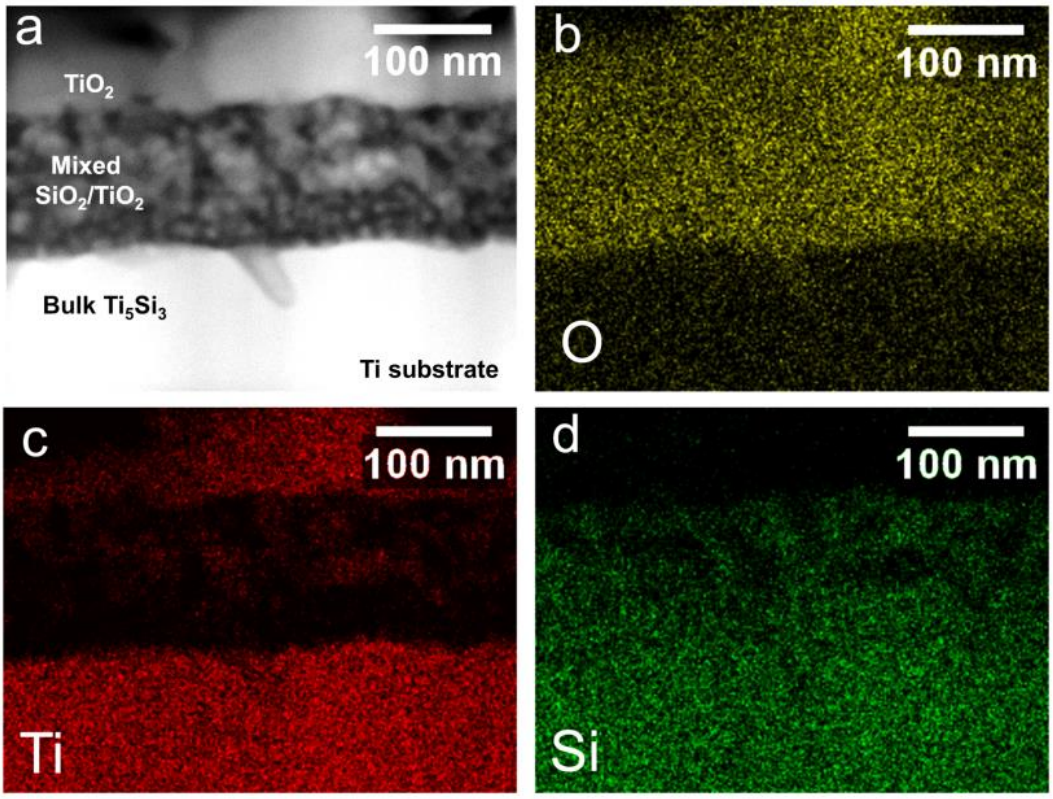

Figure IV.3: (a) STEM Z-contrast image and associated EDS maps for O, Ti, and Si (b-d) for bulk Ti_5Si_3 oxidized at 800 °C for 32 h.

Oxidation of the SiO_2-coated Ti specimens for 32 h revealed locations with distinctly different scale morphologies and internal oxide thicknesses (**Figure IV.4, IV.5**). An outward growing wedge-like external scale comprised of rutile TiO_2 was observed at all locations in the cross section. The presence of the Ti_5Si_3 layer between the internal oxide and Ti substrate, identified through EDS mapping, corresponded to regions with a thin internal nanocrystalline oxide scale (**Figure IV.4**), which was similar to Si-coated Ti oxidized specimens (**Chapter 7**). In regions where the Ti_5Si_3 layer was no longer observed, the internal oxide was much thicker (**Figure IV.5**). Si was detected through EDS mapping at the top of the internal oxide, but the underlying oxide contain very little Si signal and showed a much larger grain size. The lack of Si in the large grained portion of the internal oxide indicates that the Ti_5Si_3 layer had been fully oxidized and was no longer contributing to oxidation behavior of the Ti substrate.

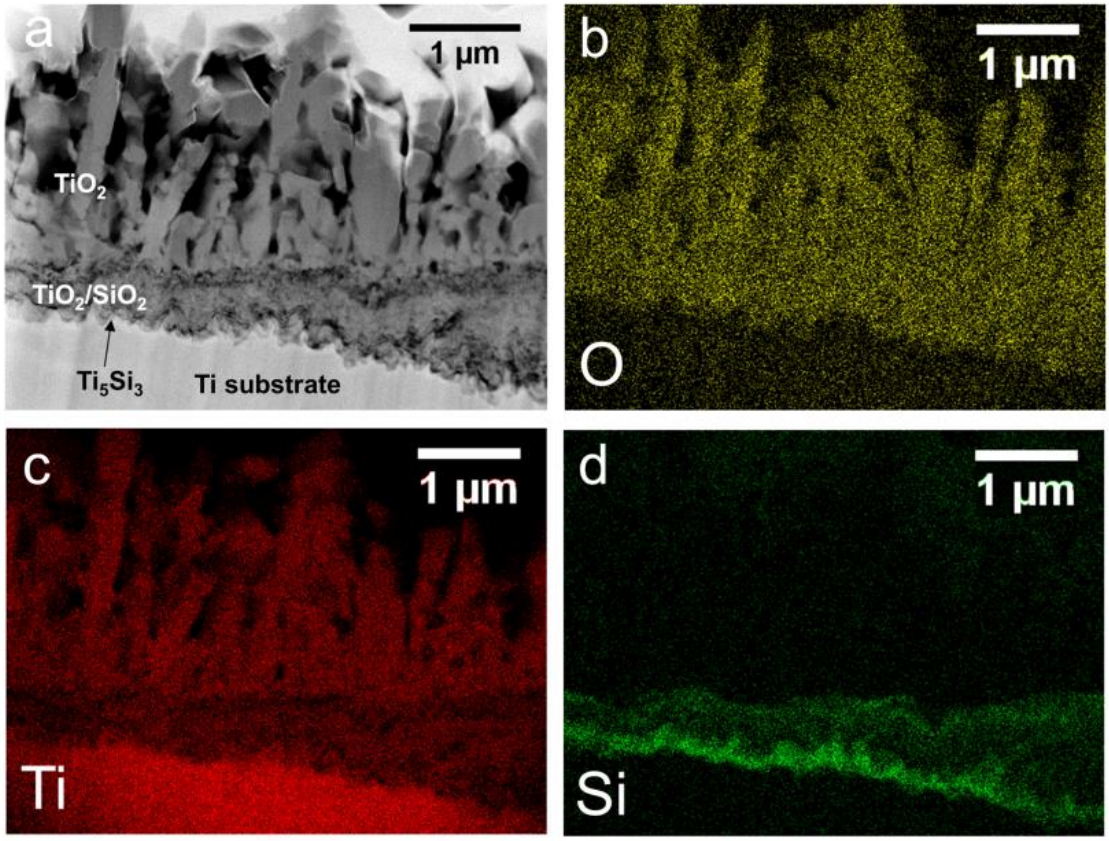

Figure IV.4: (a) STEM Z-contrast image and associated EDS maps for O, Ti, and Si (b-d) of the coating and oxide cross section for SiO_2-coated Ti oxidized at 800 °C for 32 h.

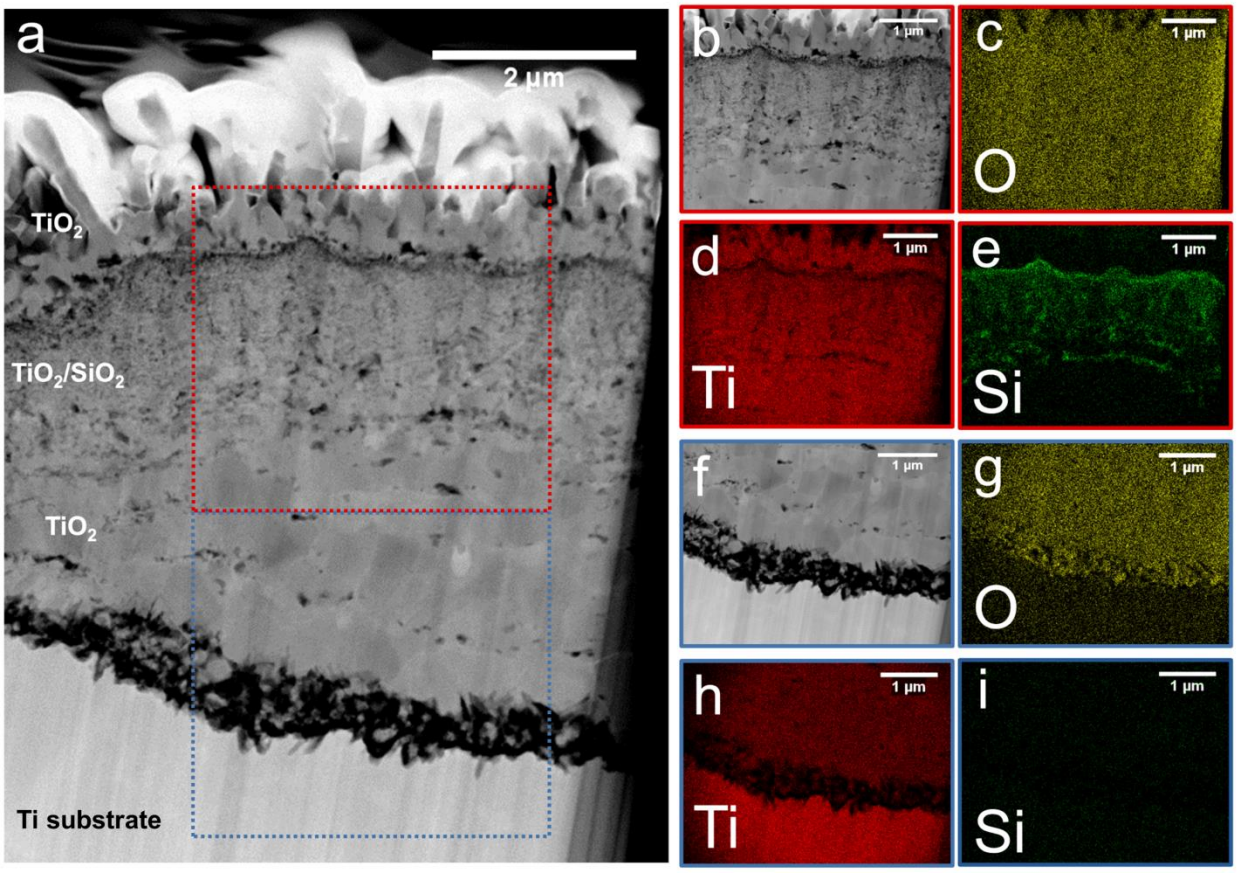

Figure IV.5: (a) STEM Z-contrast image for SiO_2-coated Ti oxidized at 800 °C for 32 h. (b) STEM Z-contrast image for subset outlined by red box and (c-e) associated EDS maps for O, Ti, and Si showing Si distributed within the internal oxide. (f) STEM Z-contrast image for subset outlined by blue box and (g-i) associated EDS maps for O, Ti, and Si, in which Si is not detected at the oxide/metal interface.

References

[1] G. Lütjering, J.C. Williams, Titanium, Springer, New York, 2003.

[2] D. Banerjee, J.C. Williams, Perspectives on Titanium Science and Technology, Acta Mater. 61 (2013) 844–879. https://doi.org/10.1016/j.actamat.2012.10.043.

[3] L. Zhang, L. Chen, A Review on Biomedical Titanium Alloys: Recent Progress and Prospect, Adv. Eng. Mater. 21 (2019) 1801215. https://doi.org/10.1002/adem.201801215.

[4] J.J. Dai, J.Y. Zhu, C.Z. Chen, F. Weng, High temperature oxidation behavior and research status of modifications on improving high temperature oxidation resistance of titanium alloys and titanium aluminides: A review, J. Alloys Compd. 685 (2016) 784–798. https://doi.org/10.1016/j.jallcom.2016.06.212.

[5] Z. Liu, G. Welsch, Effects of oxygen and heat treatment on the mechanical properties of alpha and beta titanium alloys, Metall. Trans. A. 19 (1988) 527–542. https://doi.org/10.1007/bf02649267.

[6] R. Kolli, A. Devaraj, A Review of Metastable Beta Titanium Alloys, Metals (Basel). 8 (2018) 506. https://doi.org/10.3390/met8070506.

[7] T. Saito, T. Furuta, J.H. Hwang, S. Kuramoto, K. Nishino, N. Suzuki, R. Chen, A. Yamada, K. Ito, Y. Seno, T. Nonaka, H. Ikehata, N. Nagasako, C. Iwamoto, Y. Ikuhara, T. Sakuma, Multifunctional Alloys Obtained via a Dislocation-Free Plastic Deformation Mechanism, Science (80-.). 300 (2003) 464–467. https://doi.org/10.1126/science.1081957.

[8] A. Gysler, G. Lütjering, V. Gerold, Deformation behavior of age-hardened Ti-Mo alloys, Acta Metall. 22 (1974) 901–909. https://doi.org/10.1016/0001-6160(74)90057-1.

[9] M. Niinomi, M. Nakai, M. Hendrickson, P. Nandwana, T. Alam, D. Choudhuri, R. Banerjee, Influence of oxygen on omega phase stability in the Ti-29Nb-13Ta-4.6Zr alloy, Scr. Mater. 123 (2016) 144–148. https://doi.org/10.1016/j.scriptamat.2016.06.027.

[10] D.P. Satko, J.B. Shaffer, J.S. Tiley, S.L. Semiatin, A.L. Pilchak, S.R. Kalidindi, Y. Kosaka, M.G. Glavicic, A.A. Salem, Effect of microstructure on oxygen rich layer evolution and its impact on fatigue life during high-temperature application of α/β titanium, Acta Mater. 107 (2016) 377–389. https://doi.org/10.1016/j.actamat.2016.01.058.

[11] D. Vojtěch, P. Novák, P. Macháč, M. Morťaniková, K. Jurek, Surface protection of titanium by Ti5Si3 silicide layer prepared by combination of vapour phase siliconizing

and heat treatment, J. Alloys Compd. 464 (2008) 179–184. https://doi.org/10.1016/j.jallcom.2007.10.020.

[12] H.P. Xiong, M. Wei, Y.H. Xie, Y.Y. Cheng, X.H. Li, Formation of silicide coatings on the surface of a TiAl-based alloy and improvement in oxidation resistance, Mater. Sci. Eng. a-Structural Mater. Prop. Microstruct. Process. 391 (2005) 10–18. https://doi.org/10.1016/j.msea.2004.05.026.

[13] T.W. Duerig, G.T. Terlinde, J.C. Williams, Phase transformations and tensile properties of Ti-10V-2Fe-3AI, Metall. Trans. A. 11 (1980) 1987–1998. https://doi.org/10.1007/bf02655118.

[14] Y. Zheng, D. Choudhuri, T. Alam, R.E.A. Williams, R. Banerjee, H.L. Fraser, The role of cuboidal ω precipitates on α precipitation in a Ti-20V alloy, Scr. Mater. 123 (2016) 81–85. https://doi.org/10.1016/j.scriptamat.2016.06.004.

[15] D. Choudhuri, Y. Zheng, T. Alam, R. Shi, M. Hendrickson, S. Banerjee, Y. Wang, S.G. Srinivasan, H. Fraser, R. Banerjee, Coupled experimental and computational investigation of omega phase evolution in a high misfit titanium-vanadium alloy, Acta Mater. 130 (2017) 215–228. https://doi.org/10.1016/j.actamat.2017.03.047.

[16] G. Aurelio, A. Fernández Guillermet, G.J. Cuello, J. Campo, Metastable phases in the Ti-V system: Part I. Neutron diffraction study and assessment of structural properties, Metall. Mater. Trans. A. 33 (2002) 1307–1317. https://doi.org/10.1007/s11661-002-0057-x.

[17] X.L. Wang, L. Li, W. Mei, W.L. Wang, J. Sun, Dependence of stress-induced omega transition and mechanical twinning on phase stability in metastable β Ti–V alloys, Mater. Charact. 107 (2015) 149–155. https://doi.org/10.1016/j.matchar.2015.06.038.

[18] M. Bönisch, A. Panigrahi, M. Calin, T. Waitz, M. Zehetbauer, W. Skrotzki, J. Eckert, Thermal stability and latent heat of Nb–rich martensitic Ti-Nb alloys, J. Alloys Compd. 697 (2017) 300–309. https://doi.org/10.1016/j.jallcom.2016.12.108.

[19] S. Banerjee, R. Tewari, G.K. Dey, Omega phase transformation – morphologies and mechanisms, Int. J. Mater. Res. 97 (2006) 963–977. https://doi.org/10.3139/146.101327.

[20] Y. Zheng, D. Banerjee, H.L. Fraser, A nano-scale instability in the β phase of dilute Ti–Mo alloys, Scr. Mater. 116 (2016) 131–134. https://doi.org/10.1016/j.scriptamat.2016.01.044.

[21] H.L. Wang, Y.L. Hao, S.Y. He, T. Li, J.M. Cairney, Y.D. Wang, Y. Wang, E.G. Obbard, F. Prima, K. Du, S.J. Li, R. Yang, Elastically confined martensitic transformation at the nano-scale in a multifunctional titanium alloy, Acta Mater. 135 (2017) 330–339. https://doi.org/10.1016/j.actamat.2017.06.040.

[22] Q. Liang, Y. Zheng, D. Wang, Y. Hao, R. Yang, Y. Wang, H.L. Fraser, Nano-scale structural non-uniformities in gum like Ti-24Nb-4Zr-8Sn metastable β-Ti alloy, Scr. Mater. 158 (2019) 95–99. https://doi.org/10.1016/j.scriptamat.2018.08.043.

[23] Y. Zheng, S. Antonov, Q. Feng, R. Banerjee, D. Banerjee, H.L. Fraser, Shuffle-induced modulated structure and heating-induced ordering in the metastable β-titanium alloy, Ti-5Al-5Mo-5V-3Cr, Scr. Mater. 176 (2020) 7–11. https://doi.org/10.1016/j.scriptamat.2019.09.027.

[24] H.Y. Kim, Y. Ikehara, J.I. Kim, H. Hosoda, S. Miyazaki, Martensitic transformation, shape memory effect and superelasticity of Ti–Nb binary alloys, Acta Mater. 54 (2006). https://doi.org/10.1016/j.actamat.2006.01.019.

[25] R. Davis, H.M. Flower, D.R.F. West, Martensitic transformations in Ti-Mo alloys, J. Mater. Sci. 14 (1979) 712–722. https://doi.org/10.1007/BF00772735.

[26] Y. Zheng, R.E.A. Williams, S. Nag, R. Banerjee, H.L. Fraser, D. Banerjee, The effect of alloy composition on instabilities in the β phase of titanium alloys, Scr. Mater. 116 (2016) 49–52. https://doi.org/10.1016/j.scriptamat.2016.01.024.

[27] M. Tahara, H.Y. Kim, T. Inamura, H. Hosoda, S. Miyazaki, Lattice modulation and superelasticity in oxygen-added β-Ti alloys, Acta Mater. 59 (2011) 6208–6218. https://doi.org/10.1016/j.actamat.2011.06.015.

[28] H.L. Wang, S.A.A. Shah, Y.L. Hao, F. Prima, T. Li, J.M. Cairney, Y.D. Wang, Y. Wang, E.G. Obbard, S.J. Li, R. Yang, Stabilizing the body centered cubic crystal in titanium alloys by a nano-scale concentration modulation, J. Alloys Compd. 700 (2017) 155–158. https://doi.org/10.1016/j.jallcom.2016.12.406.

[29] A. Devaraj, S. Nag, R. Srinivasan, R.E.A. Williams, S. Banerjee, R. Banerjee, H.L. Fraser, Experimental evidence of concurrent compositional and structural instabilities leading to ω precipitation in titanium–molybdenum alloys, Acta Mater. 60 (2012) 596–609. https://doi.org/10.1016/j.actamat.2011.10.008.

[30] S. Nag, A. Devaraj, R. Srinivasan, R.E. Williams, N. Gupta, G.B. Viswanathan, J.S. Tiley, S. Banerjee, S.G. Srinivasan, H.L. Fraser, R. Banerjee, Novel mixed-mode phase transition involving a composition-dependent displacive component, Phys Rev Lett. 106 (2011) 245701. https://doi.org/10.1103/PhysRevLett.106.245701.

[31] B.S. Hickman, The formation of omega phase in titanium and zirconium alloys: A review, J. Mater. Sci. 4 (1969) 554–563. https://doi.org/10.1007/bf00550217.

[32] H. Liu, M. Niinomi, M. Nakai, K. Cho, H. Fujii, Deformation-induced ω-phase transformation in a β-type titanium alloy during tensile deformation, Scr. Mater. 130 (2017) 27–31. https://doi.org/10.1016/j.scriptamat.2016.10.036.

[33] O.M. Ivasishin, P.E. Markovsky, Y.V. Matviychuk, S.L. Semiatin, C.H. Ward, S. Fox, A comparative study of the mechanical properties of high-strength β-titanium alloys, J. Alloys Compd. 457 (2008). https://doi.org/10.1016/j.jallcom.2007.03.070.

[34] S.A. Mantri, D. Choudhuri, T. Alam, G.B. Viswanathan, J.M. Sosa, H.L. Fraser, R. Banerjee, Tuning the scale of α precipitates in β-titanium alloys for achieving high

strength, Scr. Mater. 154 (2018) 139–144. https://doi.org/10.1016/j.scriptamat.2018.05.040.

[35] J.C. Williams, B.S. Hickman, D.H. Leslie, The effect of ternary additions on the decompositon of metastable beta-phase titanium alloys, Metall. Trans. 2 (1971) 477–484. https://doi.org/10.1007/bf02663337.

[36] T. Li, D. Kent, G. Sha, L.T. Stephenson, A. V Ceguerra, S.P. Ringer, M.S. Dargusch, J.M. Cairney, New insights into the phase transformations to isothermal ω and ω-assisted α in near β-Ti alloys, Acta Mater. 106 (2016) 353–366. https://doi.org/10.1016/j.actamat.2015.12.046.

[37] F. Prima, P. Vermaut, G. Texier, D. Ansel, T. Gloriant, Evidence of α-nanophase heterogeneous nucleation from ω particles in a β-metastable Ti-based alloy by high-resolution electron microscopy, Scr. Mater. 54 (2006). https://doi.org/10.1016/j.scriptamat.2005.10.024.

[38] T. Li, D. Kent, G. Sha, H. Liu, S.G. Fries, A. V Ceguerra, M.S. Dargusch, J.M. Cairney, Nucleation driving force for ω-assisted formation of α and associated ω morphology in β-Ti alloys, Scr. Mater. 155 (2018) 149–154. https://doi.org/10.1016/j.scriptamat.2018.06.039.

[39] Y. Zheng, R.E.A. Williams, D. Wang, R. Shi, S. Nag, P. Kami, J.M. Sosa, R. Banerjee, Y. Wang, H.L. Fraser, Role of ω phase in the formation of extremely refined intragranular α precipitates in metastable β-titanium alloys, Acta Mater. 103 (2016) 850–858. https://doi.org/10.1016/j.actamat.2015.11.020.

[40] Y. Zheng, R.E.A. Williams, J.M. Sosa, T. Alam, Y. Wang, R. Banerjee, H.L. Fraser, The indirect influence of the ω phase on the degree of refinement of distributions of the α phase in metastable β-Titanium alloys, Acta Mater. 103 (2016) 165–173. https://doi.org/10.1016/j.actamat.2015.09.053.

[41] M. Abdel-Hady, K. Hinoshita, M. Morinaga, General approach to phase stability and elastic properties of β-type Ti-alloys using electronic parameters, Scr. Mater. 55 (2006). https://doi.org/10.1016/j.scriptamat.2006.04.022.

[42] C.H. Wang, A.M. Russell, G.H. Cao, A semi-empirical approach to the prediction of deformation behaviors of β-Ti alloys, Scr. Mater. 158 (2019). https://doi.org/10.1016/j.scriptamat.2018.08.035.

[43] F. Sun, J.Y. Zhang, M. Marteleur, T. Gloriant, P. Vermaut, D. Laillé, P. Castany, C. Curfs, P.J. Jacques, F. Prima, Investigation of early stage deformation mechanisms in a metastable β titanium alloy showing combined twinning-induced plasticity and transformation-induced plasticity effects, Acta Mater. 61 (2013). https://doi.org/10.1016/j.actamat.2013.07.019.

[44] H. Tobe, H.Y. Kim, T. Inamura, H. Hosoda, T.H. Nam, S. Miyazaki, Effect of Nb content on deformation behavior and shape memory properties of Ti–Nb alloys, J. Alloys Compd.

577 (2013). https://doi.org/10.1016/j.jallcom.2012.02.023.

[45] A. Biesiekierski, J. Wang, M.A. Gepreel, C. Wen, A new look at biomedical Ti-based shape memory alloys, Acta Biomater. 8 (2012) 1661–1669. https://doi.org/10.1016/j.actbio.2012.01.018.

[46] J.C. Williams Hickman, B.S., Marcus, H.L., The effect of omega phase on the mechanical properties of titanium alloys, Metall. Trans. 2 (1971) 1913–1919. https://doi.org/10.1007/BF02913423.

[47] J.C. Sabol, C.J. Marvel, M. Watanabe, T. Pasang, W.Z. Misiolek, Confirmation of the ω-phase in electron beam welded Ti–5Al–5V–5Mo–3Cr by high-resolution scanning transmission electron microscopy: An initial investigation into its effects on embrittlement, Scr. Mater. 92 (2014) 15–18. https://doi.org/10.1016/j.scriptamat.2014.08.003.

[48] J.D. Cotton, R.D. Briggs, R.R. Boyer, S. Tamirisakandala, P. Russo, N. Shchetnikov, J.C. Fanning, State of the Art in Beta Titanium Alloys for Airframe Applications, Jom. 67 (2015) 1281–1303. https://doi.org/10.1007/s11837-015-1442-4.

[49] J. Gao, A.J. Knowles, D. Guan, W.M. Rainforth, ω phase strengthened 1.2GPa metastable β titanium alloy with high ductility, Scr. Mater. 162 (2019) 77–81. https://doi.org/10.1016/j.scriptamat.2018.10.043.

[50] F. Sun, J.Y. Zhang, P. Vermaut, D. Choudhuri, T. Alam, S.A. Mantri, P. Svec, T. Gloriant, P.J. Jacques, R. Banerjee, F. Prima, Strengthening strategy for a ductile metastable β-titanium alloy using low-temperature aging, Mater. Res. Lett. 5 (2017) 547–553. https://doi.org/10.1080/21663831.2017.1350211.

[51] M.J. Lai, T. Li, D. Raabe, ω phase acts as a switch between dislocation channeling and joint twinning- and transformation-induced plasticity in a metastable β titanium alloy, Acta Mater. 151 (2018) 67–77. https://doi.org/10.1016/j.actamat.2018.03.053.

[52] W. Chen, S. Cao, W. Kou, J. Zhang, Y. Wang, Y. Zha, Y. Pan, Q. Hu, Q. Sun, J. Sun, Origin of the ductile-to-brittle transition of metastable β-titanium alloys: Self-hardening of ω-precipitates, Acta Mater. 170 (2019) 187–204. https://doi.org/10.1016/j.actamat.2019.03.034.

[53] R.J. Talling, R.J. Dashwood, M. Jackson, D. Dye, On the mechanism of superelasticity in Gum metal, Acta Mater. 57 (2009) 1188–1198. https://doi.org/10.1016/j.actamat.2008.11.013.

[54] Y. Wang, J. Gao, H. Wu, S. Yang, X. Ding, D. Wang, X. Ren, Y. Wang, X. Song, J. Gao, Strain glass transition in a multifunctional beta-type Ti alloy, Sci Rep. 4 (2014) 3995. https://doi.org/10.1038/srep03995.

[55] J. Zhang, C.C. Tasan, M.J. Lai, A.C. Dippel, D. Raabe, Complexion-mediated martensitic phase transformation in Titanium, Nat Commun. 8 (2017) 14210.

https://doi.org/10.1038/ncomms14210.

[56] M. Niinomi, M. Nakai, J. Hieda, Development of new metallic alloys for biomedical applications, Acta Biomater. 8 (2012) 3888–3903. https://doi.org/10.1016/j.actbio.2012.06.037.

[57] M. Tane, T. Nakano, S. Kuramoto, M. Hara, M. Niinomi, N. Takesue, T. Yano, H. Nakajima, Low Young's modulus in Ti–Nb–Ta–Zr–O alloys: Cold working and oxygen effects, Acta Mater. 59 (2011) 6975–6988. https://doi.org/10.1016/j.actamat.2011.07.050.

[58] M. Besse, P. Castany, T. Gloriant, Mechanisms of deformation in gum metal TNTZ-O and TNTZ titanium alloys: A comparative study on the oxygen influence, Acta Mater. 59 (2011) 5982–5988. https://doi.org/10.1016/j.actamat.2011.06.006.

[59] L.S. Wei, H.Y. Kim, T. Koyano, S. Miyazaki, Effects of oxygen concentration and temperature on deformation behavior of Ti-Nb-Zr-Ta-O alloys, Scr. Mater. 123 (2016) 55–58. https://doi.org/10.1016/j.scriptamat.2016.05.043.

[60] P. Castany, A. Ramarolahy, F. Prima, P. Laheurte, C. Curfs, T. Gloriant, In situ synchrotron X-ray diffraction study of the martensitic transformation in superelastic Ti-24Nb-0.5N and Ti-24Nb-0.5O alloys, Acta Mater. 88 (2015) 102–111. https://doi.org/10.1016/j.actamat.2015.01.014.

[61] L.S. Wei, H.Y. Kim, S. Miyazaki, Effects of oxygen concentration and phase stability on nano-domain structure and thermal expansion behavior of Ti–Nb–Zr–Ta–O alloys, Acta Mater. 100 (2015) 313–322. https://doi.org/10.1016/j.actamat.2015.08.054.

[62] Y. Ishiguro, Y. Tsukada, T. Koyama, Phase-field simulation of spinodal decomposition and its effect on stress-induced martensitic transformation in Ti–Nb–O alloys, Comput. Mater. Sci. 151 (2018). https://doi.org/10.1016/j.commatsci.2018.05.003.

[63] H. Liu, M. Niinomi, M. Nakai, S. Obara, H. Fujii, Improved fatigue properties with maintaining low Young's modulus achieved in biomedical beta-type titanium alloy by oxygen addition, Mater. Sci. Eng. A. 704 (2017) 10–17. https://doi.org/10.1016/j.msea.2017.07.078.

[64] J.I. Qazi, B. Marquardt, L.F. Allard, H.J. Rack, Phase transformations in Ti–35Nb–7Zr–5Ta–(0.06–0.68)O alloys, Mater. Sci. Eng. C. 25 (2005) 389–397. https://doi.org/10.1016/j.msec.2005.01.022.

[65] T. Li, D. Kent, G. Sha, M.S. Dargusch, J.M. Cairney, The mechanism of ω-assisted α phase formation in near β-Ti alloys, Scr. Mater. 104 (2015). https://doi.org/10.1016/j.scriptamat.2015.04.007.

[66] M. Ikeda, S. Komatsu, T. Sugimoto, K. Kamei, Influence of Oxygen Content on Electrical Resistivity and Phase Constitution in Quenched Ti-V Alloys, J. Japan Inst. Met. 55 (1991) 260–266. https://doi.org/10.2320/jinstmet1952.55.3_260.

[67] N.E. Paton, J.C. Williams, The influence of oxygen content on the athermal β-ω transformation, Scr. Metall. 7 (1973) 647–649. https://doi.org/10.1016/0036-9748(73)90229-9.

[68] J.G. Niu, D.H. Ping, T. Ohno, W.T. Geng, Suppression effect of oxygen on the β to ω transformation in a β-type Ti alloy: insights from first-principles, Model. Simul. Mater. Sci. Eng. 22 (2014) 15007. https://doi.org/10.1088/0965-0393/22/1/015007.

[69] T. Homma, A. Arafah, D. Haley, M. Nakai, M. Niinomi, M.P. Moody, Effect of alloying elements on microstructural evolution in oxygen content controlled Ti-29Nb-13Ta-4.6Zr (wt%) alloys for biomedical applications during aging, Mater. Sci. Eng. A. 709 (2018) 312–321. https://doi.org/10.1016/j.msea.2017.10.018.

[70] D.L. Moffat, U.R. Kattner, The stable and metastable Ti-Nb phase diagrams, Metall. Trans. A. 19 (1988) 2389–2397. https://doi.org/10.1007/bf02645466.

[71] X. Ji, S. Emura, T. Liu, K. Suzuta, X. Min, K. Tsuchiya, Effect of oxygen addition on microstructures and mechanical properties of Ti-7.5Mo alloy, J. Alloys Compd. 737 (2018) 221–229. https://doi.org/10.1016/j.jallcom.2017.12.072.

[72] X. Min, P. Bai, S. Emura, X. Ji, C. Cheng, B. Jiang, K. Tsuchiya, Effect of oxygen content on deformation mode and corrosion behavior in β-type Ti-Mo alloy, Mater. Sci. Eng. A. 684 (2017) 534–541. https://doi.org/10.1016/j.msea.2016.12.062.

[73] Y. Zheng, T. Alam, R. Banerjee, D. Banerjee, H.L. Fraser, The influence of aluminum and oxygen additions on intrinsic structural instabilities in titanium-molybdenum alloys, Scr. Mater. 152 (2018) 150–153. https://doi.org/10.1016/j.scriptamat.2018.04.030.

[74] C. Leyens, M. Peters, Oxidation and Protection of Titanium Alloys and Titanium Aluminides, in Titanium and Titanium Alloys: Fundamentals and Applications, (2003). https://doi.org/10.1002/3527602119.ch6.

[75] P. Kofstad, P.B. Anderson, O.J. Krudtaa, Oxidation of Titanium in the Temperature Range 800-1200-Degrees-C, J. Less-Common Met. 3 (1961) 89–97. https://doi.org/Doi 10.1016/0022-5088(61)90001-7.

[76] J. Stringer, The Oxidation of Titanium in Oxygen at High Temperatures, Acta Metall. 8 (1960) 758–766. https://doi.org/Doi 10.1016/0001-6160(60)90170-X.

[77] J. Unnam, R.K. Clark, Oxidation of Commercial Purity Titanium, Oxid. Met. 26 (1986) 231–252. https://doi.org/Doi 10.1007/Bf00659186.

[78] G. Bertrand, K. Jarraya, J.M. Chaix, Morphology of Oxide Scales Formed on Titanium, Oxid. Met. 21 (1984) 1–19. https://doi.org/Doi 10.1007/Bf00659464.

[79] J.E.L. Gomes, A.M. Huntz, Correlation between the oxidation mechanism of titanium under a pure oxygen atmosphere, morphology of the oxide scale, and diffusional phenomena, Oxid. Met. 14 (1980) 249–261. https://doi.org/10.1007/bf00604567.

[80] C. Oviedo, Oxidation-Kinetics of Pure Titanium at Low-Pressures, J. Physics-Condensed Matter. 5 (1993) A153–A154. https://doi.org/Doi 10.1088/0953-8984/5/33a/037.

[81] P. Kofstad, High-Temperature Oxidation of Titanium, J. Less-Common Met. 12 (1967) 449–464. https://doi.org/Doi 10.1016/0022-5088(67)90017-3.

[82] A.L. Pilchak, W.J. Porter, R. John, Room temperature fracture processes of a near-α titanium alloy following elevated temperature exposure, J. Mater. Sci. 47 (2012) 7235–7253. https://doi.org/10.1007/s10853-012-6673-y.

[83] X.Y. Li, S. Taniguchi, Y. Matsunaga, K. Nakagawa, K. Fujita, Influence of siliconizing on the oxidation behavior of a γ-TiAl based alloy, Intermetallics. 11 (2003) 143–150. https://doi.org/10.1016/s0966-9795(02)00193-0.

[84] W. Liang, X.G. Zhao, Improving the oxidation resistance of TiAl-based alloy by siliconizing, Scr. Mater. 44 (2001) 1049–1054. https://doi.org/Doi 10.1016/S1359-6462(01)00675-3.

[85] Z.D. Xiang, S.R. Rose, P.K. Datta, Codeposition of Al and Si to form oxidation-resistant coatings on γ-TiAl by the pack cementation process, Mater. Chem. Phys. 80 (2003) 482–489. https://doi.org/10.1016/s0254-0584(02)00551-5.

[86] R. Swadźba, L. Swadźba, B. Mendala, B. Witala, J. Tracz, K. Marugi, Ł. Pyclik, Characterization of Si-aluminide coating and oxide scale microstructure formed on γ-TiAl alloy during long-term oxidation at 950 °C, Intermetallics. 87 (2017) 81–89. https://doi.org/10.1016/j.intermet.2017.04.015.

[87] J. Dutta Majumdar, A. Weisheit, B.L. Mordike, I. Manna, Laser surface alloying of Ti with Si, Al and Si+Al for an improved oxidation resistance, Mater. Sci. Eng. A. 266 (1999) 123–134. https://doi.org/10.1016/s0921-5093(99)00045-3.

[88] J.J. Dai, F.Y. Zhang, A.M. Wang, H.J. Yu, C.Z. Chen, Microstructure and properties of Ti-Al coating and Ti-Al-Si system coatings on Ti-6Al-4V fabricated by laser surface alloying, Surf. Coat. Technol. 309 (2017) 805–813. https://doi.org/10.1016/j.surfcoat.2016.10.082.

[89] T. Popela, D. Vojtěch, J.-B. Vogt, A. Michalcová, Structural, mechanical and oxidation characteristics of siliconized Ti–Al–X (X=Nb, Ta) alloys, Appl. Surf. Sci. 307 (2014) 579–588. https://doi.org/10.1016/j.apsusc.2014.04.076.

[90] D. Vojtěch, T. Kubatík, M. Pavlíčková, J. Maixner, Intermetallic protective coatings on titanium, Intermetallics. 14 (2006) 1181–1186. https://doi.org/10.1016/j.intermet.2005.11.035.

[91] S.A. Mantri, D. Choudhuri, T. Alam, V. Ageh, F. Sun, F. Prima, R. Banerjee, Change in the deformation mode resulting from beta-omega compositional partitioning in a Ti Mo alloy: Room versus elevated temperature, Scr. Mater. 130 (2017) 69–73. https://doi.org/10.1016/j.scriptamat.2016.11.013.

[92] J.J. Donovan, D. Kremser, J. Fournelle, K. Goermann, Probe For EPMA v.12.6.3 User's Guide and Reference. Xtreme Edition, (2019) 431.

[93] D.A.S. J.J. Donovan M.L. Rivers, An Improved Interference Correction for Trace Element Analysis, Microbeam Anal. 2 (1993) 23–28.

[94] J.I. Goldstein, S.K. Choi, F.J.J. Van Loo, H.J.M. Heijligers, G.F. Bastin, W.G. Sloof, The influence of oxide surface layers on bulk electron probe microanalysis of oxygen-application to Ti-Si-O compounds, Scanning. 15 (1993) 165–170. https://doi.org/10.1002/sca.4950150310.

[95] Z. Liu, G. Welsch, Literature Survey on Diffusivities of Oxygen, Aluminum, and Vanadium in Alpha Titanium, Beta Titanium, and in Rutile, Metall. Trans. A. 19 (1988) 1121–1125. https://doi.org/10.1007/BF02628396.

[96] J.C. Williams, M.J. Blackburn, The Influence of Misfit on the Morphology and Stability of the Omega Phase in Titanium-Transition Metal Alloys, Trans. Metall. Soc. AIME. 245 (1969) 2352–2355.

[97] M. Hendrickson, S.A. Mantri, Y. Ren, T. Alam, V. Soni, B. Gwalani, M. Styles, D. Choudhuri, R. Banerjee, The evolution of microstructure and microhardness in a biomedical Ti–35Nb–7Zr–5Ta alloy, J. Mater. Sci. 52 (2016) 3062–3073. https://doi.org/10.1007/s10853-016-0591-3.

[98] A. Ramarolahy, P. Castany, F. Prima, P. Laheurte, I. Peron, T. Gloriant, Microstructure and mechanical behavior of superelastic Ti-24Nb-0.5O and Ti-24Nb-0.5N biomedical alloys, J Mech Behav Biomed Mater. 9 (2012) 83–90. https://doi.org/10.1016/j.jmbbm.2012.01.017.

[99] J.G. Niu, W.T. Geng, Oxygen-induced lattice distortion in β -Ti 3 Nb and its suppression effect on β to α ″ transformation, Acta Mater. 81 (2014) 194–203. https://doi.org/10.1016/j.actamat.2014.07.060.

[100] R. Salloom, D. Reith, R. Banerjee, S.G. Srinivasan, First principles calculations on the effect of interstitial oxygen on phase stability and β–α″ martensitic transformation in Ti–Nb alloys, J. Mater. Sci. 53 (2018) 11473–11487. https://doi.org/10.1007/s10853-018-2381-6.

[101] C. Hammond, Orthorhombic martensites in titanium alloys, Scr. Metall. 6 (1972) 569–570. https://doi.org/10.1016/0036-9748(72)90093-2.

[102] B. Yuan, B. Yang, Y. Gao, M. Lai, X.H. Chen, M. Zhu, Achieving ultra-high superelasticity and cyclic stability of biomedical Ti–11Nb–4O (at.%) alloys by controlling Nb and oxygen content, Mater. Des. 92 (2016). https://doi.org/10.1016/j.matdes.2015.12.148.

[103] M. Tahara, T. Inamura, H.Y. Kim, S. Miyazaki, H. Hosoda, Role of oxygen atoms in α″ martensite of Ti-20 at.% Nb alloy, Scr. Mater. 112 (2016) 15–18.

https://doi.org/10.1016/j.scriptamat.2015.08.033.

[104] J.L. Zhang, C.C. Tasan, M.J. Lai, D. Yan, D. Raabe, Partial recrystallization of gum metal to achieve enhanced strength and ductility, Acta Mater. 135 (2017) 400–410. https://doi.org/10.1016/j.actamat.2017.06.051.

[105] M. Fatemi, C.S. Pande, H.R. Child, Detection of several ω-phase morphologies in β-III Ti by small-angle neutron scattering and transmission electron microscopy, Philos. Mag. A. 48 (2006) 479–500. https://doi.org/10.1080/01418618308234908.

[106] S. Cao, Y. Jiang, R. Yang, Q.-M. Hu, Properties of β/ω phase interfaces in Ti and their implications on mechanical properties and ω morphology, Comput. Mater. Sci. 158 (2019) 49–57. https://doi.org/10.1016/j.commatsci.2018.10.042.

[107] D.L. Moffat, D.C. Larbalestier, The compctition between the alpha and omega phases in aged Ti-Nb alloys, Metall. Trans. A. 19 (1988) 1687–1694. https://doi.org/10.1007/bf02645136.

[108] D. De Fontaine, N.E. Paton, J.C. Williams, The omega phase transformation in titanium alloys as an example of displacement controlled reactions, Acta Metall. 19 (1971) 1153–1162. https://doi.org/10.1016/0001-6160(71)90047-2.

[109] R.G. Hennig, D.R. Trinkle, J. Bouchet, S.G. Srinivasan, R.C. Albers, J.W. Wilkins, Impurities block the alpha to omega martensitic transformation in titanium, Nat Mater. 4 (2005) 129–133. https://doi.org/10.1038/nmat1292.

[110] E. Cerreta, G.T. Gray, A.C. Lawson, T.A. Mason, C.E. Morris, The influence of oxygen content on the α to ω phase transformation and shock hardening of titanium, J. Appl. Phys. 100 (2006) 13530. https://doi.org/10.1063/1.2209540.

[111] M. Tane, H. Nishiyama, A. Umeda, N.L. Okamoto, K. Inoue, M. Luckabauer, Y. Nagai, T. Sekino, T. Nakano, T. Ichitsubo, Diffusionless isothermal omega transformation in titanium alloys driven by quenched-in compositional fluctuations, Phys. Rev. Mater. 3 (2019). https://doi.org/10.1103/PhysRevMaterials.3.043604.

[112] A.E. Pontau, D. Lazarus, Diffusion of titanium and niobium in bcc Ti-Nb alloys, Phys. Rev. B. 19 (1979) 4027–4037. https://doi.org/10.1103/PhysRevB.19.4027.

[113] Y. Zheng, R.E.A. Williams, J.M. Sosa, Y. Wang, R. Banerjee, H.L. Fraser, The role of the ω phase on the non-classical precipitation of the α phase in metastable β-titanium alloys, Scr. Mater. 111 (2016) 81–84. https://doi.org/10.1016/j.scriptamat.2015.08.019.

[114] W. Weng, A. Biesiekierski, Y. Li, C. Wen, Effects of selected metallic and interstitial elements on the microstructure and mechanical properties of beta titanium alloys for orthopedic applications, Materialia. 6 (2019) 100323. https://doi.org/10.1016/j.mtla.2019.100323.

[115] H.-H. Jin, H.-D. Cho, S. Kwon, C. Shin, J. Kwon, Modified preparation technique of TEM

sample for various TEM analyses of structural materials, Mater. Lett. 89 (2012) 133–136. https://doi.org/10.1016/j.matlet.2012.08.069.

[116] M.J. Lai, C.C. Tasan, D. Raabe, Deformation mechanism of ω-enriched Ti–Nb-based gum metal: Dislocation channeling and deformation induced ω–β transformation, Acta Mater. 100 (2015) 290–300. https://doi.org/10.1016/j.actamat.2015.08.047.

[117] W. Chen, J. Zhang, S. Cao, Y. Pan, M. Huang, Q. Hu, Q. Sun, L. Xiao, J. Sun, Strong deformation anisotropies of ω -precipitates and strengthening mechanisms in Ti-10V-2Fe-3Al alloy micropillars: Precipitates shearing vs precipitates disordering, Acta Mater. 117 (2016) 68–80. https://doi.org/10.1016/j.actamat.2016.06.065.

[118] M.D. Uchic, D.M. Dimiduk, J.N. Florando, W.D. Nix, Sample dimensions influence strength and crystal plasticity, Science (80-.). 305 (2004) 986–989. https://doi.org/10.1126/science.1098993.

[119] B. Girault, A.S. Schneider, C.P. Frick, E. Arzt, Strength Effects in Micropillars of a Dispersion Strengthened Superalloy, Adv. Eng. Mater. 12 (2010) 385–388. https://doi.org/10.1002/adem.201000089.

[120] R. Gu, A.H.W. Ngan, Size effect on the deformation behavior of duralumin micropillars, Scr. Mater. 68 (2013). https://doi.org/10.1016/j.scriptamat.2013.02.012.

[121] J.P. Wharry, K.H. Yano, P. V Patki, Intrinsic-extrinsic size effect relationship for micromechanical tests, Scr. Mater. 162 (2019) 63–67. https://doi.org/10.1016/j.scriptamat.2018.10.045.

[122] H. Zhang, B.E. Schuster, Q. Wei, K.T. Ramesh, The design of accurate micro-compression experiments, Scr. Mater. 54 (2006) 181–186. https://doi.org/10.1016/j.scriptamat.2005.06.043.

[123] C. Shin, S. Lim, H. Jin, P. Hosemann, J. Kwon, Development and testing of microcompression for post irradiation characterization of ODS steels, J. Nucl. Mater. 444 (2014) 43–48. https://doi.org/10.1016/j.jnucmat.2013.09.025.

[124] C. Shin, H. h Jin, H. Sung, D.J. Kim, Y.S. Choi, K. Oh, Evaluation of Irradiation Effects on Fracture Strength of Silicon Carbide using Micropillar Compression Tests, Exp. Mech. 53 (2012) 687–697. https://doi.org/10.1007/s11340-012-9678-1.

[125] D. Kiener, C. Motz, G. Dehm, Micro-compression testing: A critical discussion of experimental constraints, Mater. Sci. Eng. A. 505 (2009) 79–87. https://doi.org/10.1016/j.msea.2009.01.005.

[126] G. Vander Voort, Measurement of Microstructure, in: Met. Handb. Desk Ed., ASM International, 1998. https://doi.org/10.31399/asm.hb.mhde2.a0003248.

[127] A.J. Ardell, Precipitation hardening, Metall. Trans. A. 16 (1985) 2131–2165. https://doi.org/10.1007/BF02670416.

[128] Y. Pan, Q. Sun, L. Xiao, X. Ding, J. Sun, Plastic deformation behavior and microscopic mechanism of metastable Ti-10V-2Fe-3Al alloy single crystal pillars orientated to <011>β in submicron scales Part I: Double size effects and martensitic transformation prediction, Mater. Sci. Eng. A. 743 (2019) 798–803. https://doi.org/10.1016/j.msea.2018.11.140.

[129] Y. Pan, H. Wu, X. Wang, Q. Sun, L. Xiao, X. Ding, J. Sun, E.K.H. Salje, Rotatable precipitates change the scale-free to scale dependent statistics in compressed Ti nano-pillars, Sci Rep. 9 (2019) 3778. https://doi.org/10.1038/s41598-019-40526-5.

[130] W. Kou, Q. Sun, L. Xiao, J. Sun, Coupling effect of second phase and phase interface on deformation behaviours in microscale Ti-55531 pillars, J. Alloys Compd. 820 (2020) 153421. https://doi.org/10.1016/j.jallcom.2019.153421.

[131] H. Gleiter, E. Hornbogen, Precipitation hardening by coherent particles, Mater. Sci. Eng. 2 (1968) 285–302. https://doi.org/10.1016/0025-5416(68)90047-5.

[132] M.F. Ashby, Oxide Dispersion Strengthening, in: G.S. Ansell, T.D. Cooper, F.V. Lenel (Eds.), Gordon & Breach, 1968.

[133] Y. Fu, W. Xiao, J. Wang, L. Ren, X. Zhao, C. Ma, Oxygen induced crystal structure transition of martensite in Ti–Nb–Fe alloys, Mater. Lett. 262 (2020) 127026. https://doi.org/10.1016/j.matlet.2019.127026.

[134] A. Devaraj, S. Nag, R. Banerjee, Alpha phase precipitation from phase-separated beta phase in a model Ti–Mo–Al alloy studied by direct coupling of transmission electron microscopy and atom probe tomography, Scr. Mater. 69 (2013). https://doi.org/10.1016/j.scriptamat.2013.06.011.

[135] S. Nag, Y. Zheng, R.E.A. Williams, A. Devaraj, A. Boyne, Y. Wang, P.C. Collins, G.B. Viswanathan, J.S. Tiley, B.C. Muddle, R. Banerjee, H.L. Fraser, Non-classical homogeneous precipitation mediated by compositional fluctuations in titanium alloys, Acta Mater. 60 (2012). https://doi.org/10.1016/j.actamat.2012.07.033.

[136] A. Boyne, D. Wang, R.P. Shi, Y. Zheng, A. Behera, S. Nag, J.S. Tiley, H.L. Fraser, R. Banerjee, Y. Wang, Pseudospinodal mechanism for fine α/β microstructures in β-Ti alloys, Acta Mater. 64 (2014). https://doi.org/10.1016/j.actamat.2013.10.026.

[137] C.A.F. Salvador, V.C. Opini, M.G. Mello, R. Caram, Effects of double-aging heat-treatments on the microstructure and mechanical behavior of an Nb-modified Ti-5553 alloy, Mater. Sci. Eng. A. 743 (2019). https://doi.org/10.1016/j.msea.2018.11.086.

[138] T. Furuhara, T. Maki, T. Makino, Microstructure control by thermomechanical processing in β-Ti–15–3 alloy, J. Mater. Process. Technol. 117 (2001). https://doi.org/10.1016/S0924-0136(01)00790-7.

[139] X. Wu, J. del Prado, Q. Li, A. Huang, D. Hu, M.H. Loretto, Analytical electron microscopy of C-free and C-containing Ti–15–3, Acta Mater. 54 (2006). https://doi.org/10.1016/j.actamat.2006.07.002.

[140] TIMETAL15-3, Https://Www.Timet.Com/Assets/Local/Documents/Datasheets/Metastablebetaalloys/15-3.Pdf. (n.d.).

[141] O.M. Ivasishin, P.E. Markovsky, Y. V. Matviychuk, S.L. Semiatin, Precipitation and recrystallization behavior of beta titanium alloys during continuous heat treatment, Metall. Mater. Trans. A. 34 (2003) 147–158. https://doi.org/10.1007/s11661-003-0216-8.

[142] O.M. Ivasishin, P.E. Markovsky, S.L. Semiatin, C.H. Ward, Aging response of coarse- and fine-grained β titanium alloys, Mater. Sci. Eng. A. 405 (2005). https://doi.org/10.1016/j.msea.2005.06.027.

[143] A. Behera, S. Nag, K. Mahdak, H. Mohseni, J. Tiley, R. Banerjee, Influence of oxygen ingress on fine scale precipitation of α-Ti during oxidation of Beta21S β-Ti alloy, J. Mater. Sci. 48 (2013). https://doi.org/10.1007/s10853-013-7470-y.

[144] T.-S. Jun, G. Sernicola, F.P.E. Dunne, T.B. Britton, Local deformation mechanisms of two-phase Ti alloy, Mater. Sci. Eng. A. 649 (2016). https://doi.org/10.1016/j.msea.2015.09.016.

[145] W. Kou, Q. Sun, L. Xiao, J. Sun, Superior plasticity stability and excellent strength in Ti-55531 alloy micropillars via harmony slip in nanoscale α/β phases, Sci. Rep. 9 (2019). https://doi.org/10.1038/s41598-019-41574-7.

[146] P. Samimi, D.A. Brice, I. Ghamarian, Y. Liu, P.C. Collins, Systematic Assessment of the Influence of Mo Concentration on the Oxygen Ingress in Ti–Mo System During High Temperature Oxidation, Oxid. Met. 85 (2016). https://doi.org/10.1007/s11085-015-9600-1.

[147] P. Zháňal, P. Harcuba, M. Hájek, B. Smola, J. Stráský, J. Šmilauerová, J. Veselý, M. Janeček, Evolution of ω phase during heating of metastable β titanium alloy Ti–15Mo, J. Mater. Sci. 53 (2018) 837–845. https://doi.org/10.1007/s10853-017-1519-2.

[148] A. Devaraj, R.E.A. Williams, S. Nag, R. Srinivasan, H.L. Fraser, R. Banerjee, Three-dimensional morphology and composition of omega precipitates in a binary titanium–molybdenum alloy, Scr. Mater. 61 (2009). https://doi.org/10.1016/j.scriptamat.2009.06.006.

[149] T.K. Roy, R. Balasubramaniam, A. Ghosh, Determination of oxygen and nitrogen diffusivities in titanium aluminides by subscale microhardness profiling, Scr. Mater. 34 (1996) 1425–1430. https://doi.org/10.1016/1359-6462(96)00005-x.

[150] P. Samimi, Y. Liu, I. Ghamarian, P.C. Collins, A novel tool to assess the influence of alloy composition on the oxidation behavior and concurrent oxygen-induced phase transformations for binary Ti–xMo alloys at 650°C, Corros. Sci. 89 (2014). https://doi.org/10.1016/j.corsci.2014.09.010.

[151] J. Il Kim, H.Y. Kim, H. Hosoda, S. Miyazaki, Shape Memory Behavior of Ti–22Nb–(0.5–

2.0)O(at%) Biomedical Alloys, Mater. Trans. 46 (2005). https://doi.org/10.2320/matertrans.46.852.

[152] Q. Wei, L. Wang, Y. Fu, J. Qin, W. Lu, D. Zhang, Influence of oxygen content on microstructure and mechanical properties of Ti–Nb–Ta–Zr alloy, Mater. Des. 32 (2011). https://doi.org/10.1016/j.matdes.2010.11.049.

[153] R.. Bryant, The solubility of oxygen in transition metal alloys, J. Less Common Met. 4 (1962). https://doi.org/10.1016/0022-5088(62)90060-7.

[154] L. Brewer, R.H. Lamoreaux, The Mo-O system (Molybdenum-Oxygen), Bull. Alloy Phase Diagrams. 1 (1980) 85–89. https://doi.org/10.1007/BF02881199.

[155] J.J. English, D.M.I.C. (U.S.), Binary and ternary phase diagrams of columbium, molybdenum, tantalum, and tungsten, (1961) 1 volume (various pagings). file://catalog.hathitrust.org/Record/102326559.

[156] J. Coakley, B.-S. Seong, D. Dye, M. Ohnuma, Isothermal omega kinetics in beta-titanium alloys, Philos. Mag. Lett. 97 (2017). https://doi.org/10.1080/09500839.2017.1282633.

[157] G.B. Gibbs, D. Graham, D.H. Tomlin, Diffusion in titanium and titanium—niobium alloys, Philos. Mag. 8 (1963). https://doi.org/10.1080/14786436308207292.

[158] J.K. Tien, S.M. Copley, The effect of orientation and sense of applied uniaxial stress on the morphology of coherent gamma prime precipitates in stress annealed nickel-base superalloy crystals, Metall. Trans. 2 (1971). https://doi.org/10.1007/BF02663347.

[159] J.K. Tien, S.M. Copley, The effect of uniaxial stress on the periodic morphology of coherent gamma prime precipitates in nickel-base superalloy crystals, Metall. Trans. 2 (1971). https://doi.org/10.1007/BF02662660.

[160] M. Kamaraj, Rafting in single crystal nickel-base superalloys — An overview, Sadhana. 28 (2003). https://doi.org/10.1007/BF02717129.

[161] A. Suzuki, H. Inui, T.M. Pollock, L1 $_2$ -Strengthened Cobalt-Base Superalloys, Annu. Rev. Mater. Res. 45 (2015). https://doi.org/10.1146/annurev-matsci-070214-021043.

[162] A.M. Jokisaari, S.S. Naghavi, C. Wolverton, P.W. Voorhees, O.G. Heinonen, Predicting the morphologies of γ′ precipitates in cobalt-based superalloys, Acta Mater. 141 (2017). https://doi.org/10.1016/j.actamat.2017.09.003.

[163] A.W. Bowen, Omega phase embrittlement in aged Ti-15%Mo, Scr. Metall. 5 (1971). https://doi.org/10.1016/0036-9748(71)90258-4.

[164] H. Okamoto, O-Ti (Oxygen-Titanium), J. Phase Equilibria Diffus. 32 (2011) 473–474. https://doi.org/10.1007/s11669-011-9935-5.

[165] G. Salomonsen, N. Norman, O. Lonsjo, T.G. Finstad, Kinetics and Mechanism of Oxide

Formation on Titanium, Vanadium and Chromium Thin-Films, J. Less-Common Met. 158 (1990) 251–265. https://doi.org/Doi 10.1016/0022-5088(90)90060-W.

[166] P. Samimi, P.C. Collins, Oxidation behavior of binary Ti-xW (0 <= x <= 30, wt%) alloys at 650 degrees C as a function of W concentration, Corros. Sci. 111 (2016) 531–540. https://doi.org/10.1016/j.corsci.2016.05.038.

[167] The Interactive Ellingham Diagram, 2017 (2015). https://www.doitpoms.ac.uk/tlplib/ellingham_diagrams/interactive.php.

[168] S.M. Howard, Ellingham Diagrams, (2006). http://showard.sdsmt.edu/MET320/Handouts/EllinghamDiagrams/Binder_All_2009_12_06.pdf.

[169] K. Chou, P.-W. Chu, C.G. Levi, E.A. Marquis, Influence of a silicon-bearing film on the early stage oxidation of pure titanium, J. Mater. Sci. 52 (2017) 9884–9894. https://doi.org/10.1007/s10853-017-1143-1.

[170] R. Mitra, Mechanical behaviour and oxidation resistance of structural silicides, Int. Mater. Rev. 51 (2013) 13–64. https://doi.org/10.1179/174328006x79454.

[171] S.P. Murarka, D.B. Fraser, Thin-Film Interaction between Titanium and Polycrystalline Silicon, J. Appl. Phys. 51 (1980) 342–349. https://doi.org/Doi 10.1063/1.327378.

[172] E. V Shalaeva, S. V Borisov, O.F. Denisov, M. V Kuznetsov, Metastable phase diagram of Ti–Si–N(O) films (CSi<30 at.%), Thin Solid Films. 339 (1999) 129–136. https://doi.org/10.1016/s0040-6090(98)01259-0.

[173] R. Beyers, R. Sinclair, M.E. Thomas, Phase-Equilibria in Thin-Film Metallizations, J. Vac. Sci. Technol. B. 2 (1984) 781–784. https://doi.org/Doi 10.1116/1.582879.

[174] R. Beyers, Thermodynamic Considerations in Refractory Metal-Silicon-Oxygen Systems, J. Appl. Phys. 56 (1984) 147–152. https://doi.org/Doi 10.1063/1.333738.

[175] M. Fiore, F.B. Neto, C.R.D. Azevedo, Assessment of the Ti-Rich Corner of the Ti-Si Phase Diagram: The Recent Dispute About the Eutectoid Reaction, Mater. Res. J. Mater. 19 (2016) 942–953. https://doi.org/10.1590/1980-5373-MR-2016-0157.

[176] M. Fiore, F. Beneduce Neto, C.R. de F. Azevedo, Assessment of the Ti-rich corner of the Ti-Si phase diagram using two sublattices to describe the Ti5Si3 phase, REM - Int. Eng. J. 70 (2017) 201–207. https://doi.org/10.1590/0370-44672016700073.

[177] C.R. de Farias Azevedo, H.M. Flower, Microstructure and phase relationships in Ti–Al–Si system, Mater. Sci. Technol. 15 (2013) 869–877. https://doi.org/10.1179/026708399101506661.

[178] M. Berti, A. V Drigo, C. Cohen, J. Siejka, G.G. Bentini, R. Nipoti, S. Guerri, Titanium Silicide Formation - Effect of Oxygen Distribution in the Metal-Film, J. Appl. Phys. 55

(1984) 3558–3565. https://doi.org/Doi 10.1063/1.332946.

[179] J.I. Goldstein, S.K. Choi, F.J.J. Vanloo, G.F. Bastin, R. Metselaar, Solid-State Reactions and Phase-Relations in the Ti-Si-O System at 1373 K, J. Am. Ceram. Soc. 78 (1995) 313–322. https://doi.org/DOI 10.1111/j.1151-2916.1995.tb08802.x.

[180] H.E. Evans, Cracking and Spalling of Protective Oxide Layers, Mater. Sci. Eng. a-Structural Mater. Prop. Microstruct. Process. 120 (1989) 139–146. https://doi.org/Doi 10.1016/0921-5093(89)90731-4.

[181] A. Szekeres, P. Danesh, Mechanical stress in SiO2/Si structures formed by thermal oxidation of amorphous and crystalline silicon, Semicond. Sci. Technol. 11 (1996) 1225–1230. https://doi.org/Doi 10.1088/0268-1242/11/8/019.

[182] E. Kobeda, E.A. Irene, A Measurement of Intrinsic Sio2 Film Stress Resulting from Low-Temperature Thermal-Oxidation of Si, J. Vac. Sci. Technol. B. 4 (1986) 720–722. https://doi.org/Doi 10.1116/1.583603.

[183] S.Q. Wang, J.W. Mayer, Thermally induced reactions of thin Ti and Nb films with SiO2substrates, J. Appl. Phys. 67 (1990) 2932–2938. https://doi.org/10.1063/1.345412.

[184] H. Lee, S. Dregia, S. Akbar, M. Alhoshan, Growth of 1-D TiO2Nanowires on Ti and Ti Alloys by Oxidation, J. Nanomater. 2010 (2010) 1–7. https://doi.org/10.1155/2010/503186.

[185] B. Dinan, D. Gallego-Perez, H. Lee, D. Hansford, S.A. Akbar, Thermally grown TiO2 nanowires to improve cell growth and proliferation on titanium based materials, Ceram. Int. 39 (2013) 5949–5954. https://doi.org/10.1016/j.ceramint.2012.12.004.

[186] X. Peng, J. Wang, D.F. Thomas, A. Chen, Tunable growth of TiO(2) nanostructures on Ti substrates, Nanotechnology. 16 (2005) 2389–2395. https://doi.org/10.1088/0957-4484/16/10/066.

[187] X.S. Peng, A.C. Chen, Aligned TiO2 nanorod arrays synthesized by oxidizing titanium with acetone, J. Mater. Chem. 14 (2004) 2542–2548. https://doi.org/10.1039/b404750h.

[188] J.M. Wu, H.C. Shih, W.T. Wu, Y.K. Tseng, I.C. Chen, Thermal evaporation growth and the luminescence property of TiO2 nanowires, J. Cryst. Growth. 281 (2005) 384–390. https://doi.org/10.1016/j.jcrysgro.2005.04.018.

[189] G.K. Mor, O.K. Varghese, M. Paulose, K. Shankar, C.A. Grimes, A review on highly ordered, vertically oriented TiO2 nanotube arrays: Fabrication, material properties, and solar energy applications, Sol. Energy Mater. Sol. Cells. 90 (2006) 2011–2075. https://doi.org/10.1016/j.solmat.2006.04.007.

[190] S. Wu, Z. Weng, X. Liu, K.W.K. Yeung, P.K. Chu, Functionalized TiO2Based Nanomaterials for Biomedical Applications, Adv. Funct. Mater. 24 (2014) 5464–5481. https://doi.org/10.1002/adfm.201400706.

[191] A.W. Tan, B. Pingguan-Murphy, R. Ahmad, S.A. Akbar, Advances in fabrication of TiO2 nanofiber/nanowire arrays toward the cellular response in biomedical implantations: a review, J. Mater. Sci. 48 (2013) 8337–8353. https://doi.org/10.1007/s10853-013-7659-0.

[192] R. Mitra, V.V.R. Rao, Elevated-temperature oxidation behavior of titanium silicide and titanium silicide based alloy and composite, Metall. Mater. Trans. a-Physical Metall. Mater. Sci. 29 (1998) 1665–1675. https://doi.org/DOI 10.1007/s11661-998-0089-y.

[193] Z.H. Tang, J.J. Williams, A.J. Thom, M. Akinc, High temperature oxidation behavior of Ti5Si3-based intermetallics, Intermetallics. 16 (2008) 1118–1124. https://doi.org/10.1016/j.intermet.2008.06.013.

[194] D. Vojtěch, T. Kubatík, K. Jurek, J. Maixner, Cyclic-Oxidation Resistance of Protective Silicide Layers on Titanium, Oxid. Met. 63 (2005) 305–323. https://doi.org/10.1007/s11085-005-4385-2.

[195] Z. Li, C.L. Liao, Y.X. Liu, X.M. Wang, Y. Wu, M.X. Zhao, Z.H. Long, F.C. Yin, 700 degrees C Isothermal Section of the Al-Ti-Si Ternary Phase Diagram, J. Phase Equilibria Diffus. 35 (2014) 564–574. https://doi.org/10.1007/s11669-014-0325-7.

[196] S. Becker, A. Rahmel, M. Schutze, Oxidation of Tisi2 and Mosi2, Solid State Ionics. 53 (1992) 280–289. https://doi.org/Doi 10.1016/0167-2738(92)90391-2.

[197] S. Melsheimer, M. Fietzek, V. Kolarik, A. Rahmel, M. Schutze, Oxidation of the intermetallics MoSi2 and TiSi2 - A comparison, Oxid. Met. 47 (1997) 139–203. https://doi.org/Doi 10.1007/Bf01682375.

[198] J.J. Williams, M. Akinc, Oxidation Resistance of Ti5Si3 and Ti5Si3Zx at 1000°C (Z = C, N, or O), Oxid. Met. 58 (2002) 57–71. https://doi.org/10.1023/a:1016012507682.

[199] W. Lengauer, The titanium-nitrogen system: A study of phase reactions in the subnitride region by means of diffusion couples, Acta Metall. Mater. 39 (1991) 2985–2996. https://doi.org/10.1016/0956-7151(91)90031-U.

[200] M. Tahara, H.Y. Kim, H. Hosoda, T. Nam, S. Miyazaki, Effect of nitrogen addition and annealing temperature on superelastic properties of Ti–Nb–Zr–Ta alloys, Mater. Sci. Eng. A. 527 (2010) 6844–6852. https://doi.org/10.1016/j.msea.2010.07.052.

[201] T. Borkar, S. Gopagoni, S. Nag, J.Y. Hwang, P.C. Collins, R. Banerjee, In situ nitridation of titanium–molybdenum alloys during laser deposition, J. Mater. Sci. 47 (2012) 7157–7166. https://doi.org/10.1007/s10853-012-6656-z.

[202] A.M. Chaze, C. Coddet, The role of nitrogen in the oxidation behaviour of titanium and some binary alloys, J. Less Common Met. 124 (1986) 73–84. https://doi.org/10.1016/0022-5088(86)90478-9.

[203] C. Dupressoire, A. Rouaix-Vande Put, P. Emile, C. Archambeau-Mirguet, R. Peraldi, D. Monceau, Effect of Nitrogen on the Kinetics of Oxide Scale Growth and of Oxygen

Dissolution in the Ti6242S Titanium-Based Alloy, Oxid. Met. 87 (2017) 343–353. https://doi.org/10.1007/s11085-017-9729-1.

[204] Z. Lei, X. Liu, Y. Wu, H. Wang, S. Jiang, S. Wang, X. Hui, Y. Wu, B. Gault, P. Kontis, D. Raabe, L. Gu, Q. Zhang, H. Chen, H. Wang, J. Liu, K. An, Q. Zeng, T.-G. Nieh, Z. Lu, Enhanced strength and ductility in a high-entropy alloy via ordered oxygen complexes, Nature. 563 (2018) 546–550. https://doi.org/10.1038/s41586-018-0685-y.

[205] M.D. Uchic, P.A. Shade, D.M. Dimiduk, Plasticity of Micrometer-Scale Single Crystals in Compression, Annu. Rev. Mater. Res. 39 (2009) 361–386. https://doi.org/10.1146/annurev-matsci-082908-145422.

[206] J.R. Greer, J.T.M. De Hosson, Plasticity in small-sized metallic systems: Intrinsic versus extrinsic size effect, Prog. Mater. Sci. 56 (2011) 654–724. https://doi.org/10.1016/j.pmatsci.2011.01.005.

[207] G.F. Bastin, H.J.M. Heijligers, Quantitative Electron Probe Microanalysis of Ultra-Light Elements (Boron-Oxygen), in: Electron Probe Quant., Springer US, Boston, MA, 1991: pp. 145–161. https://doi.org/10.1007/978-1-4899-2617-3_8.

[208] B. Kasemo, J. Lausmaa, Aspects of surface physics on titanium implants., Swed. Dent. J. Suppl. 28 (1985) 19–36. http://www.ncbi.nlm.nih.gov/pubmed/3904061.